Statistical analysis of the galaxy cluster distribution from next generation cluster surveys

Srivatsan Sridhar

Université Côte D'Azur

Ecole Doctorale de Sciences Fondamentales et Appliquées

THESIS

pour obtenir le titre de

Docteur en Sciences

de Université Côte d'Azur

Discipline : Astrophysique Relativiste

présentée et soutenue par

Srivatsan Sridhar

Statistical analysis of the galaxy cluster distribution from next generation cluster surveys

Thèse dirigée par: Sophie Maurogordato & Christophe Benoist

Soutenue le 16 Décembre 2016

Jury :

M.	Oliver Hahn	Professeur	Président
M.	Lauro Moscardini	Professeur	Rapporteur
M.	Manolis Plionis	Professeur	Rapporteur
M.	Jon Loveday	Professeur	Examinateur
Mme.	Sophie Maurogordato	Directeur de Recherches	Directeur de thèse
M.	Christophe Benoist	Astronome adjoint	Directeur de thèse

UNIVERSITÉ CÔTE D'AZUR

Université Côte D'Azur

Doctoral School of Fundamental Sciences and Applications

THESIS

presented for the degree of

Doctor in Sciences

Université Côte d'Azur

Discipline : Relativistic Astrophysics

presented by

Srivatsan Sridhar

Statistical analysis of the galaxy cluster distribution from next generation cluster surveys

Thesis supervised by : Sophie Maurogordato & Christophe Benoist

Defended on the 16th of December 2016

Jury :

Dr.	Oliver Hahn	Professor	President
Dr.	Lauro Moscardini	Professor	Referee
Dr.	Manolis Plionis	Professor	Referee
Dr.	Jon Loveday	Professor	Examiner
Dr.	Sophie Maurogordato	Director of research	Thesis supervisor
Dr.	Christophe Benoist	Associate Astronomer	Thesis co-supervisor

Acknowledgements

"Dream is not that which you see while sleeping, it is something that does not let you sleep."

—Dr.A.P.J Abdul Kalam

"I am not afraid of a person who knows 1000 kicks, but I am afraid of a person who has practised a single kick for 1000 times."

—Bruce Lee

For the past 22 years I have been a student and this thesis marks the end of my student life! In Tamil culture we acknowledge மாதா (Maathaa – Mother), பிதா (Pithaa – Father), குரு (Guru – Teacher), தெய்வம் (Dheivam – God), in this order.

So I would like to acknowledge my parents first. Coming from a country that is obsessed with engineering, where every parent wants his/her son/daughter to become an engineer, I was lucky enough to have parents who were different. The moment I said I would like to take up astrophysics as my career, they were ready to say yes. They have not only respected my ambitions, but have also helped me to regain my mental strength during times of stress.

I also would like to acknowledge my grandparents, who have shown only love and affection towards me.

Then come the teachers who have guided me in my life. I would like to take up this opportunity to thank all my teachers from kindergarten to my PhD.

During the tenure of my B.Sc Physics, I was lucky enough to have Dr.Merlin Shyla as one of my lecturers who motivated me to present my very first talk in a state level conference titled "Innovations in Green Energy". I take this opportunity to thank her.

I would also like to thank Dr. Sundara Raman (ex-scientist at Indian Institute of Astrophysics, Kodaikanal) for guiding me in several aspects of taking up astrophysics as a career.

M.Sc Astronomy was not so easy, as it was my first experience of life in international soil. I was made to feel at home thanks to Dr. Jon Loveday, my supervisor, mentor and well-wisher. He was always ready to help me in my thesis project, especially teaching me several technical aspects of galaxy formation which was something new to me. Thanks to his guidance, I passed my M.Sc with merit which paved the way for me to obtain an Erasmus Mundus grant to do my PhD.

I still remember the day I landed in Nice, and was welcomed by my PhD supervisor Dr. Sophie Maurogordato. Sophie along with Christophe and Alberto have made me feel comfortable throughout the course of my PhD and it is one of the important aspects in the life of PhD student. I was so comfortable that I consider Sophie and Alberto as my foster parents and Christophe as my uncle! Most of my friends have been really jealous as I got

to do my PhD in a city that is a tourist destination! I thank Erasmus Mundus and IRAP for sponsoring my PhD.

I would also like to thank the referees and the jury members to have taken the time to read my thesis despite their busy schedule.

Life as we know it is not complete without friends. I have been lucky throughout my life to have such wonderful friends. Be it moments of sorrow, joy or happiness, they have always been with me to share it. I would like to take this moment to acknowledge all my childhood friends, Sriram, Lalith, Ajith, Tarun, Aditya, Anbu, Anirudh, Vivek for all those night stays and uncountable moments of joy. I also take this moment to acknowledge my best friend Kalees who is no more with me to share this moment of happiness. My friends from Loyola college, Karthik Mohan, Vikram, Karthick, Arun, Praveen, Aditya with whom my three years in Loyola was a fun ride, I would like to acknowledge them at this moment.

I was really worried when I reached France as my French was and still is not really good. But I was lucky enough to have friends here at OCA who were from all over the world with whom I have shared several wonderful moments! I take this opportunity to acknowledge my friends for helping me out with many things during the tenure of my PhD. Onelda (for helping me out with several administrative stuff), Husne (for giving me the first marriage invitation that was addressed to me), Zeinab (for those moments at your place during Christmas), Samir (for those table tennis matches), Narges (for those times at Les Orangettes), Pier-Franceso (for sharing those wonder moments in the office), Marina (for those moments at the pub), Gerardo (for those talks about philosophy), Gustavo (for those talks about Brazilian football), Sarunas (for those wonderful moments at your place), Remi (for those random talks in my office), Sergey (for all the table tennis matches), Daniel (for those cricket moments), Gianluca (for all those talks about galaxy clusters), Pier Janin (for those party dances) and Andrea Chiavassa (for those table tennis matches), I acknowledge all of you!

A special acknowledgement to Suvendu (for those times at your apartment), Alkis (those football/table tennis and billiards moments), Alvaro (for the time in Tandoori Flame, those picnics at Coco beach, the Facebook “hacking” contest at OCA), Govind (for being the only person speaking Tamil!), Kateryna (all those fun times and parties), Arwa (for those umpteen chats in our office) and Sinan (for being the first person to welcome me to what is now “my” office!).

Last but not least, my fiancèe Madhumitha! I cannot imagine how lucky I have been from the moment I met her. PhD has been a tough task, and I have faced more stressful moments than joyful moments and it was her comforting words and the Skype calls that kept me pushing the boundary. Love you loads Madhu!

I would like to thank Lord Venkateshwara and Padmavati Thaayaar for showering me with their blessings.

Introduction

The theoretical framework of modern cosmology is based on Einstein's general theory of relativity. Assuming homogeneity and isotropy of space, the solution of the general relativity equations give us the Friedmann-Lemaître cosmological models, where the geometry of space and the evolution of the Universe depend on a limited number of parameters. The Big Bang theory predicts an initial singularity and implies that in the past the Universe was dense and hot. These so called cosmological parameters can be constrained by the observations of the Universe at different ages and scales. Today the most successful model which is able to reproduce the properties of the CMB, the large-scale structure and the accelerated expansion of the Universe is the ΛCDM model. This model assumes that the percentage of the energy budget of the Universe is in the form of dark matter (25%) and dark energy (70%). The nature of both dark matter and the cosmological constant still remain unknown.

The first direct evidence of the accelerated expansion of the Universe came from supernova observations (Perlmutter et al., 1999). An explanation for this accelerated expansion is a challenge faced by cosmologists, determining if it is due to a positive cosmological constant, a time–varying dark energy component or a modified theory of gravity. This fundamental question is addressed through the analysis of various complementary cosmological probes with different systematics, as for instance weak lensing, galaxy clustering, baryon acoustic oscillations and redshift-space distortions.

In this dissertation we will be concentrating on galaxy clusters, and analyse how they can be used as cosmological probes. Galaxy cluster counts as a function of redshift and mass are sensitive to dark energy through their dependence on the volume element and on the structure growth rate, and so information from cluster counts can be added with cluster-clustering information to constrain cosmology. Recent cosmological forecasting based on galaxy clusters confirms that the figure of merit significantly increases when adding cluster clustering information (Sartoris et al., 2016). Cluster clustering can be measured through the two–point correlation function, the Fourier transform of the power spectrum, which is one of the most successful statistics for analysing clustering processes (Totsuji and Kihara, 1969; Peebles, 1980). In cosmology, it is a standard tool to test models of structure formation and evolution.

Major galaxy surveys are currently ongoing (DES, BOSS, KIDS, Pan-STARRS) or in preparation (eROSITA, LSST, Euclid) and will provide cluster catalogues probing an unprecedented range of scales, redshifts, and masses with large statistics. The wide areas covered by these surveys will give access to unprecedented statistics (~100,000 clusters expected with Dark Energy Survey, eROSITA and Euclid survey) that will allow us to cover the high mass, high redshift tail of the mass distribution, to control cosmic variance, and to map the large scales at which the BAO signature is expected (~ 100Mpc). However, for the majority of these surveys, redshifts of individual galaxies will be mostly estimated by multiband photometry which implies non-negligible errors on redshift resulting in potential difficulties in

recovering the real-space clustering.

We investigate to which accuracy it is possible to recover the real-space two-point correlation function of galaxy clusters from cluster catalogues based on photometric redshifts, and test our ability to detect and measure the redshift and mass evolution of the correlation length r_0 and of the bias parameter $b(M, z)$ as a function of the uncertainty on the cluster redshift estimate.

State-of-the-art weak-lensing masses will be measured for massive $z \lesssim 1$ clusters, but it will be necessary to rely on mass proxies to estimate the mass of the high-z and low-mass tail of galaxy clusters. For this purpose, richness as a mass proxy will be investigated. One intrinsic difficulty in constraining the cosmological models with galaxy cluster counts comes from uncertainties in cluster mass estimates and on the difficulty to calibrate related mass proxies. One can overcome this difficulty adding the information related to the clustering properties of clusters, due to the fact that their power spectrum amplitude depends mainly on the halo mass. When combining the redshift-averaged cluster power spectrum and the evolution of the number counts in a given survey, the constraints on the Dark Energy equation of state are dramatically improved (Majumdar and Mohr, 2004). A key goal for cluster cosmology especially from photometric catalogues is trying to reduce the scatter between the cluster mass and richness. When the correlation between cluster richness and mass is improved, the cluster richness can be used to infer cluster masses even out to high redshifts. We calculate the evolution of this scatter at different redshift ranges from simulated catalogues.

Here we provide a synopsis of each chapter in this thesis.

In Chapter 1 we discuss the history of the current cosmological framework, starting with the critical pillars of astronomy and cosmology which include the Hubble's law, the Big Bang Nucleosynthesis and the CMB radiation. We then review some of the theoretical foundations of cosmology such as the Einstein's equations and Friedmann equations along with definitions of the several distance measurements used in cosmology. We also explain about the observational evidences for the accelerated expansion of the Universe and theoretical framework of large scale structure formation.

In Chapter 2 a brief introduction to galaxy clusters, physical processes inside clusters, how to detect them and measure their masses is discussed.

In Chapter 3 the two-point correlation function is introduced along with its different estimators. We also revisit some of the historical studies of the galaxy and cluster correlation functions.

In Chapter 4 a brief discussion about the several ways of using galaxy clusters as cosmo-

logical probes is addressed.

Results of our study from both observational and simulated catalogues are presented in two parts. First we calculate the evolution of the two-point correlation function with both mass and redshift using cosmological redshift samples.

Then we use a Gaussian probabilistic method to generate photometric redshifts with different uncertainties, apply the deprojection method and recover the real-space correlation function. The evolution of the recovered real-space correlation function with mass and redshift is then studied. We then try to find the dependence of richness on clustering and calculate the two-point correlation function of richness cut samples from both simulated and CFHTLS detected clusters.

In Chapter 5 we show how simulations in general can be used to study galaxy clustering. Our results obtained on the evolution of the two-point correlation function with mass and redshift and the cluster bias is discussed.

In Chapter 6 we study the effect of photometric redshift errors on the correlation function and how they can be addressed. We make use of a deprojection method and show that the real-space correlation function can be recovered within a given percentage for photometric redshift catalogues with different uncertainties.

The dependence of richness on clustering and its usage as a mass proxy is studied. We also calculate the two-point correlation function of clusters detected from the CFHTLS survey by dividing the sample into several richness cuts.

Finally in Chapter 7 we provide the general conclusions obtained from our study. We also give a brief outline of how this study can be extended towards a broader perspective.

Contents

Chapter 1

History of the current cosmological framework

Contents

I would like to start this thesis with a chapter that is intended for a general audience giving a brief review of modern cosmology. First we introduce the three pillars of cosmology; the Hubble's law, the Big Bang Nucleosynthesis and the Cosmic Microwave Background radiation followed by some of the theoretical foundations of cosmology such as the Friedmann-Robertson-Walker metric and Einstein's equations. We then move on to distance measurements in cosmology which gives the reader some basic information about how various types of distances to extragalactic sources are measured. We also explain the various cosmological models including the current standard ΛCDM cosmological model and how the accelerated expansion of the Universe was discovered. We finish by introducing the theoretical models and formalisms that have been proposed to explain the formation of the large-scale structures in the Universe.

1.1 Astronomy before and after 1900

One of the oldest natural sciences known to man is astronomy dating back to thousands of years. It was perhaps one of the most common subject followed all the way from India and China in the east to prehistoric Europe and Greece in the west.

Some of the most prominent Asian astronomers of the past include Aryabhata from India, who explicitly mentioned that the earth rotates about its axis, Gan de from China who made one of the very first star catalogues. Some of the most prominent European astronomers of the past include Copernicus, who described the heliocentric model of the solar system, Galileo who used telescopes for astronomical observations and was the first to do so. Kepler was the first to attempt to derive mathematical predictions of celestial motions from assumed physical causes. Combining his physical insights with the observations made by Tycho Brahe, he discovered the three laws of planetary motion. It was Isaac Newton who further developed the relation between astronomy and physics through his laws of universal gravitation. Newton was able to explain all know gravitational phenomenon in one theoretical framework which laid many of the foundations of modern physics.

Before the 20th century, astronomical knowledge was limited to our planet Earth, the Sun, the Moon, the planets of the solar system and stars of the Milky Way. People did not know that other galaxies similar to the Milky Way existed and that we were only one among the many galaxies in the Universe. The world had to wait for the 20th century, which is said to have been the golden era of astronomy as we know today.

During the 20th century, the theory of relativity and quantum mechanics, together with the development of large telescopes and new instrumentation, led to a revolution in astronomy and to the birth of cosmology as a science. Here we highlight some of the major breakthroughs that happened during this epoch as far as extragalactic astronomy is concerned.

Until the 19th century people did not know about galaxy clusters or even groups of galaxy clusters. It was William Herschel and Charles Messier who noted strange objects in the sky which they referred to as "nebulae", especially being common in some parts of the sky than other and particularly in the constellation of Virgo. For a much detailed analysis of these "nebulae" the world had to wait for the work of Wolf, who described the Virgo and Coma clusters of galaxies (Wolf, 1924). It was still not known that these "nebulae" were extragalactic system of stars which were very similar to our Milky Way.

Hubble made observations of these "nebulae" in 1922-1923 and had a convincing proof that these objects were in fact too distant to be part of our Milky Way and were in fact, entire galaxies outside our own. He went on to present his work in the form of a paper in January 1, 1925 in the meeting of the American Astronomical Society. The galaxies and galaxy clusters were no longer "nebulae" and their mystery was revealed. Hubble went on to use the 100 inch Hooker telescope and measured the distances and velocities to these objects. He made use of Cepheids [1] for closer objects, and magnitude and size comparisons for the more distance ones.

In 1927 in the Annales de la Société Scientifique de Bruxelles (Annals of the Scientific Society of Brussels) under the title "Un Univers homogène de masse constante et de rayon croissant rendant compte de la vitesse radiale des nébuleuses extragalactiques" ("A homogeneous Universe of constant mass and growing radius accounting for the radial velocity of extragalactic nebulae") Georges Lemaître published a report (Lemaître, 1927) . In this report, he derived the Hubble's law (the detailed explanation of which will be given in Section 1.2.1), and provided the first observational estimation of the Hubble constant (Belenkiy, 2012). He linked the redshift to cosmological expansion and to relativistic cosmological models.

The graph of velocity vs distance for these objects suggested that they were directly proportional (Hubble, 1929). The gradient obtained from the graph measured 500 km s^{-1} Mpc^{-1} [2]. This positive gradient meant that the Universe was smaller in the past, which in other words meant that the Universe was expanding and this came to be known as the Hubble's law.

Fritz Zwicky applied the virial theorem to the Coma cluster of galaxies in 1937 and found that there was a mass discrepancy. The application of the virial theorem stated that the Coma cluster contained 400 times more mass than that indicated by the "luminous" and visible objects. This phenomenon was explained by an unidentified type of matter called "dark matter" which has still not been directly observed.

[1] A Cepheid variable is a type of star that pulsates radially, varying in both diameter and temperature and producing changes in brightness with a well-defined stable period and amplitude.

[2] Parsec is a unit of length, which is used to measure distances to objects outside our Solar system. 1 Parsec (pc) is equal to 3.26 light years and Mpc refers to Megaparsec, which is a distance of one million parsecs. Mpc is usually used for measuring distances to galaxies and galaxy clusters.

Thus astronomy which was restricted to the studies of the Sun, the Moon and the planets in the Solar System extended its reach to the studies of other galaxies similar to our Milky Way and galaxy clusters in the nearby Universe. Observational techniques could help theoretical studies which had predicted several critical concepts such as the expansion of the Universe and the content of the Universe in detail.

1.2 The expanding Universe

How old is the Universe? How did it began? How large is it? What will be the fate of the Universe? These are all questions that we have been asking for several thousands of years. Cosmology is a study that attempts to answer all these questions by making use of both theoretical studies (which predict certain results based on a few assumptions) and observational studies (that are required to verify the theoretical predictions). Since Georges Lemaître first noted in 1931 that an expanding Universe might be traced back to a single point in time and space where it could all have begun (Lemaître, 1931), astronomers have built on the idea of cosmic expansion. From the start of the early 20$^{\text{th}}$ century, scientists have been trying to explain about the beginning of time and the formation of structures as we see them today using several cosmological models. But two theoretical perspectives namely the Steady State theory and the Big Bang theory divided the astronomers in the mid 20$^{\text{th}}$ century.

The "steady state theory" was first proposed by Hoyle (1948). The main contradicting statement of the steady state theory compared to the Big Bang theory was that there was no beginning of the Universe. The steady state theory stated that the density of the matter in the expanding Universe remains unchanged due to continuous creation of matter. The Universe was said to be expanding and a homogeneous distribution of matter being created at a rate of 10^{-24} baryon/cm^3/s, instead of a unique moment of creation as stated in the Big Bang theory. By the end of the 1960s, the steady state theory started to loose its competitiveness as it could not explain certain observations, such as why galaxies were younger at a higher redshift, why there were excessive radio sources at large distances (Ryle and Clarke, 1961) and most importantly the Cosmic Microwave Background (CMB) radiation. The Steady State theory received a lot of appreciation until the mid 20$^{\text{th}}$ century after which several observational and theoretical evidences started to favour the Big Bang theory.

It was in the 1990s that Hoyle et al. (1993) published a modified version of the steady state theory, that was called the "quasi-steady state" (QSSC) theory. This model solved some of the problems that were faced by the steady state theory such as why there were younger galaxies at higher redshifts and why there were excessive radio sources at larger distances. The QSSC model aimed to compete with the Big Bang theory but described the Universe in a different way. Several errors were found out in the QSSC model by Wright (1995) who concluded that the QSSC model failed to describe the many observable properties of the Universe.

The Big Bang theory on the other hand stated that the Universe expanded from a very

high density and high temperature scale and continues to expand rapidly. After the initial expansion, the Universe cooled sufficiently to allow for the formation of subatomic particles and later simple atoms. Clouds of these primordial elements later coalesced through gravity to form stars and eventually galaxies. According to the Big Bang paradigm, the expansion of the Universe began 13.8 billion years ago, and this is also considered as the age of the Universe. However according to the Big Bang theory, what happened during the early times of the Universe, approximately from 10^{-43} to 10^{-11} seconds after the Big Bang, are still subjects of speculation. The laws of physics as we know them could not have existed during this time and it is difficult to imagine how the Universe would have been governed.

The cosmic microwave background radiation that was discovered in 1965 favoured the Big Bang theory, as the Big Bang theory had predicted this radiation even before it was detected. Supernova experiments have went on to prove the accelerated expansion of the Universe, which maybe due to a positive cosmological constant, a time–varying dark energy component or a modified theory of gravity.

There are three pillars of Big Bang theory, namely:

- Hubble's law
- Big Bang Nucleosynthesis
- Cosmic Microwave Background (CMB) radiation

1.2.1 Hubble's law

The linear relationship between the redshift of galaxies and their distance is given by:

$$v = H_0 D \tag{1.1}$$

where v is the recessional velocity, expressed in km s^{-1}, H_0 is the Hubble's constant [3] ,and D is the proper distance from the galaxy to the observer which is measured in megaparsecs (Mpc). The value of H_0 as measured by several observational methods give a value that is close to 70 km s^{-1} Mpc^{-1}. For example as measured from the WMAP observations $H_0 = 69.32 \pm 0.80$ km s^{-1} Mpc^{-1} (Bennett et al., 2013), as measured from the Planck mission, $H_0 = 67.80 \pm 0.77$ km s^{-1} Mpc^{-1} (Planck Collaboration et al., 2014).

Equation 1.1 is only a local approximation of the relation between redshift and distance, which depends on the adopted cosmological model.

When the value of H_0 was still uncertain by a factor 2, a normalized conventional Hubble constant h was defined as:

$$h = \frac{H_0}{100} \text{ km s}^{-1}\text{Mpc}^{-1} \tag{1.2}$$

[3] It is estimated by measuring the distances to galaxies by some other method than Hubble's law.

and all quantities that depend on its value was expressed in terms of the reduced Hubble constant, h.
The inverse of the Hubble constant is the Hubble time, t_H given by:

$$t_H \equiv \frac{1}{H_0} = 9.78 \times 10^9 \, h^{-1}\text{yr} = 3.09 \times 10^{17} \, h^{-1}\text{s} \tag{1.3}$$

and the speed of light c times the Hubble time gives us the Hubble distance D_H given by:

$$D_H \equiv \frac{c}{H_0} = 3000 \, h^{-1}\text{Mpc} = 9.26 \times 10^{25} \, h^{-1}\text{m} \tag{1.4}$$

1.2.2 Big Bang Nucleosynthesis

Big Bang Nucleosynthesis (BBN) refers to the production of nuclei heavier than hydrogen during the first minutes after the Big Bang. During this period, helium along with lithium, deuterium, and two unstable radioactive isotopes, the hydrogen isotope tritium and beryllium isotope beryllium-7 are said to have been formed. All of the heavier elements up to iron were created by the nuclear cores within stars. The heaviest elements, those heavier then iron were created during supernova explosions (Copi et al., 1995). Current theory predictions and actual observed abundances of elements match very well, so well that BBN is considered the second fundamental pillar of Big Bang theory (Longair, 2008). As we know, the beginning of the Universe was a dense quark soup and the temperature was really high. At this point the mean free path of any given particle was tiny and the entire Universe was within thermodynamic equilibrium. Starting with this hot, dense quark soup and moving forward in time the Universe started to cool and expand. However, as it cooled enough eventually, particles started freezing out of equilibrium when the energy density of the Universe roughly approached their rest mass energy. The first major component to freeze out were the neutrinos and the second major components to freeze out were the photons. When the temperature decreased to a few thousand degrees, neutral atoms could form without being ionized by photons, which did not have enough energy. This process is called "recombination" and radiation could freely propagate through space.

1.2.3 The Cosmic Microwave Background radiation

As the Universe expanded and cooled to the point where the formation of neutral hydrogen was possible, the fraction of free electrons and protons decreased to a few parts as compared to neutral hydrogen. Immediately after, photons decoupled from matter and travelled freely through the Universe without interacting with normal matter and constitute what is observed today as the Cosmic Microwave Background (CMB) radiation. This radiation is strongest in the microwave region of the radio spectrum and hence the name. One of the images of the CMB radiation observed using WMAP is shown in Figure 1.1.

These photons that existed during decoupling have been travelling throughout the Universe ever since. But due to the expansion of the Universe, their wavelengths are stretched,

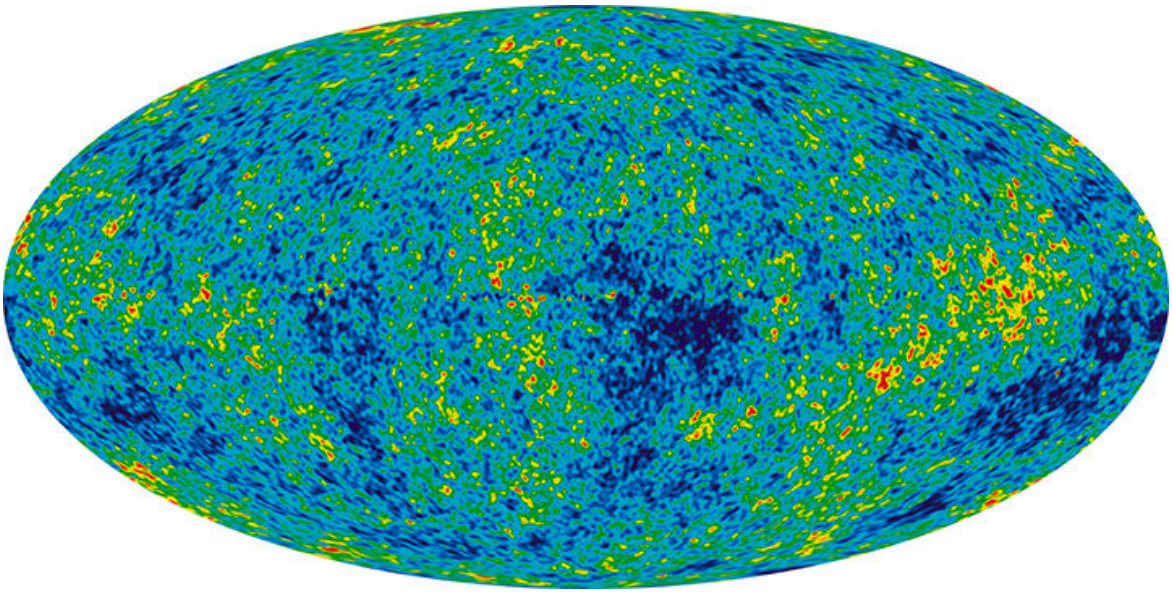

Figure 1.1: The CMB radiation as measured using WMAP which reveals the fluctuations that correspond to the seeds that grew to became galaxies. Image Credits: WMAP CMB radiation (2007)

the same way in which we see a shift in the red part of the spectrum for all objects that are far away from us (Longair, 2008). The CMB radiation has a black body spectrum, which as of today is measured at a temperature of 2.72 ± 0.0005K (Fixsen, 2009). The glow of the CMB radiation is isotropic when seen on a large scale. According to the inflation theory, quantum fluctuations were amplified to macroscopic scales during a period of fast and exponential expansion of the Universe. These density fluctuations were responsible for the temperature fluctuations in the CMB. The temperature fluctuations due to the primordial density fluctuations were first detected in 1992 by NASA's Cosmic Background Explorer (COBE) satellite which detected differences in the CMB radiation temperature in directions separated on the sky by 10° at the level of 30μK (Smoot et al., 1992).

1.3 Theoretical foundation of cosmology

Theoretical predictions have always outpaced observational studies in explaining how the Universe might have formed. During the 1900s, when observational techniques were limited to observing objects at very small distances, several cosmological frameworks were being developed, which were later proved via observational studies. One of the key assumptions of modern physical cosmology is the *cosmological principle*. It is the assumption that the distribution of matter in the Universe is homogeneous [4] and isotropic [5] when viewed on a large

[4] Homogeneity means that the Universe has the same properties in **all locations**

[5] Isotropy means that the Universe has the same properties in **all directions**

scale. It is clear that the Universe does not obey the cosmological principle on the scale of the Solar System, the galaxy and even on larger scales. Galaxy clusters, superclusters and voids reveal a complex large-scale structure. However, it is assumed that the cosmological principle holds on very large scales, and that averaging over very large volumes the statistical properties (e.g. the mean density) are the same. Assuming the cosmological principle and its validity at any time, one can adopt the Robertson-Walker metric which describes a homogeneous and isotropic Universe and derive the Friedmann equations from the Einstein equations.

1.3.1 Friedmann-Lemaître-Robertson-Walker metric and Einstein's equations

The physical distance between points in 3D space ($x = (x_1, x_2, x_3)$) that has a uniform expansion and growing with time is given by:

$$\Delta s^2 = a^2(t)\left[\Delta x_1^2 + \Delta x_2^2 + \Delta x_3^2\right] \tag{1.5}$$

where $a(t)$ is the scale factor which measures the rate of expansion and is only a function of time t and Δs gives us the spatial distance between the points. As the expansion of the Universe is uniform, the real distance between the two points $\vec{r}$ and the comoving distance (which does not change) $\vec{x}$ is given by:

$$\vec{r} = a(t)\vec{x} \tag{1.6}$$

The Hubble parameter H as we have seen can be written in terms of the scale factor as:

$$H \equiv \frac{\dot{a}(t)}{a(t)} \tag{1.7}$$

where the dot represents the first time derivative. In Equation 1.5 Δs gives us only the spatial distance between the two points, whereas in general relativity we are interested in the distance between the two points in four-dimensional space, which includes time as the fourth dimension. In that case, the separation between the points is written as:

$$ds^2 = \sum_{\mu,\nu} g_{\mu\nu} dx^\mu dx^\nu \tag{1.8}$$

where $g_{\mu\nu}$ is the metric and μ and ν are the indices taking the values 0, 1, 2, and 3, x^0 is the time coordinate and x^1, x^2 and x^3 are the three spatial coordinates. The most general spatial metric with constant curvature is written as:

$$ds_3^2 = \frac{dr^2}{1 - kr^2} + r^2\left(d\theta^2 + \sin^2\theta d\phi^2\right) \tag{1.9}$$

where ds_3^2 refers to the spatial dimensions alone. The curvature of space is given by k and the possibilities of k being positive, negative and zero correspond to the three different geometries of the Universe. The three common choices for k are:

- $k = 1$, Universe is closed
- $k = 0$, Universe is flat
- $k = -1$, Universe is open

Adding time dependency to Equation 1.9, we get the Friedmann-Lemaître-Robertson-Walker (FLRW) metric which is given by:

$$ds^2 = -c^2dt^2 + a^2(t)\left[\frac{dr^2}{1-kr^2} + r^2\left(d\theta^2 + \sin^2\theta d\phi^2\right)\right] \tag{1.10}$$

where the time coordinate is given by the term dt. This metric according to Einstein's equation which is given as:

$$R_{\mu\nu} - \frac{1}{2}g_{\mu\nu}R = \frac{8\pi G}{c^4}T_{\mu\nu} \tag{1.11}$$

where $T_{\mu\nu}$ is the energy-momentum tensor of any matter, $R_{\mu\nu}$ and R are the Ricci tensor and scalar which give the curvature of space-time, tell us how the presence of matter and energy curves space-time.

1.3.2 Friedmann equations

The Friedmann equations are one of the most important equations in cosmology as it governs the expansion of space in a homogeneous and isotropic Universe. They were first derived by Alexander Friedmann in 1922 from Einstein's field equations of gravitation for the FLRW metric and a perfect fluid with a given density ρ and pressure p. This equation has different solutions with different assumptions concerning the material content of the Universe. The first Friedmann equation is given by:

$$\left(\frac{\dot{a}}{a}\right)^2 = \frac{8\pi G}{3}\rho - \frac{kc^2}{a^2} + \frac{\Lambda}{3} \tag{1.12}$$

where G is Newton's gravitational constant, ρ is the density, c is assumed to be 1, k is a constant throughout a particular solution, k/a^2 is the spatial curvature at any time of the Universe and Λ is the cosmological constant.

It was found out that the Universe not only expands, but at an increasing rate. In cosmological terms this would mean that the cosmic scale factor $a(t)$ which is a function of time has a positive second derivative, so that the velocity of a distant galaxy with respect to the observer is increasing with time. The acceleration of the scale factor is given by the second Friedmann equation:

$$\frac{\ddot{a}}{a} = \frac{-4\pi G}{3}\left(\rho + \frac{3p}{c^2}\right) + \frac{\Lambda}{3} \tag{1.13}$$

where p is pressure of the material in the Universe. This equation is called as the acceleration equation. A positive cosmological constant gives a positive contribution to $\ddot{a}$ and so acts as a repulsive force to gravity. If the cosmological constant is sufficiently large, it can overcome the gravitational attraction represented by the first term of Equation 1.13 and lead to an Universe which is accelerating. We will see more in detail about the acceleration of the Universe in Section 1.6.

One of the most important and often used term in extragalactic astronomy is redshift. When light emitted from an object is increased in wavelength, or shifted to the red end of the spectrum, redshift occurs. In other words one can also say that the frequency of the object decreases as wavelength and frequency are inversely proportional. The wavelength of electromagnetic waves increase proportionally with the scale factor:

$$\frac{\lambda_{obs}}{\lambda_{rest}} = \frac{a(t_{obs})}{a(t_{rest})} \tag{1.14}$$

where $a(t_{obs})$ and $a(t_{rest})$ refer to the scale factors now and then respectively. This implies that the light is redshifted. Redshift can be defined as the change in this wavelength divided by the wavelength the object would have had if it were not moving (i.e. if it were at rest):

$$z = \frac{\lambda_{obs} - \lambda_{rest}}{\lambda_{rest}} \tag{1.15}$$

where z is the redshift, λ_{obs} is the observed wavelength and λ_{rest} is the wavelength of the object at rest.

Redshift does not occur explicitly due to just the expansion of the Universe, it can also occur due to the movement of objects (galaxies and galaxy clusters) relative to each other and also due to gravity, which happens when light is shifted due to the massive amount of matter inside a galaxy.

The movements of objects relative to each other create "peculiar" velocities (v_{pec}), due to which there are differences between an objects measured redshift z_{obs} and it's cosmological redshift z_{cos}. Cosmological redshifts are those redshifts which are only due to the expansion of the Universe. The relation between the observed redshift z_{obs}, the cosmological redshift z_{cos} and the peculiar redshift (z_{pec}, redshift caused by peculiar velocity) is given by:

$$1 + z_{obs} = (1 + z_{cos})(1 + z_{pec}) \tag{1.16}$$

The reason redshift is one of the most important observable is because most of the distances to extragalactic sources are measured via the redshift, and distance as we know is a primary information that is needed to study any astronomical source.

1.3.3 Density parameters of the Universe

It is useful to define the parameter Ω as the ratio of the density (of matter, or radiation, or other components) over the critical density. The critical density is the density value for which the geometry of the Universe is flat ($k = 0$). The critical density of the Universe is given by:

$$\rho_{critical}(t) = \frac{3H^2(t)}{8\pi G} \tag{1.17}$$

and it's value today is given by (Liddle, 2003):

$$\rho_{critical,0} = \frac{3H_0^2(t)}{8\pi G} = 1.86 \times 10^{-29}\, h^2 \text{g cm}^{-3} \tag{1.18}$$

where H_0 denotes the value of the Hubble constant today.

The mass density ρ_m of the Universe is usually written in terms of a dimensionless parameter Ω_M given by:

$$\Omega_M \equiv \frac{8\pi G\rho_0}{3H_0^2} \tag{1.19}$$

and the cosmological constant Λ (explained in detail in Section 1.5.1) in terms of a dimensionless parameter Ω_Λ given by:

$$\Omega_\Lambda \equiv \frac{\Lambda c^2}{3H_0^2} \tag{1.20}$$

Here the subscripted "0" indicates that the quantities (which evolve with time) are to be taken to be at the present epoch. There is a third density parameter, which defines the "curvature" of the Universe denoted by Ω_k. Together, these three density parameters are given by:

$$\Omega_M + \Omega_\Lambda = 1 - \Omega_k \tag{1.21}$$

Ω_M denotes the mass density including ordinary mass (baryonic mass) and dark matter, Ω_Λ denotes the effective mass density of dark energy and Ω_k denotes the curvature of the Universe. The values assessed by WMAP (Komatsu et al., 2011) for these parameters are $\Omega_{M,0} = 0.27 \pm 0.04$ and $\Omega_{\Lambda,0} = 0.725 \pm 0.016$ and that assessed by Planck Collaboration et al. (2016) are $\Omega_{M,0} = 0.31 \pm 0.014$ and $\Omega_{\Lambda,0} = 0.691 \pm 0.006$

1.3.4 The curvature of the Universe

As we have seen from Equation 1.9 the Universe can have three possible curvatures depending on the value of k:

- Flat – angles of a triangle add up to 180^o
- Positively curved (Spherical Universe) – angles of a triangle add up to more than 180^o

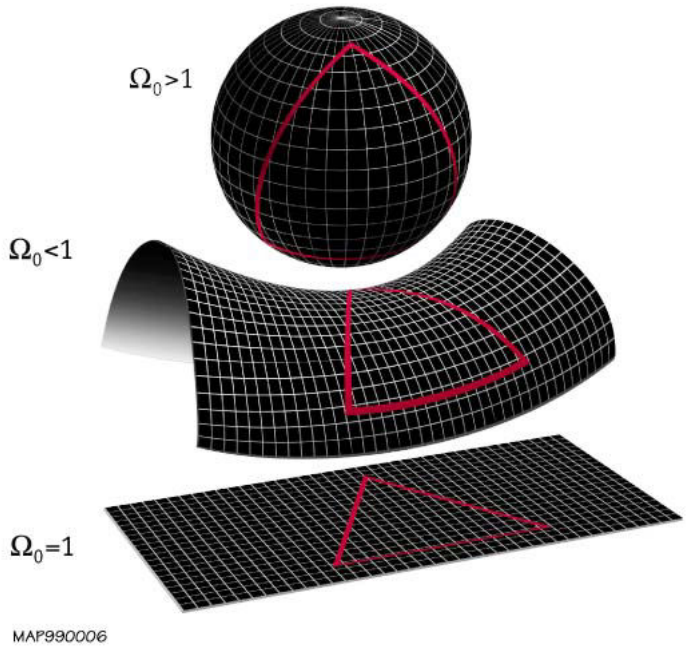

Figure 1.2: The local geometry of the Universe is determined by whether the density parameter Ω is greater than, less than, or equal to 1. From top to bottom: a spherical Universe with $\Omega > 1$, a hyperbolic Universe with $\Omega < 1$, and a flat Universe with $\Omega = 1$. Note that these depictions of two-dimensional surfaces are merely easily visualisable analogues to the 3-dimensional structure of (local) space. Image Credits: Curvature of the Universe (2016)

- Negatively curved (Hyperbolic Universe) – angles of a triangle add up to less than 180^o

The flat curvature is what we are common with, i.e. Euclidean geometry, wherein the angles of a triangle add up to 180^o. The other two geometries are often referred to as Non-Euclidean geometries. An example of a positively curved geometry would be the surface of the Earth. If we were to draw a triangle starting from the equator down to two points in the southern hemisphere, one can notice that the sides of the triangle do not look like a straight line at that particular surface. If the angles are added up, they will be exceeding 180^o. An example of a negatively curved space is a horse saddle. The same triangle experiment if repeated on the saddle would lead to the angles of the triangle adding up to less than 180^o.

Any Universe with the critical density is said to be flat. There are three cases which lead to different states of the Universe depending on the value of the mass density ρ_m with respect to $\rho_{critical}$:

- If $\rho_m > \rho_{critical}$, then the Universe is a closed one, which will eventually stop expanding and start collapsing in on itself.

- If $\rho_m < \rho_{critical}$, then the Universe is a open one, which will expand forever.

- If $\rho_m = \rho_{critical}$, the the Universe is a flat one, and it will expand forever, but with decrease in the rate of expansion with time.

In the case of the geometry of the Universe, general relativity explains us that space and time can be bent by mass and energy. This bending of space and time in the Universe decides the curvature and it can be explained via the density parameter Ω of the Universe. As we have seen in Equation 1.21, the three density parameters add up to 1, this means that the Universe as we know it, is said to be flat, which is the first scenario. If Ω on the other hand is greater than 1, it means that there is positive curvature, and if Ω is less than 1, there is negative curvature.

1.4 Distance measurements in cosmology

Due to the expansion of the Universe, the distances between comoving objects are changing, which means that there are many ways to specify the distance between two points in space. When we look at objects far far away we are literally looking back in time. One of the main ingredient from which distances to far away objects are measured is the redshift of that object.

Once we have the redshift of the object, measured either using photometry or spectroscopy and the values of our three cosmological parameters, we can calculate the distance to the object. Here we will explain some of the major distance measures used in cosmology, which include the comoving distance (line-of-sight/transverse), angular diameter distance and the luminosity distance.

1.4.1 Comoving distance (line-of-sight)

If we need to calculate the distance to an object which is stationary, we can directly do so. The same applies to distant objects in space, i.e. if we need to calculate the distance to an extragalactic source at a specific moment of cosmological time, which is called as *proper distance*, it can be calculated. But we know that the Universe is expanding, so, the far away an object is, the faster it expands from us. Comoving distance factors out this expansion, and gives us a distance that does not change with time. At the present epoch, both comoving distance and proper distance are one and the same, but at other times, they aren't.

The total line-of-sight comoving distance D_C from us to a distant object is calculated by summing up (integrating) all the small δD_C contributions in between the line-of-sight direction. We define a function $E(z)$ as:

$$E(z) \equiv \sqrt{\Omega_M(1+z)^3 + \Omega_k(1+z)^2 + \Omega_\Lambda} \tag{1.22}$$

and the total line-of-sight comoving distance is then given by:

$$D_C = D_H \int_0^z \frac{dz'}{E(z')} \tag{1.23}$$

where D_H is the Hubble distance given by Equation 1.4. There are other distance measures such as Luminosity distance, Parallax distance, Angular diameter distance, etc. but all the above distances are based on the comoving distance in one way or the other (Hogg, 1999). In other words, the fundamental distance measure in cosmology is the comoving distance.

1.4.2 Comoving distance (transverse)

The distance between two objects in the sky at the same redshift or distance but separated on the sky by some angle $\delta\theta$ is $D_M \delta\theta$ and the transverse comoving distance D_M, related to the line-of-sight comoving distance is given by:

$$D_M = \begin{cases} D_H \frac{1}{\sqrt{\Omega_k}} \sinh\left[\sqrt{\Omega_k} D_C / D_H\right] & \text{for } \Omega_k > 0 \\ D_C & \text{for } \Omega_k = 0 \\ D_H \frac{1}{\sqrt{|\Omega_k|}} \sin\left[\sqrt{|\Omega_k|} D_C / D_H\right] & \text{for } \Omega_k < 0 \end{cases} \tag{1.24}$$

where the functions sinh and sin account for the curvature of space. For $\Omega_\Lambda = 0$, there is an analytic solution to the equations:

$$D_M = D_H \frac{2\left[2 - \Omega_M(1-z) - (2-\Omega_M)\sqrt{1+\Omega_M(z)}\right]}{\Omega_M^2(1+z)} \text{for } \Omega_\Lambda = 0 \tag{1.25}$$

1.4.3 Angular diameter distance

The angular diameter distance D_A is defined as the ratio of an object's physical transverse size to its angular size (in radians) (Hogg, 1999). D_A does not increase indefinitely as $z \to \infty$; it turns over at $z \sim 1$ and so more distant objects actually appear larger in angular size. D_A is related to D_M by:

$$D_A = \frac{D_M}{1+z} \tag{1.26}$$

1.4.4 Luminosity distance

The luminosity distance D_L is defined as the relationship between bolometric [6] flux S and bolometric luminosity L and is given by:

$$D_L \equiv \sqrt{\frac{L}{4\pi S}} \tag{1.27}$$

It can also be given in terms of the transverse comoving distance and angular diameter distance by:

[6] Any property that is integrated over all the frequencies used.

$$D_L = (1+z)D_M = (1+z)^2 D_A \tag{1.28}$$

This relation follows from the fact that surface brightness of a receding object is reduced by a factor $(1+z)^{-4}$ and the angular area is reduced by D_A^{-2} (Hogg, 1999).

1.5 Towards the standard cosmological model

The development of a standard model of cosmology has been going on for the last forty years. The most widely accepted model is the ΛCDM model which can explain some of the observable properties of galaxies, clusters and large-scale structures in the Universe. Predictions of the ΛCDM model on the distribution of galaxies both nearby and out to high redshifts have been confirmed by observations (Komatsu et al., 2009; Planck Collaboration et al., 2015), although on sub-galactic scales there are several potential problems such as the model predicting an excess of halo substructures with respect to the observed number of satellite galaxies. But before the ΛCDM model became the standard model, there were several other models that were competing.

It was during the early 1980s that scientists were proposing that dark matter could be composed of non-baryonic particles. The candidate dark matter particles were classified into three families: hot, warm and cold dark matter (CDM), names that reflected their typical velocities during the early time of the Universe (Bond et al., 1980). Light neutrinos were considered as the Hot Dark Matter (HDM) candidates (Ellis et al., 1984). The CDM and HDM models with different Ω_M values were compared with the spatial distribution of galaxies observed from the CfA survey (Efstathiou et al., 1985). The results showed that there was discrepancy in the HDM models when compared with the results from the CfA survey while on the other hand the CDM models gave a far better result when compared to the CfA data. Studies on simulations based on CDM initial conditions were compared with the CfA galaxy distribution with predictions for a high-density Einstein de Sitter (EdS) Universe and with predictions for a low density Universe by Davis et al. (1985a). It was found out by Davis et al. (1985a) that a $\Omega_M \sim 0.4$ gave convincing results.

In the 1980s a flat Universe was considered as the outcome of inflation and a biased EdS model called the "standard" Cold Dark Matter (SCDM) model became the preferred choice for several investigations using N-body simulations (Frenk et al., 1985; White et al., 1987). The SCDM model was characterised by: $h = 0.5$, $\Omega_B = 0.05$ and $\Omega_M = 0.95$ (Dodelson et al., 1996). The SCDM model showed success at forming galaxies and cluster of galaxies, but problems remained, as the model required a Hubble constant that was lower than that preferred by observations. It was in the early 1990s that it had become clear that galaxy correlations were stronger on large scales than predicted by SCDM. The transition to ΛCDM model was finally forced by the exclusion of the EdS expansion history by supernova data (Perlmutter et al., 1999), which showed an accelerated expansion of the Universe.

1.5.1 ΛCDM model

The current standard model in which the Universe contains the cosmological constant Λ is called as the ΛCDM model. It is the simplest model that can reproduce the observational properties of the Universe such as:

1. The properties of the CMB radiation, as the existence of CMB is predicted by any Big Bang model.
2. The large-scale structure evolution and its distribution.
3. The accelerated expansion of the Universe, as given by the term Λ (cosmological constant) from ΛCDM.

The present composition of the Universe is:

- **Baryonic matter:** Roughly 5% of the Universe is ordinary baryonic matter Ω_b, mainly made up of Hydrogen atoms, Helium atoms and other fractions of heavier elements.
- **Dark matter:** Roughly 25% of the Universe is in the form of unknown dark matter, made up of particles that interact with ordinary matter only via the force of gravity.
- **Dark energy:** The remaining ~ 70% is in the form of unknown dark energy Ω_Λ, which is responsible for the acceleration of the Universe as we have observed today.

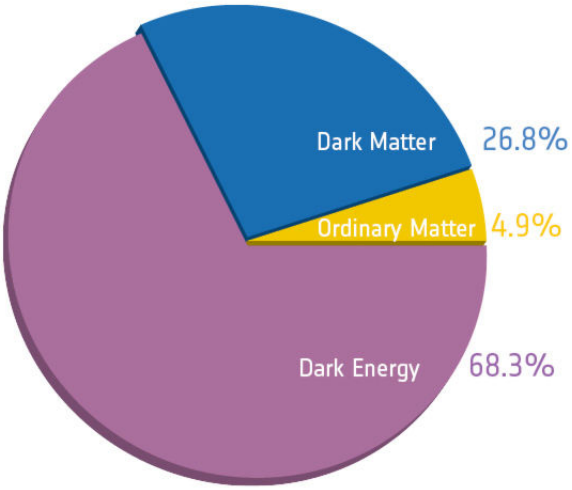

Figure 1.3: A pie-chart representing the matter-energy content of the Universe. Credits: Matter-energy content of the Universe, Planck (2015)

The dominant component of the Universe is the dark energy. However, there are other possibilities, such as a new form of energy which could evolve with time (quintessence), or a modified theory of gravity. Results from observational analysis that is model-independent can give us the proper solution, but at the moment the observational data are not up to the mark to take up this task. So we have to use the available data to constrain the model parameters. The most common way of discriminating between a cosmological constant and dynamical dark energy is to make use of the dark energy equation-of-state parameter, which in terms of the scale factor a is given as:

$$w(a) = w_0 + w_a(1 - a) \tag{1.29}$$

It can be seen that at the present time ($a = 1$) $w(a) = w_0$. The cosmological constant corresponds to $w_0 = -1$ and $w_a = 0$, constant equation of state corresponds to $w_0 = w =$ constant and $w_a = 0$, whereas the case of dynamical dark energy corresponds to $w_a \neq 0$. The difference between Λ and dynamical dark energy is that the former is constant with time and space, whereas the latter can change in time and space.

1.5.2 Modified Newtonian Dynamics: Alternative to dark matter ?

The dark matter component of the Universe was first detected using the rotation curves of galaxies, which was found to not follow the Keplerian decline with radius. Newton's law predict that stellar rotation velocities should decrease with distance from the galactic centre. The very first detections were done in 1930s when Horace Babcock reported the measurements of the rotation curve of the nearest Andromeda galaxy which suggested that the mass-to-luminosity ratio increases radially (Babcock, 1939). But detailed analysis of these measurements were done in 1970s by Vera Cooper Rubin and her team who measured the velocity curves of several stars in edge-on spiral galaxies. One such example is given in Figure 1.4 which shows that the velocity of the spiral galaxy NGC 6503 does not decline with radius but remains a constant. These observations showing the discrepancy in the rotational velocity curve meant that either there existed some form of unknown excess matter in the galaxies which boost the velocities of stars, or Newton's law does not apply to galaxies. The first statement lead to the dark matter hypothesis and the second statement lead to Modified Newtonian Dynamics (MOND) model, created by Milgrom (Milgrom, 1983), which is based on a variation of the Newton's Second Law of dynamics at low accelerations. MOND is closer to the main characteristics of the standard model, but different in minor aspects. According to Milgrom (1983) the discrepancy could be resolved if the gravitational force experienced by a star in the outer regions of a galaxy was proportional to the square of its centripetal force unlike to the centripetal force itself as given by Newton's second law.

The basic concept of MOND was that Newton's laws were tested in high-acceleration environment, but have not been verified for objects with low acceleration, such as the stars in the outer parts of a galaxy. According to MOND, the Newtonian force is given by:

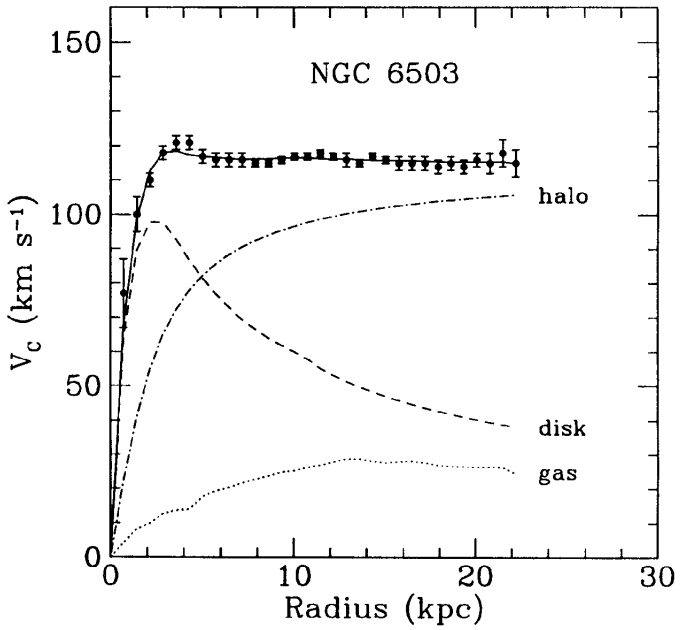

Figure 1.4: Rotation curve for the spiral galaxy NGC6503. The points are the measured circular rotation velocities as a function of distance from the center of the galaxy. The dashed and dotted curves are the contribution to the rotational velocity due to the observed disk and gas, respectively, and the dot-dash curve is the contribution from the dark halo. Credits: Kamionkowski (1998)

$$F_N = m\mu\left(\frac{a}{a_0}\right)a \tag{1.30}$$

where F_N is the Newtonian force, m is the object's gravitational mass, $\mu(x)$ is an as-yet unspecified function (known as the "interpolating function"), a is the acceleration and a_0 is a new fundamental constant which marks the transition between Newtonian and deep-MOND regimes. To agree with Newtonian mechanics requires $\mu(x) \to 1$ for $x \gg 1$ and to agree with astronomical observations requires $\mu(x) \to x$ for $x \ll 1$.

The strongest success of MOND is that all the rotation curves of galaxies imply a unique universal value for acceleration; moreover, the rotation curve features feel the baryonic component features even where dark matter is dominant; and in general the observed acceleration is strictly correlated with the acceleration expected from baryonic matter (McGaugh et al., 2016; Milgrom, 2016). On the other hand, MOND does not completely eliminate the need for a dark matter component, as galaxy clusters show a residual mass discrepancy even when analysed using MOND (McGaugh, 2015).

1.6 The accelerated expansion of the Universe

As we discussed in Section 1.1 the discovery of a linear proportionality between velocities and distances of galaxies along with the discovery of the CMB in 1965, paved the way to the acceptance of an expanding Universe. In the end of 90s, physicists were convinced that the force of gravity should be causing the expansion of the Universe to slow down. But the first evidence to favour the accelerated expansion of the Universe came from supernova observations. This meant that the scale factor had a positive second derivative.

There have been several observational evidences in favour of the accelerated expansion of the Universe. One can either look at the magnitude-redshift relation of objects that are "standard candles" [7] or use the baryon acoustic peak measurements as "standard rulers". As discussed above, we highlight here how the two methods paved the way towards understanding the acceleration of the Universe.

1.6.1 Supernova observations

The first direct evidence of the accelerated expansion of the Universe came from supernova observations, in particular Type Ia supernovae (SNIa). These are white dwarfs that explode because they exceed the Chandrasekhar limit [8]. The peak brightness of the supernova is found using repeated observations from which we can infer the luminosity distance, which is associated with the redshift of the host galaxy. The measured luminosity distance can then be compared with theoretical predictions to constrain the values of Ω_M and Ω_Λ to distinguish between several cosmological models.
Mario Hamuy (Hamuy et al., 1993) and co-workers at Cerro Tololo took a major step forward by studying the light curves of many nearby supernovae. But it was in 1998 that Saul Perlmutter heading the Supernova Cosmology Project (SCP) along with the High-z Supernova Search Team measured the brightness of 42 supernovae and compared their magnitude with redshift. In Figure 1.5 we show the redshift vs magnitude diagram obtained from SNIa observations from the Supernova Cosmology Project and the High-z Supernova Search on a logarithmic redshift scale. Here they compared the SNIa observations to a few cosmological models and found out that the observations do not match the $\Lambda = 0$ model and favours the model with $\Lambda > 0$ (Perlmutter et al., 1999). This discovery was named as "Breakthrough of the year for 1998" with Perlmutter alongside Adam Riess and Brian P.Schmidt from the High-z team being awarded the Nobel Prize in Physics. Supernovae also provide precise measurements of the Hubble parameter H_0. One of the recent works by Riess et al. (2011) obtained a value of $H_0 = 73.8 \pm 2.4 \mathrm{kms}^{-1}\mathrm{Mpc}^{-1}$.

[7] Those astronomical objects that have a known brightness, so by comparing this known brightness to the observed brightness, one can determine the distance to the object using inverse square law.

[8] Any white dwarf that reaches a mass above $M_\odot > 1.39$ will subject to gravitational collapse.

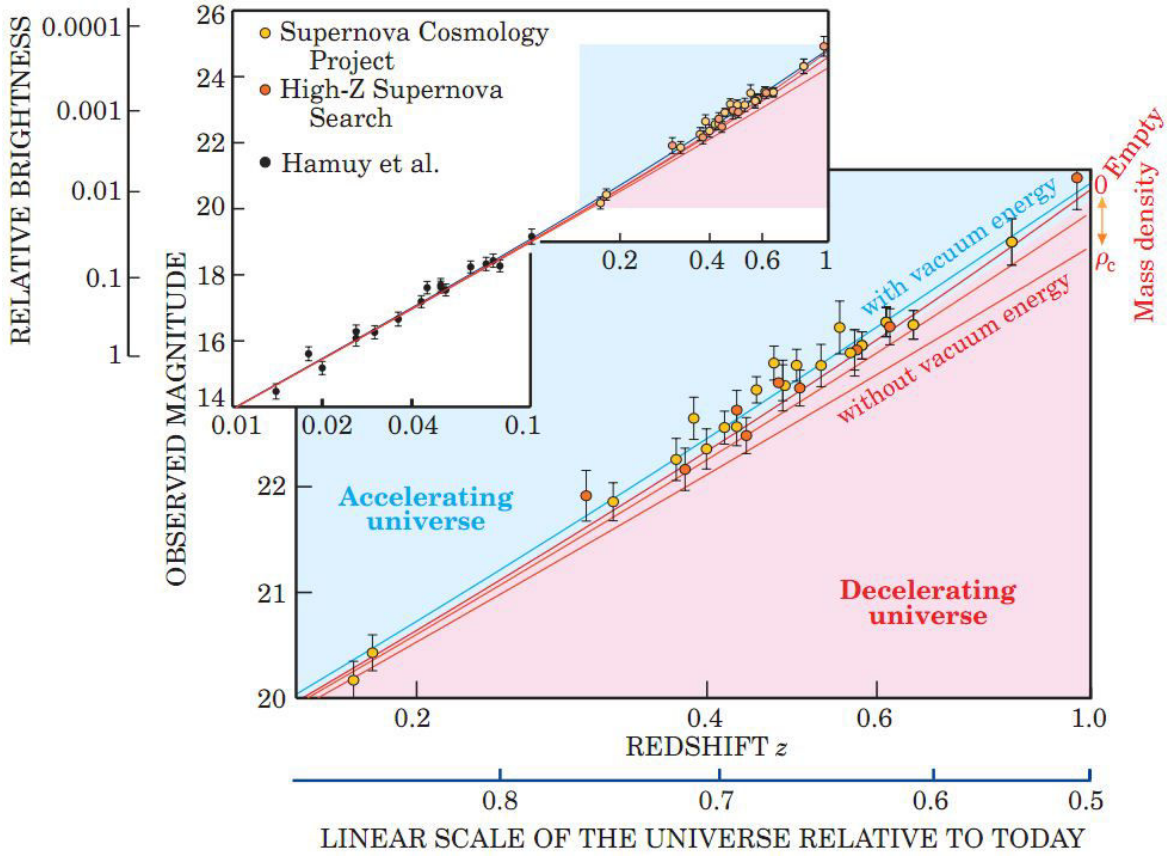

Figure 1.5: Observed magnitude versus redshift is plotted for well-measured distant and (in the inset) nearby type Ia supernovae. For clarity, measurements at the same redshift are combined. At redshifts beyond z = 0.1 (distances greater than about 109 light-years), the cosmological predictions (indicated by the curves) begin to diverge, depending on the assumed cosmic densities of mass and vacuum energy. The red curves represent models with zero vacuum energy and mass densities ranging from the critical density ρ_c down to zero (an empty cosmos). The best fit (blue line) assumes a mass density of about $\frac{\rho_c}{3}$ plus a vacuum energy density twice that large–implying an accelerating cosmic expansion. Credits: (Perlmutter, 2003)

1.6.2 Baryon acoustic oscillations

As SNIa provide a "standard candle", BAO clustering information can provide a "standard ruler" for length scale in cosmology.

The early Universe consisted of a hot plasma and the photons as we know were trapped and were not able to travel any considerable distance before interacting with this plasma. There were over dense regions of this plasma which attracted matter towards it gravitationally. This attraction lead to a high temperature region and in-turn creating a high pressure region. The counteracting forces of gravity and pressure created oscillations, analogous to

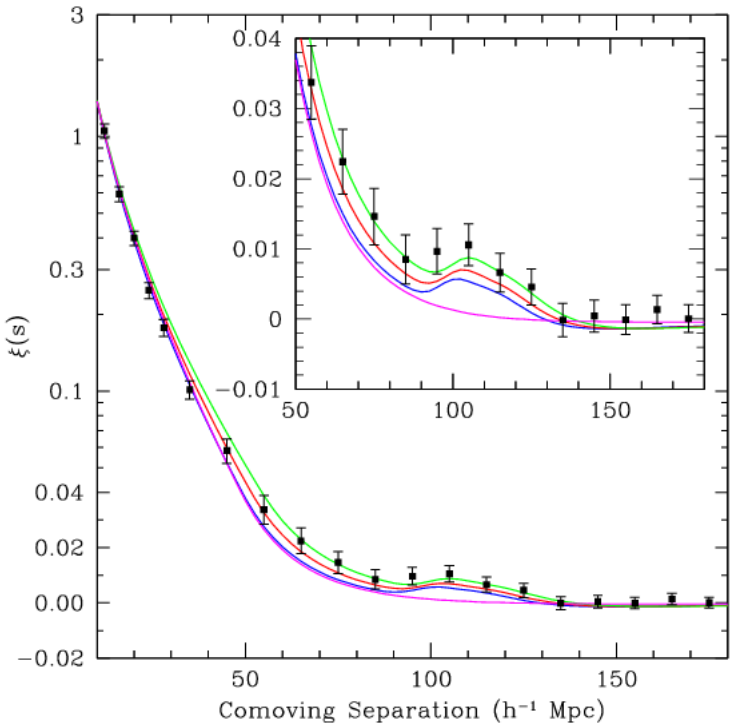

Figure 1.6: The two-point correlation function of a sample of SDSS luminous red galaxies as calculated by Eisenstein et al. (2005). The BAO peak is spotted at around 105 h^{-1}Mpc. Credits: Eisenstein et al. (2005)

sound waves created in air by pressure differences. Photons along with protons and electrons remained trapped in this high pressure region until the Universe expanded and cooled. When the temperature finally reduced, the photons were set free and started moving but the electrons and protons (baryonic matter) stopped moving and remained at the center of this high pressure region. This left behind a shell of baryonic matter at a fixed radius which can be statistically detected through the two-point correlation function $\xi(r)$. $\xi(r)$ decreases with increasing scale, but we observe a slight increase in $\xi(r)$ at a particular scale. This scale is the fixed radius where the baryonic matter can be found in excess. An example of the BAO peak measured from the two-point correlation function of LRGs from the SDSS sample by Eisenstein et al. (2005) is shown in Figure 1.6. It can be seen that this peak is more or less around 105 h^{-1}Mpc. In understanding the accelerated expansion of the Universe, observations of the sound horizon today (using clustering of galaxies) can be compared with the sound horizon at the time of recombination (using CMB). BAO thus provides a "standard ruler" and a way to understand this expansion completely independent from SNIa observations. Eisenstein et al. (2005) quoted the distance measurement as a combination of the line-of-sight and transverse distance scale given by:

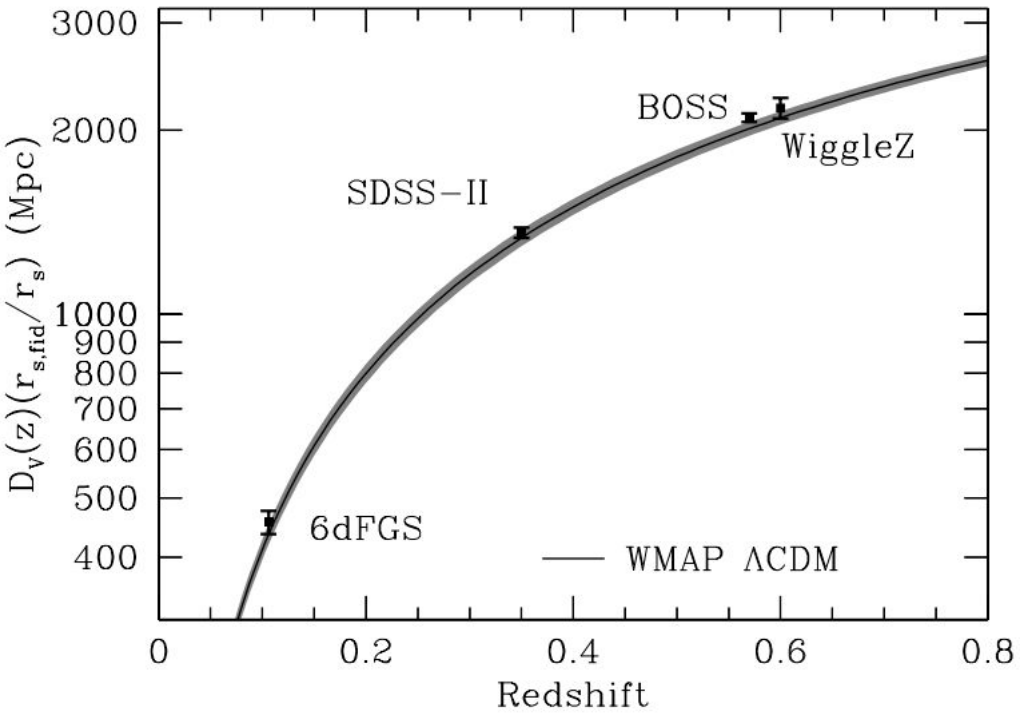

Figure 1.7: The BAO distance-redshift relation. Individual measurements are of the quantity $D_V(z)/r_s$. To yield a distance, a multiplication by the r_s of the fiducial ΛCDM model has been made. In increasing redshift, data points are from 6dFGS (Beutler et al., 2011), SDSS-II (Padmanabhan et al., 2012), BOSS (Anderson et al., 2012) and WiggleZ (Blake et al., 2011). Credits: Weinberg et al. (2013)

$$D_V(z) = [D_A(z)]^{2/3} \left[\frac{cz}{H(z)}\right]^{1/3} \tag{1.31}$$

where $D_A(z)$ is the comoving angular diameter distance and $H(z)$ the Hubble parameter. The distance-redshift relation obtained from several individual measurements of the quantity $D_V(z)/r_s$ was compiled by Weinberg et al. (2013) and the results obtained are shown in Figure 1.7. It can be seen from Figure 1.7 that the BAO measurements are all in good agreement with the 1σ edge of the WMAP7 (Komatsu et al., 2011) band.

Getting information and confirming theoretical models from different studies removes any bias that might be present if the proof were only from a single study. Several studies based on the data from 2dFGRS (Percival et al., 2007) and SDSS (Eisenstein et al., 2005; Percival et al., 2010; Veropalumbo et al., 2014, 2016) have been made in detecting the BAO peak and future surveys such as LSST and Euclid, thanks to their wide coverage and depth, will be detecting plethora of galaxies that can also be used.

1.7 Formation of large-scale structures: Models and formalisms

The observed large-scale structure, showing a pattern of sheets and filaments known as the "cosmic web", is the result of a gravitational growth which started from primordial density fluctuations, whose ultimate origin, according to inflation, are quantum fluctuations in the very early Universe. Another prediction of inflation is that these primordial fluctuations were Gaussian. Linear and high order perturbation theory descriptions of large-scale structure formation from Gaussian initial fluctuations have been developed. They describe the evolution and non-linear clustering of dark matter, but they break down when the clustering becomes highly non-linear. Here we discuss some of the key theoretical aspects of large-scale structure formation that have been laid down over the years.

1.7.1 Linear perturbation theory

The generally accepted theoretical framework for the formation of structure is that of gravitational instability. The early Universe is assumed to be perfectly smooth, with the exception of tiny density deviations with respect to the global cosmic background density. Fluctuations are described defining the density contrast:

$$\delta(x) = \frac{(\rho(x) - \overline{\rho}_m)}{\overline{\rho}_m} \tag{1.32}$$

where $\overline{\rho}_m$ refers to the mean mass density of the Universe. The primordial Gaussian density fluctuations can be fully described by the power spectrum or the two-point correlation function (Press and Schechter, 1974).
The $\delta(x)$ in the density field can be written as a sum over Fourier modes:

$$\delta(x) = \int \frac{d^3\mathrm{k}}{(2\pi)^3}\delta(\mathrm{k})\exp(i\mathrm{k}.x) \tag{1.33}$$

and the two-point Fourier-space correlation is given by:

$$\langle\delta(\mathrm{k}_1)\delta(\mathrm{k}_2)\rangle = (2\pi)^3\delta_D(\mathrm{k}_{12})P(\mathrm{k}_1) \tag{1.34}$$

where $P(\mathrm{k})$ is the power spectrum. The two-point correlation function $\xi(r)$ (explained in detail in Chapter 3) is the Fourier transform of the power spectrum $P(k)$. A quantity related to the power spectrum is the variance of the density contrast field ($\sigma^2(R)$) smoothed over a window of scale R given by:

$$\sigma^2(R) = \int \frac{dk}{k}\frac{k^3P(k)}{2\pi^2}|W(kR)|^2 \tag{1.35}$$

where $W(kR) = [3/(kR)^3]\,(\sin kR - (kR)\cos kR)$ when the window is a top-hat in real-space. At high redshifts, when fluctuations are small, a scale R corresponds to a mass $M =$

$4\pi R^3\rho_m(z)/3$, where $\rho_m(z)$ is the matter density of the Universe at redshift z. The smoothed Gaussian density field is given by a probability distribution function:

$$p(\delta_M) = \frac{1}{\sqrt{2\pi}\sigma(M)}\exp\left[\frac{-\delta_M^2}{2\sigma^2(M)}\right] \tag{1.36}$$

In the linear regime, during the earlier stages of evolution in the standard structure formation, the initial Gaussian of the density field $\delta(x)$ is preserved and they can be characterised by either a power spectrum or a two-point correlation function. The density fluctuations increase with time under the action of gravity, which generates non-zero high order correlations. They are governed by the continuity equation and the Euler equation. The continuity equation is given by:

$$\frac{\partial\delta}{\partial t} + \frac{1}{a}\bigtriangledown .(1+\delta)\mathrm{u} = 0 \tag{1.37}$$

and the Euler equation is given by:

$$\frac{\partial\delta}{\partial t} + H\mathrm{u} + \frac{1}{a}\left[(\mathrm{u}.\bigtriangledown)\mathrm{u} + \bigtriangledown\phi\right] = 0 \tag{1.38}$$

where the term 'u' is related to the peculiar velocity via the Hubble flow and is given by:

$$\mathrm{u} = \mathrm{v} - H\mathrm{v} \tag{1.39}$$

In the linear regime, the fluctuation $\delta \ll 1$ and combining the continuity and Euler equations we have:

$$\frac{\partial^2\delta}{\partial t^2} + 2H\frac{\partial\delta}{\partial t} - 4\pi G\overline{\rho}\delta = 0 \tag{1.40}$$

The above equation has two solutions and corresponding to a growing and decaying mode. The solution to the growing mode has the form:

$$\delta(k,r) = G(r)\delta(k,0) \tag{1.41}$$

where $G(r)$ is given by:

$$G(r) \propto \frac{H(r)}{H_0}\int_{z(r)}^{\infty} dz^{'}(1+z^{'})\left[\frac{H_0}{H(z^{'})}\right]^3$$
$$\approx \frac{5}{2}\frac{\Omega_m(z)/(1+z)}{\Omega_m(z)^{4/7} - \Omega_\Lambda(z) + (1-\Omega_m(z)/2)(1+\Omega_\Lambda(z)/70)} \tag{1.42}$$

The above equation shows that the linear density field can be scaled in both time and redshift via $G(z)$. For an Einstein-de Sitter (EdS) cosmology ($\Omega_{m,0}, \Omega_{\Lambda,0} = (1,0)$) the solutions for the growing and decaying modes are simple: $\delta_+ \propto a \propto t^{2/3}$ and $\delta_- \propto t^{-1}$. Also $G \propto a = (1+z)^{-1}$ as $\Omega_m \to 1$.

1.7.2 Non-linear evolution of large-scale structures

As we have seen so far, as long as the density fluctuation is $\delta \ll 1$ the linear approximation is justified. But once the amplitude of the density fluctuations reach a scale $\delta \geq 1$, the linear approximation breaks down. This happens first at small scales, where further evolution at these scales should be studied only by means of non-linear models or through numerical simulations.

1.7.2.1 Spherical top-hat collapse

One of the simplest non-linear collapse models assumes that the density peaks are characterised by a constant overdensity and spherical perturbation. The spherical collapse model of an initially top-hat density perturbation was first proposed by Gunn and Gott (1972).

We assume a spherical region of initial comoving radius R_0 and initial density δ_i at time t_i. We also assume that the initial fluctuations are Gaussian with a rms value $\ll 1$ (within scale R_0) therefore $|\delta_i| \ll 1$. The mass within this region is given by:

$$M_0 = \frac{4\pi R_0^3 \overline{\rho}(1+\delta_i)}{3} \tag{1.43}$$

where $M_0 \propto (4\pi R_0^3/3)\overline{\rho}$ and $\overline{\rho}$ denotes the comoving background density. The radius of the spherical region increases with the expansion of the Universe. The density inside the region is given by:

$$\rho = \left(\frac{R_0}{R}\right)^3 \equiv (1+\delta) \tag{1.44}$$

For an Einstein-de Sitter Universe we have the following parametric solution:

$$\frac{R(z)}{R_0} = \frac{(1+z)}{(5/3)|\delta_0|}\frac{(1-cos\theta)}{2} \tag{1.45}$$

where $0 \leq \theta \leq 2\pi$, $1/(1+z) = (3/4)^{2/3}\left[(\theta - \sin\theta)^{2/3}/(5/3)|\delta_0|\right]$ and δ_0 denotes the initial density δ_i extrapolated using linear theory to the present time t. As θ is in the range $(0, 2\pi)$, the system starts with $\theta = 0$, undergoes a "turnaround" at $\theta = \pi$ and collapses completely when $\theta = 2\pi$. The size of the overdense region according to Equation 1.45 evolves as:

$$\frac{R_0}{R(z)} = \frac{6^{2/3}}{2}\frac{(\theta - \sin\theta)^{2/3}}{(1-\cos\theta)^{2/3}} \tag{1.46}$$

At the turnaround, $\theta = \pi$, so $\left[R_0/R(z_{ta})\right]^3 = (3\pi/4)^2$. and the average density within the region is about 4.55 times the background density. After the turnaround, the region formally collapses to zero radius at $t_{col} = 2t_{ta}$. However, we can assume that at t_{col} the region virialises. From the conservation of energy law and the virial theorem it follows that the radius at virialisation is half the maximum radius at the turnaround (in physical coordinates). In this time, the background Universe has expanded by a factor of $(1+z_{ta})/(1+z_{col}) = 2^{2/3}$ so

that the virialised object is now eight times denser than what it was during the turnaround phase. The background density of the Universe at the turnaround phase is $(2^{2/3})^3 = 4$ times the background density at z_{vir}. As in the EdS model ($\Omega_m = 1, \Omega_\Lambda = 0$), the background density evolves as $\overline{\rho}_m = 1/(6\pi G t^2)$, the overdensity $\rho_{vir} = \rho_{vir}/\rho_b$ after virialisation is:

$$\Delta_{vir} \equiv (9\pi^2/16) \times 8 \times 4 = 18\pi^2 = 177.65 \tag{1.47}$$

One of the most important features of the spherical collapse model is that the equations provide a relation between the actual overdensity δ and that predicted by linear theory δ_0 since $(1+\delta) = (R/R_0)^3$.

At the turnaround:

$$\delta(t_{ta}) = \frac{9\pi^2}{16} - 1 \simeq 4.55 \quad \text{(Spherical Collapse model)} \tag{1.48a}$$

$$\delta_{lin}(t_{ta}) = \frac{3}{20}(6\pi)^{2/3} \simeq 1.062 \quad \text{(Linear theory)} \tag{1.48b}$$

At the end of the gravitational collapse:

$$\delta(t_{col}) = 176.65 \quad \text{(Spherical Collapse model)} \tag{1.49a}$$

$$\delta_{lin}(t_{col}) = \frac{3}{20}(12\pi)^{2/3} \simeq 1.686 \quad \text{(Linear theory)} \tag{1.49b}$$

1.7.2.2 Peak formalism and Press-Schechter formalism: Mass function

One can assume that when the regions in the initially linear density field reach $\delta_{col} = \delta_{lin}(t_{col}) \sim 1.686$, they collapse forming virialised dark matter haloes. We can now derive the halo mass function, i.e. the comoving number density of haloes as a function of halo mass, which is an important cosmological tool to discriminate the different cosmological models.

Let's say δ_{lin} is the linear density field smoothed over a mass scale M, i.e. $\delta_M = \delta(\vec{x}; R)$. The locations where $\delta_M = \delta_{col}(t)$ are those locations where at a time t, a halo of mass M condenses out of the evolving density field. Press and Schechter (1974) combined the linear growth of density fluctuations and the spherical top-hat collapse to analytically derive a prescription for the mass function. They postulated that the probability that $\delta_M > \delta_{col}(t)$ is the same as the mass fraction that at time t is contained in haloes with mass greater than M. In other words, the fraction of space in which $\delta_M > \delta_{col}(t)$ corresponds to the fraction of cosmic volume filled with haloes greater than mass M. Considering a Gaussian random field, this probability is given by:

$$P(\delta_M > \delta_{col}) = \frac{1}{\sqrt{2\pi}\sigma_M} \int_{\delta_{col}}^{\infty} \exp\left[-\frac{\delta_M^2}{2\sigma_M^2}\right] \mathrm{d}\delta_M = \frac{1}{2}\mathrm{erfc}\left[\frac{\delta_{col}}{2\sigma_M}\right] \tag{1.50}$$

where erfc(x) = 1 – erf(x) is the complimentary error function and $\delta_{col} = \delta_{col}(t)$. Here the mass $M = 4\pi R^3 \overline{\rho}_m/3$ and σ_M is the square root of Equation 1.35. When the whole mass range is considered and the limit $M \to 0$, one should be able to account for the whole mass range in the Universe and get $\int_0^\infty P(\delta_M > \delta_{col}) = 1$. But in reality, the Press and Schechter formalism gives only $\int_0^\infty P(\delta_M > \delta_{col}) = 1/2$, which means that half of the mass is not counted. To solve the cloud-in-cloud problem, Press and Schechter added a correction factor of 2, i,e, $2P\left[\delta_M > \delta_{col}(t)\right]$.

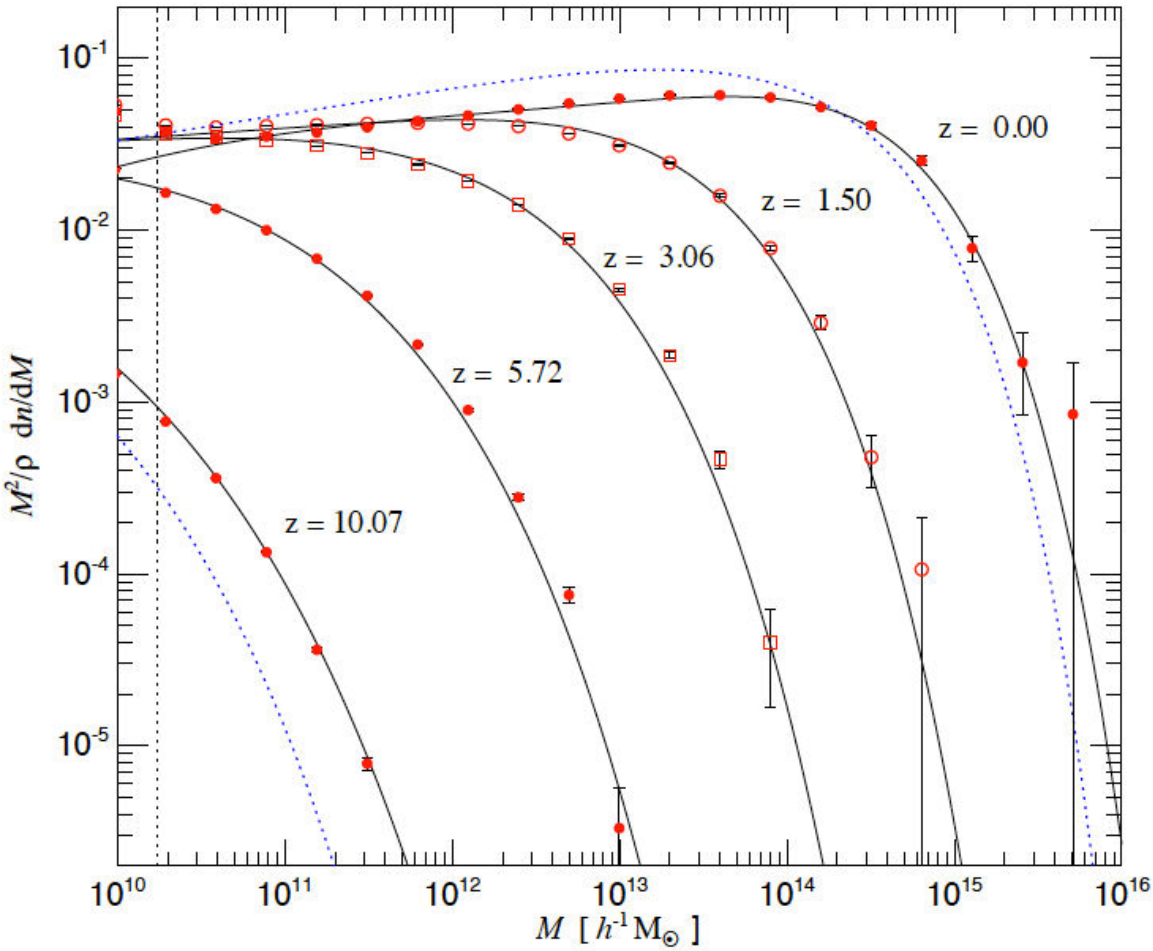

Figure 1.8: The mass function of haloes found in the Millennium run using a Friends-of-Friends algorithm (red dots connected by black line) along with the Jenkins et al. (2001) mass function (black solid lines) and Press and Schechter (1974) mass function (blue dashed lines). Credits: Springel et al. (2005)

To define the halo mass function $(n(M,t)dM)$, which is the number of haloes with masses in the range $[M, M + dM]$ per comoving volume, by differentiating Equation 1.50 with respect to mass M, we obtain:

$$\frac{dn(M,z)}{dM} = \frac{2}{V}\frac{\partial P(\delta_M > \delta_{col})}{\partial M} = -\sqrt{\frac{2}{\pi}}\frac{\overline{\rho}_m \delta_{col}}{M\sigma_M^2}\frac{d\sigma_M}{dM}\exp\left(-\frac{\delta_{col}^2}{2\sigma_M^2}\right) \tag{1.51}$$

where we have divided by the volume $V = M/\overline{\rho}_m$ to obtain a quantity with units per volume. Equation 1.51 gives the comoving number density of haloes of mass M at redshift z, in terms of σ_M and δ_{col} and is the Press-Schechter mass function.

When we define the variable $\nu \equiv \delta_{col}(t)/\sigma(M)$, Equation 1.51, i.e the Press-Schechter mass function can be written in a more compact form as:

$$n(M,z)dM = \frac{\overline{\rho}_m}{M^2} f_{\rm PS}(\nu)\left|\frac{{\rm d}\ln\nu}{{\rm d}\ln M}\right|{\rm d}M \tag{1.52}$$

where $f_{\rm PS(\nu)} = \sqrt{\frac{2}{\pi}}\nu\exp^{\nu^2/2}$ and is called as the multiplicity function (Press and Schechter, 1974) and gives the mass fraction associated with haloes in a unit range of $\ln\nu$. The evolution of the mass function is denoted through time t and it enters Equation 1.51 only through $\delta_{col}(t) \simeq 1.686/D(t)$.

The halo mass function was also studied by calculating the number density of the peaks and is given by:

$$n(>M) = n_{pk}(\delta_M) \tag{1.53}$$

where $n(>M)$ represents the number density of haloes with mass $> M$ and $n_{pk}(\delta_M)$ represents the number density of peaks above δ_{col} in the density field smoothed over the mass scale M. Bardeen et al. (1986) were the first to compute this number density, clustering properties and the density profiles of peaks in a smoothed Gaussian random, all as a function of peak height ν_{pk}. According to Bardeen et al. (1986), the peak height ν_{pk} is given by:

$$\nu_{pk} = \frac{\delta_{pk}}{\langle\delta_M^2\rangle^{1/2}} = \frac{\delta_{pk}}{\sigma_M} \tag{1.54}$$

But there is a problem with the assumption given by Equation 1.53. Some of the peaks that are part of a higher peak when smoothed with a larger filter have to be excluded when identifying the peaks with the haloes. This is called as the *cloud-in-cloud problem*. It is because of the cloud-in-cloud problem the peak formalism has largely been ruled out.

Springel et al. (2005) used the Millennium Simulation (Lemson and Virgo Consortium, 2006) which followed an evolution of 2160^3 particles in a box of $500h^{-1}$Mpc on a side using a ΛCDM cosmology and calculated the mass function of haloes (identified using a Friends-of-Friends algorithm) in the simulation and compared it with the theoretical predictions of the Press-Schechter and Jenkins et al. (2001) mass function. The results can be seen in Figure 1.8 and it can be seen that at redshift $z = 10.07$, the Press Schechter mass function systematically underpredicts haloes everywhere and at redshift $z = 0$ it overpredicts the abundance of low mass haloes and underpredicts the abundance of high mass ones.

1.7.3 Mass function of dark matter haloes

Press and Schechter (1974) assuming Gaussian density fluctuations applied linear theory to derive the first theoretical mass function. Several studies (Mo and White, 1996; Sheth and Tormen, 1999; Jenkins et al., 2001; Tinker et al., 2008) have improved upon the theory of the mass function. We highlight here the theoretical mass function of Jenkins et al. (2001) and Tinker et al. (2008).

Jenkins mass function: The mass function $f(\sigma, z; X)$ is defined as:

$$f(\sigma, z; X) \equiv \frac{M}{\rho_0} \frac{\mathrm{d}n_X(M,z)}{\mathrm{dln}\sigma^{-1}} \tag{1.55}$$

where X is a label identifying the cosmological model and halo finder under consideration, $n(M,z)$ is the abundance of haloes with mass less than M at redshift z, and $\rho_0(z)$ is the mean density of the Universe at that time and $\sigma^2(M,z) = \sigma_8 \times f$ is the variance of the linearly evolved density field smoother over a spherical top-hat filter that encloses the mass M as defined in Equation 1.35. f is a function of M, z, Ω_M and σ_8 is the present rms mass fluctuation on the scale of 8 h^{-1}Mpc. Jenkins et al. (2001) found that the numerical data in their simulations was well fitted by the following formula:

$$f(M) = 0.315\mathrm{exp}(-\left|\mathrm{ln}\sigma^{-1} + 0.61\right|^{3.8}) \tag{1.56}$$

which was valid over the range $-1/2 \leq \mathrm{ln}\sigma^{-1} \leq 1.05$.

Tinker mass function: The halo abundance has been predicted by successful theories by using the mass fraction of matter in peaks of a given height at a scale $R = (3M/4\pi\bar{\rho}_m)^{1/3}$ given by:

$$\nu \equiv \frac{\delta_c}{\sigma(M,z)} \tag{1.57}$$

where $\delta_c = 1.69$ is a constant corresponding to the critical linear overdensity for collapse as seen in Equation 1.49b and $\sigma(M,z)$ is the rms variance of the linear density smoothed on scale $R(M)$. The halo abundance is given by a functional form:

$$\frac{dn}{dM} = f(\sigma)\frac{\bar{\rho}_m}{M}\frac{d\mathrm{ln}\sigma^{-1}}{dM} \tag{1.58}$$

where the function $f(\sigma)$ is expected to be universal to the changes in redshift and is given by:

$$f(\sigma) = A\left[\left(\frac{\sigma}{b}\right)^{-a} + 1\right]e^{-c/\sigma^2} \tag{1.59}$$

where

$$\sigma = \int P(k)\hat{W}(kR)k^2 dk \tag{1.60}$$

where $P(k)$ is the linear matter power spectrum which is a function of wavenumber k, $\hat{W}$ is the Fourier transform of the real-space top-hat window function of radius R. The best-fit values of the mass function are given by Equation 1.59 where the constant A denotes the amplitude of the mass function, a and b the slope and amplitude of the low-mass power spectrum and c the cut-off scale at which the abundance of haloes decreases exponentially.

1.7.4 Density profiles of dark matter haloes

The statistical properties of the large-scale structure depend on cosmology and on the nature of dark matter: hot dark matter is relativistic and tends to suppress small scale structure, while cold dark matter is non-relativistic and can generate more power at small scales. Galaxies and clusters form from gravitational accretion of dark and baryonic matter and are associated to dark matter haloes. Therefore the comparison of the theoretical predictions for the dark halo properties and spatial distribution with observations is an important test both for cosmology and for structure formation scenarios.

The density of a halo increases as we go towards the center of the halo, which is called the core. As we move outside the core, the density steadily decreases. All the masses of dark matter haloes are measured within a virial radius. This virial radius is usually given in terms of the critical density of the Universe. The spatial distribution of dark haloes is expected to be biased with respect to the underlying dark matter field, as a function of their mass. The total mass of a halo is estimated within R_{200}, the radius within which the mean density is $200 \times \rho_{critical}$:

$$M = \frac{4\pi}{3} R_{200}^3 200 \rho_{critical} \tag{1.61}$$

By substituting the definition of critical density as given by Equation 1.17 in to the above equation we get:

$$M = \frac{100 R_{200}^3 H^2(z)}{G} \tag{1.62}$$

The mass of the halo and the size of the halo are related and change with redshift via the $H^2(z)$ parameter which is given by $H^2(z) = H_0^2(\Omega_M \times (1+z)^3 + \Omega_\Lambda)$.

The Navarro-Frenk-White profile: The density profiles of dark matter haloes can be fitted using a universal fitting formula devised by Navarro et al. (1996) and is given by:

$$\rho(r) = \frac{\rho_c \delta_{col}}{(r/r_s)(1 + r/r_s)^2} \tag{1.63}$$

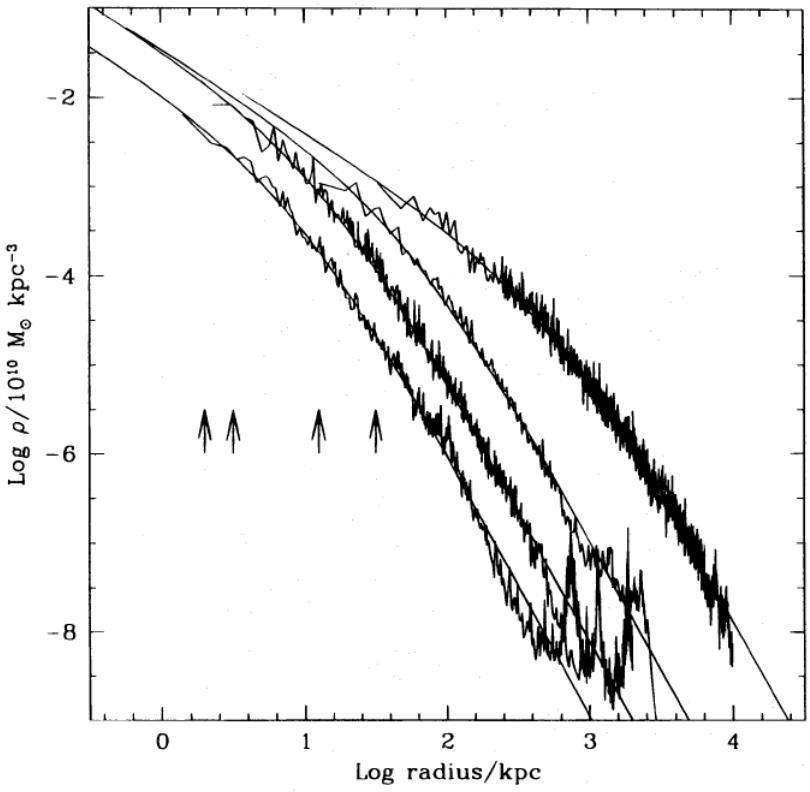

Figure 1.9: Density profiles of four haloes spanning 4 orders of magnitude in mass (3×10^{11} $M_\odot$ to 3×10^{15} $M_\odot$, left to right). Arrows indicate the gravitational softening, h_g, of each simulation used. Also shown are the fits from Equation 1.63. The fits are good over two decades in radius, approximately from h_g out to the virial radius of each system. Credits: Navarro et al. (1996)

where ρ_c is the critical density, r_s is called as the characteristic scale length and is the distance from the centre of the halo where the density of the halo changes from $\rho \propto r^{-1}$ to $\rho \propto r^{-3}$. The scale length is also specified by the concentration parameter $c = r_{200}/r_s$ which is a dimensionless parameter. The mass profile of the halo is completely defined by the mass M and the concentration parameter c. δ_{col} in Equation 1.63 is another dimensionless parameter and is linked to the concentration parameter c by:

$$\delta_{col} = \frac{200}{3} \frac{c^3}{[\ln(1+c) - c/(1+c)]} \tag{1.64}$$

Navarro et al. (1996) refer to δ_{col} as the characteristic overdensity of the halo. We show the results obtained by Navarro et al. (1996) for four haloes from their simulation which span 4 orders of magnitude from 3×10^{11} $M_\odot$ to 3×10^{15} $M_\odot$ in Figure 1.9. It can be seen that regardless of the mass of the haloes, the fit as done according to Equation 1.63 seems to fit very well the density profiles of the haloes. The gravitational softening h_g, shown by the arrows in Figure 1.9 is included in the N-body equations of motion in order to suppress

relaxation effects due to two-body encounters. h_g is obtained by modifying the gravitational potential of each particle in the simulation as:

$$\phi = \frac{-1}{\sqrt{r^2 + h_g^2}} \tag{1.65}$$

On large scales numerical simulations have shown successful results and follow the profile, but on smaller scales there are a few problems:

1. The cusp problem: The densities of the simulated galaxies possess a central cusp (when $\rho(r) \propto r^{-1}$) which is not seen in observations, especially with low mass systems. Observations of rotation curves show that there exists a flat central dark matter density profile.

2. Simulations also give a number of low mass haloes around a main massive halo which is much larger than expected from observations of satellites in the Milky Way.

Various mechanisms to explain these discrepancies have been suggested, such as for example supernova feedback or self-interacting dark matter (see Weinberg et al., 2015)

1.8 Analytic approach towards studying the spatial distribution of haloes

Kaiser (1984) introduced the concept of bias, by showing that dark matter haloes are biased tracers of the underlying dark matter distribution. He went on to propose the idea that overdense regions contained an enhanced abundance of massive objects with respect to the mean, so that these systems display enhanced clustering. One can visualise this concept in Figure 1.10, as it can be seen that those regions of density that lie above a threshold in density of ν times the rms will be strongly clustered. If objects that are forming at these high peaks (dark shaded regions, indicated by arrows), then this is a population with bias.

But to enhance the understanding of how dark haloes are distributed relative to the mass, one can use physical models and analytic approximations. A simple and accurate analytical model can help reconstruct the mass distribution from observations (Mo and White, 1996). Clustering of galaxies and clusters is understood through the bias of the haloes in which they form. Many analytical formulae have been proposed (Mo and White, 1996; Sheth and Tormen, 1999; Sheth et al., 2001) for predicting the spatial clustering of dark matter haloes and have been compared with results from $N-$body simulations.

As we have seen, Press and Schechter (1974) (PS) developed a formalism that combined the linear growth of density fluctuations and the spherical top-hat collapse to derive analytically a prescription for the mass function. However, the Press and Schechter (1974) formalism did not provide a model for the spatial clustering of dark haloes. Mo and White (1996) used the PS formalism to define dark haloes from the initial density field and to specify how a

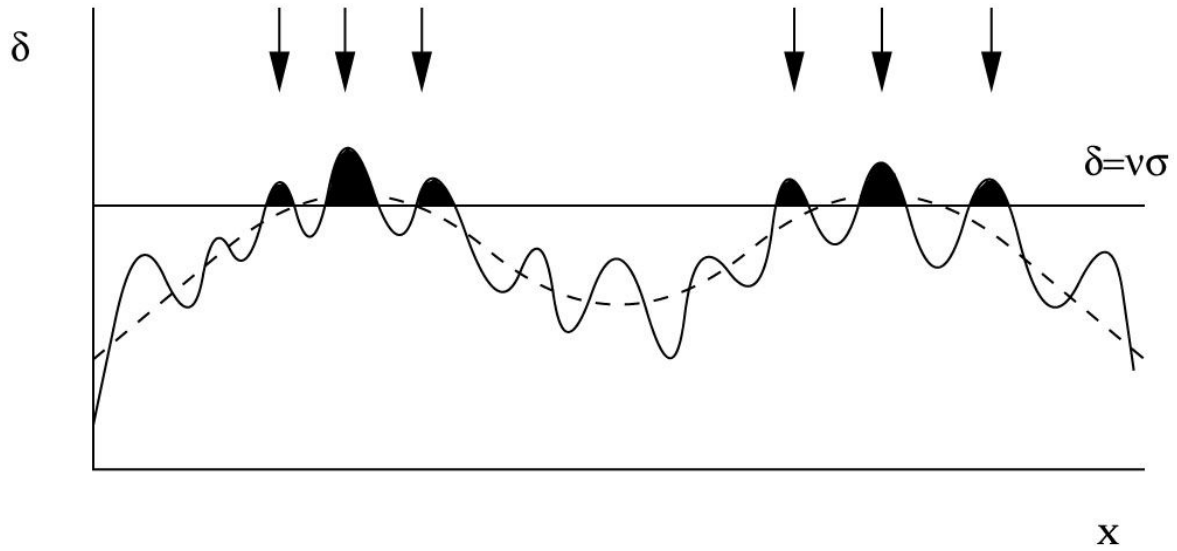

Figure 1.10: A plot of the initial primordial density fluctuations. The black line in the middle depicts the critical density of the Universe at that particular point in time. The dashed line shows the density field as a fluctuating component. Those regions of density that lie above a threshold in density of ν times the rms will be strongly clustered. If objects are presumed to form at the sites of these high peaks (shaded region, indicated by arrows), then this is a population with bias. Credits: (NED Caltech, 2016)

linear mass overdensity in a spherical region modulates the mean abundance of dark haloes in that region. They tested their simple model against results from a variety of $N-$body simulations.

It was found out that the spatial distribution of dark haloes and their relation to the underlying mass distribution could be described quite accurately. It was expected that the dark haloes were biased tracers of the underlying mass distribution and that the bias depends not only on the mass of the haloes but also on the epoch in which they are identified. On large scales the bias was given by the relation:

$$\xi_{hh}(R) = [b(M_1, z_1)]^2 \xi_m(R) \tag{1.66}$$

where ξ_{hh} is the halo-halo correlation function, b the bias factor, M_1 and z_1 denote the mass and redshift of the halo at an epoch and $\xi_m(R)$ is the standard autocorrelation function for the mass. The bias for a halo with a given mass increases with redshift and so objects that were formed at the centres of early, relatively low-mass haloes can be more strongly clustered than current haloes of equivalent or even larger mass.

Their model predicts that objects which form at a redshift z inside haloes with a mass $M = M_*(z)$ will be unbiased relative to the mass at later redshifts, where M_* is a characteristic mass for the non-linear clustering denoted as $\Delta(M_*) = \delta_c(1 + z_1)$ where $\delta_c \equiv 1.686$ as seen in Equation 1.49b. It is the mass of the halo that is typically just collapsing at redshift z.

But it was shown that their results could not be directly applied to galaxies because a 'natural' bias in the galaxy distribution could only be achieved if most galaxies formed at the centres of haloes with mass $M > M_*$. Observed galaxies, did not always correspond to the centres of the haloes present at a given epoch.

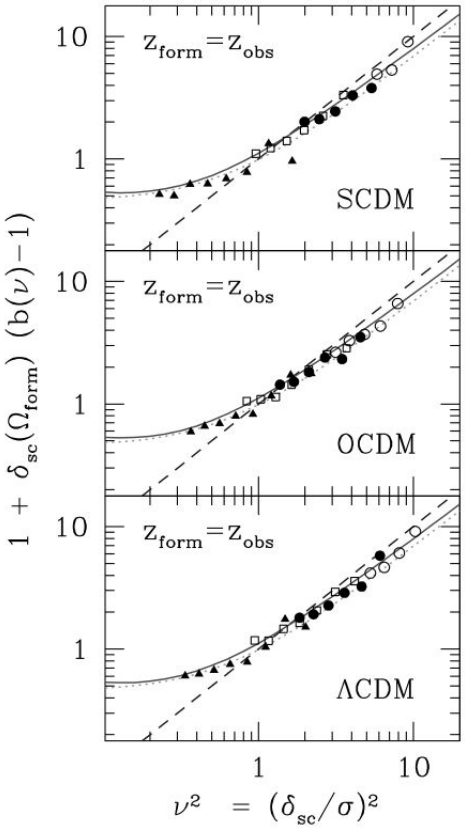

Figure 1.11: The large-scale bias factor $b(m)$ as a function of halo mass in the GIF simulations. Dashed curves show the spherical collapse prediction of Mo and White (1996), dotted curves show the peak background split formula of Sheth and Tormen (1999), and solid curves show the ellipsoidal collapse prediction of Sheth et al. (2001). Credits: Sheth et al. (2001)

Sheth and Tormen (1999) used the bias factor as calculated by Mo and White (1996) and added one step to the argument, i.e. on large scales, they realised that the peak background split [9] should be a good approximation for the bias dependence on mass. While Mo and White (1996) computed the large scale bias factor using the ratio of the volume-averaged halo and mass correlations, Sheth and Tormen (1999) computed the bias factor by measuring the ratio of the power spectra of the haloes and the dark matter. They also used a spherical overdensity group finder for measuring the mass function. They studied the halo distribution formed in the GIF simulations (Kauffmann et al., 1999) for three choices of the initial fluctuation

[9]The probability of forming a halo depends on the initial density field according to the SC model. Large-scale density field acts as a "background" enhancement of probability of forming a halo or "peak".

distribution belonging to the CDM family; a standard model (SCDM: $\Omega_0 = 1$, $\Omega_\Lambda = 0$, $h = 0.5$), an open model (OCDM: $\Omega_0 = 0.3$, $\Omega_\Lambda = 0$, $h = 0.7$) and the flat model with non-zero cosmological constant (ΛCDM: $\Omega_0 = 0.3$, $\Omega_\Lambda = 0.7$, $h = 0.7$). By using a modified version of the Press and Schechter (1974) mass function they found out that it provided a good fit to the unconditional halo mass functions in the SCDM, OCDM and ΛCDM models. On large scales, by using the peak background split, it was found out that the knowledge of the mass function was sufficient to compute a good approximation for the bias.

Moscardini et al. (2000a) went on to use the relations introduced by Sheth and Tormen (1999) to calculate the halo abundance and the bias of X-ray selected galaxy clusters. Assuming a linear-bias model, they followed the definition of an *effective* bias as introduced by Matarrese et al. (1997), given by:

$$b_{eff}(z) \equiv N^{-1}(z) \int_M \mathrm{dln}M^{-1} b(M', z) N(z, M') \tag{1.67}$$

where $N(z)$ is the expected redshift distribution for the given catalogue. They compared the bias obtained for three different X-ray catalogues with predictions for various cosmological models such as the SCDM, OCDM and ΛCDM. They found out that the bias factor is an increasing function of mass and that the Einstein-de Sitter models always give a smaller correlation amplitude compared to the models with $\Omega_M = 0.3$. This test on an observational catalogue (compared to only numerical simulations as performed) further strengthened the analytical approach towards studying the spatial distribution of haloes.

The discrepancy between theory and simulation still existed. The models by Mo and White (1996); Sheth and Tormen (1999) where not able to predict the mass function accurately, which meant that then the other model predictions, such as the large-scale halo-to-mass bias relation, were also inaccurate. It was Sheth et al. (2001) who proposed that if bound structures are assumed to form from an ellipsoidal rather than a spherical collapse, the discrepancy could be reduced. In the spherical collapse model, a region collapses if the initial density within the region exceeds a threshold value δ_{col}. This value is independent of the initial size of the region, but the mass of the collapsed object is related to its initial size. This means that δ_{col} is independent of the final mass. Whereas, in an ellipsoidal model, Sheth et al. (2001) showed that the collapse of a region depends on the surrounding shear field, as well as its initial overdensity. In Gaussian random fields, the distribution of these quantities depends on the size of the region. Since the mass of a region is related to its initial size, there exists a relation between δ_{col} and the mass of the final object. They provided a fitting to the $\delta_{ec}(m)$ (ec–ellipsoidal collapse) relation that simplified the inclusion of ellipsoidal dynamics. The GIF N–body simulations (Kauffmann et al., 1999) were used by Sheth et al. (2001) to compare their predictions of the large-scale halo bias with previous results obtained by Mo and White (1996); Sheth and Tormen (1999) as seen in Figure 1.11. They found out that the ellipsoidal collapse model represented an improvement on the spherical model on an object-by-object basis and that the mass function and the large-scale halo-to-mass bias relation, were more accurate than the standard predictions.

The first insights into the spatial clustering of dark haloes done by Mo and White (1996)

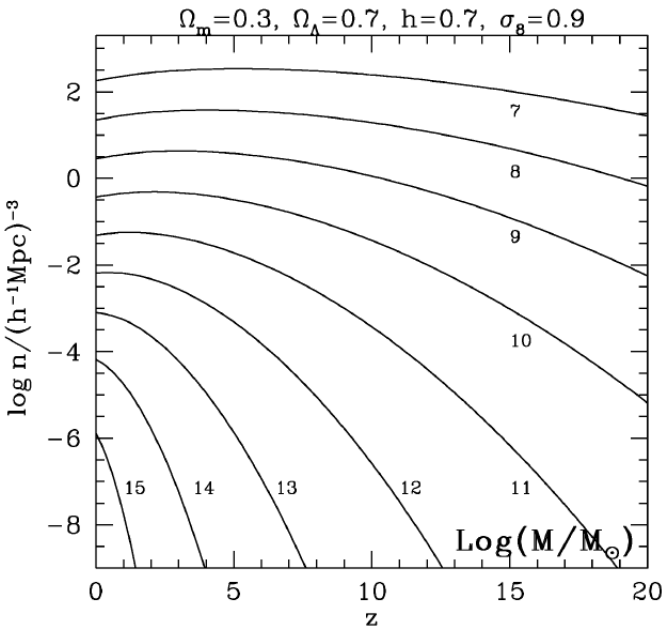

Figure 1.12: The variation with redshift of the comoving number density of dark matter haloes with masses exceeding specific value M in the ΛCDM model with $\Omega_0 = 0.3$, $\Omega_\Lambda = 0.7$, $h = 0.7$ and $\sigma_8 = 0.9$. Credits: Mo and White (2002)

was corrected by Jing et al. (1998); Sheth and Tormen (1999) who showed that at a given redshift for a halo of mass below M_*, the value of $\sigma_8(M, z)$ varies little with the mass M and for a halo of mass above M_*, the value of $\sigma_8(M, z)$ increases rapidly with M. Mo and White (2002) went on to use these corrected formulae and used 'concordance' values for the cosmological parameters to plot the halo abundance against redshift as a function of halo mass. A number of well known properties of the ΛCDM model were illustrated from their plots such as, the abundance of massive haloes ($M \sim 10^{15} M_\odot$) dropped dramatically in the relatively recent past ($z \sim 1.5$), the decline in the abundance of haloes with mass similar to the Milky Way ($M \sim 10^{12}\, M_{zodot}$) was gently, and there was no change in the abundance of less massive haloes ($M \sim 10^7$ to $10^8\, M_\odot$) over the redshift range $0 < z < 20$. It was also shown that the abundance of low mass haloes is declining slowly at low redshifts ($z \sim 2.0$) as members of these populations merge into massive systems much faster than new members that are formed. The results obtained by Mo and White (2002) are shown in Figure 1.12.

It was shown by Gao et al. (2005); Tinker et al. (2005) that the bias function derived by Sheth et al. (2001) using the peak-background split method still failed to reproduce in detail the bias of haloes found in numerical simulations. Tinker et al. (2010) demonstrated that the bias of massive, rare haloes was higher than that predicted by Sheth et al. (2001) using the ellipsoidal collapse model and approached the predictions of the spherical collapse model for the rarest haloes. Tinker et al. (2010) introduced a more flexible fitting formula for the halo bias, which was compared with a $N-$body simulation which had a minimum mass resolution of $M \sim 10^{10}\ h^{-1}$Mpc. It was concluded from their study that employing a peak-background

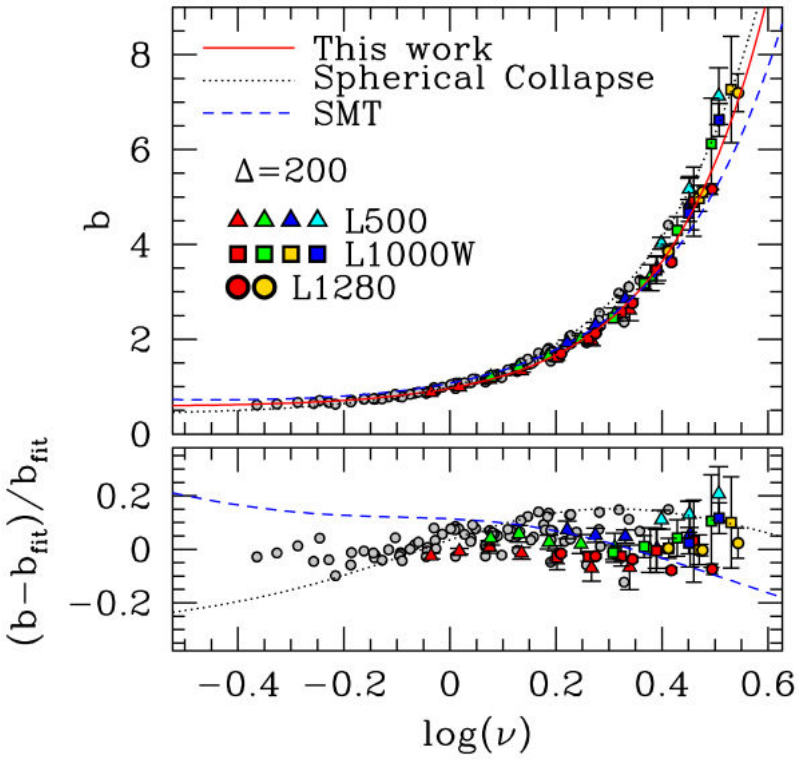

Figure 1.13: *Upper panel:* Large-scale bias as determined by the ratio $(P_h/P_{lin})^{1/2}$ for $\Delta = 200$. Results from the smaller boxes are represented by the gray circles. For these simulations, only measurements with less than 10% error are shown to avoid crowding. The larger volume simulations are represented by the coloured symbols. Each point type indicates a different simulation. The different colors, from left to right, go in order of increasing redshift from $z = 0$ to $z = 2.5$. Like colours between simulations imply the same redshift. For these large-volume simulations, measurements with less than 25% errors are shown. *Lower panel:* Fractional differences of the $N-$body results with the fitting function shown in the upper panel. Credits: Tinker et al. (2010)

split method on the mass function derived from halo catalogues, underpredicts the bias of high-peak haloes and overpredicts the bias of low-peak haloes. The comparison of the results for the bias calculated by Tinker et al. (2010) with the bias calculate by Sheth et al. (2001) is shown in Figure 1.13.

Chapter 2

What, why and how: Galaxy clusters

Contents

2.1 Galaxies and galaxy clusters: A brief introduction

A collection of dust, interstellar gas, stellar remnants, stars and dark matter bound together by gravity is what makes up a galaxy. Galaxies can vary in size, with dwarf galaxies containing only around a thousand (10^3) stars and giant galaxies that can even contain close to a billion (10^9) stars. Most of the galaxies we have so far found in the Universe seem to possess a black hole in their center core. Our own Milky way's central black hole, known as Sagittarius A*, has a mass 4 million times the mass of our Sun (Gillessen et al., 2009). From our current understanding, there are close to 170 billion to 200 billion galaxies in the observable Universe (Gott et al., 2005).

Hubble developed a now classical classification of galaxies according to their shape. He divided the galaxies into four categories, mainly, ellipticals, spirals, lenticulars and irregulars. It was later came to be known as the famous Hubble "tuning fork" diagram as it can be seen from Figure 2.1.

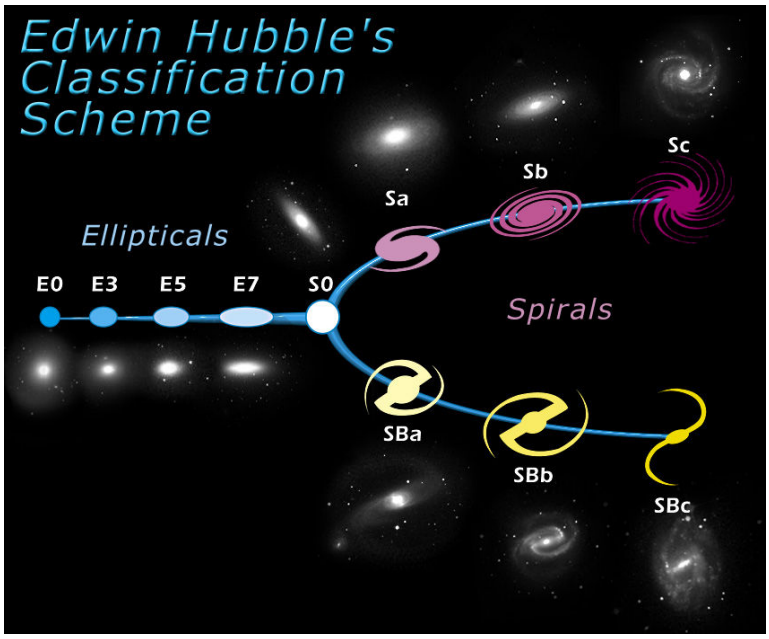

Figure 2.1: Tuning-fork style diagram to classify galaxies based on their shape as used by Hubble (Hubble sequence, 2016).

Almost all the galaxies in the observable Universe seem to be part of a group, cluster or a large-scale structure (walls, filaments) and only about 5% of the galaxies that we know today are found as solitary galaxies (Gott et al., 2005). Groups and clusters of galaxies are structures that can consist anywhere from tens to thousands of galaxies. Galaxy clusters are associated to the largest and most massive virialised dark matter haloes. The image of Abell cluster 1689, seen in both the visible and the infrared, is shown in Figure 2.2. Three components contribute to the mass of a cluster:

- **Galaxies:** They represent around 2-5% of the total mass of a galaxy cluster. They contain the baryonic matter in the form of stars and cold gas.
- **Intra-cluster medium:** The ICM constitutes 11-15% of the total mass of a galaxy cluster. It mainly consist of hydrogen and helium, the baryonic matter in ionised form and in low density. It has very high temperatures reaching close to 10^8 Kelvin. The emission from the ICM is characterised by thermal bremsstrahlung.
- **Dark matter:** It contains the major mass fraction of a galaxy cluster, i.e. around 80-87%. It follows the Navarro-Frenk-White (NFW) profile (Navarro et al., 1996).

Masses of galaxy clusters range from $10^{13}\,h^{-1}\,M_\odot$ for poor clusters to $10^{15}\,h^{-1}\,M_\odot$ for richest ones. The typical cluster virial radius is $\sim 1\ h^{-2}$Mpc (Bahcall, 1996).

Galaxy clusters are important laboratories for studying the impact of the environment on galaxy properties. For example, any galaxy that is freely falling towards the cluster center can experience speeds of up to ~1000 km s^{-1} with a pressure that is given by:

Figure 2.2: Image of Abell 1689, a massive galaxy cluster, in the constellation Virgo, at a redshift of $z = 0.183$. (ESA/Hubble Press Release, 2013).

$$P = \rho v^2 \tag{2.1}$$

where ρ is the mass density and v is the relative velocity of the galaxy with respect to the ICM. If this pressure is high enough to overcome the gravitational binding energy it can strip gas that was once bound to the galaxy that is falling in leading to star formation. It has been shown that the dense ICM in massive clusters can strip the HI disk of a galaxy and it occurs at the cores of these massive clusters (Fujita, 1998).

Galaxies that are falling into the core of a galaxy cluster eventually undergo ICM interactions. But before they can reach the ICM they interact with other galaxies inside the cluster via gravitational attraction. These interactions transform and alter the properties of these galaxies. At the core of galaxy clusters, the relative speeds of galaxies are extremely high and due to this mergers at the cores of clusters are not usually possible. Instead an infalling galaxy is likely to experience closer encounters with other galaxies at very high speeds due to the high density of galaxies in the cluster core.

2.2 Detecting a galaxy cluster

Observational studies of galaxy clusters in the modern era follow a multi-wavelength approach. These observations can reveal several components of galaxy clusters that cannot be seen at a fixed wavelength. These signatures can be used for detecting a galaxy cluster, for instance the overdensities found from optical surveys, X-ray emissions of the ICM from X-ray surveys or the distortion of the CMB through inverse Compton scattering via the SZ effect.

2.2.1 Optical and near-infrared

The first searches for galaxy clusters were done at optical wavelengths. The general method was to search for overdensities in the galaxy number counts within a given radius and magnitude interval.

It was Abell who constructed the first extensive cluster catalogue at optical wavelengths (Abell, 1958) based on the visual inspection of photographic plates. This catalogue contained 2,712 clusters and was classified into several richness groups with the condition that a cluster should contain a minimum of 50 galaxies within a magnitude range of m_3 to $m_3 + 2$ (where m_3 is the magnitude of the 3^{rd} brightest member of the cluster). The catalogue was further extended with an addition of 1,361 clusters in 1989 by co-authors Harold G. Corwin and Ronald P. Olowin by examining the southern celestial hemisphere (Abell et al., 1989).

Visual inspection was quite efficient for detecting nearby clusters, but it becomes infeasible when searching for distant clusters on large areas of the sky. Moreover, the selection process is subjective and difficult to quantify. Therefore with time different algorithms for finding clusters have been developed. The now classical matched-filter galaxy cluster finder first introduced by Postman et al. (1996) assumes a luminosity function and radial profile for galaxy clusters, scaling them to the expected distance interval corresponding to a given range in apparent magnitudes.

The fact that the central regions of galaxy clusters are dominated by red and early type galaxies, which follow a line, the so-called red sequence, in the color-magnitude diagram, has been also been used for improving cluster detection.

The red sequence selection as measured for galaxies in the "Bullet cluster" by Paraficz et al. (2012) is shown in Figure 2.3. With this method, projection effects can be minimized because galaxies in the field will generally fall outside the cluster red sequence.

Of course cluster selection is much easier when the galaxy redshifts are known: this allows to identify structures in 3D and to minimise projection effects. The simplest example is the Friend-of-Friends algorithm, first applied by Huchra and Geller (1982). Unfortunately, even with multi-object spectroscopy they are too time-consuming for large-scale searches of distant clusters.

It is however possible to estimate the redshifts from photometric data (see Chapter 6), even if errors of photometric redshifts are significantly larger than those of spectroscopic

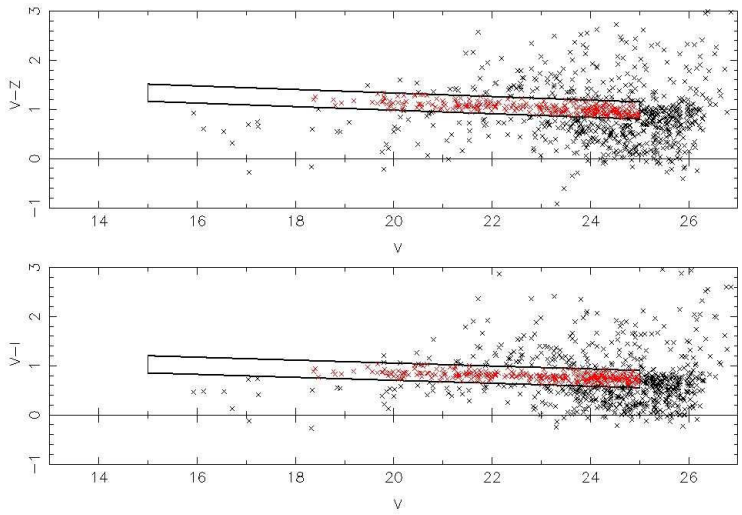

Figure 2.3: Colour-magnitude diagrams and the selection of cluster member galaxies. The red sequence selection is shown in the black boxes: all galaxies in this box are considered to be cluster galaxies. [(V-I) vs. V] or [(V-z) vs. V] colour-magnitude diagrams correspond to the main and sub-cluster components, respectively. Credits: Paraficz et al. (2012)

redshifts.

Lower redshift catalogues are comparatively easy to measure compared to high redshift catalogues, where, multicolour photometry is required to track the intrinsic 4000$\mathring{A}$ break feature [1]. The Sloan Digital Sky Survey (SDSS) made use of five-band photometry which enabled the detection of low redshift clusters (Eisenstein et al., 2011). Another cluster catalogue of 13,823 nearby clusters has been extracted from the SDSS, applying an algorithm which combines the detection of an overdensity of red galaxies in a red sequence with the presence of a brightest cluster galaxy (Koester et al., 2007)

Apart from the photometric redshift uncertainties, the major challenge for optical surveys is to get a proper richness estimate which has a lower intrinsic scatter at all mass and redshift ranges studied. Projection effects along the line-of-sight also pose a threat by the inclusion of false positive members and by the absence of true cluster members that go undetected.

2.2.2 X-ray wavelength detection

Galaxy clusters can be detected from satellite X-ray observations through the X-ray emission of their hot ICM. The observables are flux, spectral hardness and spatial extent. Follow-up observations of the same clusters can give precise measurements of density, temperature and

[1]The primary feature of an overall flat spectrum of the galaxy spectra is the 4000$\mathring{A}$ break which is caused by the blanket absorption of high energy radiation from metals in stellar atmospheres and by a deficiency of hot, blue stars.

metallicity profiles of the ICM. Typical cluster X-ray luminosities are in the range of 10^{44}erg s^{-1} or more. The ROSAT All-Sky Survey (Voges et al., 1999) was the first X-ray survey to cover the whole sky, allowing the detection of clusters up to a redshift of $z \sim 0.3$, but deeper observations of selected regions of the sky allowed the detection of clusters at higher redshifts. The flux limit of the survey was in the range of $3.0 \times 10^{-12} - 4.4 \times 10^{-12}$erg cm $^{-2}s^{-1}$.

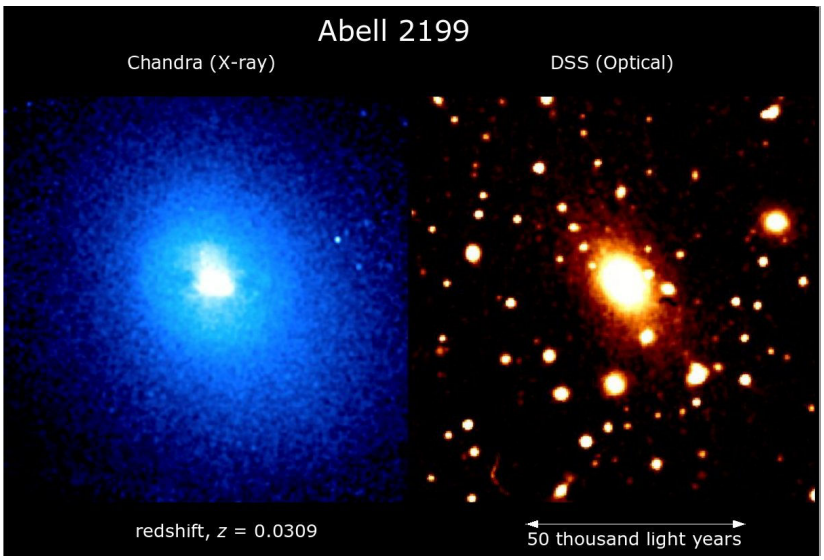

Figure 2.4: Comparison of the Chandra image of the X-ray emission from the intracluster medium in the core of the Abell 2199 galaxy cluster against the optical emission of the galaxies (from the DSS) Credits: (Chandra observatory and Digitised Sky Survey, 2016)

More recently, the ESA XMM-Newton satellite has made possible to carry out more extended and deeper cluster surveys: the XMM and the XXL cluster surveys (Lloyd-Davies et al., 2011; Pierre et al., 2016). As an example, the Abell cluster 2199 is shown in Figure 2.4 as observed both X-ray and optical wavelengths. The advantage of the X-ray surveys is the correlation between the observed X-ray luminosity and mass across the entire flux and redshift range. The major disadvantage of X-ray surveys is that it can only be carried out from space satellites which makes each mission an expensive one.

2.2.3 Sunyaev-Zel'dovich effect

The radiation coming from the CMB, hit the hot electrons that are found in the intracluster-medium and are then scattered through inverse Compton scattering. In this process, low energy CMB photons receive an energy boost. Therefore, observing the CMB in the cluster direction, one finds that the blackbody spectrum is distorted, with a lower intensity at low frequencies and a higher intensity at high frequency. The critical frequency which divides the two parts of the spectrum is 217 GHz (around 1 mm). This is the so-called thermal

Sunyaev-Zel'dovich (SZ) effect (Sunyaev and Zeldovich, 1972), which can be used to detect distant clusters. Its peculiar property is that its amplitude does not depend on distance. The intensity variation $\Delta I/I$ is of the order of 10^{-4}.

There is also a kinematic SZ (kSZ) effect, due to the peculiar motion of clusters with respect to the CMB, the electrons in the ICM cause a Doppler shift of the photons of the CMB, changing its intensity as a function of frequency.

Many SZ surveys are ongoing, such as at the South Pole Telescope (SPT) (Ruhl et al., 2004) and the Atacama Cosmology Telescope (ACT) (Menanteau et al., 2010)

The Planck mission made use of the SZ effect to detect galaxy clusters and the first results were released in 2011 Planck Collaboration et al. (2011).

2.3 Measuring the mass of a galaxy cluster: Direct measurements and mass proxies

One of the key observational challenges is that the mass estimates are usually obtained from observational properties such as:

1. Using the hot ionised intracluster medium as measured from the X-ray emission.
2. The distribution of member galaxies in a cluster, i.e. the richness estimate or using velocity distributions.
3. Sunyaev-Zel'dovich effect.
4. Using strong and weak lensing measurements.

Different assumptions are also made when calculating the mass of a cluster which are discussed in this Section. We also discuss some of the astrophysical processes that are important in measuring the mass and also discuss the pros and cons of each measurement technique.

2.3.1 Hydrostatic equilibrium: Galaxy clusters

One of the major assumptions inside galaxy clusters is that both the gas component and the galaxies within the cluster are in hydrostatic equilibrium with the cluster potential (Evrard, 1990; Bahcall and Lubin, 1994). According to this framework the ICM is assumed to collapse within the cluster dark matter halo and get heated to temperatures of around 10^7 - 10^8 K. These physical processes are described via the Euler equation:

$$\frac{dv}{dt} = - \nabla \phi - \frac{1}{\rho} \nabla P \tag{2.2}$$

where P is the total gas pressure, ϕ is the cluster potential and v is the velocity. Here the differential dv/dt is given by:

$$\frac{dv}{dt} = \frac{\partial v}{\partial t} + (v.\nabla)v \tag{2.3}$$

which is the Lagrangian derivative of the velocity. In this model the gas distribution obeys:

$$\frac{dP_{gas}}{dr} = \frac{-GM_{cl}(\leq r)\rho_{gas}}{r^2} \tag{2.4}$$

where P_{gas} and ρ_{gas} are the gas pressure and density respectively, and $M_{cl}(\leq r)$ is the total cluster binding mass within the radius r. For the cluster to be in hydrostatic equilibrium, the condition is given by:

$$\frac{dv}{dt} = 0 \tag{2.5}$$

X-ray observations of the ICM thermal properties provide us the so called hydrostatic mass of the cluster by reformulating Equation 2.5 as:

$$0 = -\nabla\phi - \frac{1}{\rho}\nabla P \tag{2.6}$$

along with assumptions of spherical symmetry and thermal pressure support of the gas. The assumption that the cluster is in hydrostatic equilibrium maybe true for virialised clusters which have settled down, but the same may not be true for all galaxy clusters (clusters that are not virialised). If any of the hypotheses in Equation 2.6 are not true, then the mass of the galaxy cluster as measured by this method will be biased. To find out if the mass estimated is biased or not, one can make use of observations of the same cluster via other wavelengths apart from X-ray. Mass of the same cluster estimated from these other observational techniques, such as lensing, SZ effect, etc. can point out the bias. It is because mass estimates from optical lensing measurements are less sensitive to the non-gravitational processes that characterise the gas present in the cluster compared to mass estimates from X-ray measurements. However, optical and lensing masses are affected by other systematics and projection effects.

A recent study by Suto et al. (2013) using the hydrodynamical simulation of Cen (2012) calculated the mass of a galaxy cluster using the hydrostatic assumption and compared the same with several other mass terms that directly correspond to the Euler equations. They found out that under the hydrostatic assumption, the mass obtained is more or less biased on the average by 10 - 20 % from the true mass for a radius $r < r_{200}$. They also found out that the hydrostatic assumption does not improve at the inner regions of the cluster.

2.3.2 Virial theorem

Galaxies and galaxy clusters are considered to be gravitationally bound systems, i.e. the objects they contain (stars in the case of galaxies and galaxies in the case of clusters) have come into dynamical equilibrium through gravity. This assumption is supported by measuring the

crossing time of an object within the system. This crossing time is defined as the time it takes for the object to fully cross the system once and is given by:

$$t_{cr} = \frac{R}{v} \tag{2.7}$$

where R is the size of the system and v is the velocity of the objects contained within the system. For example the galaxies in the Coma cluster take a time of about one-tenth the age of the Universe to cross the cluster once, indicating that the cluster is gravitationally bound (Longair, 2008).

The virial theorem refers to an energy balance of a system that is under equilibrium due to gravity. The total kinetic energy (T) and the total potential energy (U) of the system is given by:

$$T = \frac{1}{2}\sum_i m_i \dot{r}_i^2 \tag{2.8a}$$

$$U = -\frac{1}{2}\sum_{\substack{i,j \\ j\neq i}} \frac{G m_i m_j}{|r_i - r_j|} \tag{2.8b}$$

Assuming that the system is in statistical equilibrium, then:

$$\frac{d^2}{dt^2}\sum_i m_i r_i^2 = 0 \tag{2.9}$$

and therefore

$$T = \frac{1}{2}|U| \tag{2.10}$$

This is the equality which is known as the virial theorem. It can be seen that no assumptions about the velocity distributions of the particles of the system is made in the virial theorem. The velocities of the particles in the system are usually in a random order for globular clusters and elliptical galaxies and can also be in order in the case of the disc of spiral galaxies, but in all the above cases the virial theorem must hold true. In the case of galaxy clusters the positions of each galaxy in the cluster is not clearly distinguished, wherein assumptions about the cluster spatial distribution has to be made. If the velocity dispersion is independent of the masses of the galaxies in the cluster, then we can find that the total kinetic energy $T = (1/2)\sum_i m_i \dot{r}_i^2 = (3/2)M\langle v^2\rangle$ where M is the total mass of the cluster. If the system is said to be spherically symmetric, from the surface distribution of galaxies in the cluster one can get the gravitational potential energy as $U = GM^2/R_{cl}$. Thus the mass of the system using the virial theorem can be found using:

$$M = 3\langle v^2\rangle R_{cl}/G \tag{2.11}$$

The only parameters that we require to find the mass of the system is the velocity dispersion (v) and the size of the system (R_{cl}).

2.3.3 Direct methods of mass measurements: X-ray, optical and lensing masses

1. **X-ray masses:** For a spherically symmetric system in hydrostatic equilibrium, the gas density and the temperature profiles can be related to the total mass profile of the system:

$$M(r) = \frac{-rkT(r)}{G\mu m_p}\left[\frac{d\ln n(r)}{d\ln r} + \frac{d\ln T}{d\ln r}\right] \tag{2.12}$$

where $M(r)$ is the mass of the cluster within radius r, $T(r)$ is the ICM temperature, $n(r)$ is the gas particle density, G is the Newton's constant, k is the Boltzmann constant and μm_p is the mean molecular weight. For small radii, these mass measurements are fairly straightforward, but become more complicated to measure at radii larger than $r \gtrsim r_{500}$. This is because the X-ray emission becomes fainter at larger radii, and also because the levels of non-thermal pressure support increase (Nagai et al., 2007). However the hydrostatic equilibrium condition requires that the gravitational potential remain stationary and that the forces other than gas pressure and gravity to be more or less neglected. The hydrostatic mass estimate method cannot be applied to clusters that are undergoing mergers or to the regions of a system that is not relaxed. X-ray mass measurements do exhibit scatter ($\lesssim 10\%$) and are biased by $\sim$ 10-15% due to kinetic pressure arising from residual gas motions (Allen et al., 2011; Suto et al., 2013).

2. **Optical masses:** X-ray mass measurement method assumes the system to be in hydrostatic equilibrium whereas optical mass measurements are based on the assumption that the cluster is in dynamical equilibrium and the condition of the equilibrium is given by the Jeans equation (Binney and Tremaine, 2008). The Jeans equation can be written as:

$$\frac{1}{\nu}\frac{\partial}{\partial r}(\nu\sigma_{rr}^2) + 2\frac{(\sigma_{rr}^2 - \sigma_{tl}^2)}{r} = \frac{-\partial\phi}{\partial r} = \frac{-GM(r)}{r^2} \tag{2.13}$$

where $\nu(r)$ is the 3D galaxy number density profile, σ_{rr} and σ_{tl} are the radial and tangential components of the velocity dispersion, ϕ is the smooth potential. The mass within a radius r of a galaxy cluster based on optical measurements is given by:

$$M(r) = \frac{r\sigma_r^2(r)}{G}\left[\frac{d\ln\sigma_r(r)^2}{d\ln r} + \frac{d\ln\nu(r)}{d\ln r} + 2\beta(r)\right] \tag{2.14}$$

where $\sigma_r(r)$ is the 3D velocity dispersion, and $\beta = 1 - \sigma_{tl}^2/2\sigma_{rr}^2$ is the velocity anisotropy parameter defined in terms of the radial (σ_{rr}) and the tangential (σ_{tl}) velocity dispersion components. The difficulty in Equation 2.14 is the determination of $\beta(r)$ parameter. From observations one can only measure the line of sight velocity dispersion σ_{los}^2. Often from optical observations one simply derives the virial mass (Limber and Mathews,

1960). Moreover, ongoing accretion of matter and the occurrence of minor and major mergers perturb the dynamical equilibrium. Optical mass measurements may also be affected by substructure and interlopers.

3. **Lensing masses:** Another approach towards measuring the mass of galaxy clusters is by the use of gravitational lensing. The gravitational field of a cluster curves the space-time and acts as a lens for light coming from background sources. The amount of this distortion can be used to model the mass distribution in the cluster. A major advantage in using lensing masses is that it does not require any assumptions about the composition or dynamical state of the object being studied. Most of the objects in the Universe undergo weak lensing as opposed to strong lensing wherein multiple images, arcs and Einstein rings are formed. Masses from weak lensing measurements are usually calculated by fitting the observed, azimuthally averaged gravitational shear profile with a mass model (Hoekstra, 2007). For those objects that undergo strong lensing, measurements of masses are made through the regions enclosed by the gravitational arcs. If we have both weak lensing as well as strong lensing measurements, one can improve the calibration of projected mass maps (Meneghetti et al., 2010). The disadvantage in lensing mass measurements come in the form of triaxiality, which for individual mass measurements introduce a scatter at the level of 10% (Meneghetti et al., 2010).

2.3.4 Thermal structure of the ICM

Some of the very first observations did not have proper angular resolution and thus involved the total ICM emission of clusters and provided us with the bulk temperature information of the cluster ICM (Sarazin, 1986; Sarazin and Graney, 1991). It was known from these temperature studies that galaxy clusters form from the gravitational collapse of overdense regions and approach equilibrium configuration which is characterised by the virial theorem given by:

$$E_{kin} = -2E_{pot} \propto \frac{GM}{R} \tag{2.15}$$

where E_{kin} and E_{pot} are the kinetic and potential energy respectively, and M is the total mass of the galaxy cluster including all the mass of dark matter present. The ICM plasma also attains a virial temperature which shows the depth of the gravitational potential of the cluster. When collisions are taking place, the gravitational potential energy of the ICM is converted into heat. The relation between the cluster mass the the ICM temperature is given by:

$$T \propto \sigma_{DM}^2 \propto \frac{M}{R} \propto M^{2/3} \tag{2.16}$$

where σ_{DM} is the velocity dispersion of the dark matter particles. The first analysis to confirm the trend of linear proportionality between ICM temperature with velocity dispersion was done by Mushotzky (1984), the results of which can be seen in Figure 2.5. In the current era the spectroscopically confirmed ICM temperature are one of the best mass proxies as a single observable parameter (Böhringer and Werner, 2010).

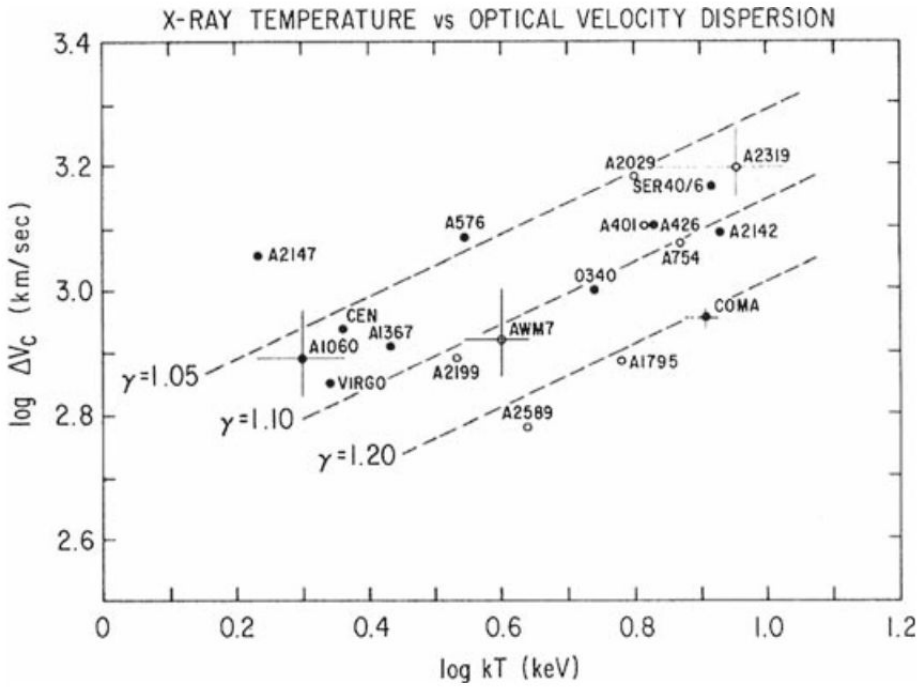

Figure 2.5: Correlation of the ICM temperature with the velocity dispersion of the galaxies in clusters (Mushotzky, 1984). The temperatures have been derived from X-ray spectra taken with the HEAO-1 satellite A-2 experiment. The dots are data for non-cD clusters and the open symbols for cD clusters (clusters with a central dominant, cD type galaxy). The lines show predictions of polytropic models with various indices (see Mushotzky (1984))
. Credits: Böhringer and Werner (2010)

2.3.5 Mass proxies: Mass observable relations

The direct methods we have discussed have some limitations and also require time-consuming observations. In order to use cluster masses as a cosmological tool, one needs large samples of clusters. Hence the importance of finding observational quantities relatively easy to measure which are correlated with mass, which are called mass proxies, is required. A good mass proxy should be easily measurable and should also have a low scatter across the mass and redshift range studied (Rozo et al., 2009; Pratt et al., 2009; Rozo et al., 2011; Rykoff et al., 2012, and references therein). Different observables of clusters are obtained at different wavelengths which can then be compared with one another to find the best possible mass

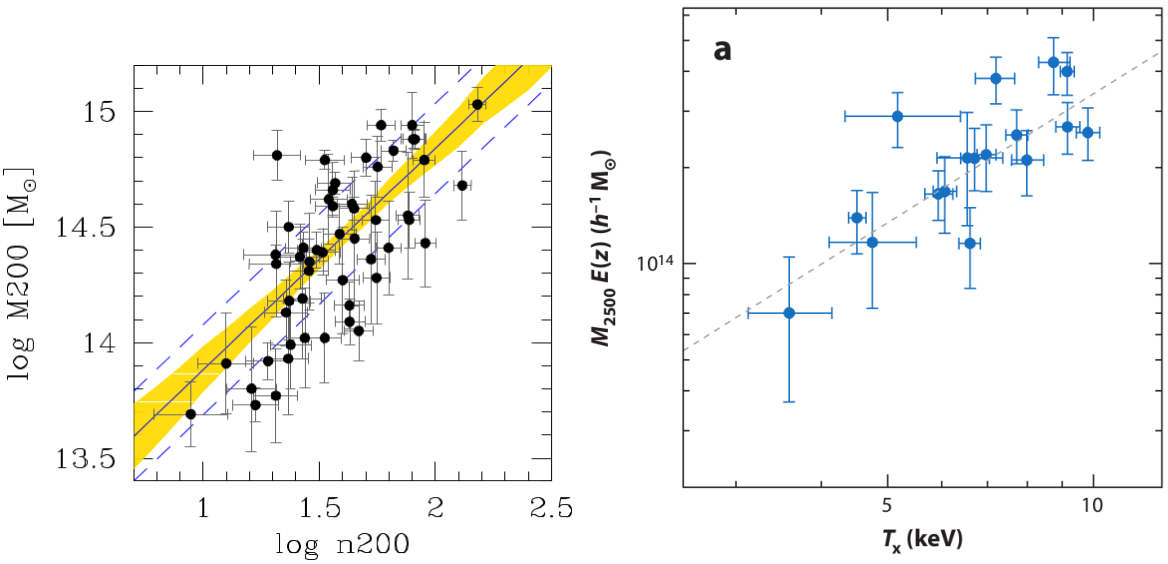

(a) (b)

Figure 2.6: *Left:* Richness-mass scaling of clusters from Rines and Diaferio (2006). The solid line marks the mean fitted regression line of log(M200) on log(n200), while the dashed line shows this mean plus or minus the intrinsic scatter σ . The shaded region marks the 68% highest posterior credible interval for the regression. Error bars on the data points represent observed errors for both variables. The distances between the data and the regression line is due in part to the measurement error and in part to the intrinsic scatter. Credits Andreon and Hurn (2010) *Right:* Scaling relations using masses estimated for individual clusters. Weak lensing masses versus intracluster medium temperature for an X-ray-selected sample imaged by the Canada-France-Hawaii Telescope from Hoekstra (2007). Credits: Allen et al. (2011)

proxy. One of the main aspects that should be taken in to account when comparing scaling relations from the different observables is that the analysis should account for the survey selection function and the cluster mass function properly. If the above properties are not taken in to account properly when two different observables from two different surveys are being compared, the result obtained on the amplitude and slope of the scaling relation may not give us the uncertainties that are expected, i.e. they will be biased.

1. For X-ray surveys, the X-ray temperature (T_X) and luminosity (L_X) and gas mass (M_{gas}) are used as mass proxies. For some of the most massive clusters, it has been found that the X-ray emitting gas mass is correlated with the total mass of the cluster, with the scatter being $< 10\%$ at a fixed mass (Allen et al., 2011). However for most X-ray surveys, the assumption of hydrostatic equilibrium is applied regardless of whether the cluster is relaxed or not and this can introduce a scatter in the scaling relations (Nagai et al., 2007). The product of the two, i.e. $Y_X = M_{gas}T_X$ is also used as a proxy and it was shown by Kravtsov et al. (2006) that Y_X is a good mass proxy

with a remarkably low scatter of only $\approx 5-7\%$ in M_{500} for a fixed Y_X, at both low and high redshifts and regardless of whether clusters are relaxed or not.

2. In the case of optical surveys, richness is the main mass proxy, which is defined as the number of cluster members above a given luminosity and within a given radius. The advantage of richness as a mass proxy is that it can be computed for any optical/near-infrared survey in the whole range of masses and redshift studied. But at the same time, measurement of richness of a galaxy cluster is hampered by background subtraction; in the case of maxBCG clusters, the scatter at a fixed mass has been estimated at $\sim 40\%$ (Rozo et al., 2009, and references therein).

In Figure 2.6a we show the scaling relation between richness N_{200} (number of cluster members within the virial radius R_{200}, where R_{200} refers to the radius within which the mean density of a cluster is $200 \times \rho_{critical}$) and mass M_{200} (mass within the virial radius) performed by Andreon and Hurn (2010) for clusters taken from Rines and Diaferio (2006). It can be seen that on the whole there exists a correlation between richness and mass even though the ± 1 intrinsic scatter band does not contain 68% of the data points which is because of the presence of measurement errors (refer to Andreon and Hurn (2010) for more details). In Figure 2.6b we plot the scaling relation between X-ray temperature T_X and mass M_{2500} for clusters observed using the Canada-France-Hawaii Telescope from Hoekstra (2007). The selection bias is relatively unimportant here because the detectability of cluster is only weakly affected by X-ray temperature. It can be seen that there exists a scatter between temperature and mass, but on the whole there exists a positive correlation between the two parameters.

Chapter 3

Galaxy and cluster clustering

Contents

3.1 Methodology: Quantifying structures

It was during the late 1980s that more and more galaxies were discovered using larger telescopes, and thus the path towards the statistical analysis of these galaxies opened. One of the earliest catalogues to study more than a million galaxies was the Lick galaxy catalogue (Shane, 1964). They were observed using photographic plates at the Lick Observatory. The maps of the counts of these galaxies were published by Seldner et al. (1977), which were a projected map of galaxies. These maps showed clearly that the distribution of galaxies on the projected sky were not uniform and that the number of galaxies per cluster were varying widely from a few pairs to several hundreds. A much deeper photographic survey was made using the 48-inch Palomar Schmidt telescope, which was used by Zwicky (Zwicky et al., 1961) who compiled a catalogue of galaxies and clusters of galaxies. It was noticed that clusters of galaxies also show a tendency of clustering similar to galaxies.

3.1.1 Definition of the correlation function

In order to measure the clustering of a distribution of objects, one of the most commonly used quantitative measure is the two-point correlation function (Totsuji and Kihara, 1969;

Davis and Peebles, 1983). The two-point correlation function ξ is defined by the joint probability δP of finding an object in each volume elements dV_1, dV_2 separated by a distance r_{12} (Peebles, 1980) and is given by:

$$\delta P = \overline{n}^2[1 + \xi(r_{12})]dV_1 dV_2 \tag{3.1}$$

where $\overline{n}$ is the mean density. Considering homogeneity and isotropy $\xi(r_{12})$ depends on the magnitude of separation vector but not on its direction (Efstathiou, 1996). The $\overline{n}^2$ factor makes $\xi(r)$ dimensionless. In a uniform random Poisson process, the probability of finding objects in volume elements dV_1, dV_2 are independent, so the joint probability is the product of the single point probabilities:

$$\delta P = \overline{n}^2 \delta V_1 \delta V_2 \tag{3.2}$$

Comparing the above equation to Equation 3.1, it can be seen that for a uniform Poisson process, the value of $\xi = 0$. If there is clustering at a distance r, then $\xi(r) > 0$. If points are anti-correlated, then $\xi(r) < 0$. $\xi(r)$ is a first order measure of clustering, giving us an analytical view of how much our dataset deviates from a uniform distribution. In the case of galaxy clusters, $\xi(r)$ is usually greater than 0 within a given range ($1 - 200\ h^{-1}$Mpc).

3.1.2 Different estimators of the correlation function

The role of the two-point correlation function is central in calculating the clustering distribution of objects, but several estimators exist in the literature for extracting ξ from a set of spatial points. The difference between all the estimators of ξ lies in their respective method of edge correction. To measure $\xi(r)$ we need to consider the fact that one cannot complete spheres of radius r everywhere in our survey. For example, at the edges of the survey, the sphere will not be complete. We need to perform edge correction so that we do not loose pairs of objects. To do so, we construct a random catalogue within the same geometry as the data catalogue. We discuss here the three major estimators that have been used extensively in clustering studies.

One of the earliest estimators widely used was the Davis and Peebles (1983) (DP) estimator which was given by:

$$\xi_{DP}(r) = \frac{N_R}{N_D}\frac{DD(r)}{DR(r)} - 1 \tag{3.3}$$

where N_R refers to the number of points in the random catalogue, N_D refers to the number of points in the data catalogue, DD refers to the data-data pairs and DR refers to the data-random pairs.

Hamilton (1993) (HAM) came with an improved estimator that had smaller statistical errors, it was given by:

$$\xi_{HAM}(r) = \frac{DD(r) \times RR(r)}{[DR(r)]^2} - 1 \tag{3.4}$$

where DD refers to the data-data pairs and RR refers to the random-random pairs.

It was during the same year that Landy and Szalay (1993) (LS) proposed another estimator that is given by:

$$\xi_{LS}(r) = 1 + \frac{N_R^2}{N_D^2}\frac{DD(r)}{RR(r)} - 2\frac{N_R}{N_D}\frac{DR(r)}{RR(r)} \tag{3.5}$$

where N_R refers to the number of points in the random catalogue, N_D refers to the number of points in the data catalogue, DD is the number of object pairs counted within a spherical shell within r and $r + dr$, DR refers to the number of data-random pairs and RR refers to the random-random pairs.

Kerscher et al. (2000) compared various estimators that were available in calculating the two-point correlation function and found out that at small scales all the estimators were comparable with one another. But at large scales, the Landy and Szalay (1993) and the Hamilton (1993) estimators significantly outperformed all the other estimators showing small deviations for a given cumulative probability. It was also shown by Kerscher et al. (2000) that the LS estimator was considerably less sensitive to the number of random points used and also handled edge corrections well, which can affect clustering measurements on large scales, compared to the HAM estimator. So the LS estimator is preferred from a practical point of view.

3.1.3 Power spectrum

An overdensity at point x is given by $\delta(x)$. Assuming that the Universe is periodic in a space of volume V and defining the Fourier transform pair as:

$$\delta(x) = \sum_k \delta_k e^{-ik.x} \tag{3.6}$$

where δ_k is given as:

$$\delta_k = \frac{1}{V}\int \delta e^{ik.x} d^3x \tag{3.7}$$

The relation between the $\xi(r)$ and δ_k is:

$$\xi(r) = \sum_k \langle|\delta_k|^2\rangle e^{-ik.r} \tag{3.8}$$

i.e. the two-point correlation function is the Fourier transform of the power spectrum $P(k) = \langle|\delta_k|^2\rangle$.

The relation between $P(k)$ and $\xi(r)$ is given by:

$$\xi(r) = \frac{1}{2\pi^2}\int d\mathrm{k}\mathrm{k}^2 P(k)\frac{\sin(kr)}{kr} \tag{3.9}$$

where k is the wavenumber which is given by $k = 2\pi/\lambda$ (λ is the wavelength of a fluctuation). It is predicted from inflation that the power spectrum of the primordial density fluctuations was nearly scale independent, i.e. following a power-law given by:

$$P(k) \propto k^n \tag{3.10}$$

where n denotes the spectral index (also known as the Harrison-Zeldovich spectrum). CMB observations confirm this prediction and show that n is very near but not exactly equal to 1 (0.968 ± 0.006 according to the results of Planck Collaboration et al. (2015)).

The usual approach in quantifying galaxy clustering at large scales is by measuring $\xi(r)$ or $P(k)$ and applying statistics to detect departures from a Gaussian distribution (Efstathiou, 1996). In the case of a density field in which the fluctuations are drawn from a Gaussian distribution, the power spectrum gives a complete statistical description of the fluctuations (Baugh, 2000).

3.1.4 Angular two-point correlation function

There were a number of surveys that sampled large volumes of space (Zwicky et al., 1961; Shane, 1964; Maddox et al., 1990) but most of the surveys only gave two-dimensional information of the galaxy distribution. So angular correlation function to these catalogues were measured. The angular two-point correlation function which can be defined by means of the conditional probability δP of finding two clusters within solid angles $d\Omega_1$ and $d\Omega_2$ and separated by an angle θ:

$$\delta P = N^2[1 + w(\theta)]d\Omega_1 d\Omega_2 \tag{3.11}$$

where N refers to the mean surface density of galaxies per unit area in the catalogue and $w(\theta)$ is the angular correlation function.

However, the spatial correlation function $\xi(r)$ can be inferred from $w(\theta)$ by means of the Limber equation (Limber, 1954) which provides an integral relation between the angular correlation function $w(\theta)$ and $\xi(r)$ for small angles:

$$w(\theta) = \int_0^\infty y^4 \phi^2(y) dy \int_0^\infty \xi(\sqrt{x^2 + (y\theta)^2}) dx \tag{3.12}$$

where y is the comoving distance, $\phi(y)$ is the radial selection function normalised such that $\int \phi(y) y^2 dy = 1$.

The real-space correlation function measured from several studies of both galaxy and cluster catalogues (Totsuji and Kihara, 1969; Peebles, 1980; Davis and Peebles, 1983; Bahcall and Soneira, 1983; Bahcall and West, 1992) was quite well approximated by a power-law of the form:

$$\xi(r) = \left(\frac{r}{r_0}\right)^{-\gamma} \quad \text{for scales } r \leq 150\ h^{-1}\,\text{Mpc} \tag{3.13}$$

where r_0 is the correlation length and γ is the slope. The so called correlation length measures the amplitude of the clustering process. In other words, it is the scale at which $\xi(r) = 1$. The larger the correlation length for a given sub-sample, the stronger is the clustering. It was shown by Peebles (1980) that if $\xi(r)$ followed a power-law model, so does $w(\theta)$ and is given by:

$$w(\theta) = A\theta^{1-\gamma} \tag{3.14}$$

where A is an amplitude which depends on the survey selection function and the Gamma function Γ.

3.2 Redshift-space distortions: Effect on the correlation function

On small scales ($\leq 1\ h^{-1}$Mpc), galaxies that reside within groups and clusters have large random motions relative to each other. These interactions can give rise to a velocity of more than 1000 km/s to a galaxy in a random direction. If the direction of this velocity is towards or away from us, then one needs to add or subtract this to the radial velocity respectively that we would expect from the Hubble flow:

$$v_{total} = H_0 \times D + v_{peculiar} \tag{3.15}$$

where H_0 is the Hubble constant, D is the distance to the cluster and $v_{peculiar}$ is the peculiar velocity.

Therefore while all of the galaxies in the group or cluster have a similar physical distance from the observer, they have somewhat different redshifts. This causes an elongation in redshift space maps along the line-of-sight within overdense regions and is referred to as the "Fingers of God" effect. The result is that groups and clusters appear to be radially extended along the line-of-sight towards the observer as seen in Figure 3.1. The lower left panel of Figure 3.1 shows the galaxies in redshift-space with "Fingers of God" pointing back to the observer, while in the lower right panel, the "Fingers of God" have been modelled and removed.

Redshift-space distortions are also seen on larger scales ($\geq 1\ h^{-1}$Mpc) due to streaming motions of galaxies that are falling in to structures that are still collapsing. Adjacent galaxies moving in the same direction lead to a coherent motion and cause an apparent contraction of structures along the line-of-sight in redshift-space, and is also called as the Kaiser effect (Kaiser, 1987).

While calculating the two-point correlation function, redshift-space distortions can complicate these measurements. Instead of the real-space correlation function $\xi(r)$, what we measure is the redshift-space correlation function $\xi(s)$, where s is the redshift-space separation between a pair of galaxies. $\xi(s)$ also does not a follow the power-law as mentioned in

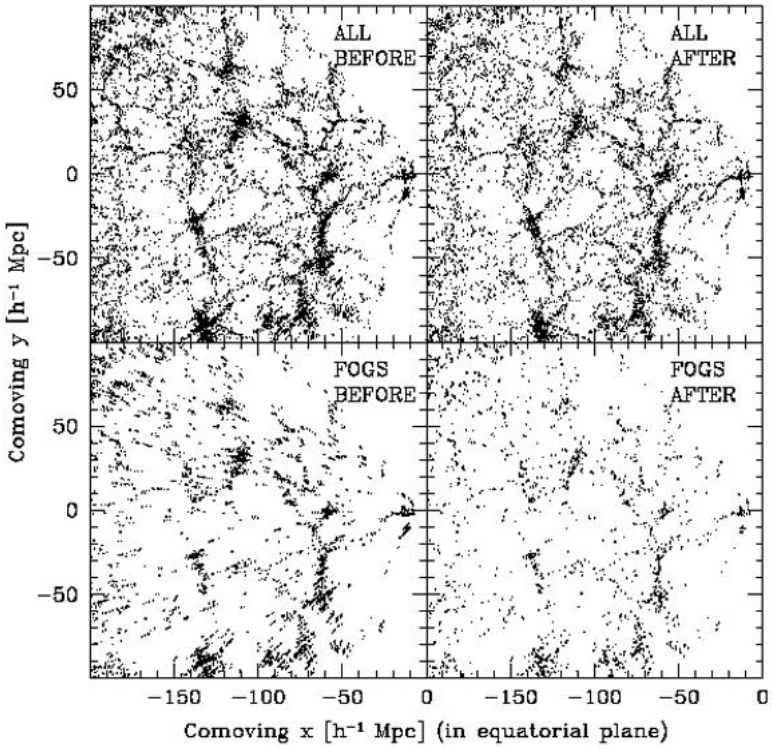

Figure 3.1: An illustration of the "Fingers of God" , or elongation of virialised structures along the line-of-sight, from Tegmark et al. (2004). Shown are galaxies from a slice of the SDSS sample (projected here through the declination direction) in two dimensional comoving space. The top row shows all galaxies in this slice (67,626 galaxies in total), while the bottom row shows galaxies that have been identified as having "Fingers of God". The right column shows the position of these galaxies in this space after modelling and removing the effects of the "Fingers of God". The observer is located at (x,y = 0,0), and the "Fingers of God" effect can be seen in the lower left panel as the positions of galaxies being radially smeared along the line of sight toward the observer. Credits: Coil (2013)

Equation 3.13 over the same range of scales as $\xi(r)$, because redshift-space distortions on both small and large scales decrease the amplitude of the clustering relative to intermediate scales (Coil, 2013). $\xi(r)$ measures the physical clustering of galaxies, independent of peculiar velocities. In order to recover the real-space correlation function, ξ is therefore measured in two dimensions, both along (π) and perpendicular (r_p) to the line-of-sight.

Given a pair of galaxies with redshift positions x_1 and x_2, the separation of the pair in redshift-space is given by $s \equiv x_2 - x_1$ and the line of sight separation is $l = \frac{1}{2}(x_1 + x_2)$. The parallel and perpendicular distances to the pair are given by:

$$\pi = \frac{s.l}{(1+\bar{z})|l|} \tag{3.16a}$$

$$r_p = \frac{\sqrt{|s|^2 - \pi^2}}{1 + \bar{z}} \tag{3.16b}$$

where $\bar{z} = \frac{1}{2}(z_1 + z_2)$. Counting pairs in both (r_p, π) dimensions will then provide the anisotropic correlation function $\xi(r_p, \pi)$. Projected correlation function $w_p(r_p)$ can be derived from $\xi(r_p, \pi)$ by integrating along r_p, which can be related to the real-space correlation function.

3.3 Galaxy correlation function, a brief review: Angular and spatial correlations

As we have seen in Section 3.1, in the mid 1950s, redshift information was not available for all galaxies. Astronomers had to calculate the angular correlation function as given by Equation 3.11. They were however able to invert the angular correlation function using Limber's equation to get the spatial correlation function $\xi(r)$ as seen in Equation 3.12. This inversion however was not a very stable process (Simon, 2007). To obtain the angular correlation function, one has to count the number of distinct galaxy pairs within a given separation θ and compare the same with the number of similar pairs found in the random catalogue.

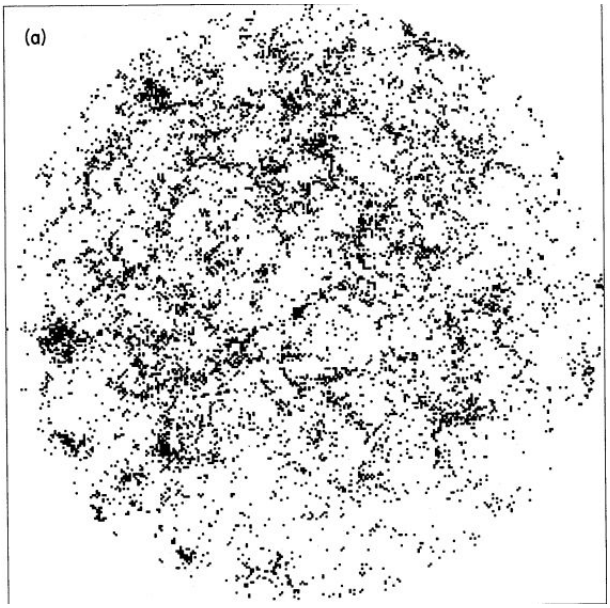

Figure 3.2: A projected plot of North Galactic Cap part of the Lick catalogue. Credits: Coles and Plionis (1991)

Totsuji and Kihara (1969) made use of the galaxy catalogue from Shane and Wirtanen (1967) to calculate the angular two-point correlation function $w(\theta)$ and were the first to derive a power-law model for $\xi(r)$ on the basis of $w(\theta)$. They obtained values of $r_0 = 4.7$ Mpc and $\gamma = 1.8$. Peebles (1975) also made use of these set of galaxies and calculated the

so called angular two-point correlation function. In Figure 3.2 the projected distribution of the galaxies detected in the North Galactic Cap in the Lick catalogue is shown.

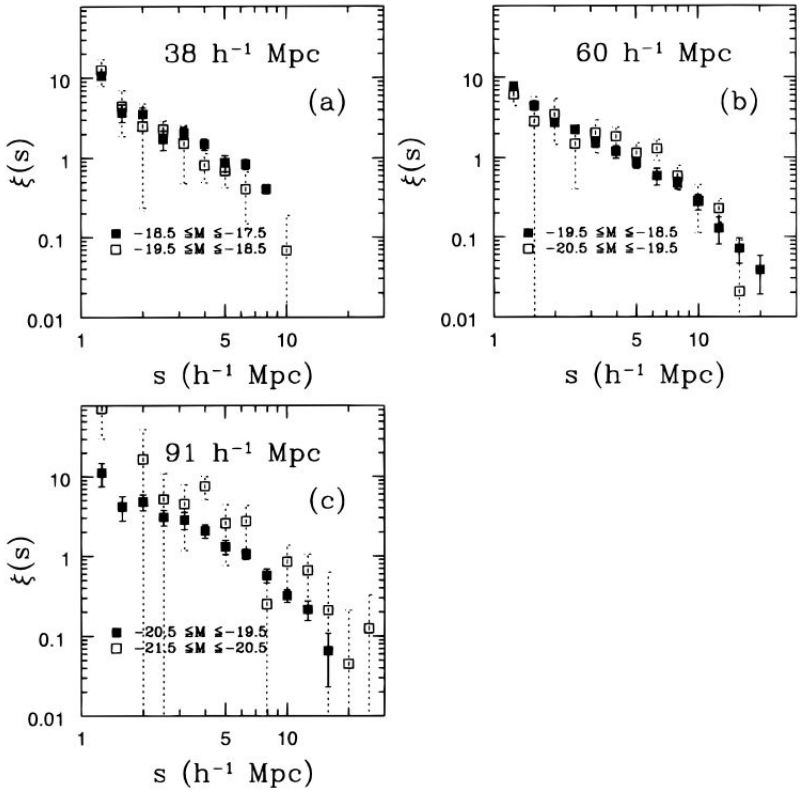

Figure 3.3: The redshift-space correlation function $\xi(s)$ is displayed in various panels, each corresponding to a given luminosity class: (a) $-19.5 < M < -18.5$, (b) $-20.5 < M < -19.5$, and (c) $-21.5 < M < -20.5$. Within each panel, $\xi(s)$ is presented for three different volumes. Symbols vary from open triangles to open squares and filled squares with decreasing size of the sample. Credits: Benoist et al. (1996)

The CfA survey (Davis et al., 1982) was started in 1977 and produced the first large area and moderately deep maps of large scale structure in the nearby Universe. It also gave the first crude but truly quantitative measurements of the 3D clustering properties of galaxies. de Lapparent et al. (1988) calculated the spatial two-point correlation function for the galaxies observed from the CfA redshift survey (Geller and Huchra, 1983) which contained a data of around 2,200 galaxies. They found out that $\xi(r)$ had a slope of $\gamma \approx 1.6$ and a correlation length of $r_0 \approx 7.5\ h^{-1}$Mpc. The correlation length obtained was larger than the "standard" value matched to the theoretical models.

Measurements of the correlation function of galaxies from the CfA survey was followed by the measurements of the samples obtained by the APM galaxy survey (Maddox et al., 1990) which was derived from the APM Galaxy Survey of the UK Schmidt Telescope plates. The real-space correlation function of the APM galaxy samples was calculated by Baugh

et al. (1995) and was also compared with the results obtained from the Stromlo-APM survey (Loveday et al., 1996). Baugh et al. (1995) found out that for $\Omega = 1$ and clustering that was fixed in comoving coordinates, the $\xi(r)$ on scales $r \leq 4\ h^{-1}$Mpc was well fitted by a power-law model $\xi(r) = (r/4.1)^{-1.7}$.

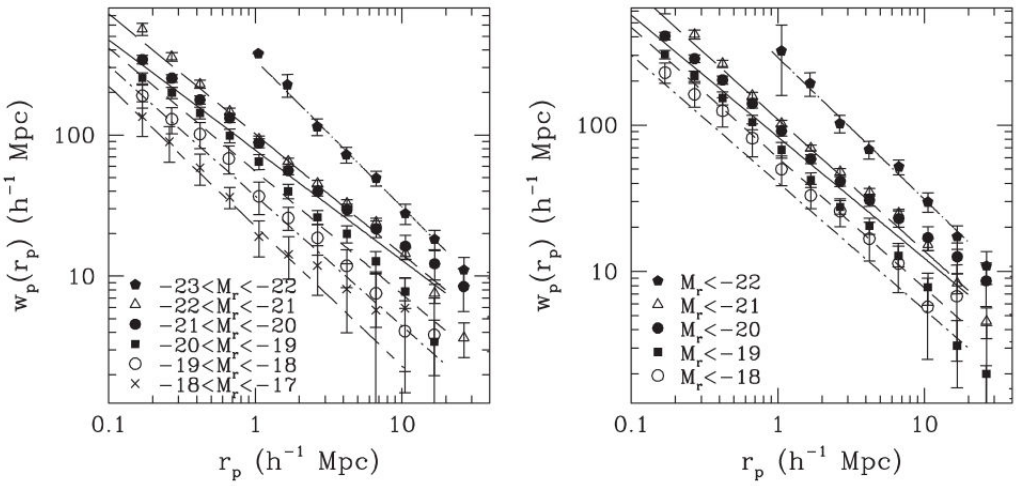

Figure 3.4: *Left:* Projected galaxy correlation functions $w_p(r_p)$ for volume-limited samples with the indicated absolute magnitude and redshift ranges. Lines show power-law fits to each set of data points, using the full covariance matrix. *Right:* Same as the left panel, but now the samples contain all galaxies brighter than the indicated absolute magnitude; i.e., they are defined by luminosity thresholds rather than luminosity ranges. Credits: Zehavi et al. (2005)

The APM survey was complete to a magnitude limit of $b_J = 17.15$, which was succeeded by the Southern Sky Redshift Survey 2 (SSRS2) catalogue (da Costa et al., 1994) which included redshifts of around 3,600 objects found in sky coverage of 5500 deg^2 with a magnitude limit of $m_B \leq 15.5$. The survey was also 99% complete to the $m_B = 15.5$ magnitude limit. Benoist et al. (1996) investigated the variation of galaxy clustering with luminosity using the SSRS2 catalogue. It was found out that clustering measurements based on $\xi(s)$ and the variance of counts in cells revealed a strong dependence of clustering on luminosities for galaxies brighter than L_*, while no significant variation was detected for fainter galaxies, as it is seen in Figure 3.3. The variation of $\xi(s)$ with luminosity was calculated for three different volumes as seen in Figure 3.3 and it was found out that galaxies brighter than a magnitude of -20.5 were significantly more clustered than those in the range $-20.5 < M < -19.5$. It was inferred from these results that galaxy clustering was dependent on luminosity.

The Las Campanas Redshift Survey (LCRS) (Shectman et al., 1996) was a survey with a sky coverage of 700 deg^2 that measured redshifts for 26418 galaxies. The galaxies were selected from a CCD-based catalogue measured in the R-band. The $\xi(r)$ for the LCRS galaxy samples was determined by Tucker et al. (1997) who obtained a correlation length of $r_0 = 6.3\ h^{-1}$Mpc and also by Jing et al. (1998) who obtained a value of $r_0 = 5.1\ h^{-1}$Mpc. Several small scale surveys followed the LCRS survey but the Sloan Digital Sky Survey

(SDSS) was the first survey that created the most detailed 3D map of the Universe.

The first batch of data obtained from SDSS was analysed by Zehavi et al. (2002), who made use of 29300 galaxies observed within a sky coverage of 690 deg^2. They made up a number of long narrow segments (2.5 - 5 degrees) and arrived at an average real-space correlation function of:

$$\xi(r) = \left(\frac{r}{6.1 \pm 0.2\ h^{-1}\text{Mpc}}\right)^{-1.75\pm0.03} \tag{3.17}$$

within the range $0.1 < r(h^{-1}\text{Mpc}) < 16$. This value of r_0 was similar to the value obtained from the LCRS result of Tucker et al. (1997). Zehavi et al. (2002) then used an updated catalogue from SDSS which contained 118,149 galaxies to calculate the real-space two-point correlation function and obtained a value of:

$$\xi(r) = \left(\frac{r}{5.77\ h^{-1}\text{Mpc}}\right)^{-1.80} \tag{3.18}$$

Thus the main discovery from the analysis of the galaxy-galaxy two-point correlation function was that it described the deviation of the galaxy distribution from homogeneity and that it scales as a simple power-law over certain range of scales.

The luminosity dependence of the galaxy correlation as shown by Benoist et al. (1996) using the galaxies from the SSRS2 sample was tested by Zehavi et al. (2005) on the SDSS catalogue using a sample of ~200,000 galaxies observed over 2500 deg^2. Zehavi et al. (2005) studied the luminosity and colour dependence of the galaxy two-point correlation function. Volume-limited samples of specified luminosity ranges were used for which the projected correlation function $w_p(r_p)$ (directly related to the real-space correlation function $\xi(r)$ as we will see in detail in Chapter 6) was calculated. It was found out that the amplitude of $w_p(r_p)$ increased continuously with luminosity form $M_r \approx -17.5$ to $M_r \approx -22.5$ with the most rapid increase occurring above the characteristic luminosity $L_*(M_r \approx -20.5)$ as seen in Figure 3.4. $\xi(r)$ was approximated by a power-law ($\xi(r) = (r/r_0)^\gamma$) over the scales $0.1 < r_p(h^{-1}\text{Mpc}) < 10$ for the samples with $M_r > -22$ and they obtained values of $\gamma \approx 1.8$ and $r_0(L_*) \approx 5.0\ h^{-1}$Mpc.

Zehavi et al. (2005) divided the galaxies by colour and found out that red galaxies have stronger clustering, steeper correlation functions at small scales, and much stronger "Fingers of God" redshift-space distortions. The correlation functions for the red galaxies were found to follow closely a power-law with $\gamma \approx 1.8$. The blue galaxies on the other hand in luminosity-bin samples had correlation functions close to a power-law with $\gamma \approx 1.7$, with amplitudes that increased with luminosity. The findings of Zehavi et al. (2005) that clustering increases with luminosity most markedly above L_*, agreed with previous studies by Loveday et al. (1995); Benoist et al. (1996).

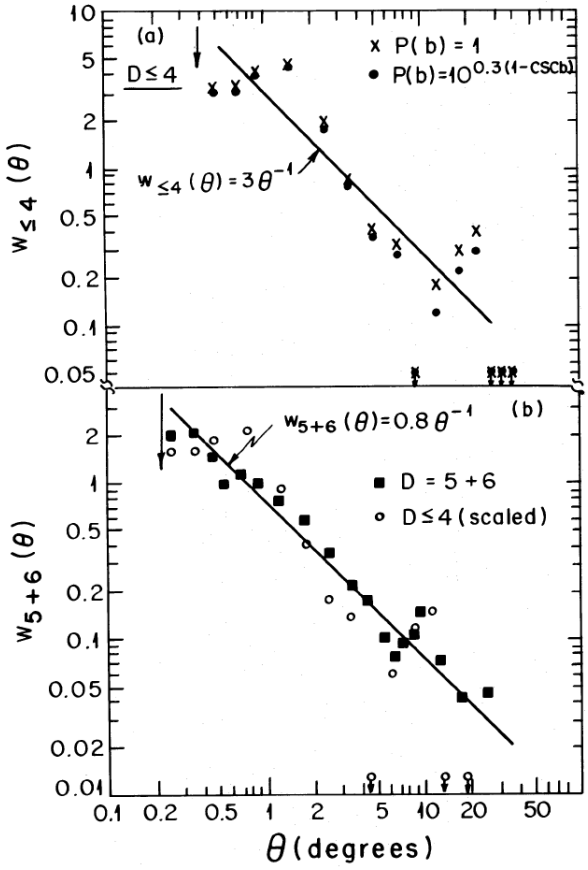

Figure 3.5: *On top:* The angular correlation function of a sub-sample (D≤ 4) of Abell clusters and *Bottom:* the same for the D = 5+6 sub-sample as calculated by Bahcall and Soneira (Bahcall and Soneira, 1983). It can be seen that the angular correlation function reaches unity at $\theta \sim 3^\circ$ in the top plot and at $\theta \sim 0.8^\circ$ in the bottom plot.

3.4 Cluster correlation function, a brief review: Angular and spatial correlations

One of the prominent studies of angular clustering of Abell clusters was done by Bahcall and Soneira (1983) and Klypin and Kopylov (1983). The angular two-point correlation function was measured for a total of 104 clusters that were determined from a complete redshift sample to distance class $D \leq 4$ ($z \lesssim 0.1$) and were tested against a deeper and larger sample at $D = 5 + 6$ (1574 clusters). One of the results obtained by Bahcall and Soneira (1983) is shown in Figure 3.5, where it can be seen that the angular correlation function reaches unity at $\theta \sim 3^\circ$ extending with weaker correlations at $\theta \sim 25^\circ$.

As more and more redshift information were becoming available, for the first time it became possible to calculate the distances to galaxy clusters (although they had errors associated) and in turn, measure directly the spatial correlation function instead of inverting the

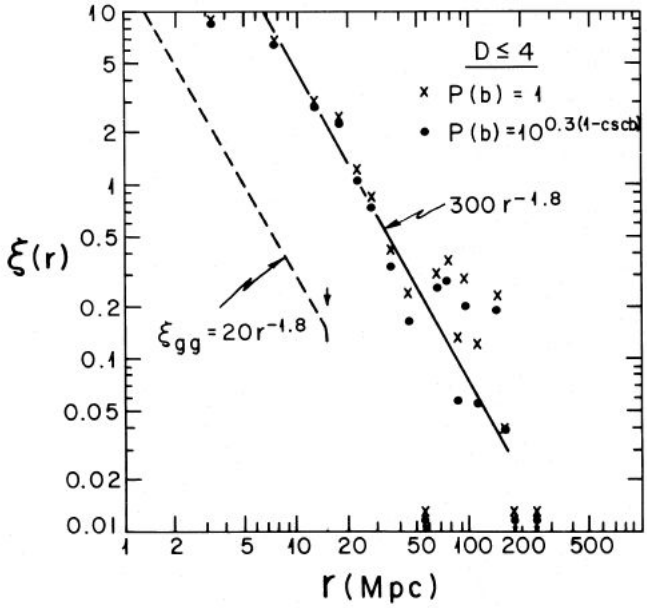

Figure 3.6: The spatial correlation function of a sub-sample (D≤ 4) of Abell clusters as calculated by Bahcall and Soneira (Bahcall and Soneira, 1983). It can be seen that the spatial correlation function reaches unity at $r \approx 25\ h^{-1}$Mpc. Strong correlations are observed at all separations below $r \leq 25\ h^{-1}$Mpc and above $r > 50\ h^{-1}$Mpc, they weaken.

angular correlation function by using the Limber's equation. Bahcall and Soneira (1983) and Klypin and Kopylov (1983) used the redshift information available for the Abell clusters and estimated the spatial correlation function. To get $\xi(r)$ they made use of the Davis and Peebles estimator. An ensemble average of 1000 random catalogues were constructed, each containing 104 clusters. The results obtained by Bahcall and Soneira (1983) are shown in Figure 3.6. Strong spatial clustering was observed for all separations below $r \leq 25\ h^{-1}$Mpc and the correlation length obtained from the power-law fit was around 25 h^{-1}Mpc. The best-fit power-law relation obtained was:

$$\xi(r) = \left(\frac{r}{25\ h^{-1}\text{Mpc}}\right)^{-1.8}, \quad 5 \lesssim r \lesssim 150 h^{-1}\text{Mpc} \tag{3.19}$$

This correlation length of 25 h^{-1}Mpc and the slope of $\gamma = 1.8$ is considered to be the standard value that is obtained for galaxy cluster catalogues compared to 5-10 h^{-1}Mpc and a slope of $\gamma = 1.8$ for galaxy catalogues. We will see in the forthcoming Sections, that the values we get for our best-fit parameters obtained for the simulated cluster catalogue and also for observed catalogues falls within this range. It can be seen from Figure 3.6 that up to a separation of 50 h^{-1}Mpc, the correlation function followed a smooth power-law distribution above which it starts to deviate from it. Bahcall and Soniera concluded that if these weak correlations at larger separations were real, they should also be found in future large redshift sample of clusters and this is exactly what we see today. But there still remained several important

questions with regard to cluster-cluster correlation function that needed answering.

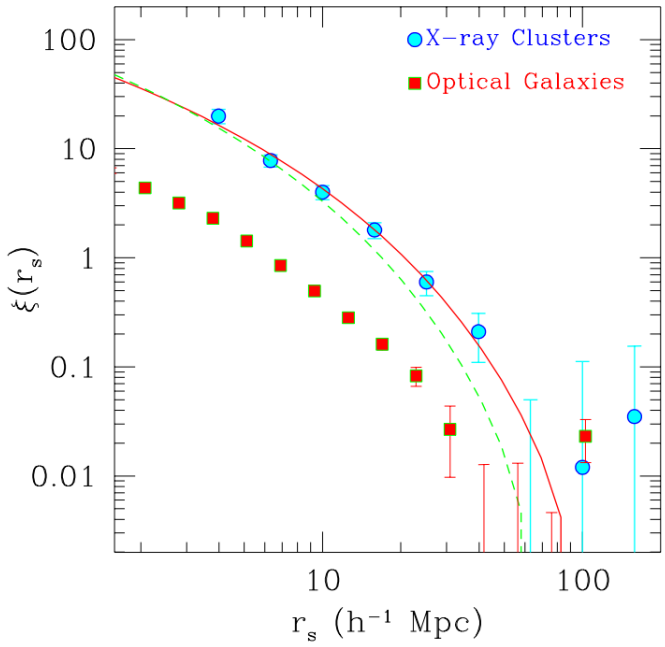

Figure 3.7: The two-point correlation function for the X-ray selected clusters from the REFLEX survey (circles) and for the Las Campanas Galaxy Redshift survey (squares). The solid and dashed lines are the expected results for an X-ray similar survey in a ΛCDM model with different values for the cosmological parameters. Credits: Borgani and Guzzo (2001)

1. The Abell catalogue which was used for the analyses was a catalogue in which clusters were identified by eye. So there was question as to whether the catalogue was free from systematic biases.

2. If some of the less rich clusters were excluded from the sample, would we obtain a different result for the correlation function?

The analogy between galaxy-galaxy clustering and cluster-cluster clustering is that both their correlation functions follow a power-law of the same form ($\xi(r) = (r/r_0)^{-\gamma}$) with the same slope $\gamma \approx 1.8$. Borgani and Guzzo (2001) calculated and compared the correlation function obtained from X-ray clusters and optically identified galaxies, the results of the same are shown in Figure 3.7. The similarity in the slope for both the galaxy catalogue and the cluster catalogue can be clearly seen up to scale of $\approx 50\ h^{-1}$Mpc. The reason for the higher amplitude of the cluster correlation function compared to the galaxy correlation function was inferred as a consequence of the fact that more massive haloes correspond to higher and rarer density fluctuations, which have a higher correlation amplitude (Kaiser, 1984). Galaxy clusters are associated to the most massive virialised dark matter haloes and as a consequence their correlation function is strongly amplified.

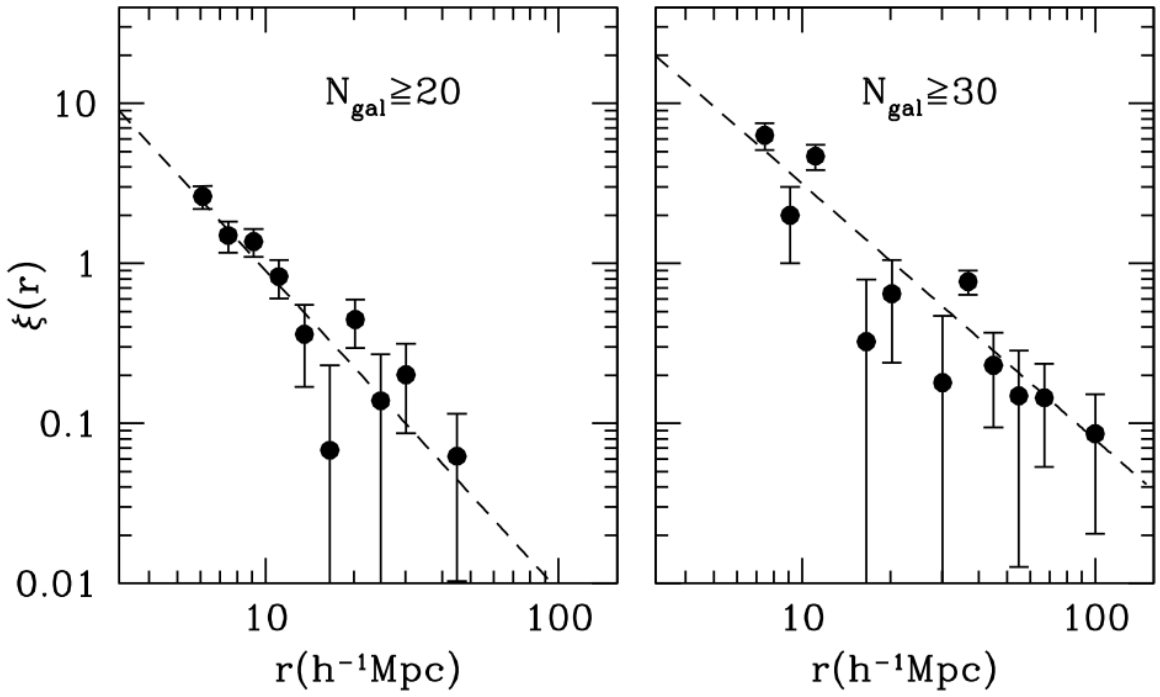

Figure 3.8: The spatial two-point correlation function (filled circles) in red- shift space for the Abell $R = 0$ richness sample (right-hand panel) and APM richness sample (left-hand panel) as measured by Basilakos and Plionis (2004). The error bars are estimated using the bootstrap procedure. The dashed lines represent the best-fitting power law as mentioned in Equation 3.13. Credits: Basilakos and Plionis (2004)

A good alternative to the Abell cluster catalogue was not available until the early 1990s. There were several cluster surveys such as the APM cluster catalogue and 2dFGRS (Colless et al., 2001) which provided possible alternatives. But it was after the advent of the SDSS (Koester et al., 2007), and more measurements of the two-point correlation function of galaxy clusters were measured. Here we highlight some of the prominent studies made on cluster-clustering in the recent years.

One of the first studies of the clustering properties of the SDSS clusters using the two-point correlation function was done by Basilakos and Plionis (2004). They made use of the SDSS Cut and Enhance (CE) cluster catalogue (Goto et al., 2002), limited to a redshift range of $z < 0.3$ and divided the sample into two richness subsamples corresponding to Abell $R \geq 0$ and Automated Plate Measuring (APM) clusters respectively. They used the power-law as mentioned in Equation 3.13 to model the correlation function and calculated it using the Hamilton estimator. The $\xi(r)$ as calculated by them is shown in Figure 3.8, and the best-fit parameters obtained for the two subsamples were $r_0 = 20.7^{+4.0}_{-3.8}\ h^{-1}$Mpc with $\gamma = 1.6^{+0.4}_{-0.4}$ and $r_0 = 9.7^{+1.2}_{-1.2}\ h^{-1}$Mpc with $\gamma = 2.0^{+0.7}_{-0.5}$ respectively. The results obtained were consistent with the dependence of the cluster richness on the correlation length.

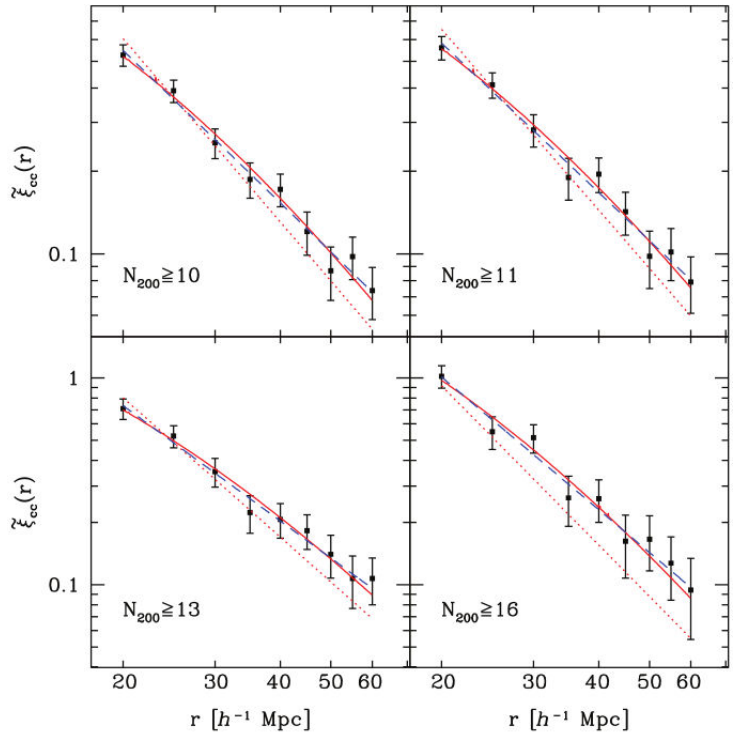

Figure 3.9: Data points show the cluster correlation function in photo-z space measured for the four richness samples in bins of width Δr = 5 h^{-1}Mpc, with jackknife errors. Dotted red curves show inferred power-law $\xi_{cc}(r)$ in real-space, assuming σ_z = 0.01. Solid red curves show best-fit power-law models convolved with the photo-z error distribution, $\widetilde{\xi_{cc}}(r)$, which should match the data. Dashed blue curves show power-law fits to the data assuming no photo-z error correction, σ_z = 0. Credits: Estrada et al. (2009)

They also went on to compare the correlation function with the predictions of three spatially flat quintessence models (Ω_M = 0.3) and estimated the cluster redshift-space distortion parameter $K(\beta)$ (refer to Basilakos and Plionis (2004) for more details). They concluded that the amplitude of the cluster redshift correlation function increases by ~12-26%.

A similar study of the two-point correlation function of optically selected galaxy clusters in the SDSS was made by Estrada et al. (2009). They made use of the clusters selected from the MaxBCG cluster catalogue, within a redshift range of $0.1 < z < 0.3$ and divided the sample into several richness cuts. A similar modelling of the correlation function as done by Basilakos and Plionis (2004) was used. Since the clusters redshifts in the sample selected were estimated photometrically, a model of the observed correlation function to include the impact of photo-z errors was proposed. Specifically they found out that a geometric smearing approach (refer to Estrada et al. (2009) for more details) removed significantly the impact of the photo-z errors. We show in Figure 3.9 the $\xi(r)$ obtained for four arbitrary richness cut samples along with the best-fit performed by Estrada et al. (2009). The values of the best-fit

Sample	R_0	γ	χ^2/d.o.f.	d
		$\sigma_z = 0.01$		
$N_{200} \geqslant 10$	15.93 ± 0.33	2.21 ± 0.11	0.45	33.1
$N_{200} \geqslant 11$	16.45 ± 0.38	2.18 ± 0.12	0.36	35.4
$N_{200} \geqslant 13$	18.14 ± 0.43	2.24 ± 0.15	0.33	40.0
$N_{200} \geqslant 16$	19.33 ± 0.48	2.56 ± 0.23	0.48	46.9
		$\sigma_z = 0.007$		
$N_{200} \geqslant 10$	14.80 ± 0.46	1.98 ± 0.10	0.42	33.1
$N_{200} \geqslant 11$	15.27 ± 0.52	1.95 ± 0.11	0.35	35.4
$N_{200} \geqslant 13$	17.14 ± 0.56	2.00 ± 0.13	0.31	40.0
$N_{200} \geqslant 16$	19.18 ± 0.58	2.26 ± 0.17	0.47	46.9
		$\sigma_z = 0$		
$N_{200} \geqslant 10$	14.42 ± 0.73	1.84 ± 0.11	0.43	33.1
$N_{200} \geqslant 11$	14.81 ± 0.81	1.80 ± 0.12	0.39	35.4
$N_{200} \geqslant 13$	16.94 ± 0.92	1.85 ± 0.14	0.30	40.0
$N_{200} \geqslant 16$	20.10 ± 0.92	2.13 ± 0.19	0.49	46.9

Table 3.1: Power-law fits to the cluster correlation function on scales $r = 20 - 60\ h^{-2}$Mpc for thee values of photo-z error variance, $\sigma_z = 0.01, 0.007$ and 0. Credits: Estrada et al. (2009)

parameters obtained for the richness cut samples with different photometric uncertainties is given in Table 3.1.

The $r_0 - d$ relation of the cluster samples from the MaxBCG cluster catalogue was also calculated by Estrada et al. (2009) and they found out that the results obtained were consistent with that predicted in N-body simulations of ΛCDM (Younger et al., 2005), but with a slightly higher value (10-15%) of r_0 at a fixed d.

Using the photometric data of the SDSS DR6 and clusters identified by Wen et al. (2009), Hong et al. (2012) went on to calculate the two-point correlation function of 13,904 clusters selected from the catalogue within $z \leq 0.4$. Hong et al. (2012) used the same power-law as used by Estrada et al. (2009) to fit the correlation function within scales of $10h^{-1}$ Mpc $\leq r \leq 50h^{-1}$ Mpc. They obtained values of $r_0 = 18.84 \pm 0.27\ h^{-1}$Mpc for clusters with a richness cut of $R \geq 15$ and a smaller value of $r_0 = 16.15 \pm 0.13\ h^{-1}$Mpc for clusters with a richness cut of $R \geq 5$. The slope of $\gamma = 2.1$ was obtained for both the samples.

More recently, Sereno et al. (2015), used the data from SDSS-III DR8 by (Wen et al., 2012) containing 132684 clusters that were optically selected. Richness samples defined using the total $r-$band luminosity within R_{200} were used to calculate the dependence of the two-point correlation function on richness. Sereno et al. (2015) find a clear increase in the correlation function with increasing richness.

It can be seen that there has been significant improvement in the cluster catalogues used from 2004 until now. The number of clusters detected, the sky coverage of the survey, the depth of the survey in terms of redshift and also in terms of magnitude limits has increased. Future cluster surveys such as LSST and Euclid are aimed at detecting large number of clusters with a large sky coverage and it has been shown by Sartoris et al. (2016) that the figure

of merit significantly increases when adding cluster clustering information.

Chapter 4

Cosmology using galaxy clusters

Contents

Galaxy clusters are the latest objects to have been formed in the formation of cosmological structures and provide information on the growth history of structures and the underlying cosmological models in many ways (see Allen et al., 2011; Hong et al., 2012; Sartoris et al., 2016, and references therein). The number counts and the spatial distribution of these objects have a strong dependence on many cosmological parameters, especially the matter density parameter Ω_M and the amplitude of the mass power spectrum. By studying the redshift evolution of the number counts of clusters and the two-point correlation function one can obtain constraints on the Cold Dark Matter (CDM) and Dark Energy density parameters (Allen et al., 2011; Sartoris et al., 2016). Here we briefly explain the several ways in which clusters on the whole can be utilised for cosmological parameter studies.

4.1 Using the brightest central galaxies as standard candles

In the past, brightest cluster galaxies have been used as "standard candles" to measure H_0 and also the traditionally called "deceleration" parameter q_0. It was named deceleration parameter because at the time of definition it was thought that the Universe was slowing down and q_0 was believed to be positive. But it has been found to be negative, which implies that the Universe is accelerating. It is defined as:

$$q_0 = -\frac{\ddot{a}a}{\dot{a}^2} \tag{4.1}$$

where a is the scale factor which is a function of time, i.e $a(t)$. This gives us $\dot{a}$ to be the first derivative of the scale factor and $\ddot{a}$ to be the second derivative of the scale factor. The deceleration parameter can also be written in terms of Ω_M and Ω_Λ as:

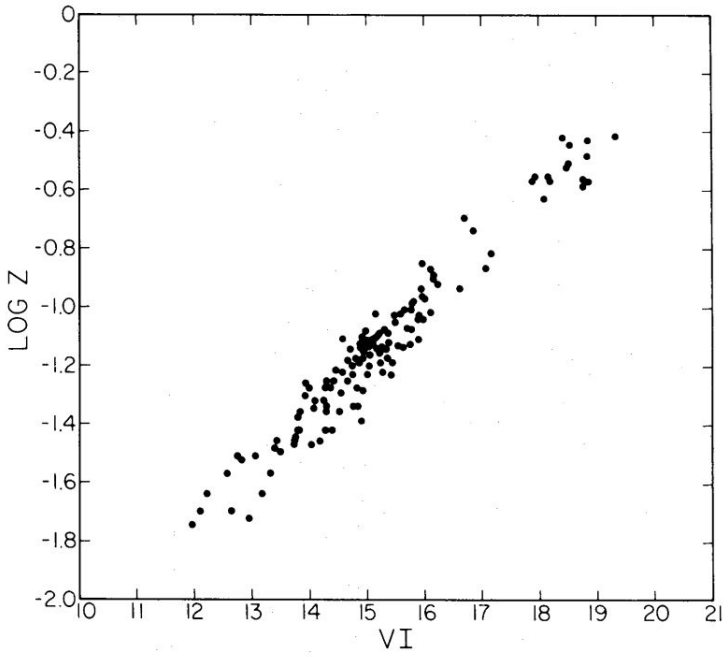

Figure 4.1: Hubble diagram for the data from Abell clusters with the x-axis denoting apparent magnitude and the y-axis denoting redshift, both in logarithmic scales. A formal value of $q_0 = -0.55$ was obtained with an error of $\sigma_{q_0} = 0.45$. Credits: Hoessel et al. (1980).

$$q_0 = \frac{\Omega_M}{2} - \Omega_\Lambda \tag{4.2}$$

Hoessel et al. (1980) analysed Abell clusters using photometric observations in the green and red passbands of the photometric system of Thuan and Gunn (1976). They obtained the redshifts and the apparent magnitudes for each cluster and derived the redshift-apparent magnitude diagram (shown in Figure 4.1) from which they inferred the value of the deceleration parameter (q_0).

From their studies they obtained a value of $q_0 = -0.55$, which implied that the Universe is accelerating and that $\Omega_\Lambda = \Omega_M/2 + 0.55$, a positive value for Ω_Λ. Their result is consistent with what has been discovered with the Supernovae Ia, but as the authors themselves noted, the result was affected by uncertainties related to the luminosity evolution of BCGs, and therefore it was not considered as a robust evidence for acceleration.

The global Hubble flow linearity was demonstrated later by Lauer and Postman (1992) using 114 BCGs from a full-sky sample of all Abell clusters within 15,000 km s^{-1}. They found out that the BCG Hubble diagram was consistent with a uniform Hubble flow over the redshift range $0.01 \leq z \leq 0.05$. But it was shown by Strauss et al. (1995) that none of the leading models of structure formation that were consistent with other measures of large-scale power could reproduce the result obtained by Lauer and Postman (1992).

Later the studies by Riess et al. (1995) (using SNIa) and Giovanelli et al. (1996) (using

the Tully-Fisher relation) suggested that the bulk motion on smaller scales that probed by the BCGs was inconsistent with the bulk flow as measured by Lauer and Postman (1992) at high levels. Thus the usage of BCGs as a distance indicator does not provide tight constraints and so remains controversial.

4.2 Mass function of galaxy clusters

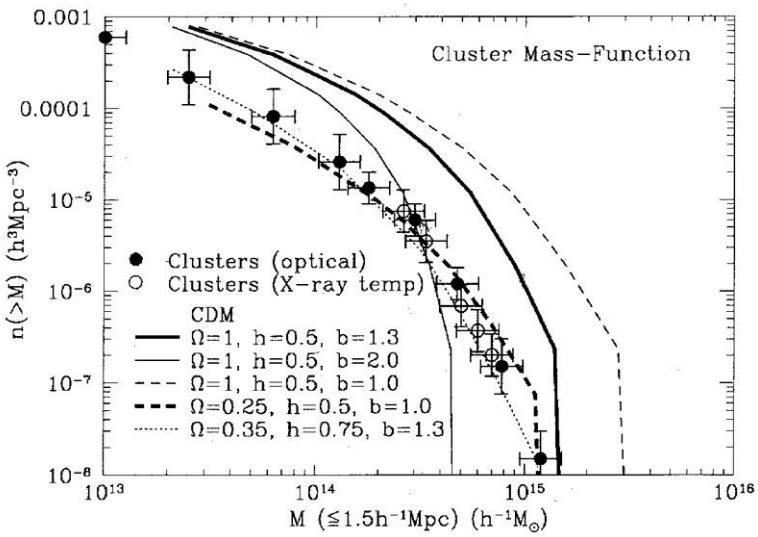

Figure 4.2: The mass function of galaxy clusters observed in both optical and X-ray, compared with CDM simulations with different values for the Ω_M parameter, as performed by Bahcall and Cen (1992).

The mass function of galaxy clusters, which is given by the number density of clusters as a function of their mass and a given redshift, can also be studied and compared with the different models of the ΛCDM framework to constrain the different cosmological parameters (Bahcall and Cen, 1992). If we can get a precise estimate of the cluster mass function and the evolution with redshift, tight constraints on cosmology can be performed.

One of the first studies that calculated the cluster mass function from observations (both in optical and X-ray) and compared them to CDM simulations was done by Bahcall and Cen (1992) and their results are shown in Figure 4.2. The optically selected cluster masses were derived from richness, velocity and luminosity whereas the X-ray selected cluster masses were derived from temperature. The mass function for the CDM simulations for different cosmological parameters were then compared with the observed mass function and the Ω_M = 1 model failed to reproduce it. On the other hand, the low-density Ω_M = $0.25, 0.35$ models were consistent with the observations quite well. and fitted the observations quite well.

More recently the mass function of galaxy clusters was analysed by Vikhlinin et al. (2009) for the Chandra observations of clusters detected in the X-ray wavelength by ROSAT.

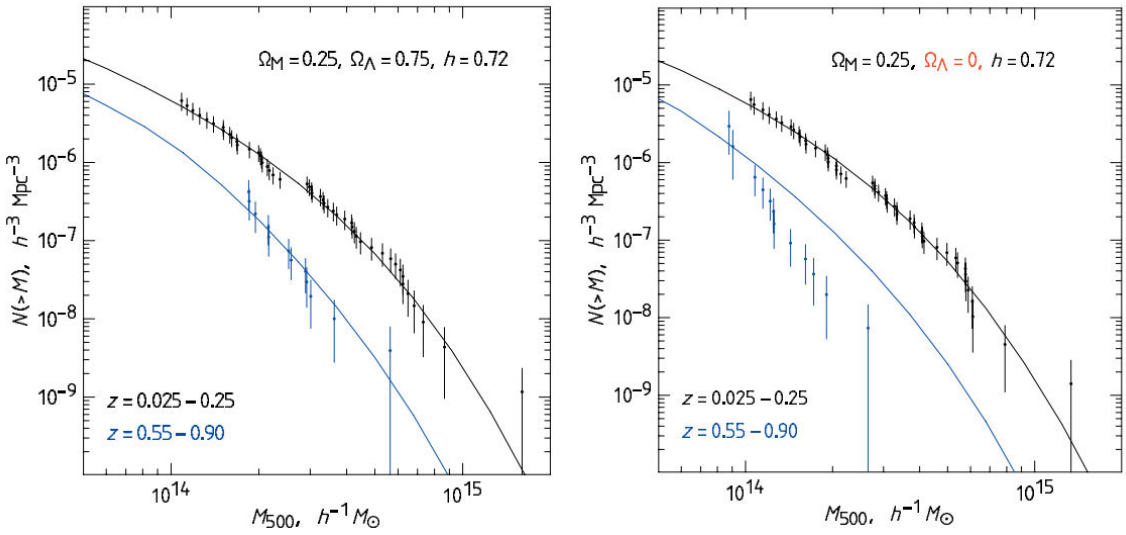

Figure 4.3: Illustration of the sensitivity of the cluster mass function to the cosmological model. The left panel shows the measured mass function and model predictions (with normalization at $z = 0$) computed for a cosmology which is close to the best-fit model is shown. For the high-z cluster only the most distant sub-sample ($z > 0.55$) is shown to better illustrate the effects. In the right panel, both the data and the models are computed for a cosmology with $\Omega_\Lambda = 0$. In this case, the predicted number density of $z > 0.55$ clusters is in strong disagreement with the data. Credits: Vikhlinin et al. (2009)

Vikhlinin et al. (2009) used a low-redshift sample that included 49 high-flux clusters at Galactic latitudes $|b| > 20°$ and $z > 0.025$ (effective depth of the sample being $z < 0.15$) and a high-redshift sample that included 37 $z > 0.35$ clusters with a redshift depth of $z \approx 0.9$. The estimated mass function was then compared with different cosmological models with varying Ω_Λ parameter as shown in Figure 4.3. They made used of the Tinker et al. (2008) mass function to obtain the corresponding best-fit line. The results obtained from their analysis confirmed the high Ω_Λ model. It can be seen from the right panel of the figure that when Ω_Λ is set to 0, the theoretical model significantly underpredicts the evolution of the mass function. Larger samples of clusters at different redshift and more precise measurements of their mass have been proving to be an important tool for cosmology (Hong et al., 2012; Sartoris et al., 2016).

4.3 Galaxy cluster counts

Theoretical approach: The abundance of clusters and their evolution are sensitive to Ω_M, σ_8 and the dark energy equation of state parameter w. Large scale surveys detect several millions of galaxies at different redshifts. We show a plot of the sample size of clusters detected in several completed and ongoing surveys in Figure 4.4, and the sample size is expected to

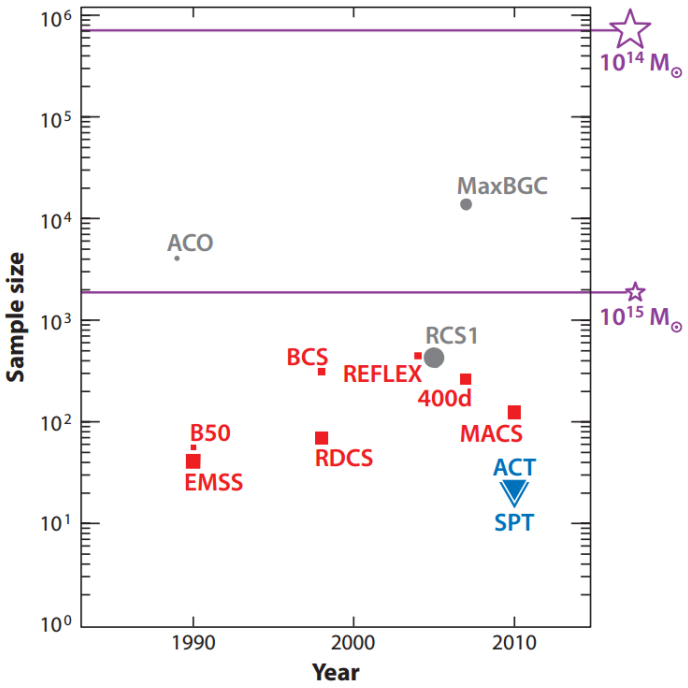

Figure 4.4: Yields from modern surveys of clusters used for cosmological studies are shown, with symbol size proportional to median redshift. Samples selected at optical (gray filled circles), X-ray (red squares), and millimeter (blue triangles) wavelengths. Stars and horizontal lines (purple) show full sky counts of haloes expected in the reference CDM cosmology with masses above 10^{15} and 10^{14} $M_\odot$. Such halo samples have median redshifts of 0.4 and 0.8, respectively. Credits: Allen et al. (2011)

increase in the upcoming cluster surveys.

The comoving number of clusters within a redshift interval $[z_1, z_2]$ with a mass cut of $M > M_0$ is given by:

$$N = \int_{z_1}^{z_2} dz \frac{dV(z)}{dz} N(M > M_0, z) \tag{4.3}$$

where the volume element is:

$$V(z) = 4\pi \int_0^z dz' \frac{d_L^2(z')}{(1+z')^2 H(z')} \tag{4.4}$$

and d_L is the luminosity distance:

$$d_L(z) = (1+z) \int_0^z \frac{dz'}{H(z')} \tag{4.5}$$

where $H(z)$ is the Hubble parameter and so can be compared with different values of the cosmological parameters.

Optical surveys make use of the richness mass proxy as we have described in Section 2.1. Predictions of the number of observed galaxies can be made given an observed richness N_{gal}^{obs} using probability distributions. The average number density of a cluster within a given richness range $[N_{gal,1}^{obs}, N_{gal,2}^{obs}]$ is given by:

$$n_i = \int_{N_{gal,1}^{obs}}^{N_{gal,2}^{obs}} d\ln N_{gal}^{obs} \int d\ln N_{gal} \frac{dn}{d\ln N_{gal}} p\left(N_{gal}^{obs}|N_{gal}\right) \tag{4.6}$$

where $p\left(N_{gal}^{obs}|N_{gal}\right)$ refers to the probability of N_{gal}^{obs} given the richness N_{gal}.

As we have seen in Equation 1.58, the mass function depends on the mean matter density of the Universe and also on the σ parameter which is the variance of the linear matter density field. Similar to Equation 1.58 where the differential was in terms of mass M, we can re-write it in terms of richness N_{gal} as:

$$\frac{dn}{d\ln N_{gal}} = \frac{dn}{d\ln M}\frac{d\ln M}{d\ln N_{gal}} = \alpha_N \frac{dn}{d\ln M} \tag{4.7}$$

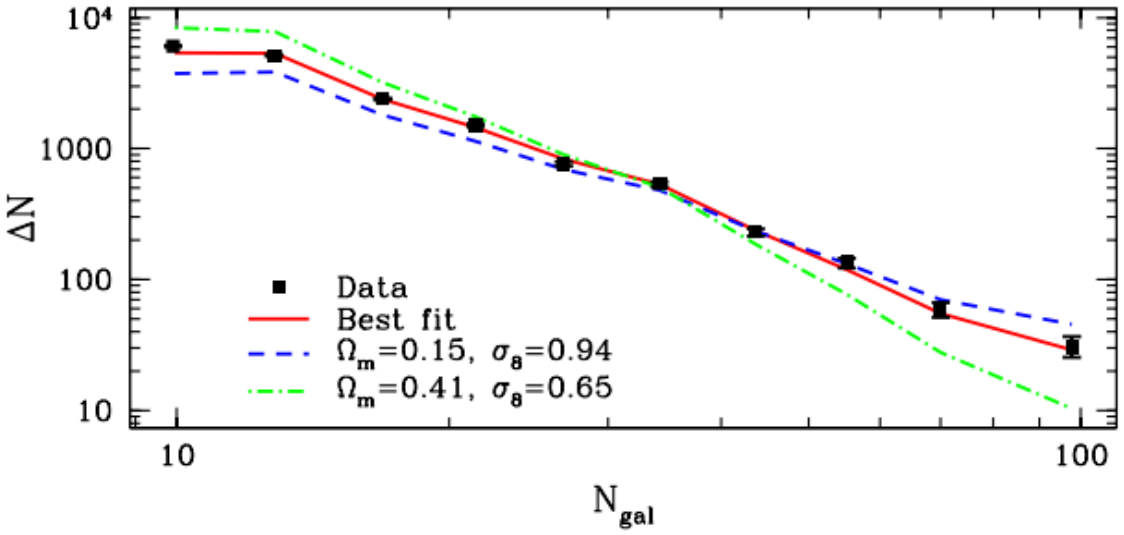

Figure 4.5: MaxBCG cluster counts data (black points) as function of richness and theoretical predictions according to the prescriptions of Equations 4.6 to 4.8 for a choice of different cosmologies (without primordial non-Gaussianity). The red line represents the best-fitting model to the full data set (counts, total masses and power spectrum) Credits: Mana et al. (2013)

The total number of predicted galaxies within a given richness bin can be calculated as:

$$\Delta N_i = \Delta\Omega \int_{z_{min}}^{z_{max}} dz \frac{d^2V}{dz d\Omega} n_i \tag{4.8}$$

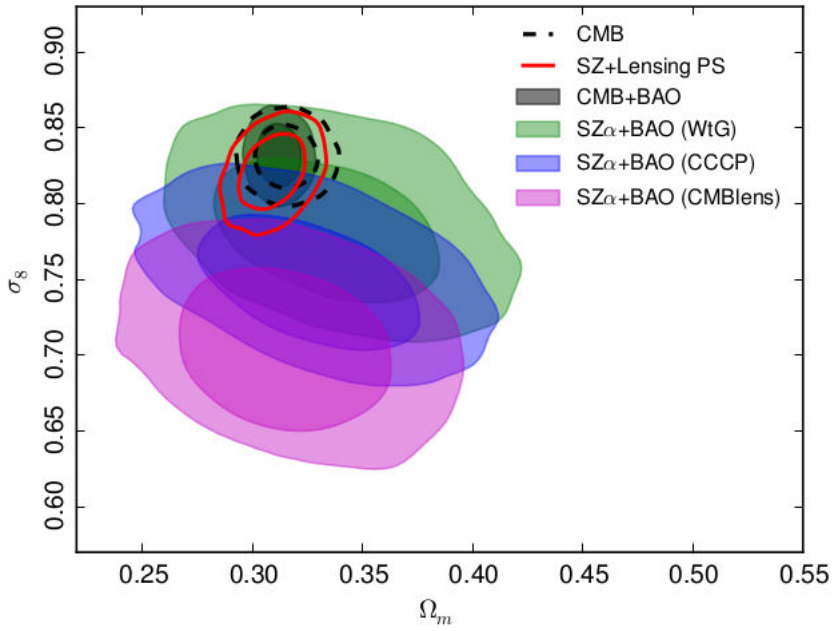

Figure 4.6: Comparison of constraints from the CMB to those from the cluster counts in the ($\Omega_M - \sigma_8$)-plane. Credits: Planck Collaboration et al. (2015)

where $\Delta\Omega$ is the sky coverage and $d^2V/dzd\Omega$ is the volume element and the cosmology dependence is given by this comoving volume element.

Observations on cluster surveys: We show an example of the MaxBCG cluster counts and their corresponding theoretical predictions of Tinker et al. (2008) with different cosmological models as obtained by Mana et al. (2013) in Figure 4.5. It can be seen from Figure 4.5 that the theoretical mass function of Tinker et al. (2008) follows the observed cluster counts.

Another approach towards galaxy cluster counts comes via observing a catalogue of clusters detected using the SZ effect. The Planck Collaboration et al. (2015) used a dataset of 493 clusters and made use of both the redshift information and the signal-to-noise ratio to constrain the cosmological parameters from cluster counts. The constraints on the $\Omega_M - \sigma_8$ plane obtained by Planck Collaboration et al. (2015) is shown in Figure 4.6. The green, blue and violet contours give the cluster constraints (two-dimensional likelihood) at 1 and 2σ for the WtG, CCCP, and CMB lensing mass calibrations, respectively. Constraints from the Planck TT, TE, EE+lowP CMB likelihood (Planck primary CMB) are shown as the dashed contours enclosing 1 and 2σ confidence regions, while the grey shaded region also include BAO. The red contours give results from a joint analysis of the cluster counts, primary CMB and the Planck lensing power spectrum (Planck Collaboration XV 2015), leaving the mass bias parameter free and α constrained by the X-ray prior. It can be seen from Figure 4.6 that depending on the mass bias [1] prior, there is varying degrees of tension with the primary

[1]Here the mass bias parameter is the bias on the mass which comes based on the assumption of hydrostatic

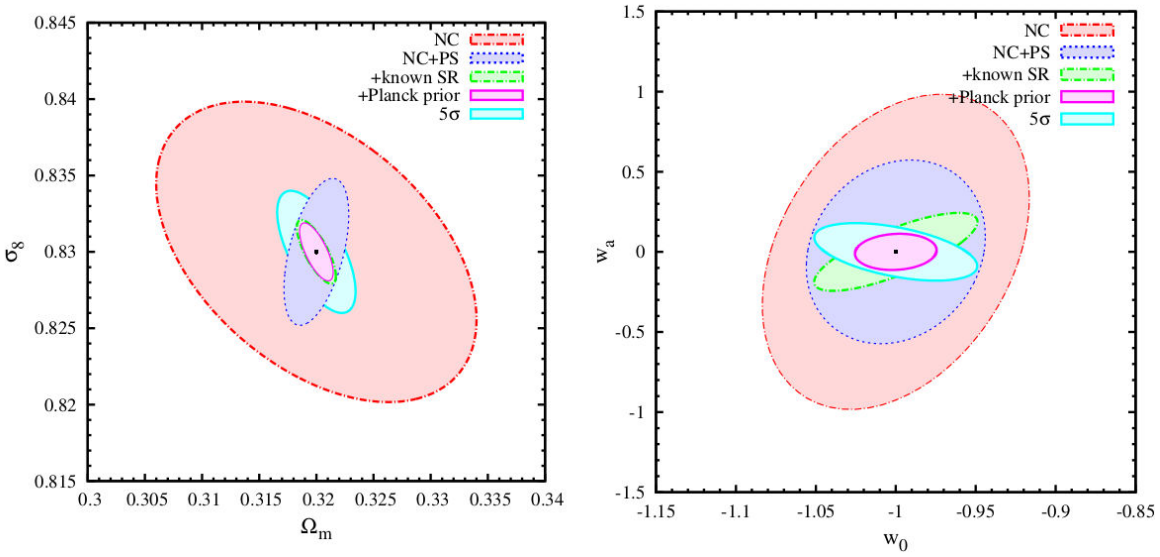

Figure 4.7: Constraints at the 68% confidence limits on the parameters Ω_M and σ_8 (left panel) and on the parameters w_0 and w_a for the dark energy equation-of-state evolution (right panel). In each panel, forecasts for the $N_{500,c}/\sigma_{field} \geq 3$ Euclid photometric cluster selection obtained by (i) number counts (NC), the fisher matrix number counts (red dash-dotted contours), (ii) number counts + power-spectrum, the combination of fisher matrix number counts and power spectrum (PS) information (blue dotted contours), (iii) NC+PS+known scaling relation (SR), i.e. by additionally assuming a perfect knowledge of the nuisance parameters (green dash-dotted contours), and (iv) NC+PS+known SR+Planck prior, i.e. by also adding information from Planck CMB data (magenta solid contours). With cyan solid lines we show forecasts for the $N_{500,c}/\sigma_{field} \geq 5$ ($M_{200} > 8 \times 10^{13}$) Euclid photometric cluster selection in the case NC+PS+known SR+Planck prior (labelled 5σ). Planck information includes prior on ΛCDM parameters and the dark energy equation-of-state parameters. Credits: Sartoris et al. (2016)

CMB. The mass bias required for the cluster counts to agree with the CMB is larger than indicated by any of the three priors. The WtG prior is in close agreement with the CMB, but both the CCCP and CMB lensing priors remain in noticeable tension. So as we have seen from Equations 4.3 to 4.5 the dependence of the volume element on the redshift and in turn on $H(z)$ via the luminosity distance can be made use of to constrain the cosmological parameters.

Future surveys such as LSST (LSST Dark Energy Science Collaboration, 2012) and Euclid (Laureijs et al., 2011) will not only be probing high redshift ranges but will also be detecting a large number of objects at these redshifts. For example the Euclid survey will be detecting $\sim 4 \times 10^5$ clusters with a mass cut of $M_{200} > 8 \times 10^{13}\ h^{-1}\, M_\odot$ at redshifts $z \geq 1$ and the number rises to $\sim 2 \times 10^6$ clusters at all redshifts (Sartoris et al., 2016). Euclid is

equilibrium of the intra cluster gas. The bias parameter has been varied in the range of 0-30% with a baseline value of 20% (Planck Collaboration et al., 2015)

expected to be on the top right corner of Figure 4.4 in terms of sample size. Sartoris et al. (2016) predicted the constraints that can be expected from the Euclid survey on the Ω_M,σ_8,w_0 and w_a parameters using the number counts, power-spectrum and scaling relations of galaxy clusters. We show in Figure 4.7 the 1σ error ellipse for the above four parameters as obtained by Sartoris et al. (2016). It can be seen that just by using the number counts alone, one can get values of $\Omega_M = 0.32 \pm 0.015$, $\sigma_8 = 0.83 \pm 0.01$, $w_0 = -1 \pm 0.01$ and $w_a = 0 \pm 1$. When the information from power spectrum along with the known scaling relations are added, the error on the parameters reduce drastically.

4.4 Combining clustering with number counts: Self-calibration approach

The potential of using galaxy clusters to constrain cosmology can only be realised if we know information about the redshift distribution and also the estimate of the cluster masses. Cluster masses are not directly observed, and one has to rely on observational quantities such as X-ray temperature, weak-lensing shear or other such signals. Relying on these observable mass tracers introduces systematic errors in the analysis (Rozo et al., 2010). To overcome these difficulties, one can either reduce these systematic errors through follow-up observations of a few clusters or use the information from the clustering of clusters and cluster abundance. The latter is a self-calibration approach, i.e. the survey containing enough information to solve for the mass-observable relation at every redshift (Majumdar and Mohr, 2004).

Cosmological constraints on the dark energy equation-of-state parameter w, mass density parameter Ω_M and the σ_8 parameter along with the uncertainties expected on them when measured using a self-calibration approach was first shown by Majumdar and Mohr (2004). They made use of the redshift-averaged power spectrum $\overline{P}_{cl}(k)$ (the two-point correlation function $\xi(r)$ is the Fourier transform of the power spectrum), derived from the correlated positions of galaxy clusters to tighten the constraints on these cosmological parameters. As constraints obtained from power spectrum alone are weaker when compared to the constraints obtained from the cluster redshift distribution (dN/dz), they combined the two along with follow-up observations and showed that the uncertainties on the three cosmological parameters (w, Ω_M and σ_8) could be reduced. Their results were based on models for the DUET X-ray survey (Jahoda and DUET Collaboration, 2003) and two SZ effect surveys, i.e. the SPT (Ruhl et al., 2004) and Planck (Planck Collaboration et al., 2011).

For the X-ray survey, the mass-observable relation was taken to be the flux-mass relation (refer to Majumdar and Mohr (2004) for a detailed description) and for the SZ survey, the mass-observable relation was taken to be the SZ flux-mass relation. As clusters are highly biased tracers of the underlying matter distribution, the cluster power spectrum is given by:

$$P_{cl}(k,z) = b_{eff}^2 P(k,z) \tag{4.9}$$

where $P(k,z)$ is the matter power spectrum and b_{eff} is the effective bias. The cluster mass

function dn/dM was obtained from $N-$body simulations based on the approach of Sheth and Tormen (1999) and Jenkins et al. (2001). The cluster power spectrum over a wide range of redshift (z_{min}-z_{max}) is given by:

$$\overline{P}_{cl}(k) = \frac{\int_{z_{min}}^{z_{max}} dz(dV/dz)n^2(z)P_{cl}(k,z)}{\int_{z_{min}}^{z_{max}} dz(dV/dz)n^2(z)} \tag{4.10}$$

Thus $\overline{P}_{cl}(k)$ depends not only on cosmology but also on the specific survey that determines the redshift dependence of the clusters. Majumdar and Mohr (2004) made use of a Fisher matrix technique to probe the relative sensitivities of cluster surveys to different cosmological and structural parameters. According to Tegmark (1997) the Fisher matrix information for a data set is defined as:

$$F_{ij} = -\langle(\partial^2 \ln \mathscr{L}/\partial p_i \partial p_j)\rangle \tag{4.11}$$

where $\mathscr{L}$ is the likelihood for an observable and p_i describes the parameter set. The inverse of F_{ij}, i.e. F_{ij}^{-1} describes the covariance matrix C_{ij} and the uncertainties on each of the parameters are given by the diagonal elements of C_{ij}. Majumdar and Mohr (2004) calculated the final Fisher matrix taking into account the cluster redshift distribution (F_{ij}^s), the cluster power spectrum F_{ij}^p and the follow-up observations (F_{ij}^f) and the priors. For the follow-up information, they made use of deep X-ray studies of clusters by summing up over 100 clusters within the redshift range $0.3 < z < 1.2$ and mass range $10^{14} - 10^{15}\ h^{-1}\ M_\odot$. Majumdar and Mohr (2004) used a fiducial cosmological model adopted from Spergel et al. (2003) and this model resulted in ~22,000 detected clusters for the DUET X-ray survey, ~29,000 clusters for SPT and ~21,000 clusters for the Planck survey.

The power-spectrum was calculated by dividing the survey into three redshift bins, with equal number of clusters in each bin and they categorised their estimates based on two approaches. Those cluster surveys that assumed full knowledge of the structure evolution and only addressed the sensitivity of the cluster survey to the cosmological parameters were named "Only Cosmology". Those surveys that did not assume knowledge of structure and let the survey solve for both cosmology and cluster scaling parameters were named "Standard Evolution". The results obtained by Majumdar and Mohr (2004) are shown in Table 4.1 and Figure 4.8.

They concluded that by adding information from the redshift-averaged cluster power spectrum with cluster counts would help in reducing the constraints by up to a factor of ~4. Mass follow-up observations of more than 100 clusters could help tighten the constraints along with the combination of $\overline{P}_{cl}(k)$ and dN/dz. They achieved a ~4% constraint on the dark energy equation-of-state parameter w for the two SZ surveys used. This was a factor of 2.5 better than the constraints given by Spergel et al. (2003) and they emphasised that it was because of the self-calibration approach, in which the cluster mass-observable relation and its evolution are taken directly from the survey, along with follow-up observations.

The self-calibration approach was later used by Wang et al. (2004), who also followed a

ESTIMATED PARAMETER CONSTRAINTS

PARAMETER (1)	ONLY COSMOLOGY dN/dz (2)	STANDARD EVOLUTION dN/dz (3)	SELF-CALIBRATION dN/dz (4)	SELF-CALIBRATION $dN/dz + \tilde{P}_{cl}$ (5)	SELF-CALIBRATION dN/dz+Follow-up (6)	SELF-CALIBRATION dN/dz+Both (7)
			SPT SZE Survey			
$\Delta\Omega_M$	0.0084	0.0190	0.0237	0.0115	0.0181	0.0108 (0.0096)
$\Delta\sigma_8$	0.0105	0.0236	0.0441	0.0196	0.0218	0.0125 (0.0111)
Δw	0.0371	0.0663	0.1745	0.1543	0.0602	0.0376 (0.0335)
			Planck SZE Survey			
$\Delta\Omega_M$	0.0078	0.0575	0.0820	0.0188	0.0344	0.0062 (0.0059)
$\Delta\sigma_8$	0.0123	0.1097	0.1747	0.0393	0.0629	0.0098 (0.0094)
Δw	0.0397	0.1977	0.3930	0.1049	0.1149	0.0404 (0.0390)
			DUET X-Ray Survey			
$\Delta\Omega_M$	0.0099	0.0290	0.0372	0.0114	0.0142	0.0096 (0.0083)
$\Delta\sigma_8$	0.0131	0.0503	0.0846	0.0127	0.0182	0.0114 (0.0100)
Δw	0.0505	0.0806	0.3540	0.2065	0.0765	0.0625 (0.0527)

Table 4.1: The 1σ parameter uncertainty on w, Ω_M and σ_8 estimated separately using the $\overline{P}_{cl}(k)$ and dN/dz along with the same by combining them with follow-up observations. Credits: Majumdar and Mohr (2004)

similar Fished matrix approach. They included constraints possible from LSST-like surveys along with SPT. They concluded that dN/dz alone could provide constraints that were better than those obtained from a high precision CMB survey such as Planck. They however assumed perfect knowledge of the mass-observable relation, i.e. used the clusters as "standard candles". But they showed that even after allowing for uncertainty in cluster evolution and structure, and using the self-calibration approach, the errors on w were still comparably respectable with Planck. The combination of the power spectrum along with cluster counts (dN/dz) derived from a LSST-like survey reduced the uncertainty on w by a factor of ~2.

After the advent of SDSS, and the announcement of surveys like DES and LSST, there were works using the self-calibration approach on cluster surveys to also find out the effects of combining cluster counts with shear-shear correlations from weak lensing (Fang and Haiman, 2007), halo bias in cluster surveys (Wu et al., 2008) and cluster counts as a probe of primordial Non-Gaussianity (Oguri, 2009). More recently, Lacasa and Rosenfeld (2016) employed the Halo Occupation Distribution (HOD) model and used the Fisher matrix technique to examine the prospects of combining cluster number counts with angular power spectrum. They found out that the combination gave improvements of the order ~20% on cosmological parameters compared to the single cosmological probe and also better improvements on HOD parameters.

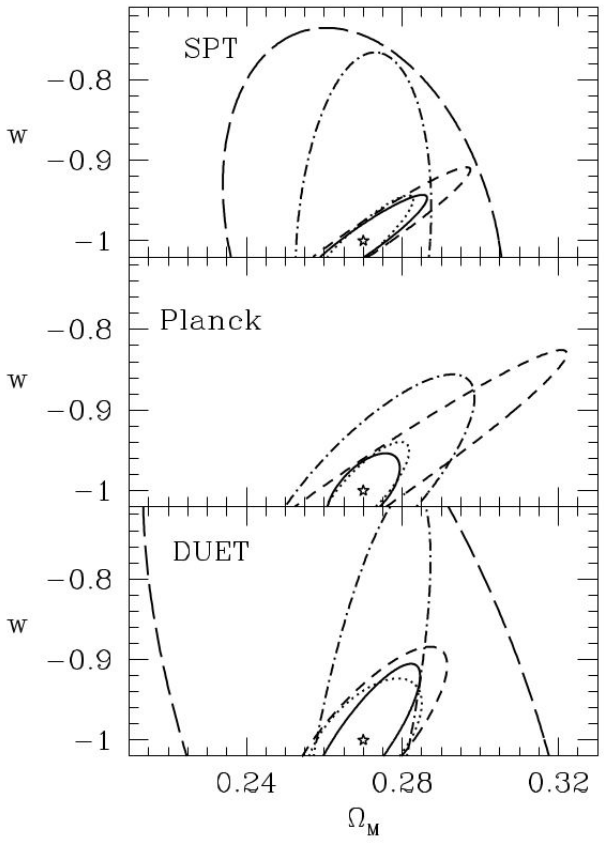

Figure 4.8: Constraints on w and Ω_M for an SPT SZE survey (top), a Planck SZE survey (middle) and a DUET X-ray survey (bottom). Contours denote joint 1σ constraints in five scenarios: (1) dN/dz for the only-cosmology case (dotted line), (2) dN/dz for the self-calibration case (long-dashed line), (3) $dN/dz + \overline{P}_{cl}(k)$ (dot-dashed line), (4) $dN/dz + 100$ cluster follow-up (short-dashed line), and (5) $dN/dz + \overline{P}_{cl}(k) + 100$ cluster follow-up (solid line). A flat Universe is assumed for all cases. Credits: Majumdar and Mohr (2004)

4.5 Cosmology using baryon acoustic oscillations (BAO)

Clusters are not just massive and rare objects in the Universe, but are also excellent tracers of the large-scale structure. Thus by studying their clustering properties one can derive more constraints on cosmological parameters as it has been demonstrated by many recent studies (Governato et al., 1999; Bahcall et al., 2003; Estrada et al., 2009; Hong et al., 2012; Veropalumbo et al., 2014). Specifically in calculating the two-point correlation function in large scale surveys, we can detect the Baryon Acoustic Oscillation (BAO) peak. As baryons represent only a small fraction of the total Universe, to detect the BAO feature we not only need precision but also coverage of large area of the sky so that we can detect large abundances of clusters. One of the primary advantages of using BAO to constrain cosmological parameters is that at the low-redshift regime it is not affected by systematic uncertainties, it's

	Distance	$H_0[\mathrm{km\,s^{-1}Mpc^{-1}}]$		Ω_M		$\Omega_\Lambda/\Omega_{DE}$		w	
		Prior	Posterior	Prior	Posterior	Prior	Posterior	Prior	Posterior
ΛCDM	D_V	$\mathcal{U}(30,120)$	72^{+13}_{-13}	$\mathcal{U}(0,1)$	$0.32^{+0.21}_{-0.14}$	–	–	–	–
	d_z	"	64^{+17}_{-9}	"	$0.32^{+0.22}_{-0.15}$	–	–	–	–
$o\Lambda$CDM	D_V	$\mathcal{N}(67,20)$	70^{+11}_{-10}	$\mathcal{U}(0,1)$	$0.32^{+0.15}_{-0.14}$	$\mathcal{U}(0,1.5)$	$0.63^{+0.30}_{-0.29}$	–	–
	d_z	"	62^{+14}_{-12}	"	$0.36^{+0.19}_{-0.13}$	"	$0.65^{+0.33}_{-0.37}$	–	–
wCDM	D_V	$\mathcal{N}(67,20)$	69^{+11}_{-10}	$\mathcal{U}(0,1)$	$0.39^{+0.16}_{-0.18}$	–	–	$\mathcal{U}(-2,0)$	$-1.15^{+0.43}_{-0.54}$
	d_z	"	64^{+12}_{-8}	"	$0.38^{+0.19}_{-0.12}$	–	–	"	$-1.01^{+0.44}_{-0.44}$
owCDM	D_V	$\mathcal{N}(67,2)$	$67.0^{+1.4}_{-1.4}$	$\mathcal{N}(0.31,0.02)$	$0.31^{+0.01}_{-0.01}$	$\mathcal{U}(0,1.5)$	$0.66^{+0.45}_{-0.24}$	$\mathcal{U}(-1.5,0)$	$-0.91^{+0.23}_{-0.38}$
	d_z	"	$67.0^{+1.4}_{-1.4}$	"	$0.31^{+0.01}_{-0.01}$	"	$0.66^{+0.46}_{-0.21}$	"	$-0.88^{+0.24}_{-0.36}$

Table 4.2: Summary of the cosmological parameters obtained by fitting the calibrated BAO distance D_V and the uncalibrated BAO distance d_z. Priors used in the fitting procedures are also reported. Credits: Veropalumbo et al. (2016)

affected only by statistical uncertainties (Weinberg et al., 2013). The sound horizon of the BAO oscillation is given by:

$$r_s = \int_{z_{drag}}^{\infty} \frac{c_s(z)}{H(z)} dz \tag{4.12}$$

where z_{drag} is the redshift at which the influence of the Compton drag from photons no longer affects the baryons and $c_s = c/\sqrt{3(1+R)}$ is the sound speed where $R = 3\rho_b/4\rho_\gamma$ (ρ_b →baryon momentum density and ρ_γ →photon momentum density). This typical length scale of the sound horizon is around $r_s = 150$Mpc, i.e. the maximum distance a sound wave can travel before decoupling [2] given its sound speed. Eisenstein et al. (2005) first detected the BAO signal ($\sim 3.4\sigma$) at a scale of $r \sim 100\ h^{-1}$Mpc by calculating the two-point correlation function of Luminous Red Galaxies (LRGs) detected in the SDSS.

To get the exact best-fit parameters, the two-point correlation function is fitted through the following approximation as followed by Anderson et al. (2012):

$$\xi(r) = B^2 \xi_{DM}(\alpha r) + A_0 + \frac{A_1}{r} + \frac{A_2}{r^2} \tag{4.13}$$

where $\xi_{DM}(r)$ is the dark matter two-point correlation function, B is the bias (described in detail in Section 1.8), α is the main parameter that contains the distance information, A_0, A_1 and A_2 are the parameters of an additive polynomial that are used to overcome systematics coming from signals that are not fully taken into account. The distance constraint is entirely given by the α parameter seen in Equation 4.13 and it can be written in terms of the volume distance $D_V(z)$ as:

$$D_V(\bar{z}) = \alpha D_V^{fid}(\bar{z}) \left(\frac{r_s}{r_s^{fid}} \right) \text{ Mpc} \tag{4.14}$$

[2] It refers to the period when all the different types of particles fall out of thermal equilibrium as a result of the expansion of the Universe.

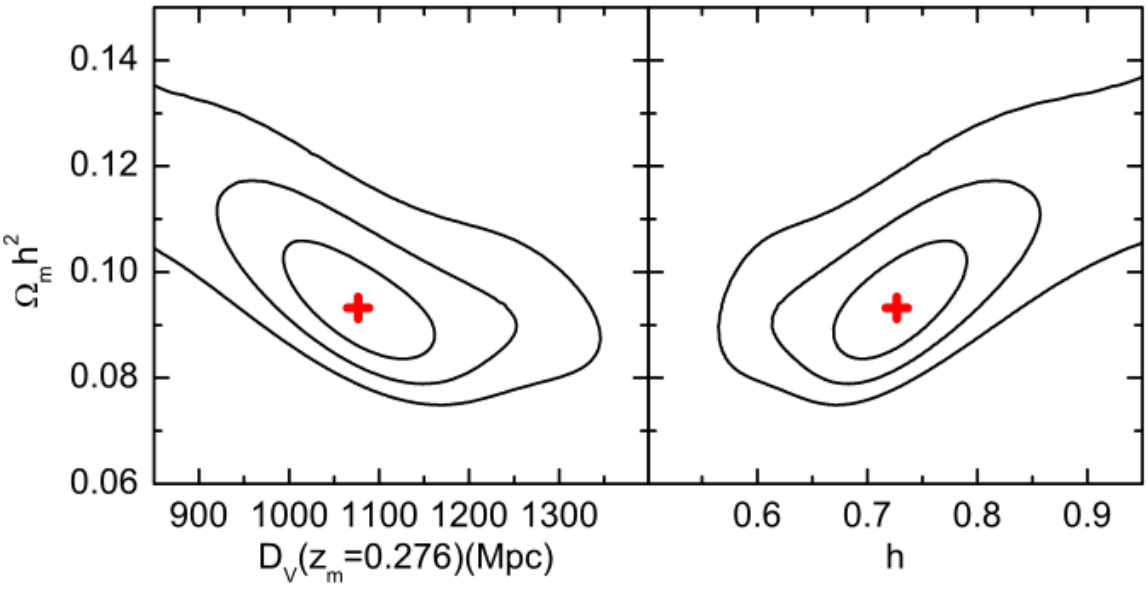

Figure 4.9: Likelihood contours for the best fit as $\Omega_M h^2 = 0.093$ and $D_\nu(0.276) = 1077$Mpc as a function of $D_\nu(z_m = 0.276)$ and $\Omega_M h^2$ (left), and the likelihood contours for h and $\Omega_M h^2$ (right). From the inner to the outer, contours corresponding to 1σ, 2σ and 3σ respectively. Credits: Hong et al. (2012)

where $D_V(\bar{z})$ is the isotropic volume distance at the mean redshift $\bar{z}$, $D_V^{fid}(\bar{z})$ is the volume distance at the given fiducial cosmology, r_s and r_s^{fid} are the true and fiducial sound horizon respectively. The volume distance $D_V(\bar{z})$ can be written as:

$$D_V(z) = \left[(1+z)^2 D_A^2(z)\frac{cz}{H(z)}\right] \tag{4.15}$$

where $D_A(z)$ is the angular diameter distance, c is the speed of light, $H(z)$ is the Hubble parameter at redshift z. These distance measurements described above can be used to derive constraints on cosmological parameters as D_V is a function of $D_A(z)$ and $H(z)$ which in turn depend on the comoving distance $D_C(z) = \int_0^z dz'/H(z')$ as seen from Equation 4.15.

Estrada et al. (2009) analysed cluster samples (13,823 clusters) derived from the SDSS MaxBCG catalogue (Koester et al., 2007) which had a redshift range of $0.1 < z < 0.3$. Since the catalogue covered range of 7500 deg^2 they also modelled the large-scale correlation function on scales $r = 20 - 195\ h^{-1}$Mpc using a non-linear model of the ΛCDM power spectrum that included the effects of non-linear damping of the BAO peak. Non-linear damping was combined along with the photo-z errors and so the detection of the BAO peak was not robust. For the sample with richness cut $N_{200} \geq 10$, the significance for the best-fit BAO model was about $1.4 - 1.7\sigma$.

Wen et al. (2009) published a cluster catalogue that had a total of 39,668 clusters detected within the redshift range $0.05 < z < 0.6$. Hong et al. (2012) made use of the cluster catalogue

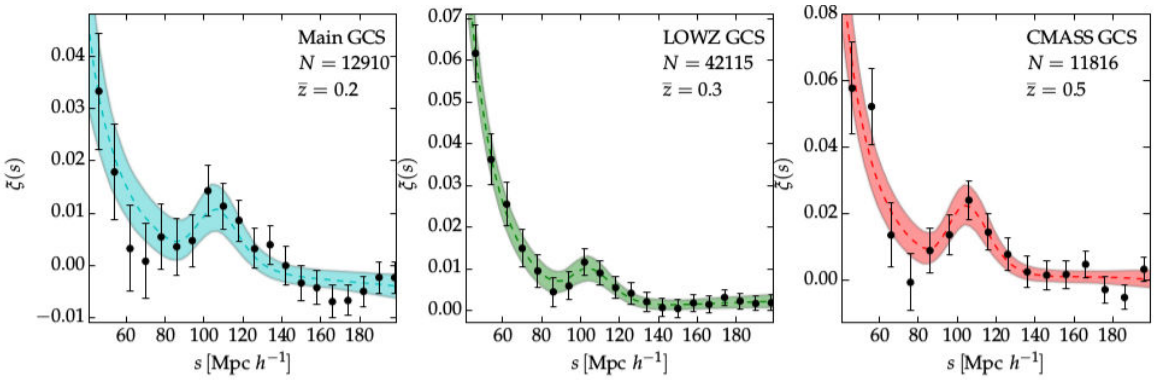

Figure 4.10: The redshift-space 2PCF of galaxy clusters, respectively Main-GCS (left panel), LOWZ-CGS (central panel) and CMASS-CGS (right panel). The errorbars are computed with the lognormal mock method. The dashed line shows the best-fit model from Eq. 6. The shaded area represents the 68% posterior uncertainties provided by the MCMC analysis. Credits: Veropalumbo et al. (2016)

of Wen et al. (2009), and from the entire sample, clusters with at least one member galaxy for which the spectroscopic redshift was available were selected. Using the 3D spatial distribution of the clusters, $\xi(r)$ was calculated for a final sample of 13,904 clusters in a sky area of ~7100 deg^2. They made use of the Landy and Szalay estimator and modelled the correlation function on small scales using the power-law mentioned in Equation 3.13. The best-fit parameters obtained for fitting the $\xi(r)$ within the range $10 \leq r \leq 50$ h^{-1}Mpc were $r_0 = 18.84 \pm 0.27$ h^{-1}Mpc and $\gamma = 2.08 \pm 0.07$ (richness cut $R \geq 15$); $r_0 = 16.58 \pm 0.13$ h^{-1}Mpc and $\gamma = 2.14 \pm 0.04$ (richness cut $R \geq 10$) and $r_0 = 16.15 \pm 0.13$ h^{-1}Mpc and $\gamma = 2.11 \pm 0.04$ (richness cut $R \geq 5$). The results obtained were consistent with previous works (Basilakos and Plionis, 2004; Estrada et al., 2009).

The BAO peak was measured at $r \sim 110$ h^{-1}Mpc (1.9σ) which was then fitted with a parametrised theoretical curve, determined by the physical matter density parameter $\Omega_M h^2$, the stretch factor s (refer to Hong et al. (2012) for more details) and the galaxy bias. Constraints were obtained with the values $\Omega_M h^2 = 0.093 \pm 0.0077$ (1σ), $D_\nu(0.276) = 1077 \pm 55$ (1σ) which is the reduced distance at the mean redshift of the sample (similar to the volume distance mentioned in Equation 4.15 , but without the $(1+z)^2$ term) and $h = 0.73 \pm 0.039$ (1σ). We show the constraints obtained by Hong et al. (2012) on the parameters in Figure 4.9.

More recently Veropalumbo et al. (2016) made use of the largest spectroscopic samples of galaxy clusters extracted from the SDSS at three median redshifts of $z = 0.2$ (Main GCS), $z = 0.3$ (LOWZ GCS) and $z = 0.5$ (CMASS CGS) with 12910, 42215 and 11816 being the number of objects respectively. The parent catalogue from which the clusters were extracted was from Wen et al. (2012) which covered a sky area of 15000 deg^2 in a redshift range of $0.05 < z < 0.8$. The cluster identification was based on the friends-of-friends algorithm. To

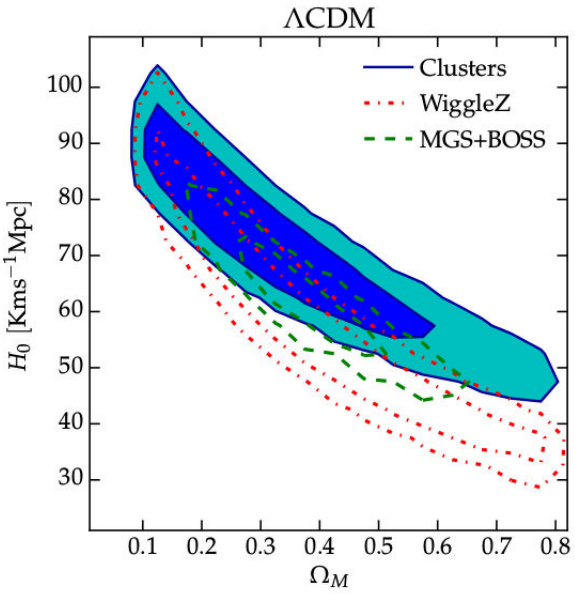

Figure 4.11: Comparison of the $1-2\sigma$ confidence contours in the $\Omega_M - H_0$ plane between our work (blue filled contours) and previous measurements from galaxy samples - WiggleZ (red dot-dashed contours) and MGS+BOSS (green dashed contours). Credits: Veropalumbo et al. (2016)

fit the BAO peak, the model as mentioned in Equation 4.13 was used, where the parameter α contains the distance information. For extracting cosmological parameters from the BAO peak, the BAO distance constraint as explained in Section 4.5, i.e. Equations 4.14 and 4.15 were used. The α parameter obtained from the fit is dependant on the volume distance $D_V(z)$ which is dependant on the angular diameter distance $D_A(z)$ and $H(z)$ which in turn depend on the comoving distance $D_C(z)$. We show in Figure 4.10 the redshift-space $\xi(s)$ for the galaxy clusters in the three median redshifts. The constraints obtained on the parameters H_0, Ω_M is shown in Figure 4.11 where a comparison is made with previous measurements from WiggleZ galaxy sample and MGS+BOSS samples (refer to Veropalumbo et al. (2016) for details about WiggleZ and MGS+BOSS BAO measurements).

The framework of next generation cluster surveys such as LSST (LSST Dark Energy Science Collaboration, 2012) and Euclid (Laureijs et al., 2011) are aimed at detecting large number of clusters with a sky coverage that will be large enough for the BAO feature to be detected. Hence tight constraints on parameters such as Ω_M, Ω_Λ, H_0 and w the dark energy equation of state parameter can be placed. We show in Table 4.2 the recent work done by Veropalumbo et al. (2016) in placing constraints on these parameters using the study of the BAO detection. It can be seen that the BAO-only constraints on Ω_M and w are reasonably accurate enough to be directly compared with those from SNIa measurements, without requiring an external constraint on the standard ruler scale r_s from CMB anisotropy.

Chapter 5

Halo clustering: Results from cosmological simulation

Contents

5.1 Cosmological simulations

Alongside the observational surveys that were being prepared to understand the large-scale structure formation, there were several attempts to create detailed simulations from the early 1970s and 1980s (Peebles, 1970; White, 1976) and were instrumental in testing the general idea of gravitational instability as the driving process of cluster formation. The first simulations of galaxy clusters which were following both the dark matter and baryon process were carried out during the late 80s and early 90s (Evrard, 1988; Katz and White, 1993; Kang et al., 1994; Navarro et al., 1995), which provided a means of understanding these complex processes which occur on times scales which can span several billions of years. These simulations were also used to study phenomena as small as galaxy collisions and galaxy evolution and as large as the entire large-scale structure evolution of the Universe.

One of the most famous simulations that depicted the entire evolution of the Universe was the Millennium Run (Lemson and Virgo Consortium, 2006) which adopted the ΛCDM

cosmology. 10^{10} particles were used to follow the dark matter distribution in a cubic region of 500 h^{-1}Mpc on a side. The spatial resolution [1] of the simulation was 5 h^{-1}kpc and around 10^7 galaxies more luminous than the Small Magellanic Cloud with detailed physics were generated.

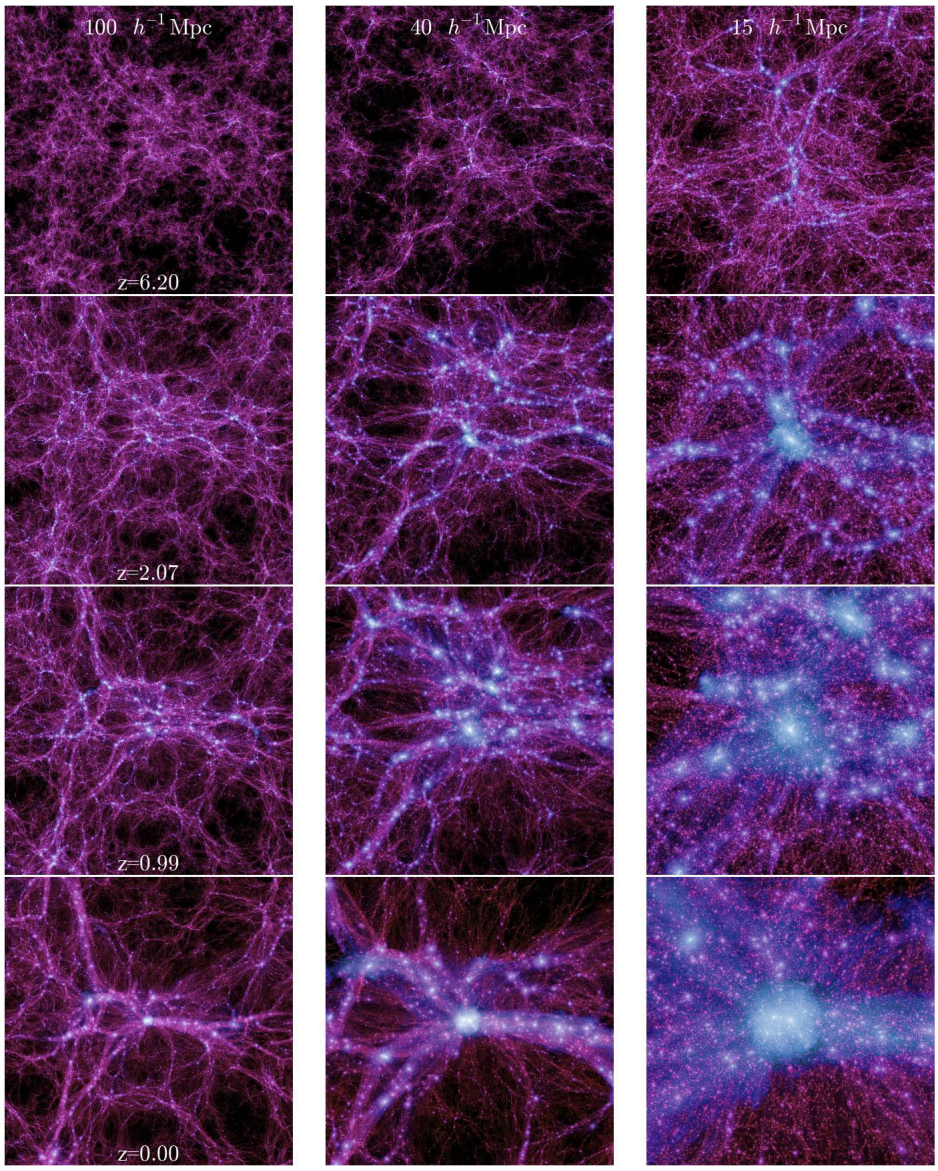

Figure 5.1: Time evolution of the formation of the most massive halo. *From left to right:* 100, 40, and 15 h^{-1}Mpc (all in comoving units). *From top to bottom:* z = 6.2, 2.07, 0.99, and 0.

Image credits: Millennium II simulation (2016)

[1] This meant that the simulation could clearly distinguish objects smaller than the Milky Way which has a size of about 30 kpc.

The Millennium simulation was run a second time in 2008, with the same cosmology and same number of particles as the first run, but in a box which was 5 times smaller. By reducing the size of the box, a resolution that was 125 times better compared to the first one was achieved. This meant that by having simulations with different resolutions allowed one to analyse a broader range of galaxy mass and redshift. One of the evolutions of the most massive halo from the Millennium II run is shown in Figure 5.1. Starting from a redshift of $z = 6.2$ the evolution is followed in redshift snapshots up to $z = 0$. It is clearly evident how the initial density perturbations contribute to the gradual clustering of the haloes .

Observational probes such as the Cosmic Microwave Background, Type Ia supernovae, gravitational lensing effects, quasars have provided tight constraints on the cosmological model (Komatsu et al., 2009). This implies that the initial conditions which are needed for cosmological simulations can be fixed more accurately compared to what was being done several years ago. The main challenge however for cosmological simulations is to follow both the dynamics of matter which is driven by the gravitational instability and also the gas-dynamical processes affecting the evolution of cosmic baryons (Borgani and Kravtsov, 2011).

There is another aspect of a simulation that needs further discussion. It is whether the simulation is dark matter only (DM-only) or whether the complex physical processes of baryons and gas are taken into account. DM-only simulations have reached very large scales including on the order of 1 trillion particles and the Millennium run is one such example. In this thesis we use a DM-only $N-$body simulation to analyse the evolution of dark matter haloes with mass and redshift. Current simulations like the Bolshoi (Klypin et al., 2011) and Illustris (Vogelsberger et al., 2014) take into account also these components so that the simulations can provide a much detailed description of the evolution of the large-scale structure of the Universe.

There can be many insights that one can infer from cosmological simulations depending on the analysis being performed. For example, the evolution of large-scale structure with both mass and redshift can be studied in detail. Precise knowledge of the evolution of galaxy clusters directly denotes the constrain of cosmology as they are the most virialised structures in the Universe. If the simulation spans a wide range of redshift along with more spatial resolution, massive objects that are rare at high redshifts and also contribute to the evolution of large-scale structure can be studied. Future observational surveys are going to reach a redshift limit of $z \approx 2.0$ and beyond with a sky coverage of around 10,000-15,000 deg^2. So results from these simulations can be directly compared with future observational data.

5.2 The simulation used in this thesis

We use a public light-cone constructed using a semi-analytic model of galaxy formation (Merson et al., 2013) onto the N-body dark matter halo merger trees of the Millennium Simulation, based on a ΛCDM cosmological model with the following parameters: $\Omega_M, \Omega_\Lambda, \Omega_b, h =$

$0.25, 0.75, 0.045, 0.73$ (Springel et al., 2005), corresponding to the first year results from the Wilkinson Microwave Anisotropy Probe (Spergel et al., 2007). The Millennium simulation was carried out using a modified version of the GADGET2 code (Springel, 2005). Haloes in the simulation were resolved with a minimum of 20 particles, with a resolution of M_{halo} = $1.72{\times}10^{10}h^{-1}\,M_{\odot}$. The groups of dark matter particles in each snapshot were identified through a Friends-Of-Friends algorithm (FOF) following the method introduced by Davis et al. (1985b). However, the algorithm was improved with respect to the original FOF, to avoid those cases where the FOF algorithm merge groups connected for example by a bridge, while they should be considered instead as separated haloes (Merson et al., 2013). A comparison between the masses obtained with this improved D-TREES algorithm, M_{halo}, and the classical M_{FOF}, and their relation with M_{200}, was done by Jiang et al. (2014), where it is shown that at redshift z = 0 on average, M_{halo} overestimates M_{200}, but by a lower factor with respect to M_{FOF}: they found that only 5% of haloes have $M_{halo}/M_{200} > 1.5$.

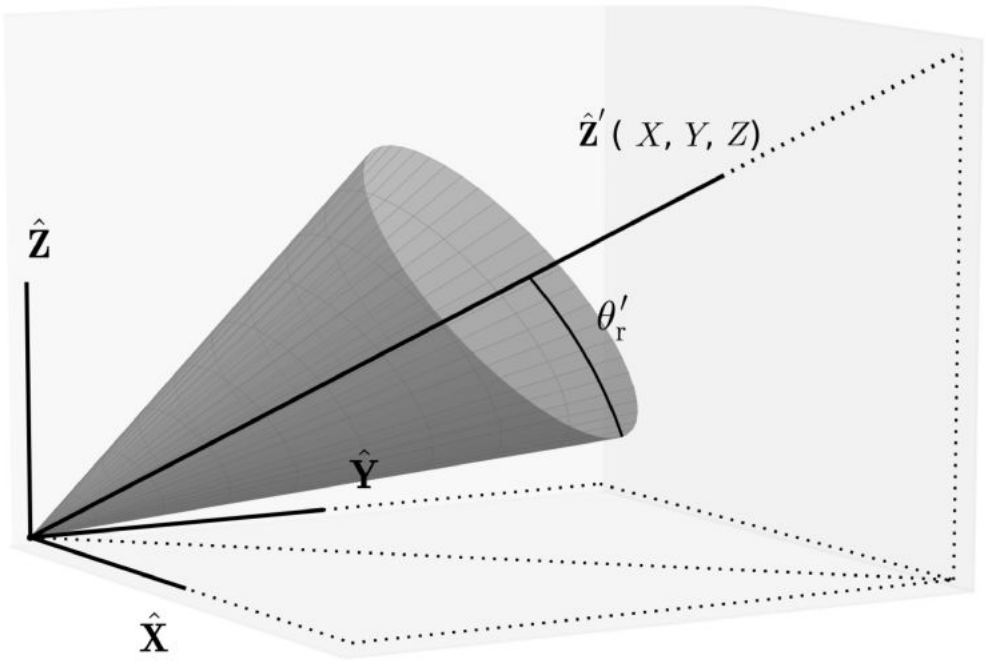

Figure 5.2: Schematic of a light-cone geometry. The $\hat{Z}'$ axis defines the line-of-sight vector of the observer. The angle θ'_r defines the angular size of the field-of-view of the light-cone. Any galaxy whose position vector, $\vec{r}'(X, Y, Z)$ is offset from the $\hat{Z}'$ axis by an angle $\theta' > \theta'_r$ is excluded from the light-cone. Image credits: Merson et al. (2013).

The results obtained by Jiang et al. (2014) on the masses are shown in Figure 5.3. However, when comparing the halo mass function of the simulation with that expected from the Tinker et al. (2008) approximation, it appears that there is a dependence on redshift, and beyond $z \approx 0.3$ the M_{halo}/M_{200} ratio becomes less than 1 (Mauro Roncarelli, private com-

munication). This has to be taken into account in further analysis using the masses.

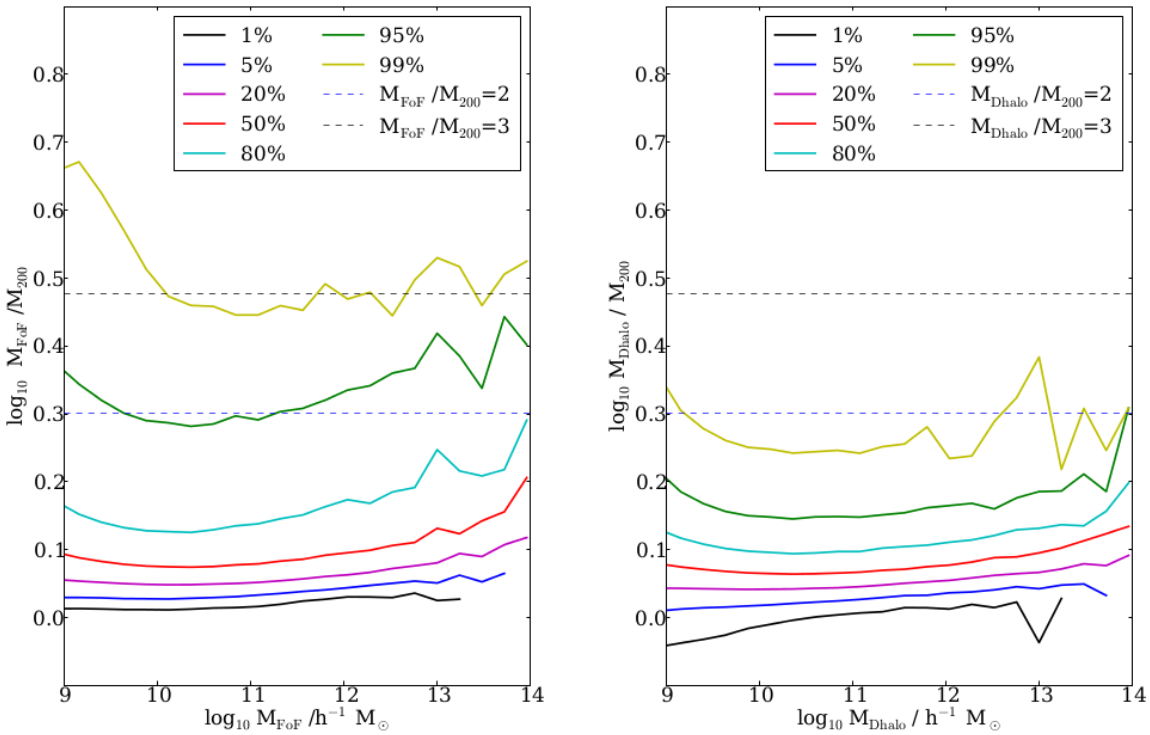

Figure 5.3: *On left:* Median percentiles 1,5,20,80 and 95 of the distribution of the mass ratios between FoF halo mass, M_{FoF} and virial mass M_{200} as a function of FoF halo mass. *On right:* Same percentiles for the distribution of mass ratio between Dhalo mass, M_{Dhalo} and M_{200} as a function of Dhalo mass. Image credits: (Jiang et al., 2014)

Galaxies were introduced in the light-cone using the Lagos 12 GALFORM model (Lagos et al., 2012). The GALFORM model populates dark matter haloes with galaxies using a set of differential equations to determine how the baryonic components are regulated by "subgrid" physics. These physical processes are explained in detail in a series of papers: (Bower et al., 2006; Font et al., 2008; Lagos et al., 2012; Merson et al., 2013; Guo et al., 2013; Gonzalez-Perez et al., 2014). The area covered by the light-cone is 500 deg^2; the final mock catalogue is magnitude–limited to $H = 24$ (to mimic the Euclid completeness) with a maximum redshift at $z = 3$. with halo masses in the range $13.0 < \log_{10}(M_{halo}) < 15.0$ ($h^{-1}\ M_{\odot}$).

For each galaxy the mock catalogue provides different quantities, such as the identifier of the halo in which it resides, the magnitude in various passbands, right ascension and declination, and the redshift, both cosmological and including peculiar velocities. For each halo in the cluster mass range, the redshift was estimated as the mean of the redshifts of its galaxies, while the central right ascension and declination were estimated as those of the brightest cluster galaxy (BCG). We show the cosmological redshift distribution of all our haloes (above the minimum mass cut of $M_{halo} > 1 \times 10^{13}\ h^{-1}\ M_{\odot}$ in Figure 5.4. It can be seen that the distribution peaks at $z \simeq 1.0$ and the abundance of haloes decreases at $z > 2.0$.

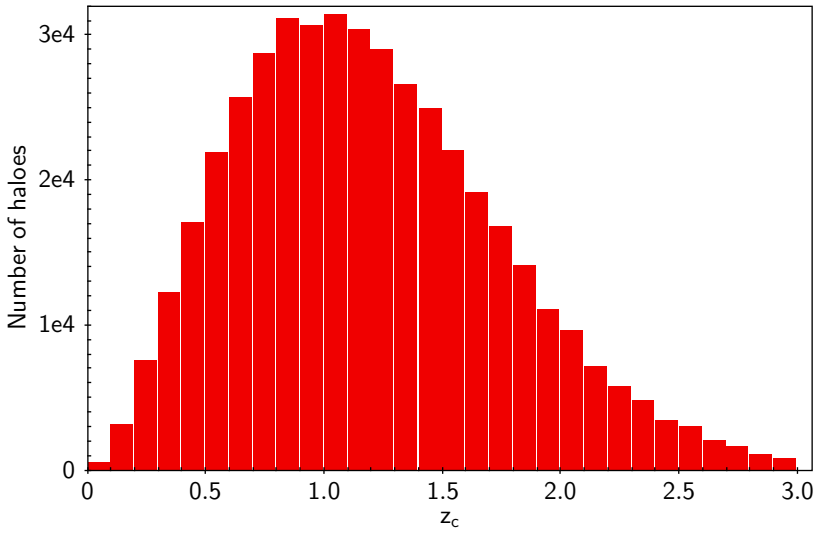

Figure 5.4: The cosmological redshift distribution of all the haloes in the simulation (above the minimum mass cut of $M_{halo} > 1 \times 10^{13}\ h^{-1}\ M_{\odot}$). It can be seen that the distribution peaks at $z \simeq 1.0$ and haloes are less abundant above $z > 2.0$.

.

5.3 Calculating the two-point correlation function: Cosmological redshift sample

When we have a simulated cluster catalogue, we are given with cosmological and "observed" redshifts, i.e. including the peculiar velocities. We will also be identifying clusters to haloes in this Chapter. In our case wherein simulated data is used, Equation 3.1 can be used to compute the real-space correlation function as distances are calculated using the cosmological redshift. To measure the two-point correlation function for all our samples, we use `CosmoBolognaLib` (Marulli et al., 2016), a large set of Open Source C++ libraries for cosmological calculations. [2]

5.3.1 Creating the random catalogue

To measure the two-point correlation function $\xi(r)$ we need to create a random catalogue [3]. There are two aspects of creating the random catalogue, i.e. the angular positions (RA and DEC) and the redshift (z). To generate the RA and DEC, we simply generate random points in the sky, but within the same geometrical limits as the data (cluster) catalogue.

For the redshift distribution, we generate a distribution that reproduces the data redshift

[2] More information about `CosmoBolognaLib` can be found at `http://apps.difa.unibo.it/files/people/federico.marulli3/CosmoBolognaLib/Doc/html/index.html`

[3] This is random in the sense that the points we create inside this catalogue have random right ascension and declination, yet they follow the same redshift distribution as the data catalogue.

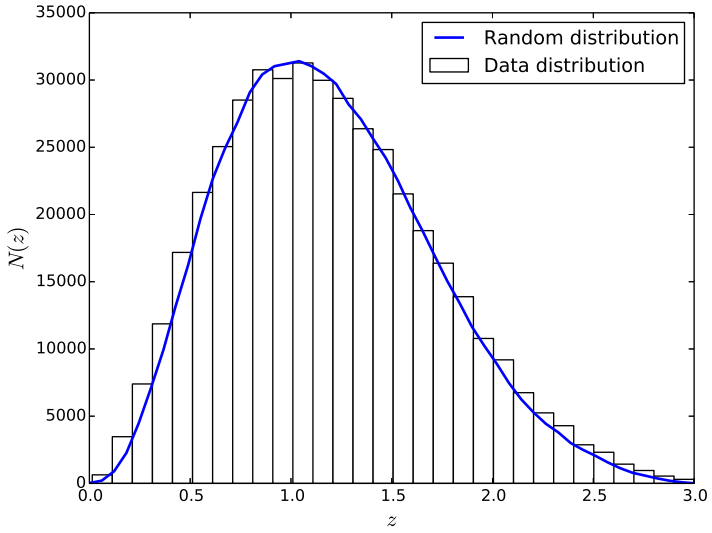

Figure 5.5: The entire data redshift distribution ($0.0 < z < 3.0$) shown by the histogram with the *blue* line specifying the distribution of the random catalogue we will be using for calculating the two-point correlation function.

distribution, but does not follow the clustering fluctuations that exist. The random redshifts follow only the global shape of the data distribution so that the real physical correlations of pairs are washed out. We estimate it by smoothing the cluster redshift distribution through a kernel density estimation method. The bandwidth of the kernel is carefully adjusted in order to follow the global shape but not the clustering fluctuations in the redshift distribution. To this aim we use a Gaussian kernel twice larger than the bin size, and sample the data in 30 redshift bins. Figure 5.5 shows the redshift distributions of the simulation and of the random catalogue for the whole sample. The random catalogue is 10 times denser than the simulated sample in order to minimize the effect of shot noise. This also makes sure that we do not introduce any Poisson error in the estimate.

Each time, random catalogues following the same footprint and redshift selection function as the sub-sample to be analysed is generated and used to compute the correlation function.

Once we have our random RA, DEC and redshift, we convert it to Cartesian (X,Y,Z) co-ordinates.

5.3.2 Error estimation

Errors are calculated from the covariance matrices using the jackknife resampling method (see e.g. Zehavi et al. (2005); Norberg et al. (2011)). To perform a jackknife estimate we divide the data into N equal subsamples and we calculate the two-point correlation function omitting one sub-sample at a time. For k jackknife samples and i bins, the covariance matrix

is then given by:

$$C_{ij} = \frac{N-1}{N}\sum_{k=1}^{N}(\xi_i^k - \bar{\xi}_i)(\xi_j^k - \bar{\xi}_j) \tag{5.1}$$

where $\bar{\xi}_i$ is the average of the values obtained for bin i. We make use of $N = 9$ subsamples in our calculation.

One can use Poisson errors, which are given by:

$$err_{Poisson} = 1 + \frac{\xi(r)_i}{DD(i)} \tag{5.2}$$

where $\xi(r)_i$ is the two-point correlation function obtained in the i^{th} bin and DD are the data-data pairs in the i^{th} bin. Poisson errors in general are easier to obtain compared to jackknife errors as you can see that it is a straightforward process. But, Poisson errors tend to under predict the errors in the case of the correlation function. This plays a major role when it comes to the final fitting of the correlation function using Equation 3.13. If the errors are under predicted then the best-fit parameters (r_0 and γ) will be under predicted as well.

Another approach of dealing with error estimation is by using a Bayesian analysis, but for this thesis all the errors computed have been done using jackknife resampling.

5.4 Redshift evolution of the correlation function

The spatial distribution of galaxy clusters and its evolution can be a first test of the cosmological model. In fact, the results obtained by Bahcall and Soneira (1983) about the strong cluster correlations were one of the first evidences against the then standard $\Omega_M = 1$ SCDM model. In this section we shall study the redshift evolution of $\xi(r)$.

The redshift evolution of the cluster correlation function has been studied both observationally (Bahcall and Soneira, 1983; Huchra et al., 1990; Peacock and West, 1992; Croft et al., 1997; Borgani et al., 1999), numerically (Bahcall et al., 2004; Younger et al., 2005) and theoretically (Mo and White, 1996; Governato et al., 1999; Moscardini et al., 2000b; Sheth et al., 2001). Two main results are prominent from these works, i.e.

1. The cluster correlation amplitude increases with redshift for both low- and high-mass clusters.

2. The increase with redshift of the correlation amplitude is stronger for more massive clusters compared to low mass ones.

Although the numerical and theoretical studies of galaxy clusters probe high redshift ranges (even $z \approx 3.0$), the observational surveys have not yet reached such progress. From the SDSS data release III for example (Wen et al., 2012) clusters within the redshift range $0.05 < z < 0.8$ were identified and studied. Future large surveys are expected to probe the high

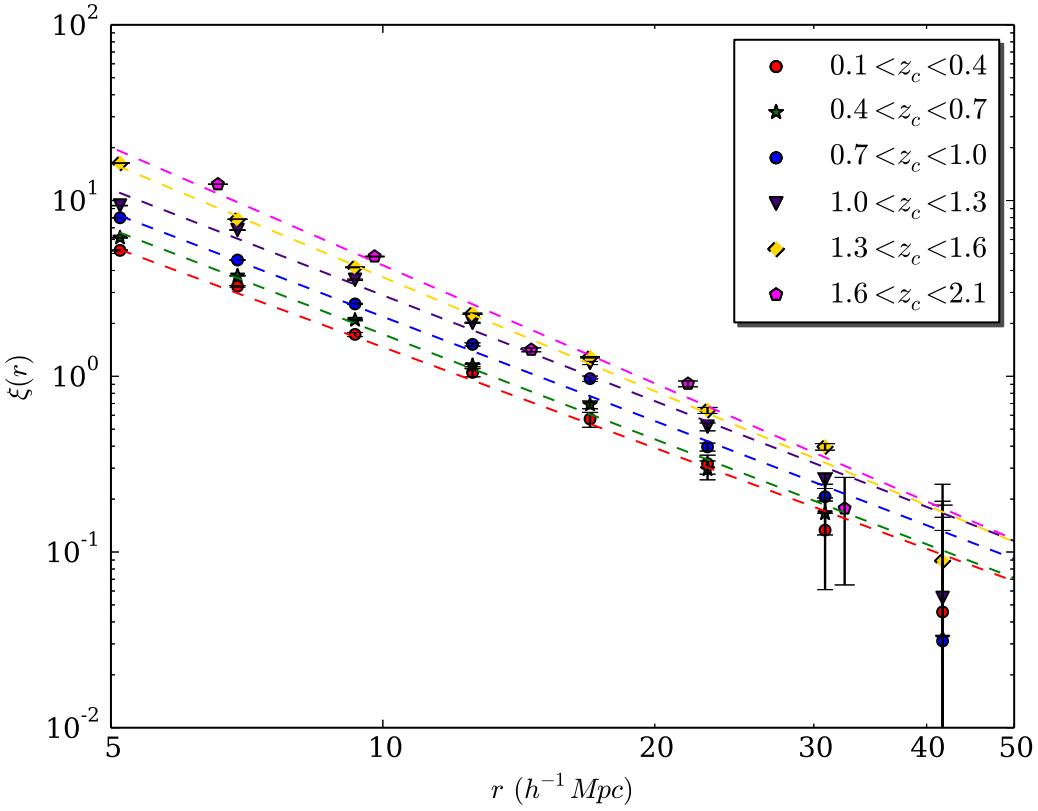

Figure 5.6: The correlation functions for clusters with $M_{halo} > 5 \times 10^{13}\ h^{-1}\ M_{\odot}$ in 6 different redshift slices. The dashed lines show the corresponding power-law best-fits. The parameter values for the fits can be found in Table 5.1.

redshift domain with good statistics. This will enable us to study the redshift evolution of clustering on a large range of redshifts and provide independent cosmological tests (Younger et al., 2005). In this section, we investigate the expected redshift evolution of the cluster correlation function in the redshift range [0,2], assuming a concordant ΛCDM model and using the light-cone catalogue detailed in Section 5.2.

The light-cone catalogue we have contains 443,726 clusters with a redshift range $0.0 < z < 3.0$ as seen from Figure 5.4 and a mass range of $1 \times 10^{13} < M_{halo} < 2 \times 10^{15}\ h^{-1}\ M_{\odot}$. For this particular analyses we will make a common mass cut of $M_{halo} > 5 \times 10^{13}\ h^{-1} M_{\odot}$ and split our samples into 6 redshift slices, $0.1 < z_c < 0.4$, $0.4 < z_c < 0.7$, up to $1.6 < z_c < 2.1$ (where z_c refers to the cosmological redshift). Typical cluster masses are in the range $M_{halo} \approx 1 \times 10^{13}\ h^{-1} M_{\odot}$ to $M_{halo} \approx 1 \times 10^{15}\ h^{-1} M_{\odot}$ (Bahcall, 1996). So by choosing an intermediate mass cut of $M_{halo} > 5 \times 10^{13}\ h^{-1} M_{\odot}$, we allow ourselves to sample the redshift range in several redshift bins with a sufficient number of clusters per bin. The reason we are not probing beyond this redshift range although the redshift limit of the light-cone being 3.0

is because of the number of clusters we have. With the given mass cut, the number of clusters above $z_c > 2.1$ is only 463 and errors become larger beyond $z_c > 2.1$. The correlation function starts to deviate from a power-law because of the poor statistics we have above $z_c > 2.1$.

We apply Equation 3.5 for each of our samples and obtain the two-point correlation function at difference separations. We split the separations into 20 bins within a range of 5-50 Mpc and calculate $\xi(r)$.

For each sub-sample, the correlation function is fitted by a power-law as mentioned in Equation 3.13 leaving both r_0 and γ as free parameters. The results of the fits can be visualised in Figure 5.6 and can be numerically seen in the second panel of Table 5.1 . The number of objects, the values of the best-fit parameters obtained for the mass and redshift limit of each sub-sample are given in the four panels of Table 5.1. A non-linear least squares analysis is used to fit the set of observations with a model that is non-linear in $n = 2$ unknown parameters (r_0 and γ). The fit is performed in the range $5 - 50h^{-1}$ Mpc and the error bars are obtained using the jackknife estimate method (see Section 5.3.2).

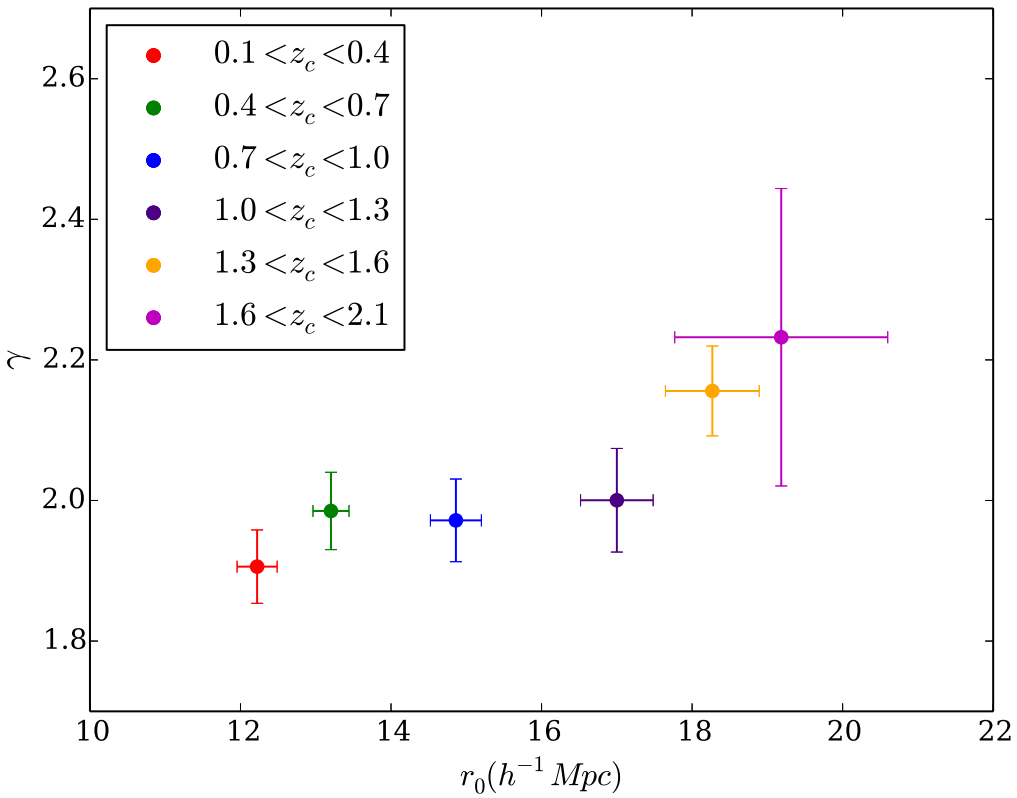

Figure 5.7: The evolution of r_0 and γ for clusters observed in different redshift slices and with mass $M_{halo} > 5 \times 10^{13}\ h^{-1}\ M_\odot$. The parameter values for the fits can be found in Table 5.1.

Mass ($h^{-1}\ M_{\odot}$)	z_c	r_0	γ	r_0 (γ = 2.0)	$N_{clusters}$	bias
$M_{halo} > 2 \times 10^{13}$	$0.1 < z_c < 0.4$	9.89±0.20	1.76±0.05	9.53±0.29	10492	1.81±0.03
	$0.4 < z_c < 0.7$	10.22±0.14	1.84±0.04	10.01±0.17	27224	2.00±0.03
	$0.7 < z_c < 1.0$	11.10±0.15	1.87±0.04	10.85±0.17	35133	2.52±0.02
	$1.0 < z_c < 1.3$	11.62±0.23	1.98±0.05	11.58±0.19	31815	3.01±0.06
	$1.3 < z_c < 1.6$	12.41±0.42	2.13±0.09	12.49±0.52	22978	3.37±0.19
	$1.6 < z_c < 2.1$	14.78±0.21	2.06±0.05	14.78±0.22	18931	4.65±0.23
$M_{halo} > 5 \times 10^{13}$	$0.1 < z_c < 0.4$	12.22±0.26	1.90±0.05	11.97±0.25	3210	2.21±0.05
	$0.4 < z_c < 0.7$	13.20±0.23	1.98±0.05	13.16±0.17	7301	2.62±0.13
	$0.7 < z_c < 1.0$	14.86±0.33	1.97±0.05	14.52±0.28	8128	3.38±0.22
	$1.0 < z_c < 1.3$	17.00±0.48	2.00±0.07	17.00±0.38	5963	4.38±0.19
	$1.3 < z_c < 1.6$	18.26±0.62	2.15±0.06	19.73±0.43	3365	5.29±0.31
	$1.6 < z_c < 2.1$	19.18±1.41	2.23±0.21	20.05±1.13	2258	6.21±0.62
$M_{halo} > 1 \times 10^{14}$	$0.1 < z_c < 0.4$	14.60±0.35	1.93±0.06	14.33±0.24	1119	2.67±0.19
	$0.4 < z_c < 0.7$	17.26±0.96	1.90±0.08	16.35±0.42	2228	3.45±0.23
	$0.7 < z_c < 1.0$	18.93±1.18	2.08±0.12	19.55±0.75	2072	4.64±0.37
	$1.0 < z_c < 1.3$	22.36±1.90	2.11±0.17	23.33±1.30	1221	6.15±0.82
	$1.3 < z_c < 1.6$	26.09±4.10	2.28±0.30	28.96±3.17	590	7.64±2.50
$M_{halo} > 2 \times 10^{14}$	$0.1 < z_c < 0.4$	19.98±1.92	1.95±0.22	19.73±1.22	322	3.98±0.38
	$0.4 < z_c < 0.7$	22.23±1.54	2.16±0.18	22.27±1.17	538	4.57±0.45
	$0.7 < z_c < 1.0$	24.65±1.89	2.19±0.29	25.28±1.68	407	6.01±1.63

Table 5.1: The best-fit values of the parameters of the real-space correlation function $\xi(r)$ for the light-cone at different (1) mass thresholds and (2) redshift ranges. For each sample we quote (3) the correlation length r_0, (4) slope γ, (5) correlation length r_0 at fixed slope γ = 2.0, (6) number of clusters $N_{clusters}$ and (7) the bias b obtained.

It can be seen that, starting from the low redshift sample ($0.1 < z_c < 0.4$) the cluster correlation amplitude increases up to the highest redshift sample ($1.6 < z_c < 2.1$). The power-law has a relatively stable slope varying between 1.9 and 2.1 between the 6 samples. In the two highest redshift slices, however, the slope appears to be slightly higher, but the variation is at the $\sim 2\sigma$ level for the $1.3 < z_c < 1.6$ sub-sample and at the $\sim 1\sigma$ level for the $1.6 < z_c < 2.1$ sub-sample. On the average, $\gamma \approx 2.0$, is close to the measured value for both galaxy and cluster catalogues (Borgani and Guzzo, 2001) and our values are within this limit. There is however a slight redshift dependence for γ as it can be seen that the last three redshift samples have $\gamma > 2.0$ compared to the first three samples which have $\gamma < 2.0$ (see Table 5.1).

The above effect can be visually seen in Figure 5.7 wherein we plot the two-best fit parameters. The correlation length starts to increase from 12.22 ± 0.26 to 14.86 ± 0.33 for the $0.1 < z_c < 0.4$ and $0.7 < z_c < 1.0$ sample which is an increase of 17.7%. The same increases from 17.00 ± 0.48 to 19.18 ± 1.41 for the $1.0 < z_c < 1.3$ and $1.6 < z_c < 2.1$ sample respectively, which is only a 12.8% increase.

On the contrary, the increase in the correlation length is systematic and statistically significant. When we fix the slope at $\gamma = 2.0$, r_0 is shown to increase from $11.97 \pm 0.25\ h^{-1}$ Mpc for the lowest redshift slice ($0.1 < z_c < 0.4$), to $20.05 \pm 1.13\ h^{-1}$ Mpc for the highest redshift slice ($1.6 < z_c < 2.1$). Our results can be compared to Younger et al. (2005)(see their Figure 5), who obtained similar results for clusters identified in the high-resolution simulations of Hopkins et al. (2005).

Using our simulations we have studied the redshift evolution of clusters with a mass $M_{halo} > 5 \times 10^{13}\ h^{-1}\ M_\odot$ up to a redshift of $z \approx 2.1$. Future surveys such as Euclid (Laureijs et al., 2011) and LSST (LSST Dark Energy Science Collaboration, 2012) will be probing up to these high redshifts and the $\xi(r)$ calculated from the data gathered from these surveys can be directly compared with our results.

5.5 Mass evolution of the correlation function

The clustering properties of clusters are not only expected to vary with redshift, but are also expected to vary with mass. One has to rely on cluster mass proxies such as number counts, cluster richness and other observables. Using cluster richness as a probable mass proxy in particular will be dealt in in later sections.

Several studies were made to study this evolution of clustering with respect to mass (Governato et al., 1999; Bahcall et al., 2004; Younger et al., 2005) and two main results are prominent from the studies:

1. Cluster correlation amplitude increases with mass, both for low redshift and high redshift clusters

2. The increase with redshift of the correlation amplitude is stronger for more massive clusters compared to less massive ones.

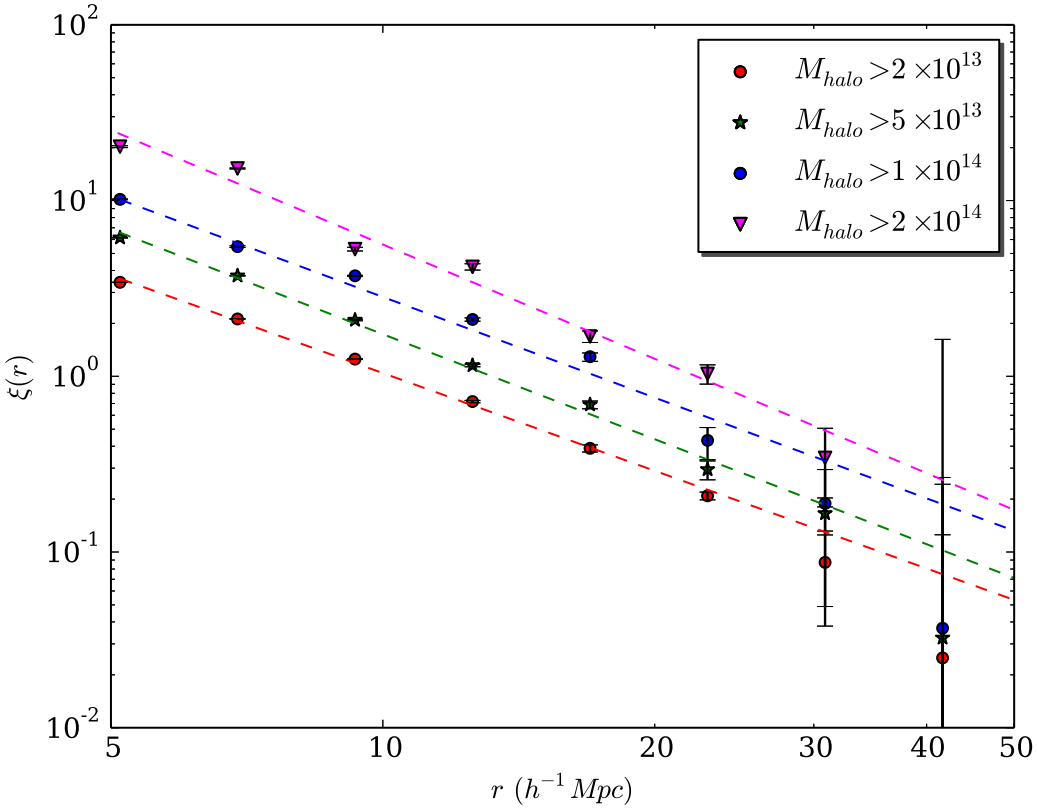

Figure 5.8: The correlation functions for clusters with $0.4 < z_c < 0.7$ in 4 different mass thresholds. The dashed lines show the corresponding power-law best-fits. The parameter values for the fits can be found in Table 5.1.

All the above studies were primarily done using cosmological simulations. Future cluster surveys such as LSST (LSST Dark Energy Science Collaboration, 2012) and EUCLID (Laureijs et al., 2011) will be having the advantage of calculating the mass from weak-lensing measurements and other methods. So a calculation of the mass evolution of the two-point correlation function (also with redshift) is an important aspect of this study. Our results can be directly compared with the results that will be obtained from the cluster samples these surveys will be detecting.

In this section we investigate how much of an effect mass variation plays in the clustering strength of galaxy clusters. For this purpose, we considered 4 different mass thresholds: $M_{halo} > 2 \times 10^{13}\ h^{-1}\ M_{\odot}$, $M_{halo} > 5 \times 10^{13}\ h^{-1}\ M_{\odot}$, $M_{halo} > 1 \times 10^{14}\ h^{-1}\ M_{\odot}$ and $M_{halo} > 2 \times 10^{14}\ h^{-1}\ M_{\odot}$. As a first test, we fix the redshift range to $0.4 < z_c < 0.7$ (arbitrary) and calculate $\xi(r)$ for the above 4 mass cuts. The plot of the correlation function at different separations r is seen in Figure 5.8. It can be seen that the amplitude of the correlation function increases with limiting mass. The values of the best-fit parameters can be found in Table 5.1.

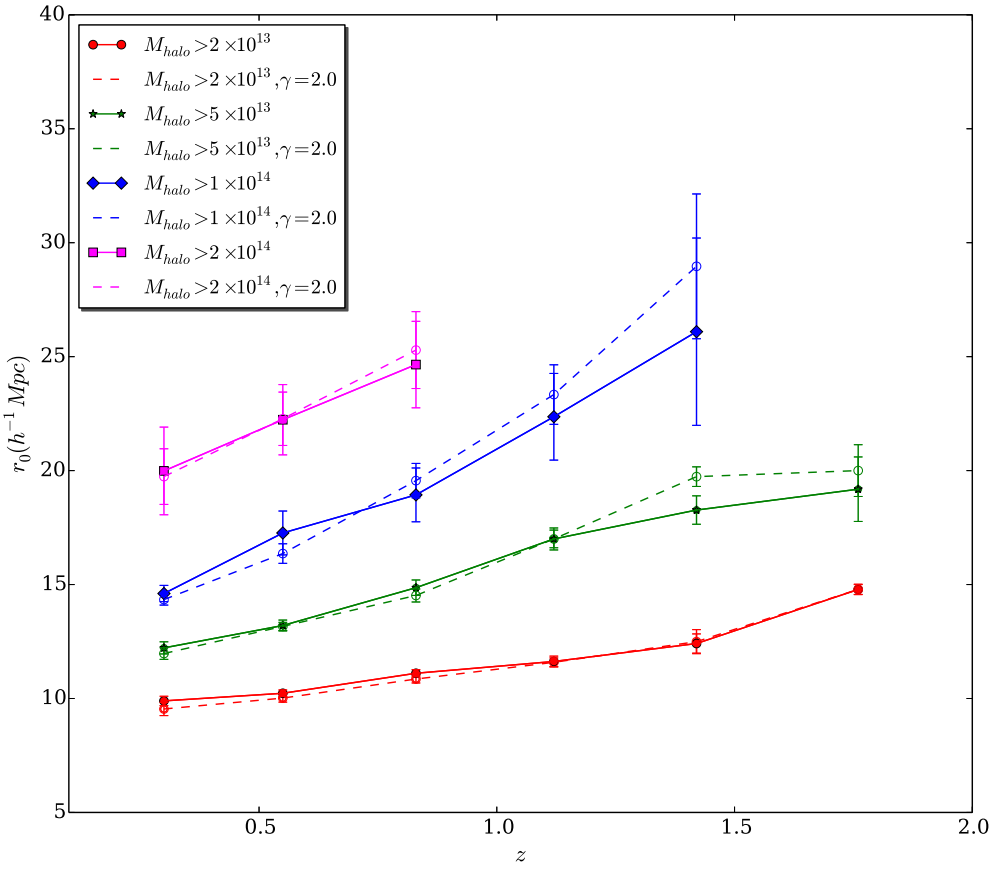

Figure 5.9: The evolution of r_0 with redshift for different limiting masses. The filled symbols connected by solid lines correspond to the free slope fits, while the the open symbols connected by dashed lines correspond to a fixed slope γ = 2.0. The different limiting masses are colour coded as shown in the figure. The values of r_0 and γ for all the samples can be found in Table 5.1.

We know now that the correlation strength of galaxy cluster increases separately with both mass and redshift, but we would also like to know what the evolution is like when both the parameters are varied. The analysis is performed in the same redshift slices previously defined. The correlation function is fitted with a power-law (as in Equation 3.13), both with a free slope and with a fixed slope γ = 2.0.

In both cases, the correlation length r_0 increases with the limiting mass at any redshift and increases with redshift at any limiting mass, as shown in Figure 5.9. The higher the mass threshold, the larger is the increase of r_0 with redshift. For example, the ratio of the correlation lengths for the [1.3-1.6] and the [0.1-0.4] redshift slices is 1.25 with M_{halo} >

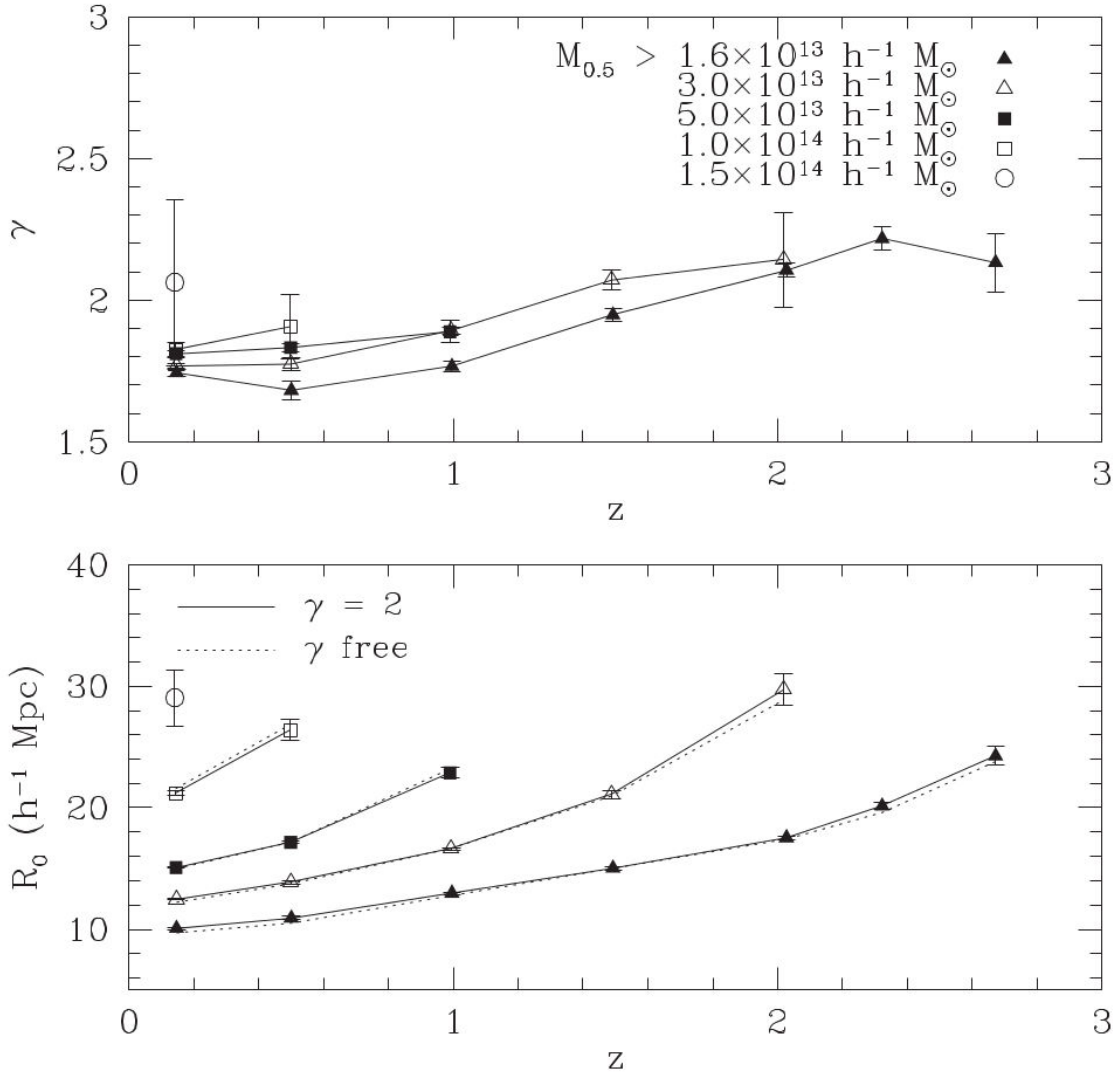

Figure 5.10: *Top panel:*The evolution of γ with redshift for different limiting mass thresholds and *Bottom panel:* the evolution of r_0 with redshift for different limiting mass thresholds as obtained by Younger et al. (2005)

$2 \times 10^{13}\ h^{-1}\ M_\odot$, while it reaches 1.8 with $M_{halo} > 1 \times 10^{14}\ h^{-1}\ M_\odot$. For the largest limiting mass ($M_{halo} > 2 \times 10^{14}\ h^{-1}\ M_\odot$), the number of clusters becomes small at high z and the analysis must be limited to $z = 1$.

We can compare our results with the analysis of Younger et al. (2005). Younger et al. (2005) used a Tree Particle Mesh (TPM) code (Bode and Ostriker, 2003) to evolve $N = 1260^3$ particles in a box of 1500 h^{-1}Mpc, reaching a redshift $z \approx 3.0$. while we use a simulation extracted from the Millennium simulation (Springel, 2005), a 2160^3 particle N-body simulation in a cubic volume of $500h^{-1}Mpc^2$ which extends up to a redshift of $z \approx 3.0$. We find a good agreement with the analysis of Younger et al. (2005) as it can be seen from Figure

5.10 for the masses and redshift ranges we can compare; our analysis probes the correlation function of $M_{halo} > 1 \times 10^{14}\ h^{-1}\ M_{\odot}$ clusters up to $z \approx 1.6$, and of $M_{halo} > 2 \times 10^{14}\ h^{-1}\ M_{\odot}$ clusters up to $z \approx 0.8$, thus extending the $r_0(z)$ evolution shown by Younger et al. (2005) to higher redshifts.

Given the redshift depth of the simulation we use, we dwell deeper close to $z \approx 1.5$ for clusters with a mass cut $M_{halo} > 5 \times 10^{13}\ h^{-1}\ M_{\odot}$ and $M_{halo} > 1 \times 10^{14}\ h^{-1}\ M_{\odot}$ whereas Younger et al. (2005) restrict their analysis for the same mass clusters at $z \approx 1.0$.

5.6 Bias: Evolution with mass and redshift

Starting from the initial matter density fluctuations, structures grow with time under the effect of gravity. This means that galaxy clusters at the current epoch ($z \approx 0$) should depict a stronger clustering amplitude when compared with galaxy clusters at a distant epoch ($z >> 0$). We have seen so far that this is not the case. From Section 5.4 and 5.5 we see that the opposite holds true, i.e. high redshift and high massive haloes are more strongly clustered compared to the low redshift and low massive ones. This implies that the distribution of haloes, hence of galaxies and clusters, is biased with respect to the underlying matter distribution.

On large scales it is expected that the bias is linear and is given by:

$$\left(\frac{\Delta\rho}{\rho}\right)_{light} = b \times \left(\frac{\Delta\rho}{\rho}\right)_{mass} \tag{5.3}$$

where b is the bias factor and ρ is the density. The higher the halo mass, the higher the bias.

The amplitude of the halo correlation function is amplified by a b^2 factor with respect to the matter correlation function:

$$\xi(r)_{CL} = b^2 \times \xi(r)_{DM} \tag{5.4}$$

this bias is a function of both mass and redshift, i.e. $b(M, z)$ and the above describes the bias in a linear regime which is sufficient to describe the clustering on large scale. Here the $\xi(r)_{DM}$ is the Fourier transform of the dark matter power spectrum and $\xi(r)_{CL}$ denotes the cluster two-point correlation function. To calculate $\xi_{DM}(r)$ we adopt the de-wiggled template for the dark matter power spectrum:

$$P_{DM}(k) = \left[P_{lin}(k) - P_{nw}(k)\right] e^{-k^2\Sigma_{NL}^2/2} + P_{nw}(k) \tag{5.5}$$

where P_{lin} is the linear power spectrum (we use CAMB (Lewis and Bridle, 2002) to calculate it), P_{nw} is the power spectrum without the BAO feature as obtained by Eisenstein and Hu (1998), Σ_{NL} controls the smearing effect of the BAO. The power-spectrum is then Fourier transformed to obtain $\xi_{DM}(r)$:

$$\xi_{DM}(r) = \frac{1}{2\pi^2} \int dk k^2 P_{DM}(k) \frac{sin(kr)}{kr} \tag{5.6}$$

Fry (1996) and Tegmark et al. (1998) calculated the redshift evolution of the bias and found out that the bias is larger at earlier epochs of structure formation as the first structures formed will eventually collapse into the most over-dense regions in space. They also went on to prove that with time, eventually these structures will be unbiased tracers of the mass distribution. The amplitude of the matter correlation function increases with time and decreases with redshift, but the halo bias decreases with time and increases with redshift. The cluster correlation amplitude increases with redshift, as it is clear from Figure 5.7.

If one utilises cluster clustering to constrain cosmology, then one should have precise knowledge of the cluster bias. The same way in which we calculated the mass and redshift evolution of the two-point correlation function, here we calculate the evolution for the bias of the haloes present in our simulation. First we need to calculate the evolution of the dark matter two-point correlation function. To do so we follow Equation 5.6 and we make use of the function `xi_DM` inside the class `Cosmology` from `CosmoBolognaLib`. The comparison is not straightforward because, as we have previously noticed, in the simulation halo masses are not M_{200}, but the so–called Dhalo masses M_{halo}.

To visually compare the change in $\xi(r)$ between the dark matter and our haloes, we compare in Figure 5.11 the calculated $\xi_{DM}(r)$ for a given mass cut of $M_{halo} > 5 \times 10^{13}\ h^{-1}\ M_{\odot}$ and in the redshift range $0.1 < z < 0.4$ with that of $\xi(r)$ calculated for our haloes in the same redshift and mass range. It can be seen from Figure 5.11 that the amplitude of the correlation function of our haloes (given by the red line) is higher compared to the same obtained for dark matter (given by the blue line). The fraction of the two, i.e. $\xi(r)_{CL}/\xi(r)_{DM}$ is given in the sub-panel of the Figure. The bias for this particular mass and redshift range for our haloes is calculated using Equation 5.4 and is given in Table 5.1.

For each sub-sample we calculate the bias only within the range where $\xi(r)$ follows a power-law. For most of our samples this range is 5-50 Mpc, but in cases where we don't have enough clusters we restrict ourselves within 5-30 Mpc or 5-20 Mpc depending on power-law approximation. This exercise is then performed for all our mass cut and redshift cut samples (the same as defined in Sections 5.5 and 5.4). The values of the bias calculated for each sub-sample is given in the last column of Table 5.1.

There are several theoretical predictions for the evolution of the halo bias (Mo and White, 1996; Sheth et al., 2001; Tinker et al., 2010), but before we compare our results to these predictions, as a first order approximation we fit the bias obtained using a simple power law defined as:

$$b(M, z) = b_0(1 + z)^{b_1} + b_2 \tag{5.7}$$

where the three parameters b_0, b_1 and b_2 are function of mass. We show the results of the fit for our first three mass cut samples, i.e. $M_{halo} > 2 \times 10^{13}, 5 \times 10^{13}, 1 \times 10^{14}\ h^{-1}\ M_{\odot}$ in Figure 5.12. The values of the three best-fit parameters is given in Table 5.2.

There were several halo bias theoretical models developed wherein the bias of the haloes were determined by the relative abundance of haloes in large-scale environments. They were all derived from the mass function obtained for the haloes using the peak-background split

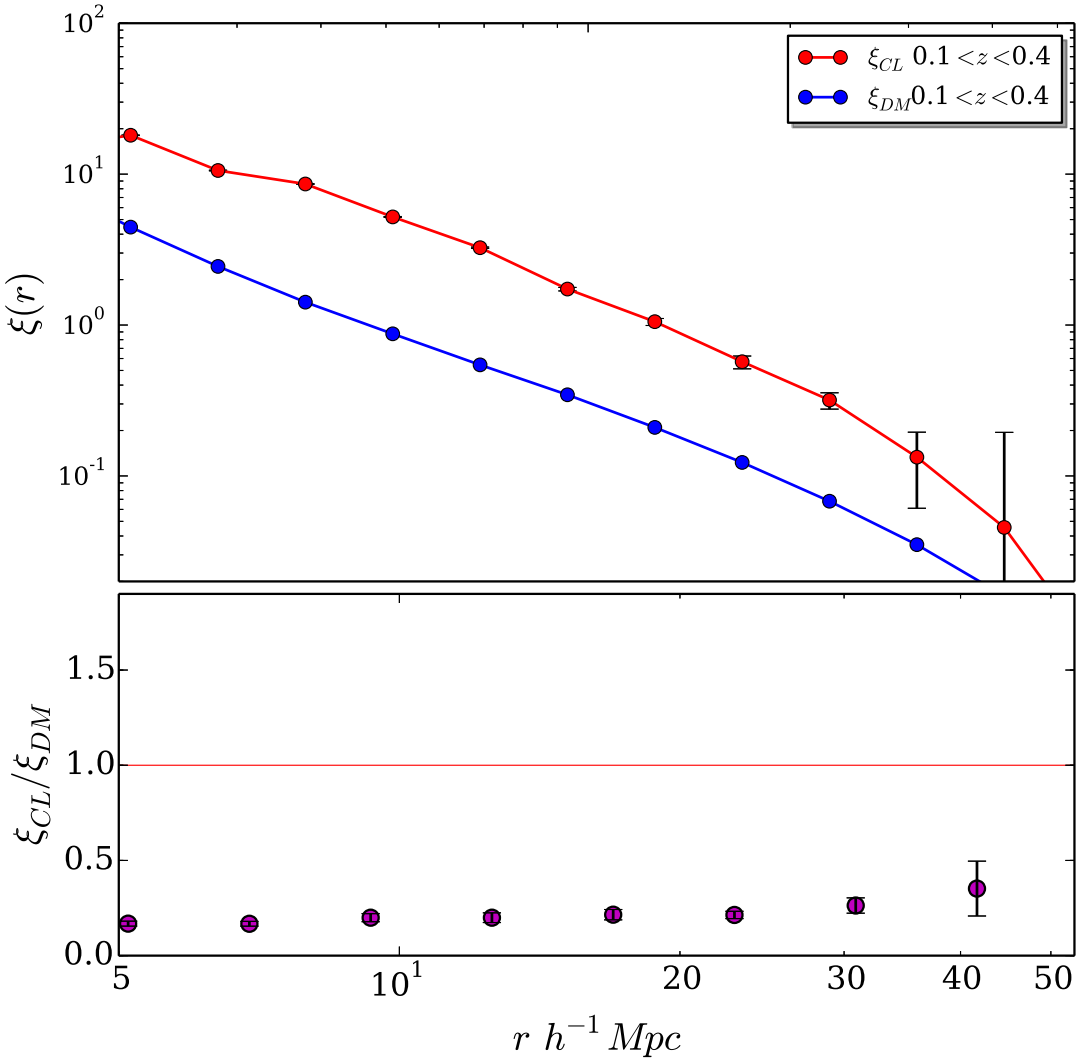

Figure 5.11: The two-point correlation function of our haloes above the mass cut of $M_{halo} > 5 \times 10^{13}\ h^{-1}\ M_{\odot}$ within the redshift range $0.1 < z < 0.4$ (given by the *red line*) and the two-point correlation function for dark matter in the same mass and redshift cut (given by the *blue line*). The sub-panel shows the fraction $\frac{\xi(r)_{CL}}{\xi(r)_{DM}}$. The error bars plotted for the cluster correlation function has been obtained from the jackknife resampling method as mentioned in Section 5.3.2.

(Mo and White, 1996; Sheth et al., 2001). These studies made use of the friends-of-friends (FOF) halo finding algorithm which was found to group distinct haloes together into one object (Tinker et al., 2010). Although these theoretical models reproduced the evolution of the bias fairly accurately, they failed to do so with numerical simulations (Tinker et al., 2010).

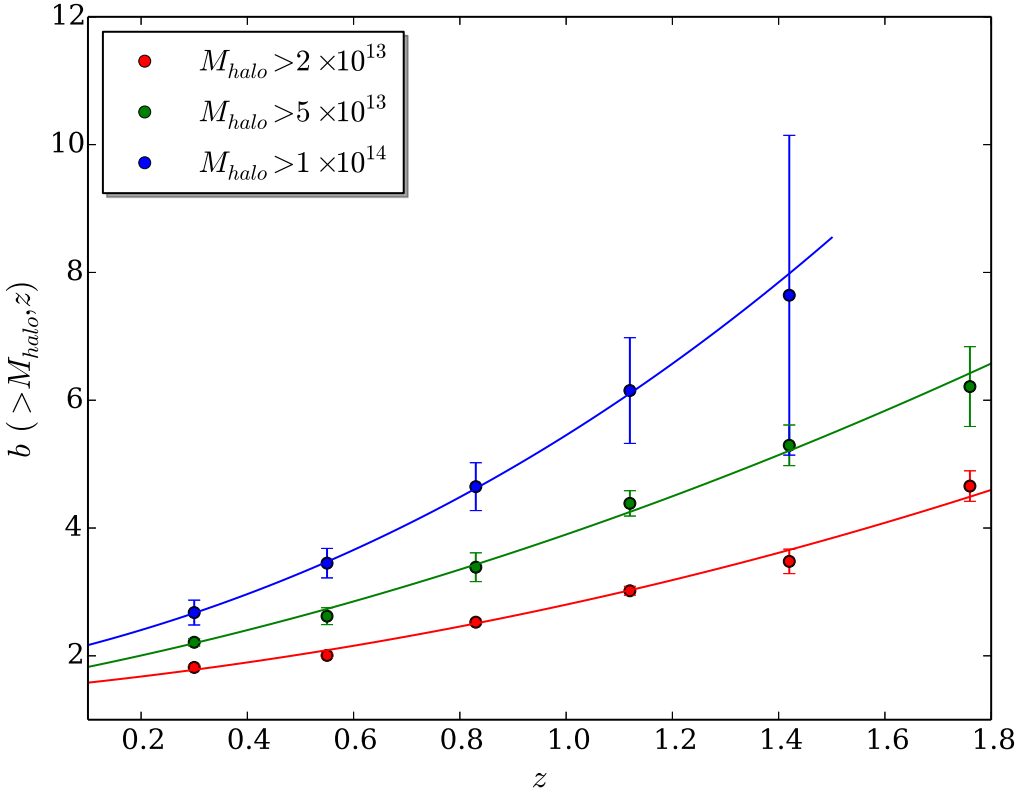

Figure 5.12: The bias obtained for our haloes with different mass and redshift cut samples given by the dotted points along with the fit done using Equation 5.7 given by the solid line. The different mass cut samples are colour coded as mentioned in the Figure.

It was shown by Manera et al. (2010) that using the peak-background split method to calculate the bias of massive haloes from their mass function results in a bias which is not accurate. So we compare the bias obtained from our haloes to those of Tinker et al. (2010) who have identified haloes using the spherical overdensity algorithm which finds mass around peaks in the density field such that the mean density is Δ times the background density. In our case we will be using Δ = 200. To compare the halo bias of our sample of dark matter haloes, we calculate the effective bias, i.e. the halo bias convolved with the halo mass function defined as:

$$b(z) = \frac{\int_{M_{min}}^{M_{max}} n(M,z) b_{Tinker}(M,z) dM}{\int_{M_{min}}^{M_{max}} n(M,z) dM} \tag{5.8}$$

where M_{min} and M_{max} are the minimum and maximum masses up to which we integrate. The comparison of this effective bias to our bias values is shown in Figure 5.13. The error bars for the bias are calculated by fitting the fraction $\xi_{CL}(r)/\xi_{DM}(r)$ using a simple power-

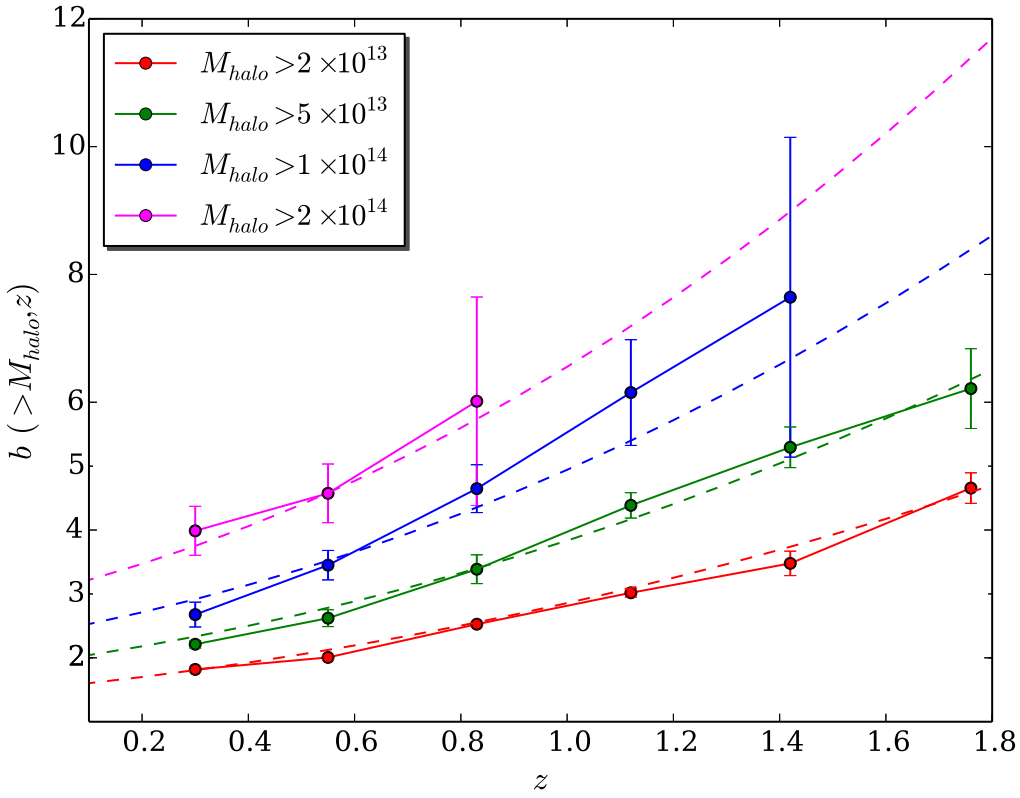

Figure 5.13: The bias as a function of redshift for different limiting masses where the solid lines just connect the points. The dashed line is the theoretical expectation of the bias as given by Tinker et al. (2010) for the same limiting masses and evolving redshift. The different limiting masses are colour coded as shown in the figure. The bias values for all the samples can be found in Table 5.1.

law (within the range where $\xi_{CL}(r)$ follows a power-law) of the form $b = rA + B$, where the best-fit parameter B gives us the bias and the error on parameter B is the error on the bias obtained.

It can be seen that for all our mass cut samples, the redshift evolution of the bias is clearly traced by the theoretical Tinker et al. (2010) bias function. For the first two mass cut samples, i.e. $M_{halo} > 2 \times 10^{13}, 5 \times 10^{13}\ h^{-1}\ M_{\odot}$, since we have abundant clusters (as can be seen in Table 5.1) even at high redshifts ($z \approx 2.0$) we calculate the bias up to $z \approx 1.8$, which is the median redshift of our redshift cut sample ($1.6 < z < 2.1$). It is also due to the abundance of clusters that the $\xi(r)$ even at these high redshifts, for the two samples, does not deviate from a power-law out to ≈ 50 Mpc. But for our remaining two mass cut samples, i.e. $M_{halo} > 1 \times 10^{14}, 2 \times 10^{14}\ h^{-1}\ M_{\odot}$ we restrict our calculations to lower redshifts.

The $\xi(r)_{CL}$ from Equation 5.4 can be denoted as $b_{eff}^2 \times \xi(r)_{DM}$. Just as an added confir-

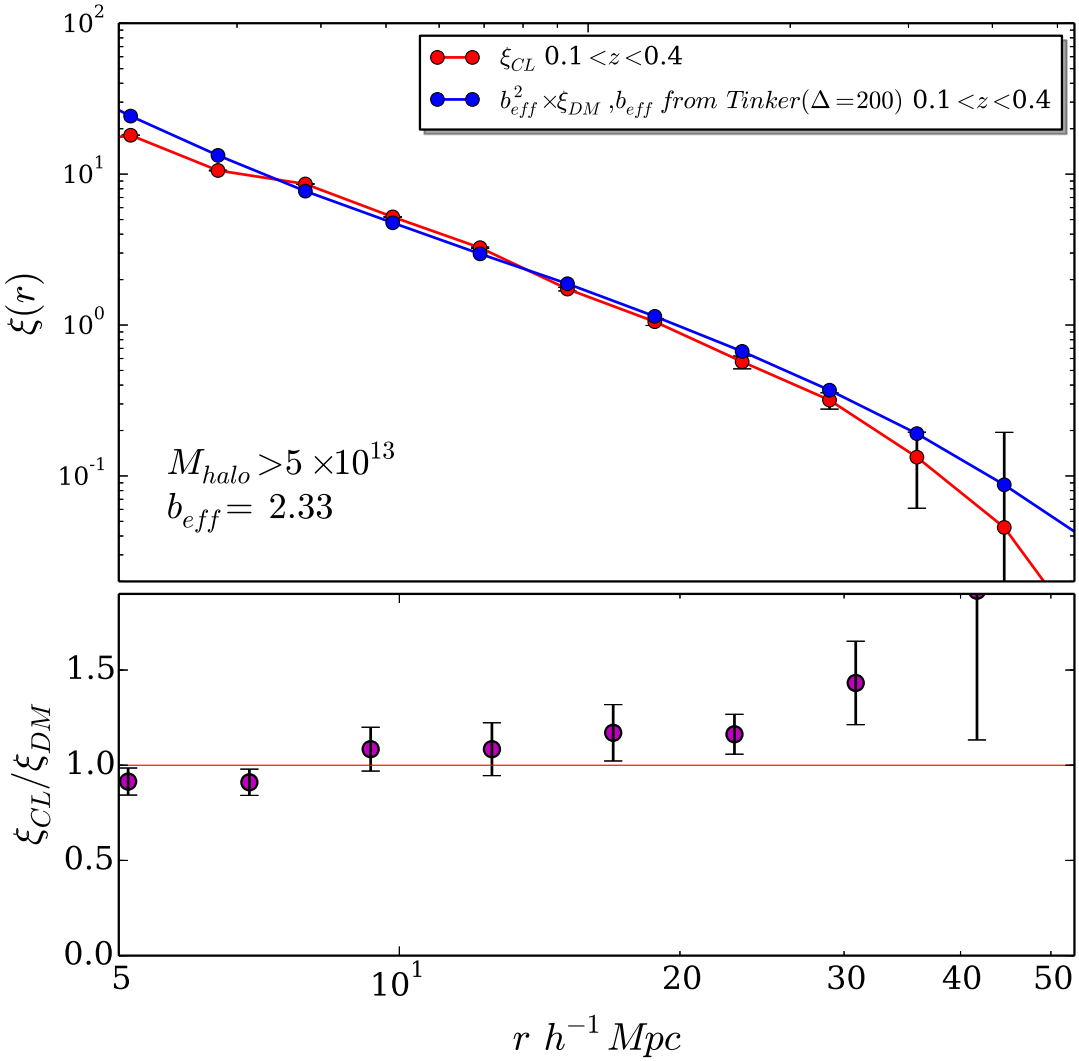

Figure 5.14: The two-point correlation function of our haloes above the mass cut of $M_{halo} > 5 \times 10^{13}\ h^{-1}\ M_{\odot}$ within the redshift range $0.1 < z < 0.4$ (given by the *red line*) and the two-point correlation function for dark matter in the same mass and redshift cut (given by the *blue line*) multiplied by the effective bias obtained for this particular sub-sample. The sub-panel shows the fraction $\xi(r)_{CL}/b_{eff}^2 \times \xi(r)_{DM}$.

mation, we multiply the dark matter correlation function obtained for one of our sub-sample with the effective bias obtained to see if the amplitude of the dark matter correlation function matches with that of the amplitude of the correlation function of our haloes. The result is shown in Figure 5.14 for the mass cut sample $M_{halo} > 5 \times 10^{13}\ h^{-1}\ M_{\odot}$ in the redshift range $0.1 < z < 0.4$ wherein the bias calculated is $b_{eff} = 2.33$. It can be seen that we do get con-

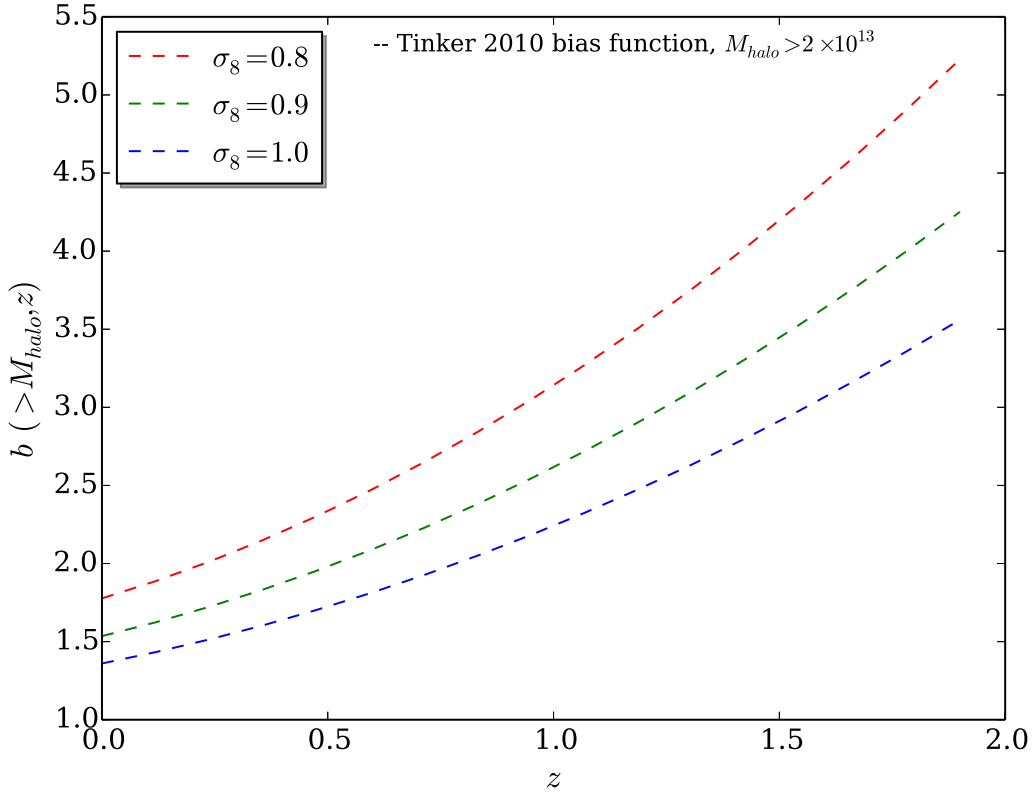

Figure 5.15: The redshift evolution of the Tinker et al. (2010) bias function calculated for a common mass cut of $M_{halo} > 2 \times 10^{13}\ h^{-1}\ M_{\odot}$ by varying the σ_8 parameter. The samples are colour coded as mentioned in the figure.

vergence of the amplitudes of the correlation functions as expected. One can also see that above 40 Mpc, the comparison is not so accurate and that the fraction deviates to 2.0.

The cluster bias of a given observational sample is often inferred by comparing the observed clustering of clusters with that of the clustering of dark matter measured in simulations. So the bias depends very much on the cosmological model used in the simulation. One of the most important cosmological parameter for calculating the bias is the σ_8 parameter which measures the amplitude of the (linear) power spectrum on the scale of $8h^{-1}$Mpc. In other words it is the standard deviation of cluster count fluctuations in a sphere of radius $8h^{-1}$Mpc. The variance of linearly evolved CDM fluctuations on a mass scale M is given by Equation 1.35 when it is smoothed with a top-hat filter of scale $R = 8\ h^{-1}$Mpc. Equation 1.35 in this context can be written as:

$$\sigma^2(M,a) = \int \frac{d^3k}{(2\pi)^3} W^2(kR) P_m(k,a) \tag{5.9}$$

where the function $W(y)$ is a filter function given by $W(y) = 3[sin(y)/y^3 - cos(y)/y^2]$ for

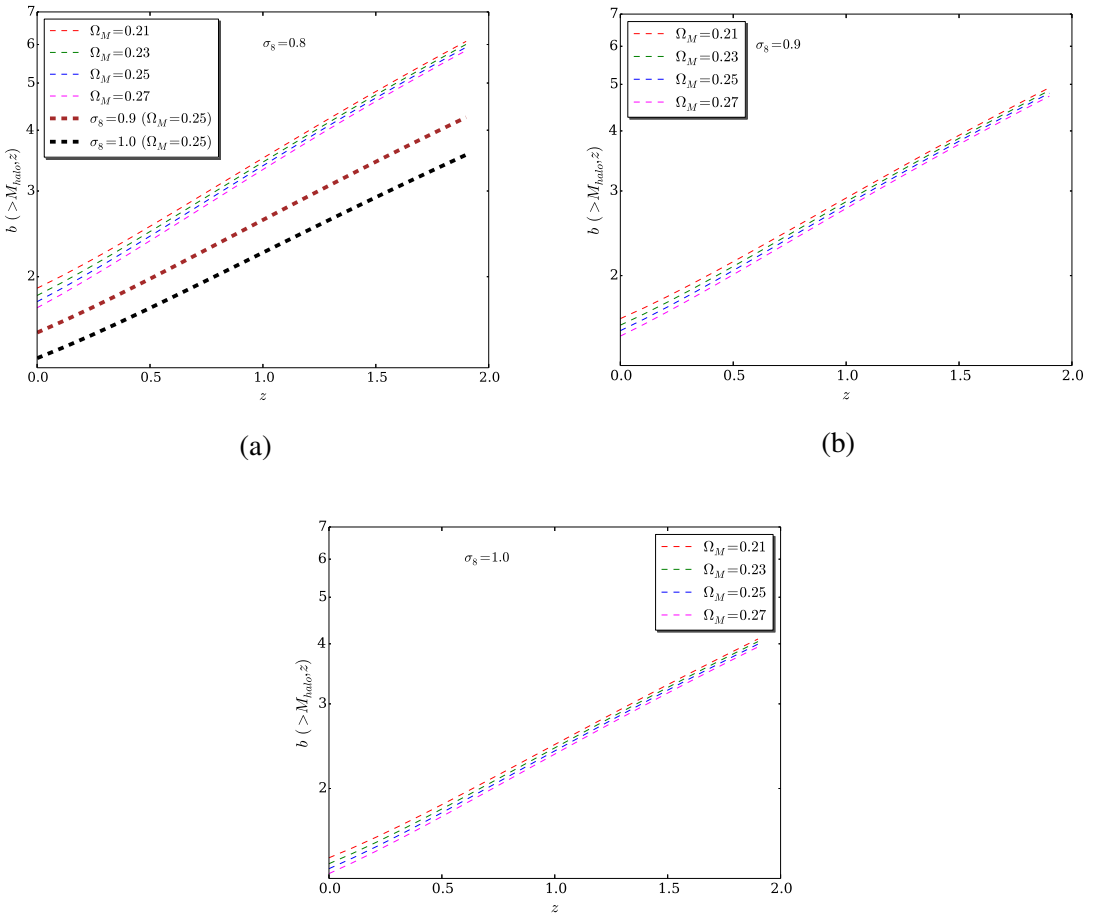

Figure 5.16: *Top left:* The redshift evolution of the Tinker et al. (2010) bias function calculated for a common mass cut of $M_{halo} > 2 \times 10^{13}\ h^{-1}\ M_{\odot}$ by varying the Ω_M parameter (for a fixed $\sigma_8 = 0.8$) and also by varying the σ_8 parameter (for a fixed $\Omega_M = 0.25$). *Top right:* The same as the left plot, but for a fixed $\sigma_8 = 0.9$. *Bottom panel:* The same as the top two panels, but for a fixed $\sigma_8 = 1.0$. The samples are colour coded as mentioned in the figure.

spatial filtering within a radius R. When we calculate Equation 5.9 at a distance of $8h^{-1}$Mpc with $a = 1$, we get the often used amplitude of the power spectrum σ_8.

As we have mentioned in Section 5.2, our simulation uses a value of 0.9 for the σ_8 parameter which also happens to be value calculated from WMAP and SDSS data (Seljak et al., 2005). By changing the value of σ_8 in calculating the bias, the results obtained will differ by a large margin. To show an example, we calculate the redshift evolution of the Tinker et al. (2010) bias function for a common mass cut of $M_{halo} > 2 \times 10^{13}\ h^{-1}\ M_{\odot}$ by altering the value of σ_8 from 0.8 to 1.0, the results are shown in Figure 5.15. It can be seen that the amplitude of the bias decreases as σ_8 increases. This is an important behaviour to notice, as using the

Mass cut ($h^{-1}\,M_{\odot}$)	b_0	b_1	b_2
2×10^{13}	0.37±0.19	2.15±0.48	0.90±0.29
5×10^{13}	0.85±0.46	1.84±0.47	1.05±0.30
1×10^{14}	0.79±0.17	2.43±0.23	1.16±0.24

Table 5.2: The table with the best-fit parameters obtained using Equation 5.7 for the different mass cut samples.

wrong σ_8 value in calculating the bias can lead to incorrect comparisons to both simulations and observations.

Another important parameter that has an effect on the theoretical bias obtained is Ω_M. To show the effect of Ω_M on the bias, we plot in Figures 5.16a, 5.16b and 5.16, the redshift evolution of the theoretical bias of Tinker et al. (2010) for a mass cut of $M_{halo} > 2 \times 10^{13}\ h^{-1}\ M_{\odot}$ for four values of $\Omega_M = 0.21, 0.23, 0.25, 0.27$, fixing σ_8 each time. It can be seen that from Figure 5.16a that for a fixed value of $sigma_8 = 0.8$, the amplitude of the bias decreases with increase in Ω_M. But it also be seen from Figure 5.16a that the change in the amplitude of the bias is stronger when σ_8 is changed from 0.8 to 0.9 and 1.0. The difference in the amplitude of the bias obtained for $\Omega_M = 0.21$ compared to $\Omega_M = 0.27$ is much less compared to the difference in the bias obtained for $\sigma_8 = 0.9$ and $\sigma_8 = 1.0$.

5.7 The r_0 vs *d* relation

As we have seen from Section 5.6 the dependence of the bias on the cluster mass is based on theory. A complementary and empirical characterization of the cluster correlation function is the dependence of the correlation length r_0 as a function of the mean cluster comoving separation d (Bahcall and Soneira, 1983; Governato et al., 1999; Croft et al., 1997; Bahcall et al., 2003), defined as:

$$d = \sqrt[3]{\frac{1}{\rho}} \tag{5.10}$$

where ρ is the mean number density of the cluster catalogue for a given mass threshold.

As we have seen from Section 5.6 that according to theory, more massive clusters have a higher bias, which in turn means that they have a higher r_0. Massive clusters also tend to be more rare objects which means that they have also a larger mean separation d. Therefore it is expected that r_0 increases with d. To visualise the above, we show a 3D density plot of X,Y,Z cartesian coordinates for two mass cut samples ($M_{halo} > 5 \times 10^{13}\ h^{-1}\ M_{\odot}$ and $M_{halo} > 1 \times 10^{14}\ h^{-1}\ M_{\odot}$) in Figure 5.17. It is clearly evident from the Figure that the less massive cluster sample is more denser as well as more abundant compared to the more massive one. So the larger the density the lesser the mean intercluster comoving separation and vice versa.

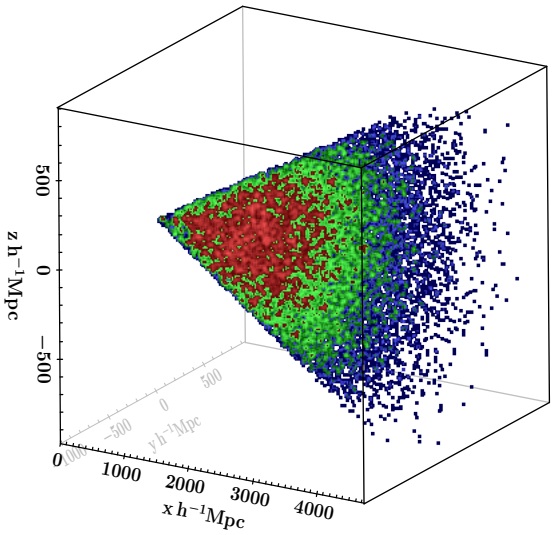

(a) $M_{halo} > 5 \times 10^{13}\ h^{-1} M_{\odot}$

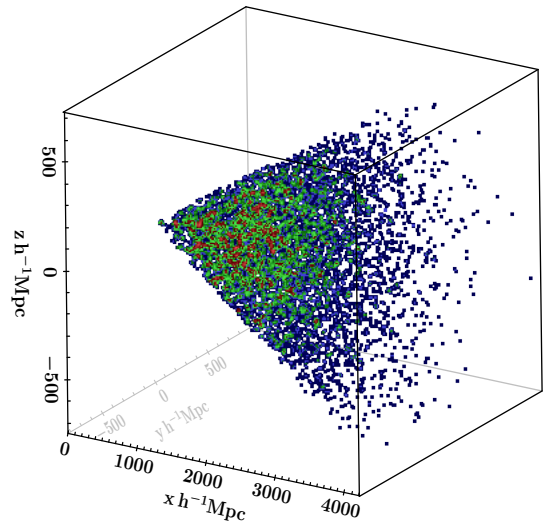

(b) $M_{halo} > 1 \times 10^{14}\ h^{-1} M_{\odot}$

Figure 5.17: *On top:* The XYZ 3D cartesian coordinate density plot for the sample with a mass cut of $M_{halo} > 5 \times 10^{13}\ h^{-1}\ M_{\odot}$. *Bottom:* The XYZ 3D cartesian coordinate density plot for the sample with a mass cut of $M_{halo} > 1 \times 10^{14}\ h^{-1}\ M_{\odot}$. Red regions denote more density and blue regions denote less density.

This relation has been investigated both in observational data (Bahcall and West, 1992; Estrada et al., 2009) and in numerical simulations (Bahcall et al., 2003; Younger et al., 2005).

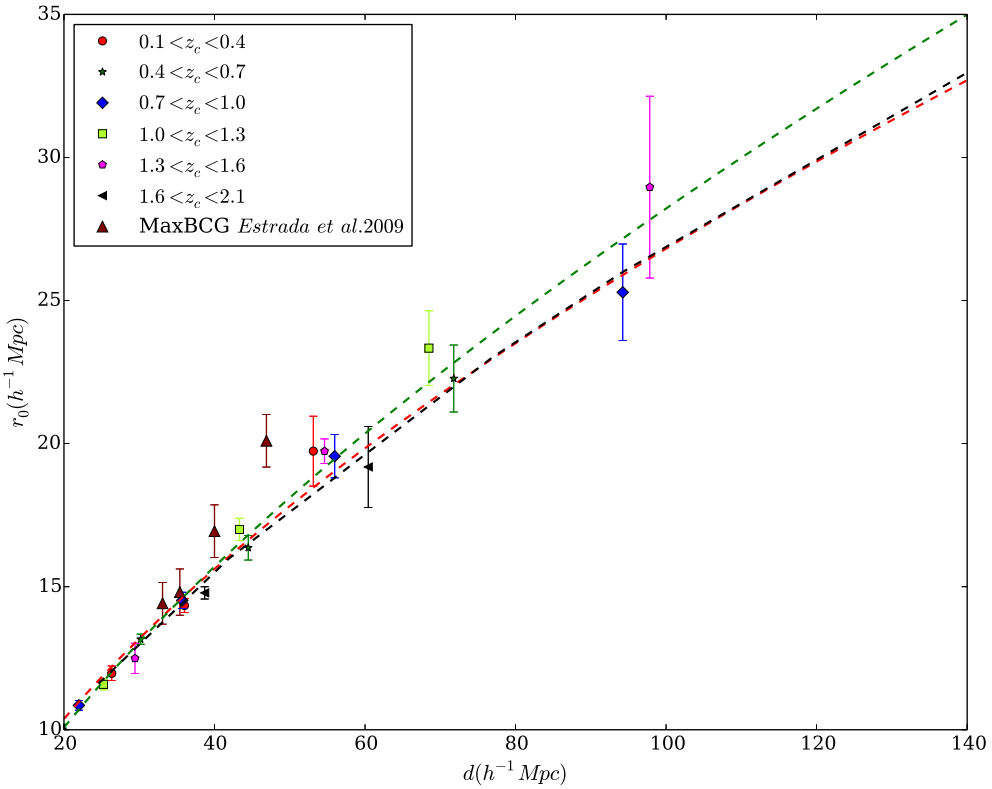

Figure 5.18: The evolution of r_0 with d for clusters [of different masses] in different redshift slices. The *red* dashed line shows the overall fit obtained for the data points considering a free slope and the *green* dashed line shows the fit when $\gamma = 2.0$. The analytic approximation in the ΛCDM case obtained by Younger et al. (2005) is shown by the dashed *black* line. The different redshift slices are colour coded as mentioned in the figure, and all the points plotted are for the fixed slope $\gamma = 2.0$.

Younger et al. (2005) give an analytic approximation in the ΛCDM case in the redshift range z = 0-0.3 for $20 \leq d \leq 60h^{-1}$Mpc:

$$r_0 = 1.7\big(d\big)^{0.6}\ h^{-1}\ \text{Mpc} \tag{5.11}$$

We determine the r_0 dependence with d for the various subsamples previously defined. The results obtained for a free γ along with the best fit obtained for both free and fixed $\gamma = 2$ are shown in Figure 5.18.

The best-fit r_0 - d relation in the redshift range $0 \leq z \leq 2.1$ and for the cluster mean separation range $20 \leq d \leq 140h^{-1}$Mpc is given by:

$$r_0 = 1.77 \pm 0.08\big(d\big)^{0.58\pm0.01}\ h^{-1}\ \text{Mpc} \tag{5.12}$$

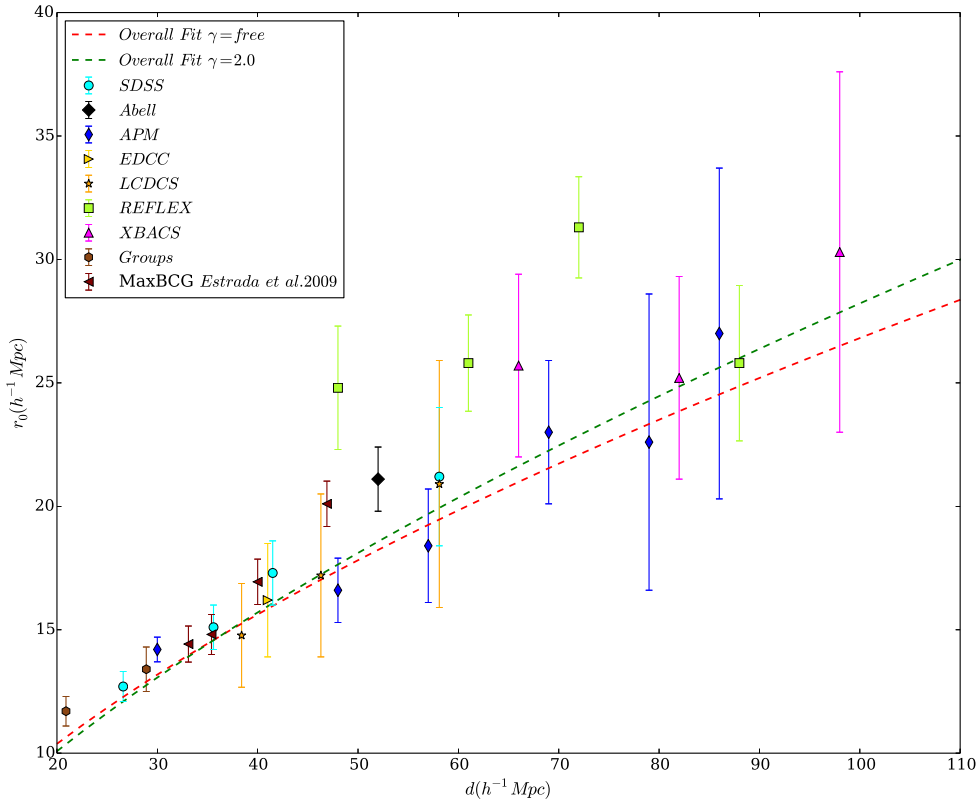

Figure 5.19: The evolution of r_0 with d for clusters [of different masses] in different redshift slices from observational cluster samples. The red dashed line and the $green$ dashed line show the overall fit obtained from simulations considering a free slope and when γ = 2.0 respectively. The analytic approximation in the ΛCDM case obtained by Younger et al. (2005) is shown by the dashed *black* line. The different redshift slices are colour coded as mentioned in the figure, and all the points plotted are for the fixed slope γ = 2.0.

The r_0 - d relation which appears to be scale–invariant with redshift, is consistent with what was found by Younger et al. (2005) and is also consistent with the theoretical predictions of Estrada et al. (2009) (see their figure 7).

The scale invariance of the $r_0 - d$ relation up to a redshift $z \approx 2.0$ implies that the increase of the cluster correlation strength with redshift is matched by the increase of the mean cluster separation d. It suggests that the cluster mass hierarchy does not evolve significantly in the tested redshift range: for example, the most massive clusters at an earlier epoch will still be among the most massive at the current epoch.

There have also been calculations of both r_0 and d from observations to which we can directly compare the results obtained for our ΛCDM simulations. We make use of data from

Abell clusters, SDSS, APM, 2dFGRS groups, all of which has been compiled by Bahcall et al. (2003). Some of the samples are optically selected, whereas some are X-ray selected clusters. We convert all our correlation lengths and mean intercluster comoving separations to comoving scales in a ΛCDM cosmology. The $r_0 - d$ from simulations is compared with the $r_0 - d$ obtained from observations along with the best-fit and is shown in Figure 5.19. The results show a general agreement between the ΛCDM model and the observations. The optically selected clusters are more or less in agreement with the fit within 1σ. There is a wide scatter at large d scales ($d > 70\,h^{-1}$Mpc). It is because of this large scatter, this relation cannot be comprehensively used to constrain cosmological parameters.

As we expect to observe more clusters at higher redshifts, the $r_0 - d$ relation can be used for direct comparison with observations. This comparison will prove an important test of the current ΛCDM cosmology. All the bias models we know so far are based on theory, this relation however is an empirical characterisation and will still hold true, even if all the theoretical bias predictions are proven wrong.

5.8 Conclusions from this chapter

We have used the light-cone simulations of Merson et al. (2013) and have studied the redshift and mass evolution of the two-point correlation function of haloes corresponding to galaxy clusters up to $z \approx 2.1$.

- Redshift evolution was studied using the clusters from the simulations. A common mass cut of $M_{halo} > 5 \times 10^{13}\ h^{-1}\ M_\odot$ was made for the clusters from the simulations. From the best-fit parameters obtained, we find an increasing clustering strength with redshift, all the way up to $z \approx 2.1$. Results were compared with Younger et al. (2005) and we found the same evolutionary trend up to a redshift of $z \approx 1.0$ for the above samples. For our samples we find that the same evolutionary trend continues up to $z \sim 2$.

- The mass evolution of clusters with redshift was also studied by slicing the samples into four mass threshold ranges (see Section 5.5). A clear trend of increasing clustering strength with redshift was seen for all the above mass cut samples, both for $\gamma = 2.0$ (fixed) and γ set as a free parameter. In particular, we find a stronger evolutionary trend for more massive clusters as compared to the less massive ones. For example, clusters with $M_{halo} > 2 \times 10^{13}\ h^{-1}\ M_\odot$ have a $r_0 = 9.89 \pm 0.20\ h^{-1}$Mpc at $z = 0.25$, $r_0 = 11.10 \pm 0.15\ h^{-1}$Mpc at $z = 0.85$ and $r_0 = 12.41 \pm 0.42\ h^{-1}$Mpc at $z = 1.45$; while clusters with $M_{halo} > 1 \times 10^{14}\ h^{-1}\ M_\odot$ have a $r_0 = 14.60 \pm 0.35\ h^{-1}$Mpc at $z = 0.25$, $r_0 = 18.93 \pm 1.18\ h^{-1}$Mpc at $z = 0.85$ and $r_0 = 26.09 \pm 4.10\ h^{-1}$Mpc at $z = 1.45$.

- The bias parameter was calculated for the z_c sample with increasing mass cuts and we find a strong increase of the bias with redshift. The increase is stronger for more massive clusters compared to the less massive ones. Our bias evolution was also compared

with the theoretical expectation of Tinker et al. (2010) and we find the evolution for all our mass samples to be within 1σ of the theoretical values. The bias evolution is stronger for larger σ_8 values. This is to be taken into account every time one wants to compare the bias obtained from either simulations or from observations to theoretical predictions.

- The $r_0 - d$ relation was studied up to a redshift of $z = 2.1$. Positive correlation was found all the way up to $z = 1.6$. We find that the scatter at larger redshift is somewhat higher compared to the low redshifts. The overall relation obtained for the best-fit was found to be $1.77 \pm 0.08(d)^{0.58\pm0.01}$ h^{-1}Mpc compared to $1.70(d)^{0.60}$ h^{-1}Mpc obtained by Younger et al. (2005). Our results are consistent with those of Estrada et al. (2009). We also compared the fit obtained for the $r_0 - d$ relation with values obtained from observational surveys of clusters such as Abell, 2dGFRS, SDSS etc and found that the results show a consistency between the ΛCDM model and the observations.

Chapter 6

Towards clustering of clusters from observational catalogues

Contents

6.1 Introduction

The results we have obtained so far have been on the clustering of haloes, whose position and redshift were perfectly known. But for a real observational survey, we will be detecting galaxy clusters, associated with a number of uncertainties in their position, redshift etc. Observational surveys in the modern era follow a multi-wavelength approach and galaxy clusters are detected either in the optical/near-infrared, X-ray or radio wavelengths. For the study of this thesis, we will focus our attention towards optically selected galaxy clusters.

The angular position of galaxy clusters are defined in several ways, such as the position of the brightest central galaxy (BCG) in the sample or the centroid positions of peaks identified in weak lensing mass maps etc. But the positions derived from these methods are usually associated with an error of around a few hundred kilo parsecs (Dietrich et al., 2012). This can also be due to projection effects that arise in the case of observational surveys. However, in the case of galaxy clusters, when one counts pairs of clusters to study clustering, the effect of this error is minimal and can be ignored.

Distance to galaxy clusters are inferred from redshift which is measured either spectroscopically or photometrically. Spectroscopic redshift measurements of galaxies is a hard task, and are fairly accurate. Photometric redshifts on the other hand have large errors associated with them. This in turn leads to errors on the distances measured to galaxy clusters.

The fact that cluster mass is not a direct observable also complicates matters. Mass estimates are commonly inferred adopting scaling relations between independent weak-lensing masses and mass proxies such as richness (defined as the number of galaxies in a cluster within a given radius). The mass-observable relation usually depict a scatter that varies with redshift and must be constrained using additional data. Theoretical predictions and numerical estimates for cluster clustering depends on the mass (as we have seen in the previous chapter). From cluster catalogues, one can measure the richness dependence of cluster clustering. To compare an observational richness evolution of cluster clustering to the theoretical/numerical mass evolution of cluster clustering, one has to address the mass-richness relation.

Another difficulty in observational catalogues is that several clusters along the line-of-sight can be misidentified as a single massive galaxy cluster, which can lead to errors in number counts and mass estimates. Clusters that can be distinguished in spectroscopic surveys can be merged as a single cluster in photometric surveys, if the difference in the redshift of the two clusters (Δz) is similar to the associated photometric uncertainty. Although this systematic effect has been drastically suppressed in modern surveys with multi-band photom-

etry, one still expects 5%-20% of photometrically selected clusters to suffer from projection effects (Cohn et al., 2007; Rozo et al., 2011). Observational cluster samples also suffer in terms of purity and completeness. Not all clusters above a given mass and redshift limit are detected and false positive sources are also wrongly included in the sample.

All the above effects need to be taken into account when analysing data obtained from observational cluster catalogues. However, in this thesis, we restrict ourselves to study, how in particular, the impact of redshift errors affect the two-point correlation function and provide a solution to our simplistic scenario. We analyse how the two-point correlation function evolves with the true richness (all members of the cluster being true members) and also try to find out if we can derive $\xi(> mass)$ from $\xi(> richness)$. We make use of the deprojection method, and as a preliminary test, study the evolution of the two-point correlation function of clusters detected in the CFHTLS survey.

6.2 Impact of redshift errors on the correlation function

6.2.1 Modelling of the errors associated with cluster redshifts

Redshift as we have seen can be measured from spectroscopic and photometric techniques. Spectroscopic information of all or at least a few galaxies is a difficult task since it is enormously time consuming and also challenging for samples with redshift $z \gtrsim 1$.

While galaxy clustering in real-space is statistically isotropic, it is not the same in redshift-space. This is because the spatial distribution of galaxies appear squashed and distorted when their positions are plotted in redshift-space due to the line-of-sight components of the galaxy peculiar velocities. This effect as we have seen before is called as the "Fingers-of-God" effect. Galaxy clusters themselves interact with each other producing peculiar velocities, which are of the order of $\sim 300 \mathrm{km} s^{-1}$ (Bahcall and Oh, 1996), but the effects of peculiar velocities of clusters compared to galaxies are relatively smaller. The peculiar velocities of galaxy clusters are dependent on the mass, distance of separation etc., and the effect is dominant only on small scales (a few Mpc).

Large-scale surveys are usually performed using photometric techniques. Photometric redshifts are estimated by using multi-band photometry as inputs to one or more different techniques that map galaxy photometric properties into a redshift. By using multi-band photometry we can crudely measure the redshift of all objects in a field simultaneously. Using deep multi-band information spanning all of the visible and the near-IR range we can even measure redshifts of extremely faint objects, for example reaching to AB mag $\simeq 29$ for the Hubble deep field objects (Fernández-Soto et al., 2001). Since these objects are so faint it is nearly impossible to obtain spectra for the bulk of detected objects. There are mainly two approaches in measuring photometric redshifts: the first is known as template-based methods (Benítez, 2000; Csabai et al., 2000; Blanton et al., 2003; Feldmann et al., 2006; Ilbert et al., 2009, and references therein), in which a set of calibrated galaxy spectral energy distributions (SEDs) is fit to the photometric data to find the one that best represents the observed fluxes.

To obtain accurate results, the filter set is chosen in order to bracket some of the prominent features such as the 4000Å break or the Lyman Alpha break. The second approach towards measuring photometric redshifts is to use a spectroscopic training set and machine learning algorithms, such as artificial neural networks (Firth et al., 2003; Collister and Lahav, 2004; Li et al., 2006, and references therein).

Although photometric surveys can provide us with large samples of galaxy clusters, the uncertainty in the determination of redshifts by using photometry is larger compared to spectroscopy (Connolly et al., 1995; Fernández-Soto et al., 2001; Blake and Bridle, 2005; Arnalte-Mur et al., 2009). The precision of photometric redshifts are also dependent on magnitude and spectral type. However it is a common notion to provide photometric redshift errors as a function of redshift only, through a relation like $\sigma_z = \sigma_{(z=0)} \times (1+z)$. The photometric redshift uncertainties in upcoming surveys are expected to be within $0.03 < \sigma_z/(1+z) < 0.05$ for galaxies and within $0.01 < \sigma_z/(1+z) < 0.03$ for clusters (Ascaso et al., 2015). Ideally, the error on the cluster redshift should scale proportionally to ${N_{mem}}^{-1/2}$ (where N_{mem} refers to the members of the cluster), therefore for clusters with 10 detected members the error would be reduced approximately by a factor of 3; but of course contamination from non-member galaxies will affect the redshift estimate and practically the photometric uncertainty becomes $\sigma_z \sim \frac{\sigma_{(z=0)}}{2} \times (1+z)$.

In a realistic observational scenario, we expect to have catastrophic failures as it happens for galaxy samples. Catastrophic failures are those redshifts that are found well outside the scatter existing between z_{spec} and z_{phot}, i.e. they usually have photometric redshifts that are $> 3\sigma$ away from z_{spec}. An example of catastrophic failures from photometric redshifts of galaxies is shown in Figure 6.1. All those redshifts that lie outside the two grey lines denote the catastrophic failures, and they can arise either due to false photometric results or even due to false spectroscopic results. Fernández-Soto et al. (2001) explained in detail about the possible occurrence of incorrect redshift measurements from spectroscopy which can also lead to catastrophic failures. But in the case of galaxy clusters, we do not expect to have catastrophic failures, as all galaxies of the cluster are not expected to have the same redshift deviation and we will therefore not consider this point.

In this thesis we would like to analyse how photometric redshift errors, in particular, affect the two-point correlation function, and to what extent it can be recovered. For this study, we generate photometric redshifts typical of what we expect from photometric redshift galaxy catalogues from our simulated cluster catalogue assuming a Gaussian distribution with a known dispersion, ignoring the dependence on mass.

For example, the ongoing Dark Energy Survey aims to have a sky coverage of 5000 deg^2 of the southern sky in five different optical filters to get detailed information about each and every individual galaxy. The survey aims to cover galaxies with a photometric accuracy of $\sigma_z/(1+z) = 0.07$ out to $z = 1$ (The Dark Energy Survey Collaboration, 2005), which roughly translates into a photometric accuracy of $\sigma_z/(1+z) = 0.02$ for clusters. Future surveys such as LSST (Ivezic et al., 2008; LSST Dark Energy Science Collaboration, 2012) and Euclid (Laureijs et al., 2011, 2014) are expected to provide accurate photometric redshifts

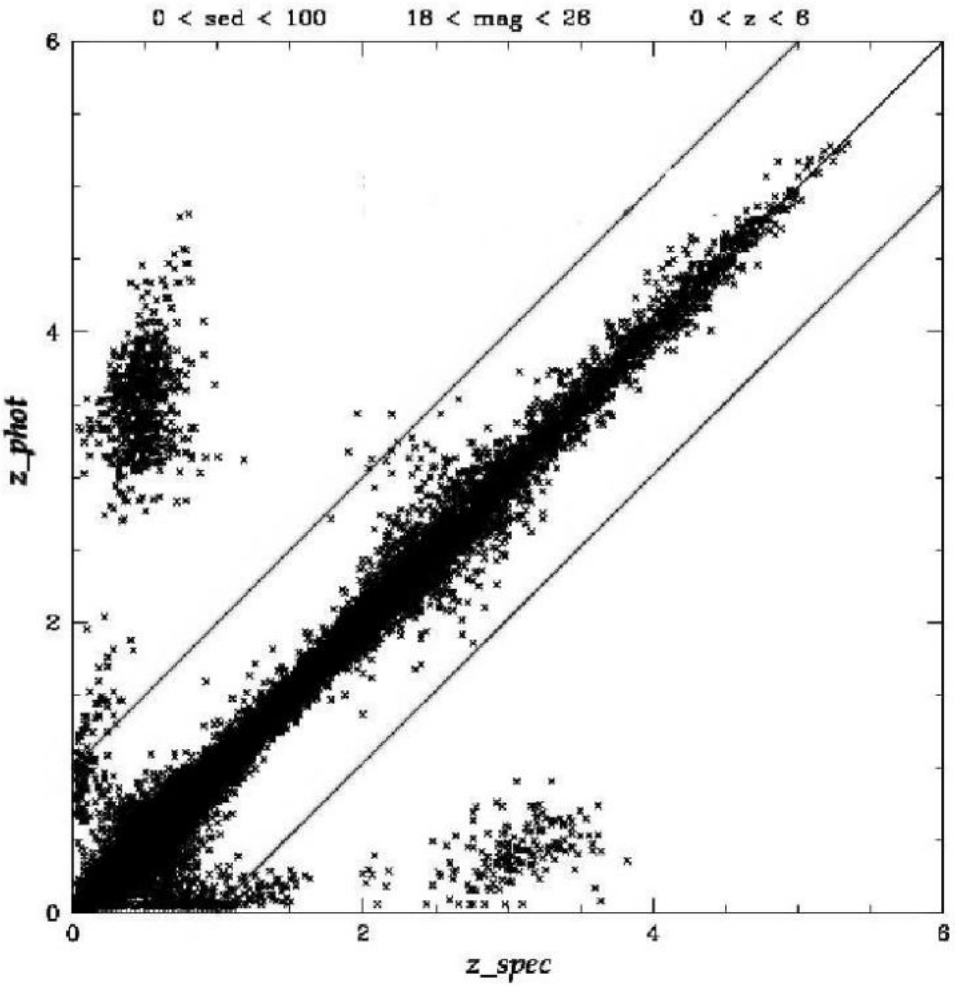

Figure 6.1: Spectroscopic redshifts vs photometric redshifts of galaxies taken from LePhare simulations with a 9-filter set. The grey lines show the borders within which the relation $|z_{spec} - z_{phot}| < 1$ holds true, all those redshifts samples outside these lines denote the catastrophic failures. Image credits: Sun et al. (2009)

on an extended redshift range. The Euclid Wide Survey requirement for galaxy photometric redshifts are $\sigma_z/(1+z) < 0.05$ and goals are $\sigma_z/(1+z) < 0.03$ (Laureijs et al., 2011). For comparison, $\sigma_z/(1+z) = 0.001$ corresponds to the requirement for the Euclid spectroscopic redshift error.

Thus, to span the typical uncertainties on cluster redshift estimates expected in the context of upcoming large surveys, we build five mock samples with errors $\sigma_{(z=0)} = \sigma_z/(1+z_c) = 0.001, 0.005, 0.010, 0.030, 0.050$. From the original light-cone catalogue, we extract mock cluster samples with cosmological redshifts in a given range of masses and redshifts and use them to generate out photometric redshifts; these are assigned to each cluster by random extraction from a Gaussian distribution with mean equal to the cluster cosmological redshift

and standard deviation equal to the assumed photometric redshift error of the sample.

6.2.2 Recovering the real-space correlation function: Deprojection method

The use of photometric redshifts affects the two-point correlation in two ways:

1. The derived distances have large errors that cause a damping of the clustering strength.
2. The errors only affect the line of sight distance (π) and not the transverse plane (r_p). So correlation is lost only in one direction, which destroys isotropy.

To show an example of the degree of uncertainty that will exist in the determination of distances from photometric redshifts we plot in Figure 6.2 a projected plot of clusters from our simulations. Distances are separated into two planes, i.e. the line of sight plane (π) and the across the line of sight plane (r_p). We first plot them with distances inferred from cosmological redshifts and then do so for distances inferred from photometric redshifts. It can be seen from Figure 6.2 that clustering seen in real-space diminishes in photo-z space. One can also notice that as the error on the photometric redshift increases, the more the clustering is diminished. Here we have to keep in mind that the number of clusters seen in each panel are the same and that the degradation in clustering gives us the look as though we have lost a few clusters.

So the Landy & Szalay estimator as defined by equation 3.5 can no longer be used. So to recover the real-space correlation function from photometric redshifts we will take into account separately the line of sight π and the transverse r_p components of the two-point correlation function and apply the deprojection method (Arnalte-Mur et al., 2009; Marulli et al., 2012). The method is based on Davis and Peebles (1983) and Saunders et al. (1992). Pairs are counted at different separations parallel (π) and perpendicular (r_p) to the line of sight and what we calculate is $\xi(r_p, \pi)$ as we have seen in Section 3.2. The projected correlation function can be derived from $\xi(r_p, \pi)$ by:

$$w_p(r_p) = \int_{-\infty}^{+\infty} \xi(r_p, \pi) d\pi \tag{6.1}$$

The projected correlation function $w_p(r_p)$ (Farrow et al., 2015) is related to the real-space correlation function $\xi(r)$ by Equation 6.2:

$$w_p(r_p) = 2 \int_{r_p}^{\infty} r dr \xi(r) (r^2 - r_p^2)^{-1/2} \tag{6.2}$$

which can be inverted to obtain the real-space correlation function:

$$\xi(r) = \frac{-1}{\pi} \int_{r}^{\infty} w'(r_p) (r_p^2 - r^2)^{-1/2} dr_p \tag{6.3}$$

Theoretically, the upper limits of integration are infinite, but in practice we need to choose finite values both in Equation 6.1 and Equation 6.3 which then become:

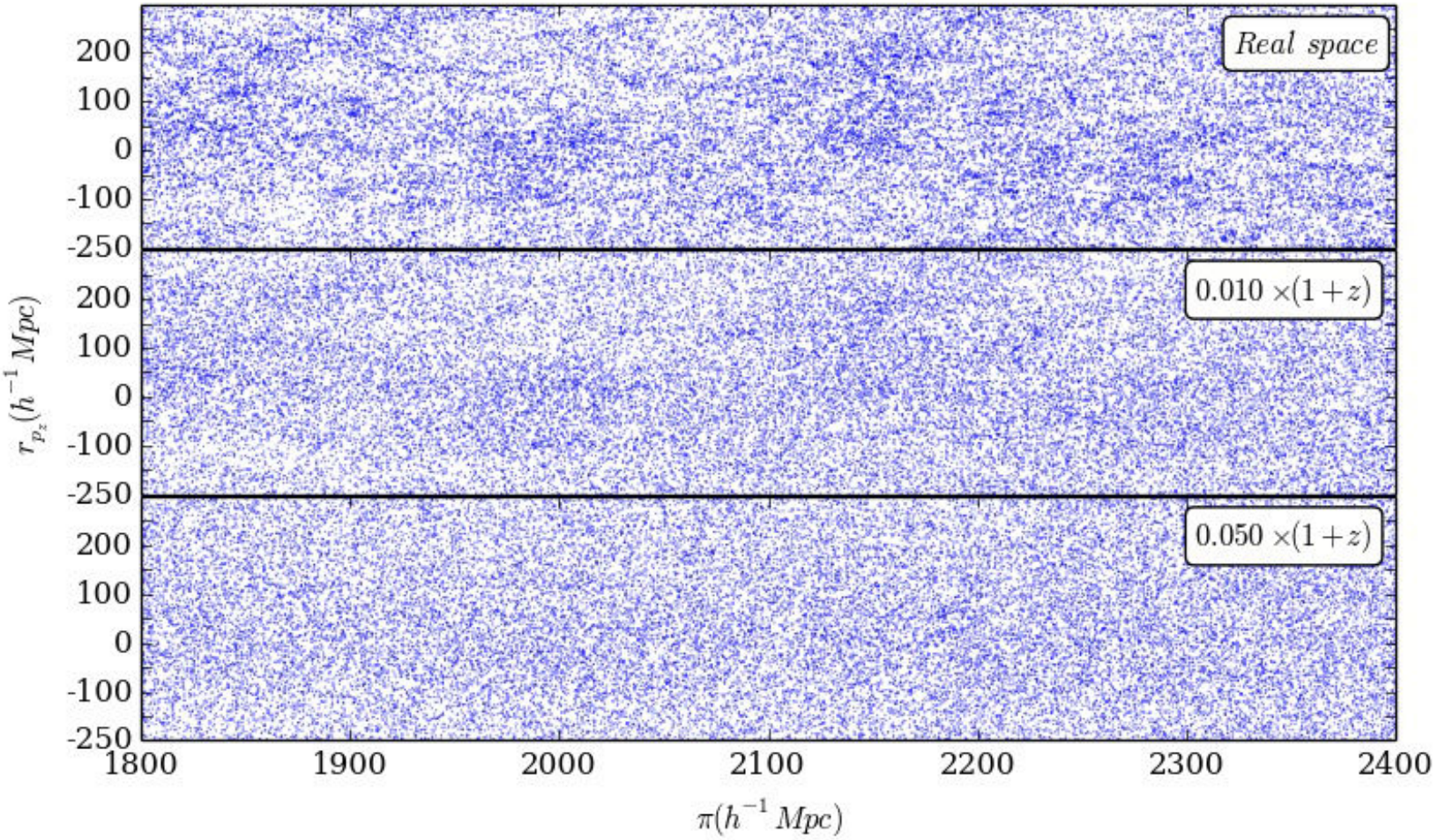

Figure 6.2: The projected view of a sub-sample of the haloes from the simulation with distances inferred from cosmological redshifts compared with the same calculated using photometric redshifts of a given uncertainty. *Top panel:* The real-space clustering, i.e. distances inferred from cosmological redshifts. *Middle panel:* Distances inferred from photometric redshift with an uncertainty of $\sigma_z = 0.010 \times (1 + z_c)$. *Bottom panel:* Distances inferred from photometric redshift with an uncertainty of $\sigma_z = 0.050 \times (1 + z_c)$. It can clearly be seen that as the photometric uncertainty increases, clusters that were clearly distinguished in real-space are not so clearly distinguished in photo-z space.

$$w_p(r_p, \pi_{max}) = \int_0^{\pi_{max}} \xi(r_p, \pi) d\pi \tag{6.4}$$

and

$$\xi(r) = \frac{-1}{\pi} \int_r^{r_{p_{max}}} w'(r_p)(r_p^2 - r^2)^{-1/2} dr_p \tag{6.5}$$

where π_{max} and $r_{p_{max}}$ refer respectively to the maximum line of sight separation and the maximum transverse separation.

Given that above a certain value of π, pairs are uncorrelated and $\xi(r_p, \pi)$ drops to zero, it is possible to find an optimal choice for π_{max}. This will be explained in detail in Section 6.2.5.1. We estimate the real-space correlation function following the method of Saunders et al. (1992). We use a step function to calculate $w_p(r_p)$, where $w_p(r_p) = w_{p(i)}$ in the logarithmic interval centred on $r_{p(i)}$, and we sum up in steps using the equation:

$$\xi(r_{p(i)}) = \frac{-1}{\pi} \sum_{j \geq i} \frac{w_{p(j+1)} - w_{p(j)}}{r_{p(j+1)} - r_{p(j)}} ln \left(\frac{r_{p(j+1)} + \sqrt{r_{p(j+1)}^2 - r_{p(i)}^2}}{r_{p(j)} + \sqrt{r_{p(j)}^2 - r_{p(i)}^2}} \right) \tag{6.6}$$

Assuming that the correlation function follows a perfect power–law, $w_p(r_p)$ is given by the formula:

$$w_p(r_p) = r_p \left(\frac{r_0}{r_p} \right)^{\gamma} \frac{\Gamma(\frac{1}{2})\Gamma(\frac{\gamma-1}{2})}{\Gamma(\frac{\gamma}{2})} \tag{6.7}$$

where Γ is the Euler's gamma function.

Once we have used the deprojection method to recover the real-space two-point correlation function, we then fit it using the power-law as defined by equation 3.13. We also fit the projected correlation function obtained, using equation 6.7. The results of the fit and the values obtained will be discussed in forthcoming sections.

In Figure 6.3 we plot the photometric redshifts we have generated with different uncertainties along with the cosmological redshifts. It can be seen that as we increase the redshift uncertainty, the scatter increases.

6.2.3 Photo-z selection

The mean relation between photometric and cosmological redshift and its dispersion is known and we will compare the catalogues in photometric and cosmological redshift-space respectively. As mentioned in Crocce et al. (2011), doing the selection in a top-hat photometric redshift window and in a top-hat cosmological redshift window with the same boundaries is not equivalent. Figure 6.4 compares the distribution in cosmological redshift of the clusters

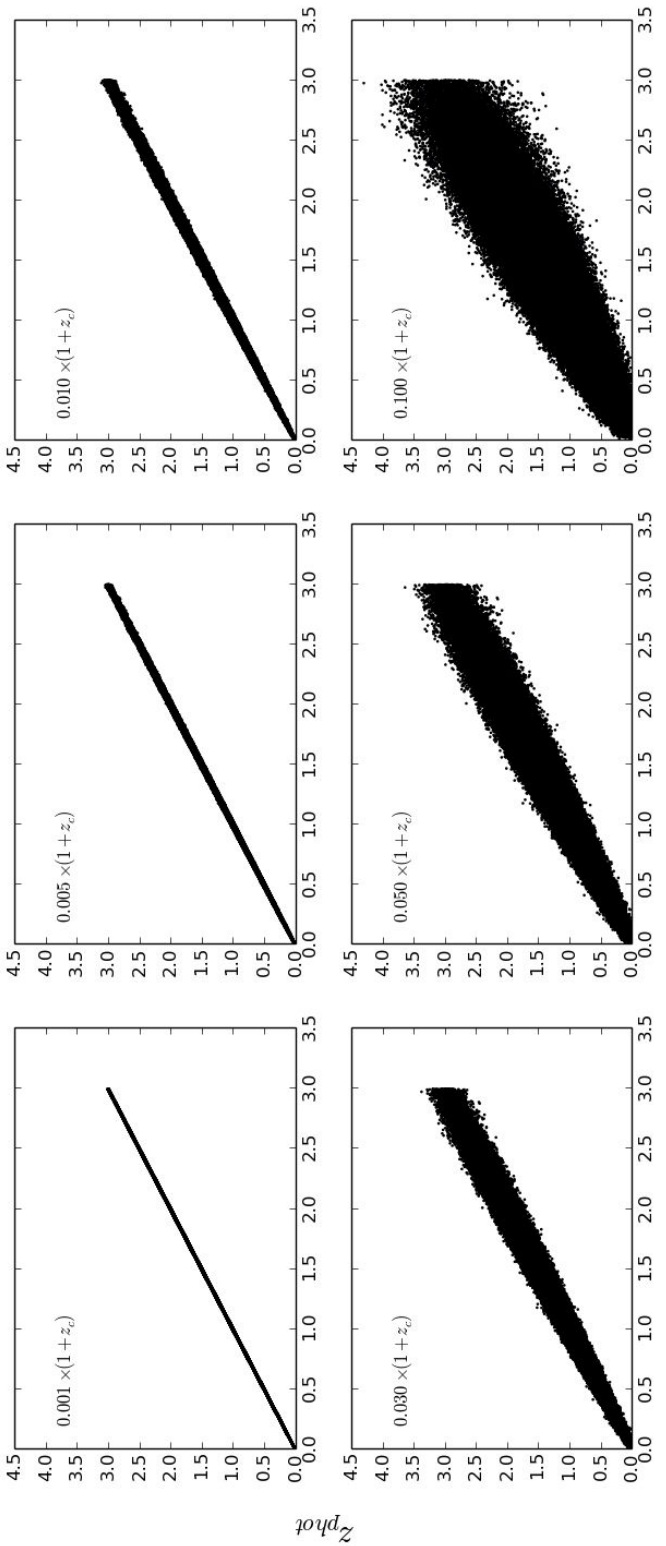

Figure 6.3: Cosmological redshifts of the clusters vs the photometric redshifts with different values of uncertainties associated. It can be seen that the scatter increases with photometric uncertainty.

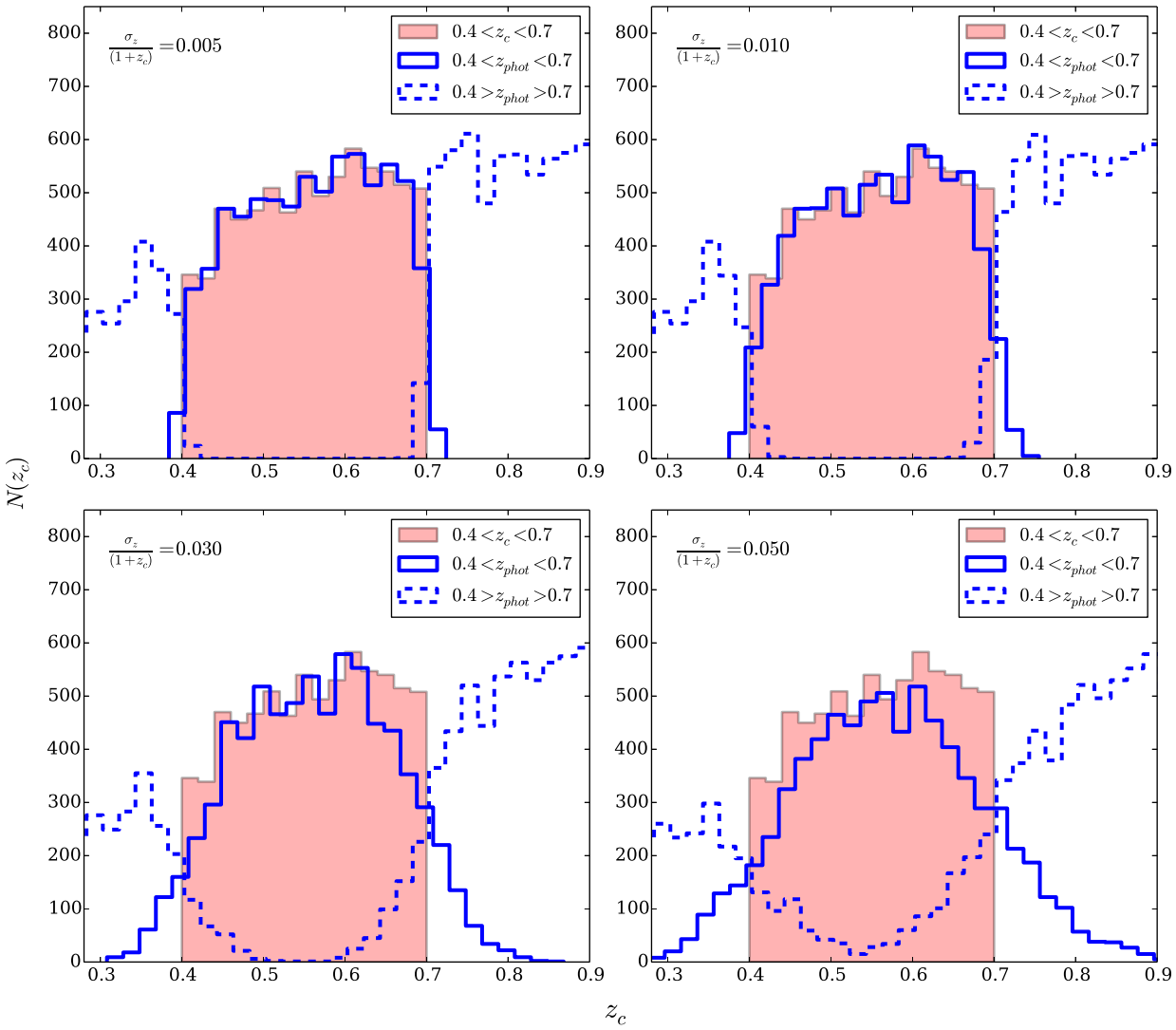

Figure 6.4: Distribution of clusters selected in the top-hat cosmological redshift window compared with the clusters selected in the top-hat photometric redshift window. Filled histograms correspond to distribution of clusters as a function of cosmological redshift when the top-hat selection is done using the cosmological redshift within the range $0.4 < z < 0.7$. Solid blue lines correspond to distribution of clusters as a function of cosmological redshift when the top-hat selection is done using the different photometric uncertainties we have used ($\sigma_z/(1+z_c)$ = 0.005,0.010,0.030 and 0.050) with the range $0.4 < z < 0.7$ and the dashed blue lines correspond to the outliers, i.e. distribution of clusters as a function of cosmological redshift when the top-hat selection is done using photometric redshifts outside the range $0.4 < z < 0.7$

selected in the top-hat cosmological redshift window $0.4 < z_c < 0.7$ (given by the filled histogram), the clusters selected by the top hat photometric redshift window $0.4 < z_{phot} < 0.7$ (given by the solid blue line) and the clusters for which the photometric redshifts are outside the slice limits [0.4,0.7] (outliers, given by the dashed blue line) for four of our photometric samples. The distribution in cosmological redshift $N(z_c)$ of the objects selected by the top-hat z_{phot} window is broader than that selected by the top-hat z_c window. When performing the selection in z_{phot} window rather than in z_c window, a fraction of clusters with z_c will be included outside these slice limits but with z_{phot} within the slice limits [0.4,0.7]. Thus they result as contaminants. A fraction of clusters with z_c within the slice limits [0.4,0.7] but z_{phot} outside [0.4,0.7] will be lost. This effect increases with the photometric redshift uncertainty. The fraction of contaminating and missing clusters depends on the photometric redshift uncertainty and also on the $N(z)$ distribution.

We calculate the fraction of common objects between the top hat z_{phot} and z_c selections for the different σ_z and redshift windows considered. It varies from 99% to 70% for samples with $\sigma_z/(1+z_c) = 0.001$ (at $z \approx 0.1$) to $\sigma_z/(1+z_c) = 0.050$ (at $z \approx 1.3$) respectively. Only the samples with $\sigma_z/(1+z_c) = 0.050$ and above a redshift of $z > 0.7$ have less than 80% objects in common, as we know that the photo-z error scales as $\sigma_z = \sigma_{(z=0)} \times (1+z_c)$. In our case there are four samples that fall in this category (can be seen numerically in the fourth panel of Table 6.1). For all the other samples we choose, the average fraction of common clusters is more than 80%. To calculate the effect of $N(z)$ on contaminated and missing clusters, we calculate both the mean and median redshift for the photometric redshift samples we have. It can be seen from Table 6.4 that both the mean and the median redshift do not vary much when compared to the same of the cosmological redshift sample. The percentage of contaminants for each redshift slice and given photometric uncertainty along with the $N_{clusters}$ in z_c and z_{phot} window and the number of common clusters is mentioned in Table 6.1. From Table 6.1, it can be seen that the average fraction of common clusters is more than 80% for all the samples considered.

6.2.4 Weighting scheme for photometric redshifts

To overcome this effect of the top-hat photo-z redshift selection we tried to adopt a weighting scheme. To calculate the correlation function of these objects with photometric redshifts, each object is assigned a weight. This weight $W(z_{phot})$ is assigned according to the formula:

$$W(z_{phot}) = \int p(z_{phot}|z_c)dz_c = \int_{z_{c_{min}}}^{z_{c_{max}}} \frac{e^{\frac{-(z_c - z_{phot})^2}{2\sigma^2(1+z_c)^2}}}{\sqrt{2\pi}\sigma(1+z_c)} dz_c \times N(z) \tag{6.8}$$

where $\sigma \rightarrow$ uncertainty and $N(z) \rightarrow$ the redshift distribution.

The weight assigned is defined as the probability for this object to have a photometric redshift with a given uncertainty, given the cosmological redshift. The integral is performed within the minimum and maximum limits of the cosmological redshift sample considered. It

Redshift range	Clusters in z_c window	Clusters in z_{phot} window	Common	Uncommon	% contaminants
		$\sigma_z = 0.005 \times (1 + z_c)$			
0.1< z <0.4	3210	3214	3160	50	1.55
0.4< z <0.7	7301	7310	7162	139	1.90
0.7< z <1.0	8128	8088	7933	195	2.39
1.0< z <1.3	5963	6001	5842	121	2.02
1.3< z <1.6	3365	3356	3252	113	3.35
1.6< z <2.1	2258	2251	2197	61	2.70
		$\sigma_z = 0.010 \times (1 + z_c)$			
0.1< z <0.4	3210	3216	3115	95	2.95
0.4< z <0.7	7301	7338	7042	259	3.54
0.7< z <1.0	8128	8095	7745	383	4.71
1.0< z <1.3	5963	5973	5676	287	4.81
1.3< z <1.6	3365	3350	3144	221	6.56
1.6< z <2.1	2258	2239	2133	125	5.53
		$\sigma_z = 0.030 \times (1 + z_c)$			
0.1< z <0.4	3210	3196	2884	326	10.15
0.4< z <0.7	7301	7396	6492	809	11.08
0.7< z <1.0	8128	8053	6972	1156	14.22
1.0< z <1.3	5963	5880	4958	1005	16.85
1.3< z <1.6	3365	3388	2712	653	19.40
1.6< z <2.1	2258	2251	1922	336	14.88
		$\sigma_z = 0.050 \times (1 + z_c)$			
0.1< z <0.4	3210	3205	2647	563	17.53
0.4< z <0.7	7301	7433	5906	1395	19.10
0.7< z <1.0	8128	7937	6153	1975	24.29
1.0< z <1.3	5963	5859	4294	1669	27.98
1.3< z <1.6	3365	3352	2248	1117	33.19
1.6< z <2.1	2258	2277	1717	541	23.95

Table 6.1: The number of clusters in a given redshift range for z_c and z_{phot} with mass cut $M_{halo} > 5 \times 10^{13}\ h^{-1}\ M_{\odot}$. The z_{phot} uncertainties are $\sigma_z/(1 + z_c) = 0.005, 0.010, 0.030$ and 0.050. (1) Redshift range, (2) number of clusters in z_c window, (3) number of clusters in z_{phot} window, (4) common clusters, (5) uncommon clusters and (6) the percentage of contaminants are quoted.

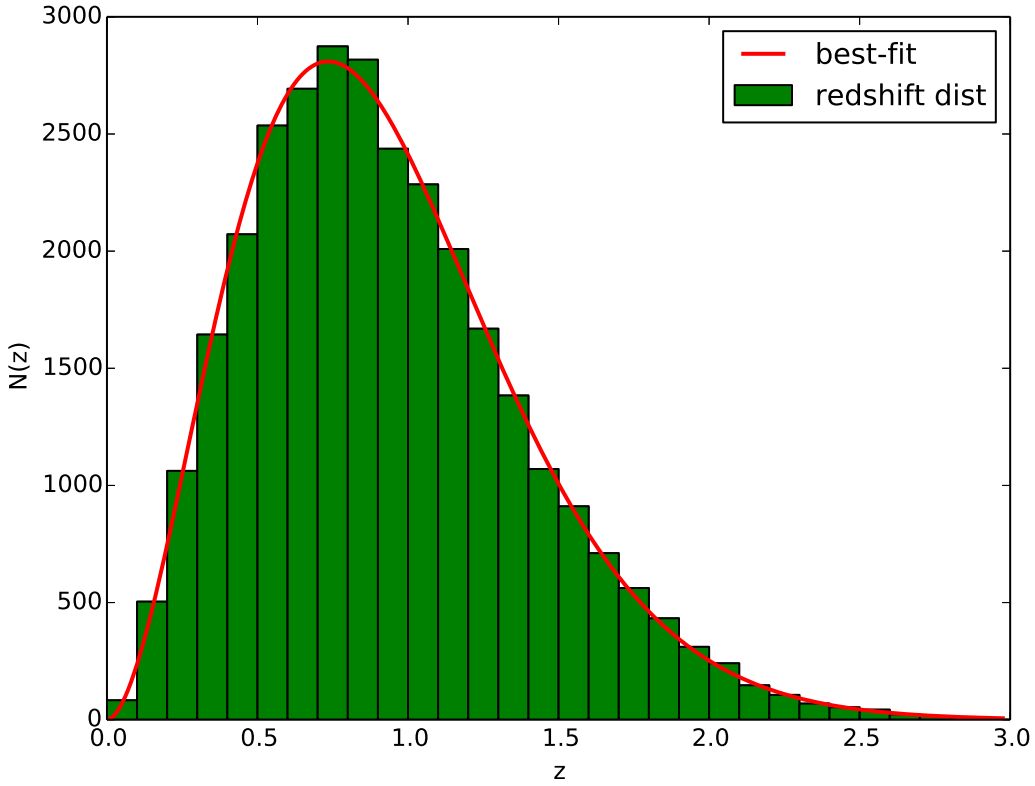

Figure 6.5: The fit made to the redshift distribution of the sample with a photometric uncertainty of $0.01 \times (1 + z_c)$

can be seen that the redshift distribution $N(z)$ is present in Equation 6.8. So before we can calculate the above integral to get the weights, we fit the $N(z)$ distribution to get the best-fit parameters, which are then used in calculating the PDF. The fit of the $N(z)$ distribution done for the photometric redshift sample with an uncertainty of $0.01 \times (1 + z_c)$ is seen in Figure 6.5. Also shown in Figure 6.6 is the final weights that are assigned to our reference sample with $\sigma_z = 0.01 \times (1 + z_c)$ within the arbitrary redshift range $0.4 < z_c < 0.7$.

It can be seen from Figure 6.6 that clusters with a z_{phot} within $0.4 < z_{phot} < 0.7$ are assigned weight ~ 1.0 and clusters that are outside this limit are assigned a weight that is < 1.0, which gradually decreases to zero. Once the weights have been assigned to all our clusters according to their respective photometric uncertainties, we perform several tests to check if the weights have been assigned correctly (explained in Section 6.2.4.1) and then calculate the two-point correlation function using these "weighted" clusters.

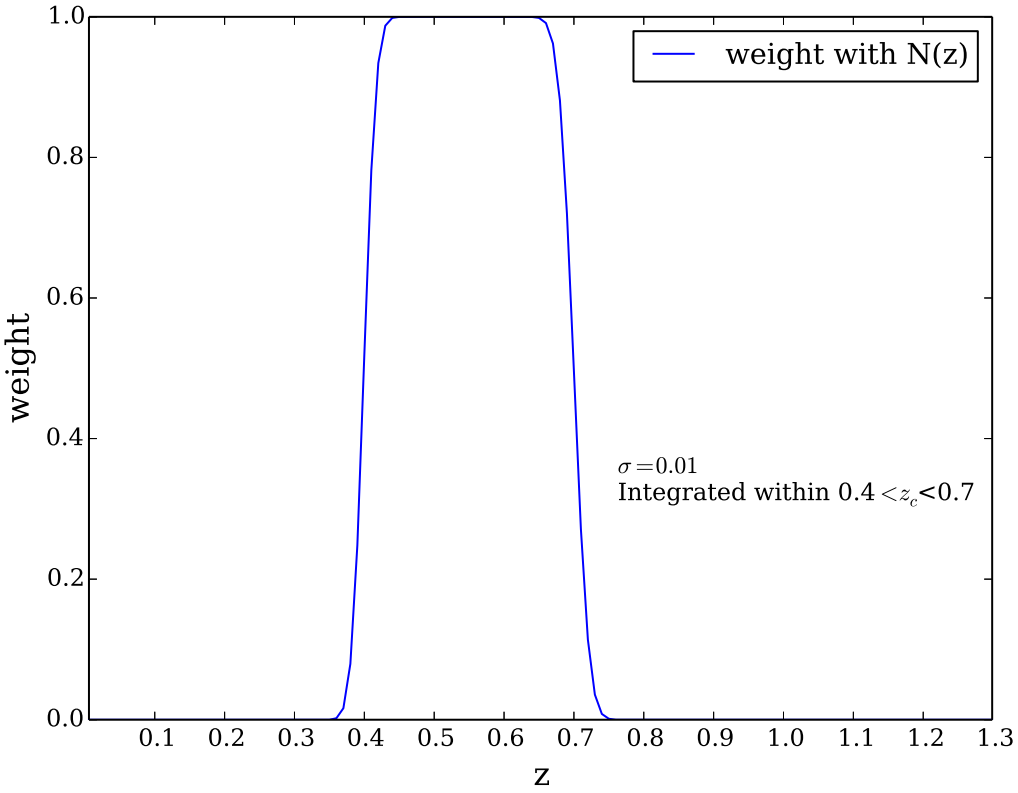

Figure 6.6: Weights assigned to photometric redshifts with an uncertainty of $0.01 \times (1 + z_c)$ within the redshift range $0.4 < z < 0.7$. It can be seen that all the redshifts between 0.4 and 0.7 are assigned a weight which is ~ 1.0 and all those outside are assigned a much lesser weight.

6.2.4.1 Tests performed before calculating the two-point correlation function using weights

Before we go ahead in calculating the two-point correlation function, we test if the weights have been assigned properly to each photometric redshift. The test includes the comparison of the $N(z)$ distribution of both z_{spec} and z_{phot} within given minimum and maximum limits.

The method followed is:

1. Plot the $N(z_c)$ distribution for $z_{min} < z_c < z_{max}$.
2. Plot the $N(z_{phot})$ distribution for $z_{min} < z_{phot} < z_{max}$ (with z_{min} and z_{max} being the same as above).
3. Plot the $N(z_c)$ distribution for $z_{min} < z_{phot} < z_{max}$ (with z_{min} and z_{max} being the same as above).

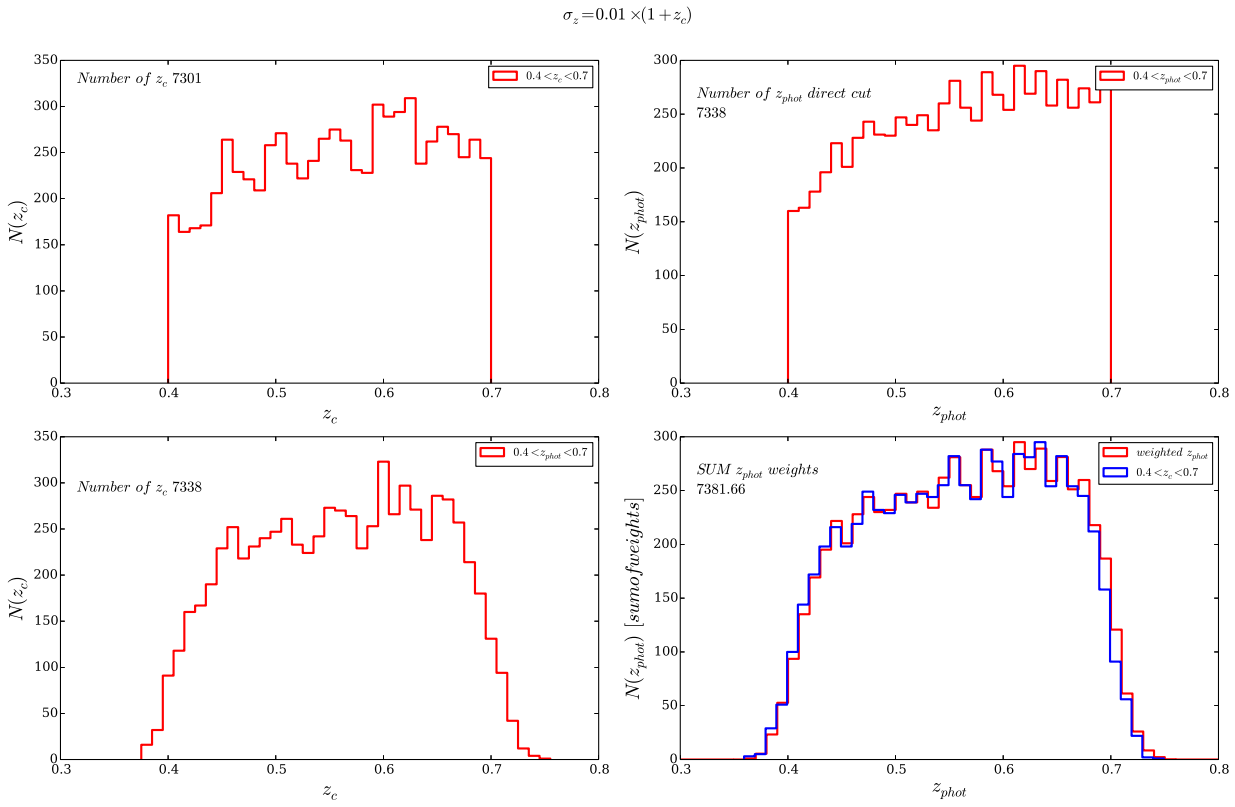

Figure 6.7: $N(z)$ of z_c and z_{phot} distributions for the data catalogue. Photometric redshifts have an uncertainty of $0.01 \times (1 + z_c)$

4. Plot the $N(z_{phot})$ distribution for $z_{min} < z_c < z_{max}$ (with z_{min} and z_{max} being the same as above).

5. Plot the $N(z_{phot})$ weighted distribution, with each bin containing the sum of $W(z_{phot})$ of the objects, and compare the same with the above $N(z_{phot})$ distribution for $z_{min} < z_c < z_{max}$.

The above test is repeated for the random catalogue constructed. The results of the above test for $\sigma_z = 0.01 \times (1 + z_c)$ within $0.4 < z_c < 0.7$ is seen in Figure 6.7 for the data catalogue. Now we would like to analyse each sub-plot of Figure 6.7 one at a time. Plotted are the $N(z_c)$ and $N(z_{phot})$ distributions in the top panel of Figure 6.7. Then we consider all those cosmological redshifts for which the corresponding photometric redshift is within the minimum and maximum limit tested ($0.4 < z < 0.7$ in this case) and plot the $N(z_c)$ distribution which is shown in the first sub-plot of the second panel. Then we consider all those photometric redshifts for which the cosmological redshift is within the minimum and maximum limit tested and plot the $N(z_{phot})$ distribution (shown as the red line), along which we plot the sum of the weights assigned to our photometric redshift sample (shown in blue). It

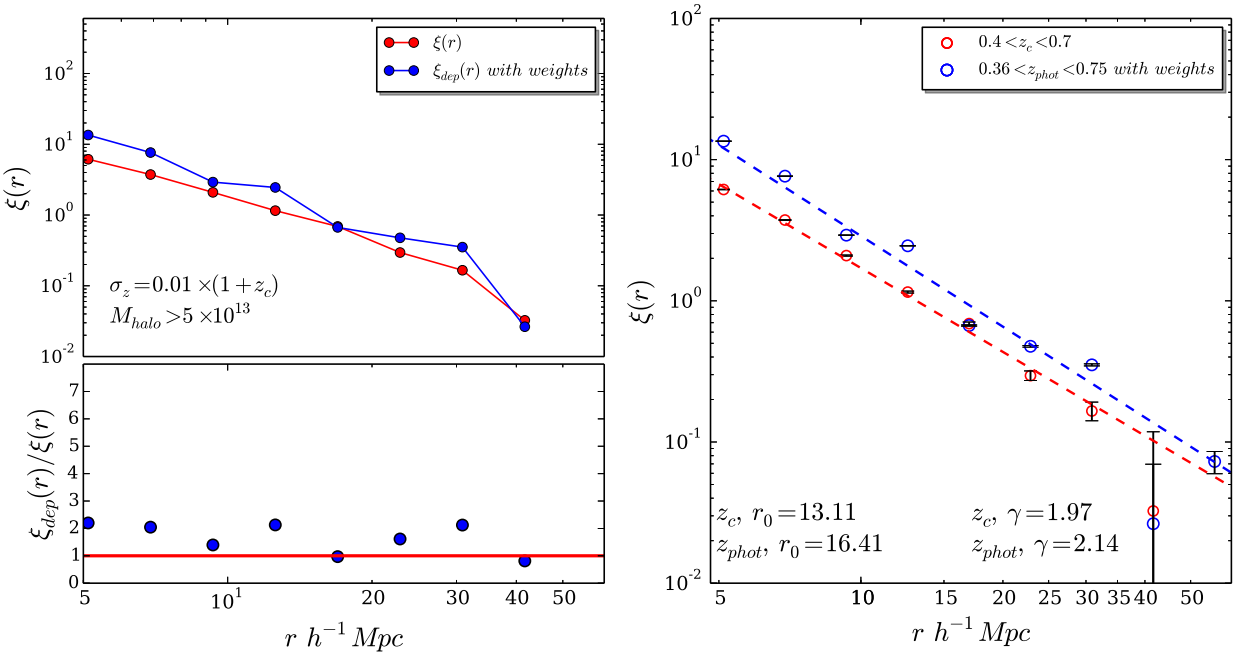

Figure 6.8: *Left:* The real-space correlation function (shown in red) along with the recovered deprojected correlation function (shown in blue) for the sample with a mass cut of $M_{halo} > 5 \times 10^{13}$ and within the redshift range $0.4 < z < 0.7$. *Right:* The power-law fit performed on the correlation function using Equation 3.13.

can be seen that the sum of the weights closely resembles the $N(z_{phot})$ distribution of those clusters for which z_c is within $0.4 < z_c < 0.7$. Using this test we can confirm that the weights are properly assigned to each photometric redshift.

6.2.4.2 Two-point correlation function from weighted photometric redshifts

We calculate the two-point correlation function by including the weights given to each photometric redshift as defined by Equation 6.8. For our tests, we choose an arbitrary redshift range $0.4 < z < 0.7$ and a mass cut of $M_{halo} > 5 \times 10^{13}\ h^{-1}\ M_\odot$ to ensure that we have enough clusters to be statistically significant. The recovered correlation function using weights is then compared with the real-space correlation function obtained from the cosmological redshift sample. The results of the same is shown in Figure 6.8 and it can be seen that by using weights defined in Equation 6.8, the recovered two-point correlation function is overestimated. The slope obtained from the recovered correlation function along with the correlation length is mentioned in the figure. We make use of Poisson error bars for the test, which more or less underestimate the errors on the $\xi(r)$ obtained. But we can clearly see that it still cannot explain the higher amplitude obtained for the recovered correlation function with weights.

As we have seen in Section 6.2.4.1, even though the sum of the weights for each photo-

metric redshift bin is similar to the $N(z_{zphot})$ for which z_c is within $0.4 < z_c < 0.7$ (as seen in Figure 6.7) the final result is overestimated. This we believe is due to the way in which the weights are taken into account when counting the pairs. The redshift range we are considering here is $0.4 < z < 0.7$, but as we can see from Figure 6.6 when assigning the weights, we are including clusters from outside this redshift range. There are a handful of clusters that are both less than 0.4 and greater than 0.7 that are coming into the final sample considered as it can be seen from Figure 6.6. We repeated the same analysis for other redshift slices along with different photometric redshift uncertainties. The final correlation function obtained using the weights always has an amplitude that is higher than the real-space correlation function obtained using cosmological redshift sample.

6.2.5 Real-space correlation function obtained from the deprojection method

As discussed in Section 6.2.3, doing the selection in a top-hat photometric redshift window and in a top-hat cosmological redshift window with the same boundaries is not equivalent. But at the same time as we can see from Table 6.1, the percentage of contaminants for each photometric redshift uncertainty considered varies from 1.5% to 25%. Only the samples with $\sigma_z/(1 + z_c) = 0.050$ and above a redshift of $z > 0.7$ have less than 80% objects in common. By choosing the same redshift boundaries in both the cosmological redshift sample and the photometric redshift sample, we believe that the final recovered clustering should not be affected by a huge margin. So we recover the real-space correlation function from all our photometric redshift samples using the method of deprojection as mentioned in Section 6.2.2 within the same redshift limits as used for our cosmological redshift sample.

For the test of the deprojection method, the parent sample we use is within the redshift range $0.4 < z < 0.7$ and with a mass cut above $M_{halo} > 5 \times 10^{13}\ h^{-1}\, M_{\odot}$ to include enough objects to be statistically significant.

6.2.5.1 Selecting the integration limits

As we have seen in Section 6.2.2, to recover the real-space correlation function from photometric redshifts, $\xi(r_p, \pi)$ is calculated on a grid with logarithmically spaced bins both in r_p and π. Theoretically the integral limits in Equation 6.1 and 6.2 are infinity, but while calculating the function we need fix a maximum value for both r_p and π. The maximum value of r_p depends on the survey dimension in the transverse plane. In the redshift range $0.4 < z < 0.7$, the maximum separation across the line of sight direction in our light-cone is $\approx 500\ h^{-1}$Mpc. For the upper limit of integration in Equation 6.5 we fix a value $r_{p(max)} = 400\ h^{-1}$Mpc, corresponding to 80% of the maximum transversal separation. For higher redshift samples we are aware that the maximum separation across the line of sight increases, but we find that the value of 400 h^{-1}Mpc includes almost all correlated pairs without adding any noise. In the case of clusters where we have low statistics as compared to galaxy catalogues, the choice of

Table 6.2: Main parameters used for the analysis of the original catalogue and the 5 mock photometric redshift catalogues: (1) the redshift uncertainty, (2) the maximum values of π_{max} and (3) $r_{p(max)}$, (4) the values of $\Delta\xi$, (5) $\widehat{\Delta\xi}$. The range of scales r used for the fit is fixed at 5-50 Mpc.

Redshift uncertainty $\left(\frac{\sigma_z}{1+z_c}\right)$	π_{max} $(h^{-1}Mpc)$	$r_{p(max)}$ $(h^{-1}Mpc)$	$\Delta\xi$	$\widehat{\Delta\xi}$
0.000	50	400	0.028	0.031
0.001	60	400	0.042	0.052
0.005	130	400	0.055	0.055
0.010	300	400	0.065	0.063
0.030	400	400	0.091	0.080
0.050	550	400	0.148	0.109

the bin width must be taken into account, if not the Poisson noise will dominate.

For choosing the maximum line of sight distance we make use of a convergence test for each photometric redshift sample. Since higher photometric errors produce larger redshift-space distortions, a different value of π_{max} has to be fixed for each photometric redshift mock. We determine its value in the following way. We recover the real-space correlation function with the method described in Section 6.2.2, using increasing values of π_{max}. Initially the amplitude of $\xi_{dep}(r)$ is underestimated (when the π_{max} chosen is less than the convergence value) because many correlated pairs are not taken into account; it increases with increasing π_{max} up to a maximum value, beyond which it starts to fluctuate and noise starts to dominate. Applying this convergence test to each mock, we select the π_{max} value corresponding to the maximum recovered amplitude. For a larger photometric redshift uncertainty, the convergence value of π_{max} is larger compared to a lower photometric redshift uncertainty, so as to include all the correlated pairs along the line of sight direction. The value of π_{max} used for our parent sample is given in Table 6.2 along with $\Delta\xi$ and $\widehat{\Delta\xi}$ which are parameters that denote the quality of the recovery, which will be explained in the next section. It can be seen that π_{max} increases with the photometric redshift uncertainty, starting from $50h^{-1}$Mpc for the ideal zero-error sample and reaching 550 h^{-1}Mpc for the sample with $\sigma_z = 0.050 \times (1 + z_c)$. We have checked that by applying this method to the original light-cone with cosmological redshifts we recover its real-space correlation function.

6.2.5.2 The quality of the recovery

We use the deprojection method on all the five mock photometric samples we have created to obtain the deprojected correlation function ($\xi_{dep}(r)$) and then compare it with the results

obtained for the real-space correlation function $\xi(r)$ which is estimated directly from the ideal zero error simulation (cosmological redshifts used). The results of the comparison are shown in Figure 6.9.

It is clear that $\xi_{dep}(r)$ reproduces quite well $\xi(r)$, but shows increasing fluctuations with increasing σ_z. The ratio $\xi_{dep}(r)/\xi(r)$ is slightly smaller than 1 but within 1σ at all scales for all the mocks up to $\sigma_z/(1+z_c) = 0.05$ indicating that $\xi_{dep}(r)$ is not biased

The quality of the recovery is determined using $\Delta\xi$, an "average normalised residual" defined by Arnalte-Mur et al. (2009) as:

$$\Delta\xi = \frac{1}{N}\sum_i \left|\frac{\xi_{dep}(r_i) - \xi(r_i)}{\xi(r_i)}\right| \tag{6.9}$$

where r_i refers to the values in the i^{th} bin considered and $\xi(r_i)$ is the real-space correlation function.

In the case of real data, where z_c is not available, one can still calculate the quality of the recovery using the covariance matrix and is defined as:

$$\widehat{\Delta\xi} = \frac{1}{N}\sum_i \frac{\sqrt{C_{ii}}}{|\xi_{dep}(r_i)|} \tag{6.10}$$

wherein we use the covariance matrix that we have obtained using the jackknife resampling method mentioned in Equation 5.1.The values of $\Delta\xi$ and $\widehat{\Delta\xi}$ estimated in the range 5-50 h^{-1}Mpc, are listed in Table 6.2. The reason for choosing the lower limit of 5 h^{-1}Mpc is because the typical size of clusters range from 2-4 h^{-1}Mpc (Bahcall, 1996).

One can see from Table 6.2 that for the lowest photometric error considered, $\sigma_z/(1+z_c) = 0.001$, the real-space correlation function is recovered within 5%. For $\sigma_z/(1+z_c) = 0.005$ and $\sigma_z/(1+z_c) = 0.010$ it is recovered within 7%, within 9% for $\sigma_z/(1+z_c) = 0.030$ and finally within 15% for $\sigma_z/(1+z_c) = 0.05$.

One has to stress that the previous errors investigated are on the mean photometric redshift of the cluster, which is expected to be significantly lower than that of individual galaxies as it scales as $1/\sqrt{N}$, where N is the number of cluster members. When the redshift uncertainty on individual galaxies is $\sigma_z \approx 0.050\times(1+z_c)$, the redshift uncertainty on the cluster will become $\sigma_z \approx 0.01\times(1+z_c)$ for a poor cluster with $\approx 10-15$ members and $\sigma_z \approx 0.005\times(1+z_c)$, for a rich cluster with ≈ 100 members. This uncertainty will be reduced to $\sigma_z \approx 0.001\times(1+z_c)$, when spectroscopic redshifts will be measured for even a small number of cluster members (which will hopefully be the case for Euclid and LSST). We are therefore more likely in the case of the lowest uncertainties tested in this analysis in which the correlation function will be recovered well within $\approx 10\%$.

The best-fit parameters of the deprojected correlation functions are shown in Table 6.3. The fitting is performed with both a free and fixed slope $\gamma = 2.0$. The correlation length obtained for our 5 mock photometric samples is consistent within $\sim 1\sigma$ with the real-space correlation length $r_0 = 13.20\pm0.23$ h^{-1}Mpc and $r_0 = 13.16\pm0.17$ h^{-1}Mpc obtained for the z_c sample for $\xi(r)$ (free slope) and $\xi(r)$ (fixed slope) respectively. The best-fit r_0 obtained for

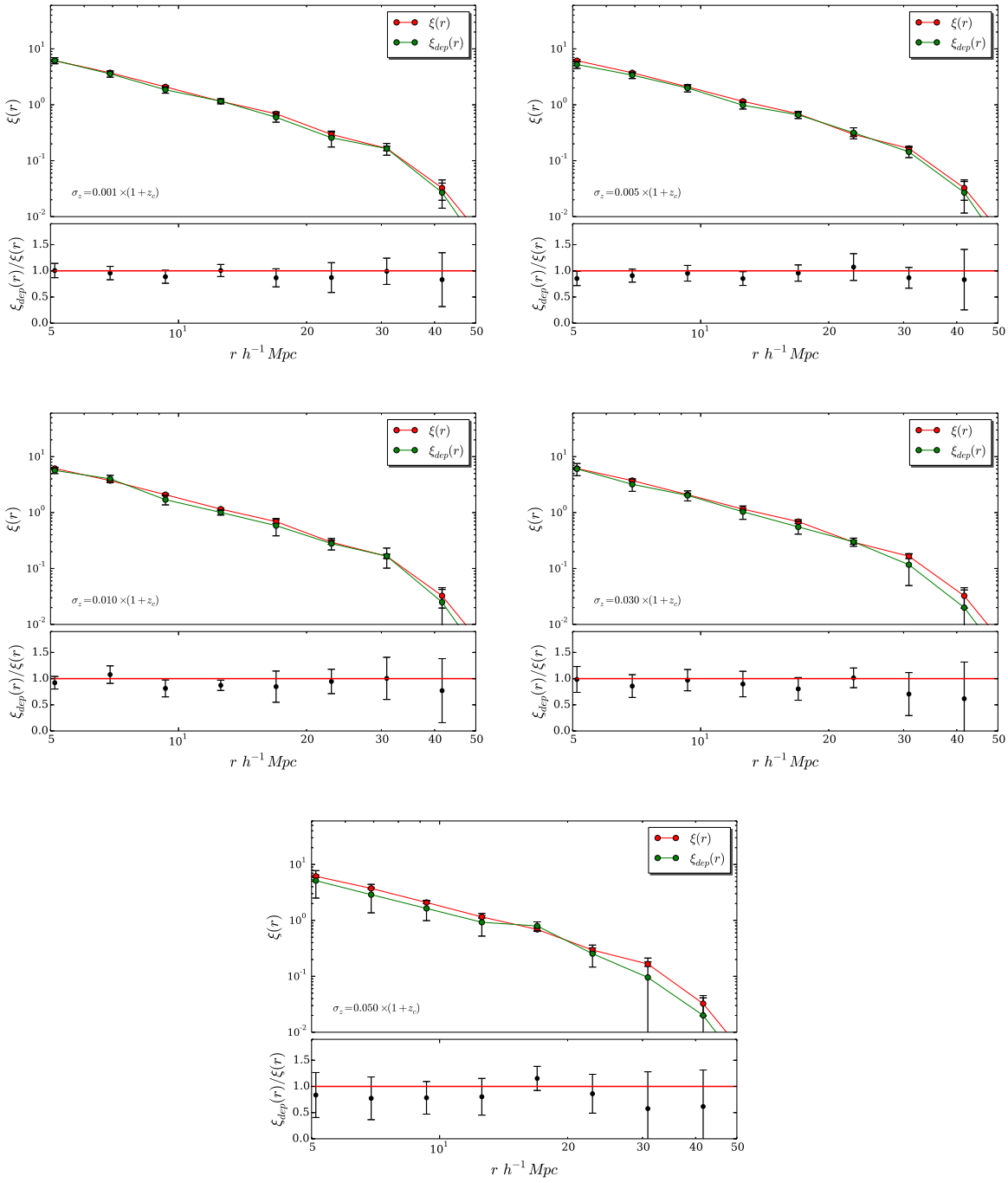

Figure 6.9: The recovered correlation function (*green line*) compared with the real-space correlation function (*red line*) for 5 mock photometric samples in the redshift range $0.4 < z < 0.7$, with increasing redshift uncertainty. Values of the best-fit parameters obtained are given in Table 6.2 and the quality of the recovery for each sample is given in Table 6.3.

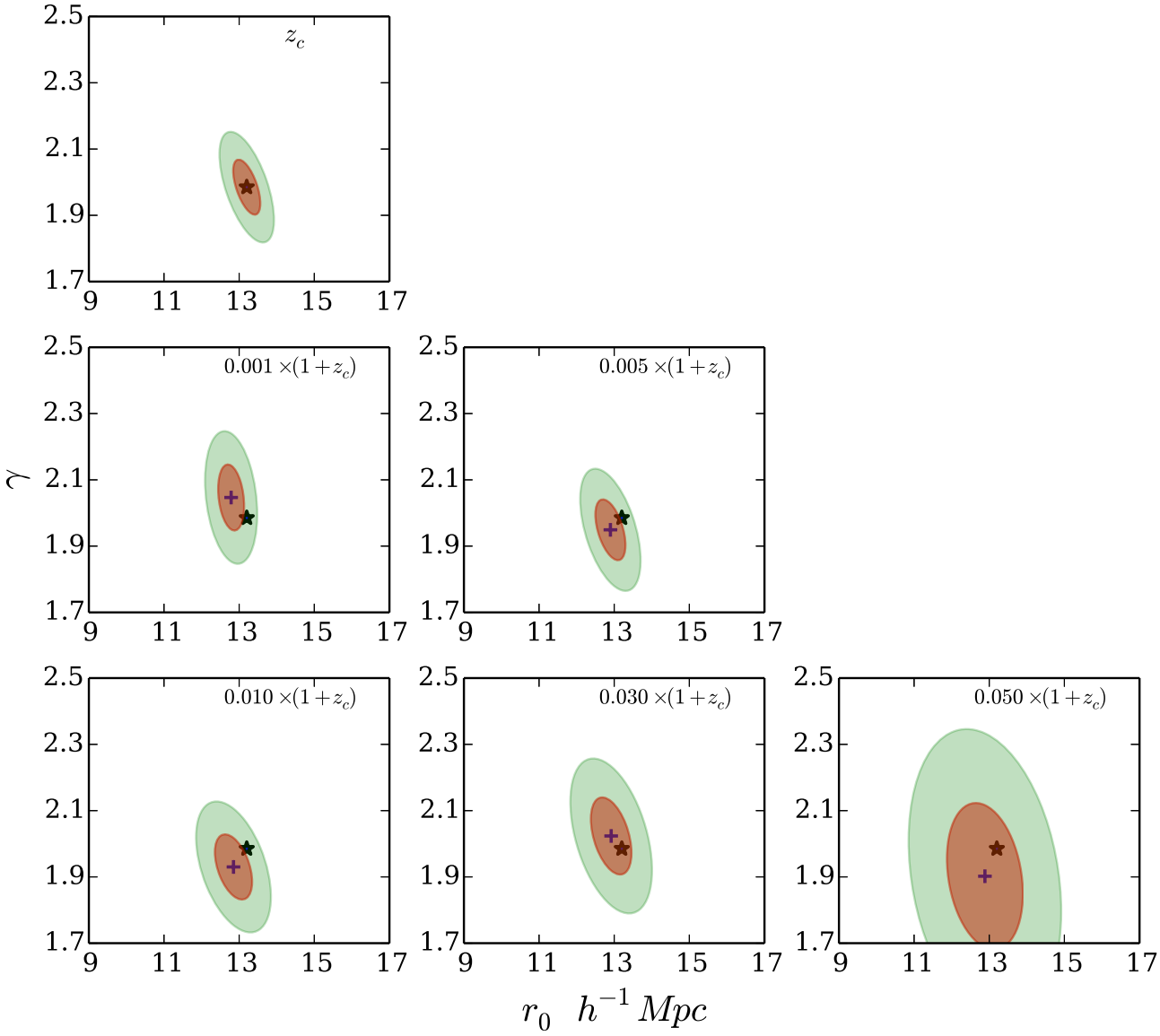

Figure 6.10: The 1 σ (shaded *brown*) and 3 σ (shaded *green*) error ellipses for the parameters r_0 and γ. *Top panel:* The original catalogue with cosmological redshifts *Central and bottom panels:* Mock catalogues with increasing photometric redshift errors. The solid star represents the center of the ellipse for the original catalogue, while the cross denotes the centres of the other ellipses.

this particular sample ($0.4 < z_c < 0.7$) seems to have a value that is always lower, regardless of the photometric uncertainty, when compared to the r_0 obtained for the true z_c sample. This is just a coincidence and is not always the case, as it can be seen for other samples with different redshift limits in the next section. When the slope is set free, direct comparison

Table 6.3: The best-fit parameters obtained for the real-space correlation function $\xi(r)$ of the original sample and the recovered deprojected correlation function $\xi_{dep}(r)$ for the mock photometric redshift samples. We quote the (1) redshift uncertainty, (2) the correlation length r_0, (3) slope γ. The mass cut used is $M_{halo} > 5 \times 10^{13}\ h^{-1}\ M_{\odot}$ and the fit range is fixed at 5-50 Mpc. The fits have been performed both with fixed (γ = 2.0) and free slope.

Redshift uncertainty $\left(\frac{\sigma_z}{1+z_c}\right)$	r_0 $(h^{-1}Mpc)$	γ
z_c	13.16±0.17	2.0 (*fixed*)
	13.20±0.23	1.97±0.05
0.001	12.82±0.17	2.0 (*fixed*)
	12.91±0.22	2.02±0.05
0.005	12.52±0.22	2.0 (*fixed*)
	12.89±0.26	1.94±0.06
0.010	12.33±0.28	2.0 (*fixed*)
	12.84±0.63	1.93±0.08
0.030	12.29±0.30	2.0 (*fixed*)
	12.91±0.72	2.02±0.12
0.050	11.73±0.65	2.0 (*fixed*)
	12.88±0.76	1.90±0.14

of r_0 between the samples cannot be made and so in Figure 6.10 we plot the 3 sigma error ellipses around the best-fit values of r_0 and γ for all the mocks. As expected, the errors on both r_0 and γ increase with the photometric uncertainty, but are always within $\sim 1\sigma$ with respect to the real space values.

We also applied the deprojection method for higher photometric redshift errors to test how far the method could be applied. It was found that from $\sigma_z/(1 + z_c) = 0.1$, the error on the recovery is very large and the recovered correlation function becomes biased.

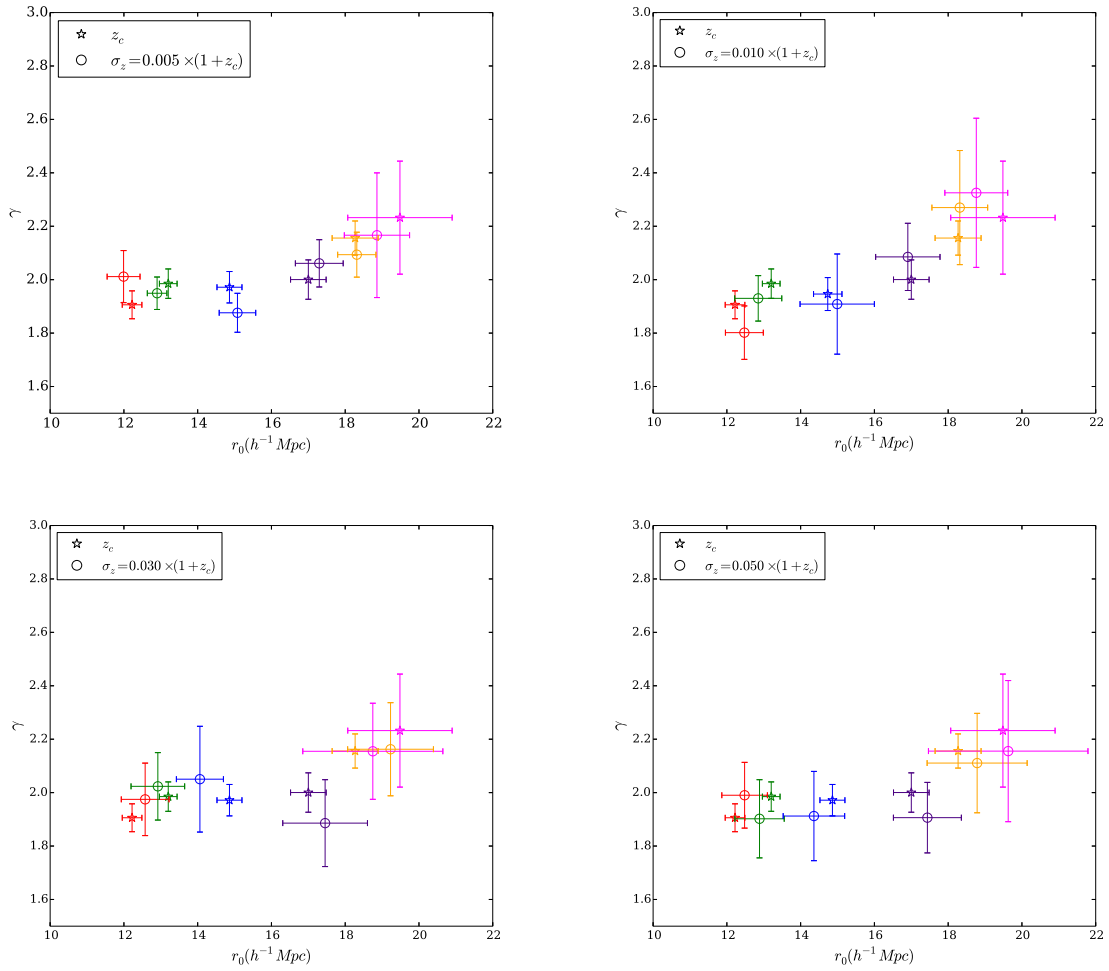

Figure 6.11: The evolution of r_0 and γ with redshift for clusters with a mass cut $M_{halo} > 5\times10^{13}\ h^{-1}\ M_\odot$ for samples with increasing redshift uncertainty ($\sigma_z/(1+z_c)$ = 0.005, 0.010, 0.030 and 0.050). The cosmological redshift sample is denoted with ☆ and the photometric redshift samples are denoted with ∘. *Red* $(0.1 < z < 0.4)$, *Green* $(0.4 < z < 0.7)$, *Blue* $(0.7 < z < 1.0)$, *Indigo* $(1.0 < z < 1.3)$, *Gold* $(1.3 < z < 1.6)$, *Magenta* $(1.6 < z < 2.1)$.

6.2.5.3 Recovering the redshift evolution of the correlation function from sub-samples selected using photometric redshifts

We check how accurately we can follow the redshift evolution of the cluster real-space correlation function when using photometric redshifts and the deprojection method to recover the real-space correlation function. We have previously shown the redshift evolution of $\xi(r)$ for the samples with cosmological redshifts in Figure 5.7.

Table 6.4: The parameters obtained from the fit for the real-space correlation function $\xi(r)$ on the ideal zero-error simulation for the different redshift cut catalogues and the same obtained from the photometric redshift catalogues with $\sigma_z/(1+z_c) = 0.005, 0.010, 0.030$ and 0.050. (1) redshift cut used, (2) photometric uncertainty $\sigma_z/(1+z_c)$, (3) correlation length r_0, (4) slope γ and (5) the number of clusters $N_{clusters}$, (6) median redshift and (7) mean redshift.

Redshift range	$\sigma_z/(1+z_c)$	$r_0\ h^{-1}$Mpc	γ	$N_{clusters}$	Median z	Mean z
$0.1 < z < 0.4$	z_c	12.22±0.26	1.90±0.05	3210	0.30	0.29
	0.005	11.99±0.44	2.01±0.09	3214	0.30	0.29
	0.010	12.47±0.51	1.80±0.10	3216	0.30	0.29
	0.030	12.57±0.64	1.97±0.13	3196	0.30	0.28
	0.050	12.48±0.61	1.99±0.12	3205	0.29	0.28
$0.4 < z < 0.7$	z_c	13.20±0.23	1.98±0.05	7301	0.56	0.55
	0.005	12.89±0.26	1.94±0.06	7310	0.56	0.55
	0.010	12.84±0.63	1.93±0.08	7338	0.56	0.56
	0.030	12.91±0.72	2.02±0.12	7396	0.56	0.55
	0.050	12.88±0.76	1.90±0.14	7433	0.56	0.55
$0.7 < z < 1.0$	z_c	14.86±0.33	1.97±0.05	8128	0.84	0.84
	0.005	15.07±0.49	1.87±0.07	8088	0.84	0.84
	0.010	14.99±1.00	1.90±0.18	8095	0.84	0.84
	0.030	14.06±0.63	2.05±0.19	8053	0.84	0.84
	0.050	14.36±0.83	1.91±0.16	7937	0.84	0.84
$1.0 < z < 1.3$	z_c	17.00±0.48	2.00±0.07	5963	1.13	1.13
	0.005	17.29±0.64	2.06±0.08	6001	1.13	1.13
	0.010	16.90±0.87	2.08±0.12	5973	1.13	1.14
	0.030	17.45±1.14	1.88±0.16	5880	1.13	1.14
	0.050	17.43±0.92	1.90±0.13	5859	1.13	1.14
$1.3 < z < 1.6$	z_c	18.26±0.62	2.15±0.06	3365	1.43	1.43
	0.005	18.31±0.51	2.09±0.08	3356	1.43	1.43
	0.010	18.31±0.75	2.26±0.21	3350	1.43	1.43
	0.030	19.22±1.16	2.16±0.17	3388	1.42	1.43

	0.050	18.78±1.35	2.11±0.18	3352	1.43	1.43
$1.6 < z < 2.1$	z_c	19.48±1.41	2.23±0.21	2258	1.76	1.79
	0.005	18.86±0.88	2.16±0.23	2251	1.77	1.79
	0.010	18.76±0.85	2.32±0.27	2239	1.77	1.79
	0.030	18.74±1.89	2.15±0.17	2251	1.77	1.79
	0.050	19.62±2.16	2.15±0.26	2277	1.77	1.79

For this purpose, we analyse 4 mocks with redshift uncertainties of $\sigma_z/(1+z_c) = 0.005, 0.010, 0.030$ and 0.050 respectively, in 5 redshift slices, from $0.1 < z < 0.4$ to $1.6 < z < 2.1$ with the same mass cut $M_{halo} > 5 \times 10^{13}\ h^{-1}\ M_\odot$ as done in Section 5.4. The results are shown in Figure 6.11 and the values of the best-fit parameters for all the 4 photometric samples are given in Table 6.4 along with the number of clusters ($N_{clusters}$) and the mean and median redshift for each sample.

Figure 6.11 shows the evolution of the best-fit parameters r_0 and γ for the different redshift slices. The four panels correspond to the different photometric redshift errors tested. It can be compared to Figure 5.7 which shows the values of r_0 and γ estimated for the same redshift slices but using cosmological redshifts. The fits are performed in the range within which $\xi(r)$ can be described using a power-law. As in Figure 5.7, r_0 and γ are shown to increase with redshift but the errors on their estimates become larger as the photometric redshift error increases. As a result, the error bars on the r_0 estimates for consecutive redshift slices tested tend to superimpose when considering large values of σ_z. The increase of r_0 with redshift remains detectable, but a larger binning in redshift is requested to detect this effect significantly when working with large σ_z. One can note that the parameters estimated from the deprojected correlation function are within 1σ from the ones estimated directly in real-space, and that remains true even for high redshifts and for high values of the photometric errors. The large error bars for the last two redshift slices ($1.3 < z < 1.6$ and $1.6 < z < 2.1$) are both due to the small number of clusters at high redshift (see the histogram shown in Figure 5.5) and the scaling of the photometric error $\sigma_z = \sigma_{(z=0)} \times (1 + z_c)$. However, it can be seen that the low number of clusters makes the correlation function hard to measure even using cosmological redshifts. From our tests we can conclude that the correlation function can be recovered from photometric redshift surveys using the deprojection method up to a redshift of $z \approx 2.0$ within 10% percent with a photometric redshift error of $\sigma_z/(1+z_c) = 0.030$. In this sense, the recovery performed with this method can be considered as successful. Even in the last redshift slice chosen ($1.6 < z < 2.1$), the correlation function can be recovered within 1σ for all the four photometric redshift uncertainties tested. It can be numerically visualised in the last panel of Table 6.4. This point is of particular importance as the $1.5 < z < 2.0$ redshift range has been shown to be very discriminant for constraining cosmological parameters with clusters (Sartoris et al., 2016) because future surveys as we have mentioned will be probing

up to these redshift ranges.

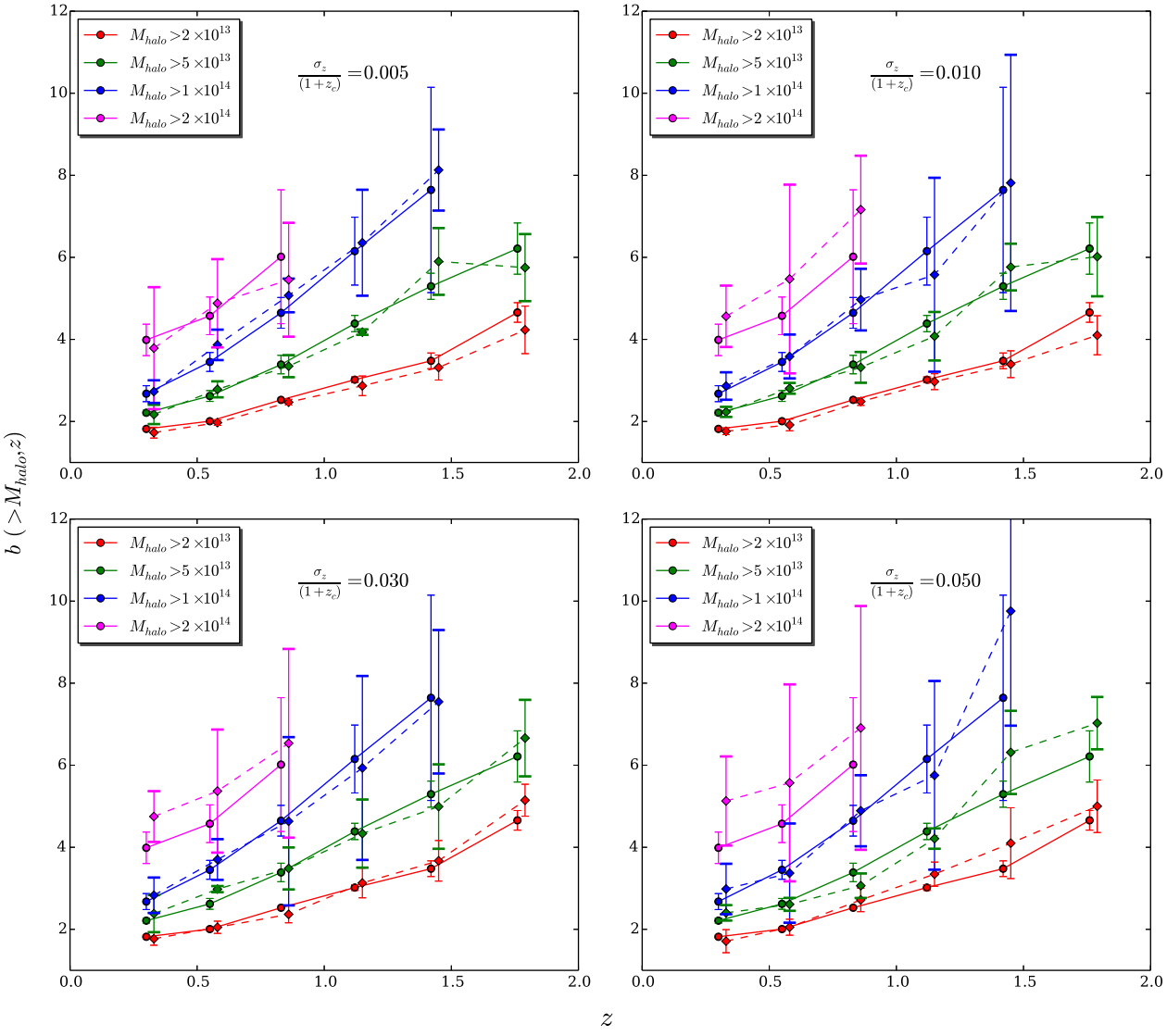

Figure 6.12: The evolution of bias with redshift and mass (with units $h^{-1}\ M_{\odot}$) for the z_c sample (*solid lines*) compared with the photometric samples (*dashed lines*) with redshift uncertainties of $\sigma_z/(1+z_c) = 0.005, 0.010, 0.030$ and $\sigma_z/(1+z_c) = 0.050$.

6.2.5.4 Calculating the bias for the photometric redshift samples

We have already stressed in Section 5.6 the fact that galaxy clusters are highly biased tracers of mass, and that, precise information of the bias is needed if we are to use galaxy clusters to constrain cosmology. As we have to calculate the bias, we need two parameters, i.e. the

dark matter correlation function and the cluster correlation function. If we are provided only with photometric information, we have shown in the previous chapter that by using the deprojection method we can recover the real-space correlation function within a few percent. In this section we try to estimate the bias as defined for samples with $\sigma_z/(1+z_c) = 0.005, 0.010, 0.030$ and 0.050.

The calculated bias values are given in Tables 6.5 and 6.6 along with the number of clusters($N_{clusters}$) in each sample. The results can be seen in Figure 6.12. The bias values obtained for the photo-z samples are consistent with the values obtained for the reference sample and are within 1σ error bars. For the first two mass cut samples ($M_{halo} > 2 \times 10^{13}\ h^{-1}\ M_\odot$ and $5 \times 10^{13}\ h^{-1}\ M_\odot$), the calculated bias from the photometric samples are within 1σ even up to a median redshift of $z \approx 1.8$. Up to a mass cut of $M_{halo} > 1 \times 10^{14}\ h^{-1}\ M_\odot$ one can see that the redshift evolution of the bias can be traced very well (even up to redshifts of $z \approx 1.5$).

However we notice that for the highest mass cut sample ($M_{halo} > 2{\times}10^{14}\ h^{-1}\ M_\odot$) chosen, only the bias values obtained for the photometric sample with $\sigma_z/(1+z_c) = 0.005$ seem to be similar to that obtained by the reference sample. The remaining three photometric samples depict a much higher bias (even though they fall within 1σ) when compared to the reference sample. One reason for this behaviour and also for the large error bars for this mass cut sample is due to the smaller abundance of clusters at this mass threshold cut as it can be seen from Table 6.5 and 6.6. We also believe that it can be due to the percentage of contaminants that are present in this mass cut sample for three different photometric uncertainties. We have calculated the contaminants for this mass cut sample and they seem to be higher at certain redshifts when compared to the contaminants at the same redshifts found for the low mass cut samples.

However up to a mass cut of $M_{halo} > 5 \times 10^{13}\ h^{-1}\ M_\odot$, the evolution in redshift and mass of the bias is clearly distinguished up to the highest redshift $z \approx 2.1$, and up to a mass cut of $M_{halo} > 1 \times 10^{14}\ h^{-1}\ M_\odot$, it is clearly distinguished up to $z \approx 1.5$.

$\sigma_z/(1+z_c)$	Mass ($h^{-1}\ M_\odot$)	Redshift range	Bias	$N_{clusters}$
0.005	2×10^{13}	$0.1 < z < 0.4$	1.71±0.13	10521
		$0.4 < z < 0.7$	1.97±0.06	27224
		$0.7 < z < 1.0$	2.46±0.06	35045
		$1.0 < z < 1.3$	2.86±0.23	31845
		$1.3 < z < 1.6$	3.31±0.30	23017
		$1.6 < z < 2.1$	4.23±0.57	18904
	5×10^{13}	$0.1 < z < 0.4$	2.17±0.23	3214
		$0.4 < z < 0.7$	2.78±0.19	7310

		$0.7 < z < 1.0$	3.34±0.26	8088
		$1.0 < z < 1.3$	4.17±0.06	6001
		$1.3 < z < 1.6$	6.10±0.81	3356
		$1.6 < z < 2.1$	5.75±0.81	2251
	1×10^{14}	$0.1 < z < 0.4$	2.72±0.27	1116
		$0.4 < z < 0.7$	3.86±0.37	2231
		$0.7 < z < 1.0$	5.07±0.41	2065
		$1.0 < z < 1.3$	6.35±1.29	1218
		$1.3 < z < 1.6$	8.12±0.98	594
	2×10^{14}	$0.1 < z < 0.4$	3.78±1.48	316
		$0.4 < z < 0.7$	4.88±1.07	544
		$0.7 < z < 1.0$	5.45±1.38	399
0.010	2×10^{13}	$0.1 < z < 0.4$	1.76±0.08	10536
		$0.4 < z < 0.7$	1.91±0.14	27283
		$0.7 < z < 1.0$	2.48±0.09	35022
		$1.0 < z < 1.3$	2.96±0.19	31763
		$1.3 < z < 1.6$	3.39±0.32	23021
		$1.6 < z < 2.1$	4.10±0.47	18898
	5×10^{13}	$0.1 < z < 0.4$	2.23±0.12	3216
		$0.4 < z < 0.7$	2.80±0.13	7338
		$0.7 < z < 1.0$	3.31±0.37	8095
		$1.0 < z < 1.3$	4.07±0.59	5973
		$1.3 < z < 1.6$	5.76±0.56	3350
		$1.6 < z < 2.1$	6.01±0.96	2239
	1×10^{14}	$0.1 < z < 0.4$	2.86±0.33	1124
		$0.4 < z < 0.7$	3.58±0.53	2235
		$0.7 < z < 1.0$	4.96±0.75	2069
		$1.0 < z < 1.3$	5.57±2.36	1210
		$1.3 < z < 1.6$	7.81±3.12	587

	2×10^{14}	$0.1 < z < 0.4$	4.56±0.74	318
		$0.4 < z < 0.7$	5.47±2.3	547
		$0.7 < z < 1.0$	7.16±1.31	394

Table 6.5: The bias values obtained for the first 2 photometric redshift catalogues ($\sigma_z/(1 + z_c)$ = 0.005 and 0.010) with the 4 mass threshold cuts in the 5 redshift bins used. (1) Photometric uncertainty $\sigma_z/(1 + z_c)$, (2) mass cut M_{halo} cut, (3) redshift range, (4) the bias and (5) the number of clusters $N_{clusters}$ are given.

$\sigma_z/(1 + z_c)$	Mass ($h^{-1}\ M_\odot$)	Redshift range	Bias	$N_{clusters}$
0.030	2×10^{13}	$0.1 < z < 0.4$	1.77±0.15	10581
		$0.4 < z < 0.7$	2.05±0.14	27475
		$0.7 < z < 1.0$	2.36±0.20	34849
		$1.0 < z < 1.3$	3.13±0.36	31457
		$1.3 < z < 1.6$	3.67±0.49	23028
		$1.6 < z < 2.1$	5.14±0.38	18863
	5×10^{13}	$0.1 < z < 0.4$	2.38±0.45	3196
		$0.4 < z < 0.7$	2.97±0.07	7396
		$0.7 < z < 1.0$	3.48±0.51	8053
		$1.0 < z < 1.3$	4.33±0.83	5880
		$1.3 < z < 1.6$	4.99±1.02	3388
		$1.6 < z < 2.1$	6.66±0.93	2251
	1×10^{14}	$0.1 < z < 0.4$	2.83±0.43	1115
		$0.4 < z < 0.7$	3.70±0.49	2253
		$0.7 < z < 1.0$	4.63±2.05	2041
		$1.0 < z < 1.3$	5.93±2.24	1228
		$1.3 < z < 1.6$	7.54±1.74	580
	2×10^{14}	$0.1 < z < 0.4$	4.74±0.61	317
		$0.4 < z < 0.7$	5.37±1.50	554
		$0.7 < z < 1.0$	6.53±2.30	383

0.050	2×10^{13}	$0.1 < z < 0.4$	1.71±0.28	10835
		$0.4 < z < 0.7$	2.05±0.19	27570
		$0.7 < z < 1.0$	2.71±0.28	34575
		$1.0 < z < 1.3$	3.34±0.29	31168
		$1.3 < z < 1.6$	4.20±0.86	22733
		$1.6 < z < 2.1$	5.01±0.63	18889
	5×10^{13}	$0.1 < z < 0.4$	2.40±0.18	3205
		$0.4 < z < 0.7$	2.62±0.21	7443
		$0.7 < z < 1.0$	3.06±0.29	7937
		$1.0 < z < 1.3$	4.21±0.24	5859
		$1.3 < z < 1.6$	6.31±1.01	3352
		$1.6 < z < 2.1$	7.02±0.63	2277
	1×10^{14}	$0.1 < z < 0.4$	2.98±0.61	1109
		$0.4 < z < 0.7$	3.37±1.20	2258
		$0.7 < z < 1.0$	4.89±0.86	1992
		$1.0 < z < 1.3$	5.75±2.30	1257
		$1.3 < z < 1.6$	9.75±2.79	562
	2×10^{14}	$0.1 < z < 0.4$	5.12±1.08	311
		$0.4 < z < 0.7$	5.57±2.40	560
		$0.7 < z < 1.0$	6.91±2.97	370

Table 6.6: The bias values obtained for the last 2 photometric redshift catalogues ($\sigma_z/(1 + z_c) = 0.030$ and 0.050) with the 4 mass threshold cuts in the 5 redshift bins used. (1) Photometric uncertainty $\sigma_z/(1 + z_c)$, (2) mass cut M_{halo} cut, (3) redshift range, (4) the bias and (5) the number of clusters $N_{clusters}$ are given.

6.2.6 Effects of Purity and Completeness on the two-point correlation function

Observational cluster samples suffer in terms of purity and completeness, which affects the recovered correlation function. Not all clusters above a given mass and redshift range are

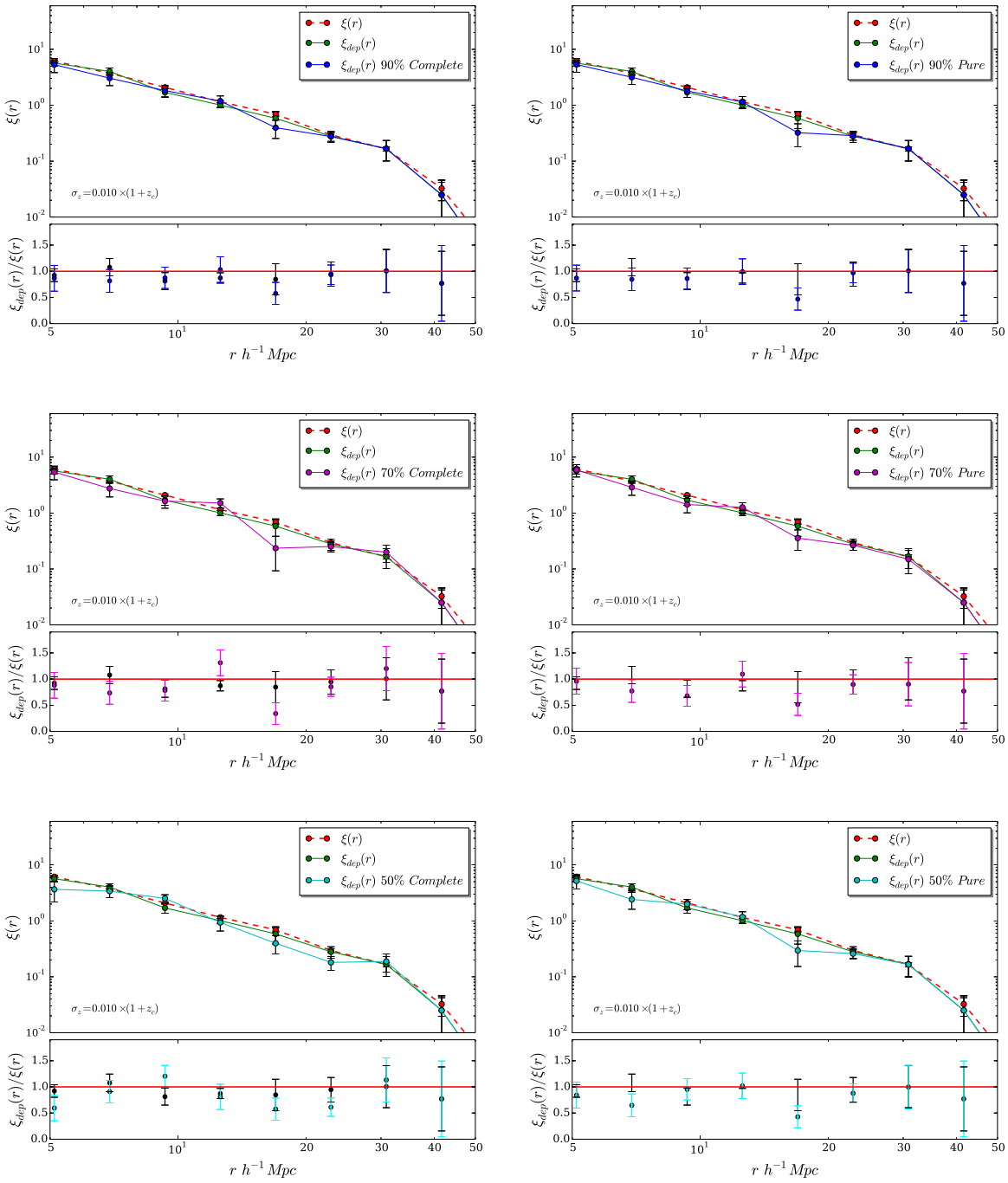

Figure 6.13: *Left column:* The real-space correlation function (*red dotted line*), the recovered correlation function for the photometric redshift sample (*green line*) along with the recovered correlation function for the photometric redshift sample with varying completeness values (*coloured as indicated in the figure*). *Right column:* The real-space correlation function (*red dotted line*), the recovered correlation function for the photometric redshift sample (*green line*) along with the recovered correlation function for the photometric redshift sample with varying purity values (*coloured as indicated in the figure*). The quality of the recovery for each completeness and purity sample is given in Table 6.7 and 6.8 .

Table 6.7: The quality of recovery obtained for the three completeness samples. It can be seen that the quality of the recovery starts to diminish for samples with increasing incompleteness compared to the sample that is 100% complete. The columns indicate: (1) Completeness, (2) the values of $\Delta\xi$ and (3) $\widehat{\Delta\xi}$ for the sample with a photometric uncertainty of $0.010\times(1+z_c)$. The range of scales r used for the fit is fixed at 5-50 Mpc.

Completeness	$\Delta\xi$	$\widehat{\Delta\xi}$
100%	0.065	0.063
90%	0.097	0.101
70%	0.113	0.111
50%	0.166	0.162

detected, which means that the sample is not always 100% complete. At the same time, there will be certain clusters that are detected as false positives, which means that the sample is not always 100% pure. So far, we have shown that by using the deprojection method, the correlation function can be recovered within a given percentage for samples with different photometric uncertainties (not taking into account any purity and completeness issue). As a preliminary test, we add to the photometric redshift uncertainty, different purity and completeness values and separately investigate the effect of completeness and purity on the recovered real-space correlation function.

For the analysis several completeness and purity samples are generated from the original light-cone catalogue. For the preliminary test, we take into account samples within the redshift range $0.4 < z_{phot} < 0.7$ with a photometric uncertainty of $\sigma_z = 0.010 \times (1 + z_c)$.

For generating different completeness samples, we remove randomly a given percentage of objects from the original catalogue so that it mimics different completeness values. We generate six realisations for each of the samples that are 90%, 70% and 50% complete and investigate its effect on the final recovered correlation function (for which we take the average over the recovered correlation function obtained for each of the six realisations).

With regard to the effect of purity, we randomly include a given percentage of objects from the original catalogue so that it mimics different purity values. We use the same number of realisations for our purity samples, i.e. we generate six realisations for each of the samples that are 90%, 70% and 50% pure and investigate its effect on the final recovered correlation function (for which we take the average over the recovered correlation function obtained for each of the six realisations).

The results of the same are seen in Figure 6.13 and the values obtained for the quality of the recovery are given in Table 6.7 and 6.8. Considering the sample that is 90% complete, the correlation function is recovered within 90%, whereas for the same sample (with $0.010\times(1+z_c)$) that is 100% complete, we see that the correlation function is recovered within 95% as seen from Figure 6.9 and Table 6.7. The same can be seen for the sample that is 90% pure,

Table 6.8: The quality of recovery obtained for the three purity samples. It can be seen that the quality of the recovery starts to diminish for samples with increasing impurity compared to the sample that is 100% pure. The columns indicate: (1) Purity, (2) the values of $\Delta\xi$ and (3) $\widehat{\Delta\xi}$ for the sample with a photometric uncertainty of $0.010 \times (1 + z_c)$. The range of scales r used for the fit is fixed at 5-50 Mpc.

Purity	$\Delta\xi$	$\widehat{\Delta\xi}$
100%	0.065	0.063
90%	0.108	0.104
70%	0.127	0.127
50%	0.152	0.160

i.e. the correlation function is recovered within 89% compared to a recovery within 95% for the sample that is 100% pure. This indicates that the recovery of the real-space correlation function is affected when we use incomplete and impure samples and that the quality of the recovery starts to diminish with decreasing completeness and purity.

However, for this preliminary test, we have only investigated the effect of purity and completeness separately on the recovered correlation function and we can see that the recovery starts to decrease with increasing impurity and incompleteness for the chosen photometric sample as expected. The result of combining the two effects on the recovery of the correlation function will be addressed in a future work.

6.2.7 Towards the usage of more realistic photo-z errors

The photometric redshifts used so far have been drawn from a Gaussian distribution centred at the cosmological redshift (z_c) of each cluster and with a standard deviation $\sigma_{z_c} = \sigma_{(z=0)}(1 + z_c)$ which is equal to the assumed photometric redshift error of the sample. We have used values of $\sigma_{(z=0)} = 0.001, 0.005, 0.010,$ up to 0.050 and tested the effect these errors have on the recovery of the correlation function. In a more realistic scenario, we expect to have catastrophic failures, as it can happen for galaxy samples and the photometric redshifts are also dependent on mass. We have not taken into account both these issues so far.

Cluster finding algorithms that are applied on realistic data/simulations, do take into account these issues and so the photometric redshifts calculated by them are more realistic compared to the Gaussian approximation method we have used so far. As a preliminary test, we would like to compare the distribution of $(z_{phot} - z_c)$ (with z_{phot} generated using the Gaussian approximation method) for the sample with an uncertainty of $0.010 \times (1 + z_c)$ to the distribution of $(z_{phot} - z_c)$ with z_{phot} obtained from the cluster finder algorithm applied on the simulated cluster catalogue. To do so, the cluster finder we use is WAZP (Benoist et al. in prep) which uses a wavelet adaptive technique, and is applied on the simulated cluster

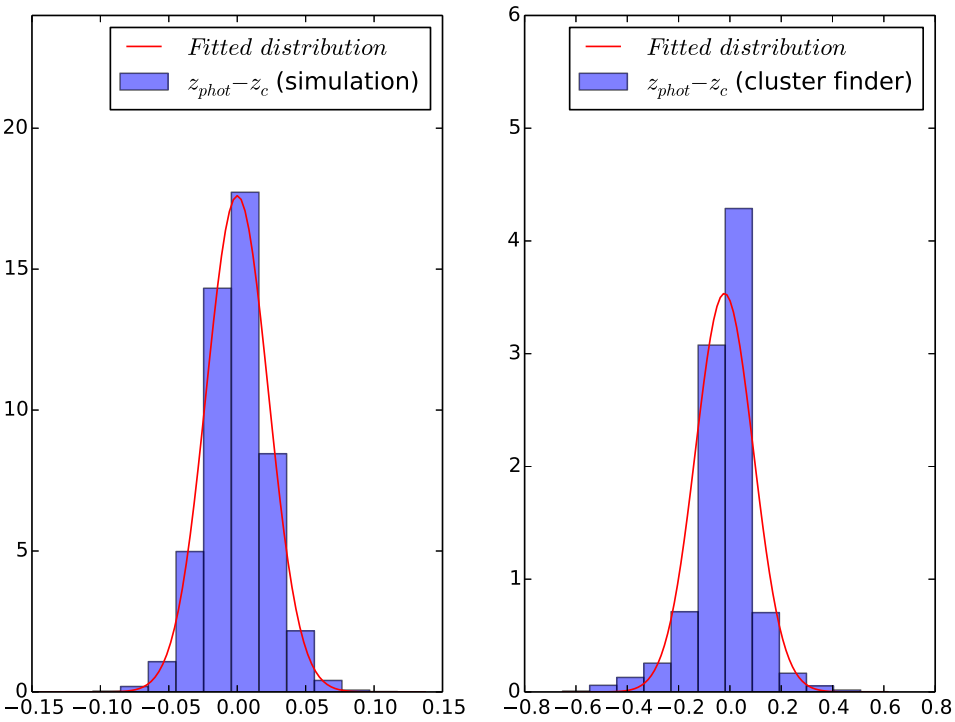

Figure 6.14: *Left:* The blue histogram shows the distribution of $(z_{phot} - z_c)$ for the photometric sample with a redshift uncertainty of $0.010 \times (1 + z_c)$ obtained directly from the simulated cluster catalogue and the red solid line shows the fitted distribution for the data. *Right:* The blue histogram shows the distribution of $(z_{phot} - z_c)$ for the photometric sample obtained from the cluster finder algorithm applied on the simulated cluster catalogue, and the red solid line shows the fitted distribution for the data. It can be seen that the photometric redshift distribution obtained from the cluster finder algorithm (on the right) is close to a Gaussian distribution and also closer to the photometric redshift distribution that we have generated using the Gaussian approximation method (on the left).

catalogue. The distributions $(z_{phot} - z_c)$ of both the redshifts, i.e. the one generated via the Gaussian approximation technique and the one calculated via the cluster finder can be seen in Figure 6.14. It can be seen from Figure 6.14 that the redshift distribution obtained from the cluster finder is closer to a Gaussian distribution.

As we have discussed, photometric redshift distributions calculated from cluster finding algorithms are more closer to reality and so will be the recovery of the correlation functions calculated from them. Due to the similarity in the photometric redshift distributions as seen from Figure 6.14 the Gaussian approximation technique we have used so far to generate the photometric redshifts is a reasonable one. The results obtained on the recovery of the two-point correlation function (with the photometric redshifts generated from the Gaussian approximation method) so far are thus not far away from what we expect when we apply the deprojection method on cluster catalogues obtained from cluster finding algorithms, either on simulations or on real data.

6.3 Impact of selecting in Richness on the two-point correlation function

Optical cluster finder algorithms in general do not produce mass estimates, but instead produce a quantity that we refer to as 'Richness'. For photometric surveys, optical richness is the primary mass proxy. Richness refers to the number of galaxies in a cluster within a given radius and so can be directly estimated from an optical survey.

Cluster mass estimates are commonly inferred from independent weak-lensing studies or adopting scaling relations between weak-lensing masses and mass proxies. Weak-lensing mass estimates are unfortunately limited to the high mass, intermediate redshift tail of the (M, z) distribution. Richnesses are in principle available for the whole set of clusters detected. However, richness estimates are expected to be noisy tracers of the underlying mass (Rykoff et al., 2012) and there exists an intrinsic scatter between the mass-observable relation. This intrinsic scatter varies with redshift and the evolution of the scaling relation gives us information on the mass dependence. From studies based on numerical simulations it has been argued that the intrinsic scatter of the mass-richness relation at the cluster scale is around $\sigma_{M|N} = 0.20 - 0.25$ at a mass $M_{200} \sim 2 \times 10^{14}$ (Rozo et al., 2011; Rykoff et al., 2012, and references therein).

Extrinsic sources of scatter can impact the observed scatter in the mass-richness relation (Rozo et al., 2011). Source of noise for a photometric cluster catalogue comes from the density of background galaxies within which a cluster is fixed. Due to galaxy clustering, this background exhibits large cluster-to-cluster fluctuations, and so a small percentage of galaxy clusters end up fixed in very large galaxy overdensities. Thus the richness estimates obtained are usually overestimated, i.e. projection onto correlated structures. Improper estimates of galaxy cluster centres on the other hand can lead to underestimates of the richness (Rykoff et al., 2012).

A key goal for cluster cosmology especially from photometric catalogues is trying to reduce the scatter between the cluster mass and richness. There have been several studies (Berlind et al., 2003; Kravtsov et al., 2004; Zheng et al., 2005; Rozo et al., 2009; Rykoff et al., 2012) that have been made previously both on catalogues from observations and simulations. On the whole, an ideal mass proxy should be characterised by a low scatter with mass. When the correlation between cluster richness and mass is improved, the cluster richness can be used to infer cluster masses even out to high redshifts. However, the source of intrinsic scatter will still exist.

In this thesis, as a preliminary test, we make use of the true richness, taking into account only the intrinsic scatter and test if we can recover the two-point correlation function of a mass cut sample $\xi(> mass)$ from the two-point correlation function of a true richness cut sample $\xi(> richness)$. We also calculate the cluster bias for arbitrary richness cut samples and compare the same with mass cut samples, for which the mass is obtained by fitting the mass-richness relation using a simple power-law. Provided the two cluster samples depict a similar evolution of the bias with redshift, i.e. trace the underlying dark matter distribution in a similar way, we can combine the result with the $\xi(r)$ obtained for the two samples to compare mass and richness.

6.3.1 Richness definition

There are several ways in which one can define richness. We explain here the richness definition we have used, i.e $N_{200}(H^* + 2)$. Galaxies brighter than $0.4L^*$ is a common choice used, where L^* is the luminosity of a galaxy at the knee of the galaxy luminosity function (Rykoff et al., 2012). H^* is the apparent H-band magnitude an L^* galaxy would have if located at redshift z and has been derived from the evolution of the SED of an elliptical galaxy taken from the PEGASE2 SED library (Fioc and Rocca-Volmerange, 1997) and calibrated with Coma cluster (de Propris et al., 1998). The richness $N_{200}(H^* + 2)$ is defined to be all those galaxies within a radius R_{200} which have an apparent magnitude that is brighter than $H^* + 2$. The choice of such a richness is consistent with that adopted for richness estimates with galaxies brighter than $0.4L^*$. Here R_{200} refers to a radius within which the mean density of a cluster is 200 times the critical density of the Universe:

$$R_{200} = \sqrt[3]{\frac{3M_{200}}{4\pi\rho_c}} \tag{6.11}$$

where $\rho_c \equiv 3H(z)^2/8\pi G$. The H^* is a characteristic magnitude that evolves with redshift so that derived richness at different redshift intervals can be compared. The luminosity function provides us the clusters with a given luminosity range. Usually we work with magnitudes and not luminosities, so the luminosity function is converted from the absolute luminosities L to apparent magnitudes m as and is written as:

$$\phi(M)dM = 0.4\ln(10)\phi^* 10^{0.4(H^*-m)(\alpha+1)} \exp^{-10^{0.4(H^*-m)}} dM \tag{6.12}$$

where H^* is the characteristic magnitude. From now on we refer to $N_{200}(H^* + 2)$ as just N_{200} and refer to the richness with all those galaxies within R_{200} and without a magnitude cut as $N_{200}(total)$.

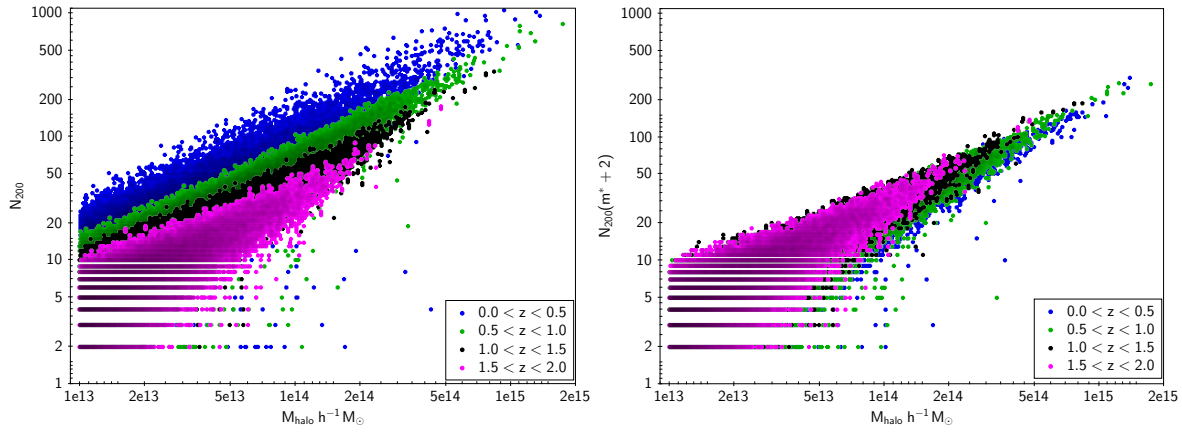

(a) (b)

Figure 6.15: *Left panel:* $N_{200}(total)$ richness vs M_{halo} mass plotted for the entire sample of clusters. The sample is divided into four redshift ranges and are colour coded as mentioned in the figure. *Right panel:* N_{200} richness vs M_{halo} mass plotted for the entire sample of clusters. The sample is divided into four redshift ranges and are colour coded as mentioned in the figure.

If absolute magnitudes are available in the catalogue, one can directly make a cut at a specific absolute magnitude with the galaxies within R_{200} to get their richness estimate. In a real observational catalogue, apparent magnitudes are what we will be using. As we are using a simulated catalogue, the richness we are using is the true richness, i.e. contains all true members of the cluster. In a real observational scenario, this will not be the case due to several observational disabilities.

We have explained before in Section 5.2 that the M_{halo} masses provided in the simulation are close to M_{200} values and so using N_{200} should be a good compromise. We show in Figure 6.15a and 6.15b the plot of $N_{200}(total)$ vs M_{halo} and N_{200} vs M_{halo} for all the cluster samples binned in redshift slices. It can be seen that the overall scatter between $N_{200}(total)$ and M_{halo} is larger compared to the overall scatter between N_{200} and M_{halo}. This is because of the evolution of the characteristic magnitude with redshift for richness N_{200}, whereas for richness $N_{200}(total)$, we include all the galaxies within the virial radii regardless of the survey magnitude cut. It can also be seen from Figures 6.15a and 6.15b that the low redshift cut samples ($0.0 < z < 0.5$ and $0.5 < z < 1.0$) depict different slopes. But it can be seen that as we reach a higher redshift range ($z \gtrsim 1.0$) it can be seen that the N_{200} values and $N_{200}(total)$ values depict a similar slope and become comparable.

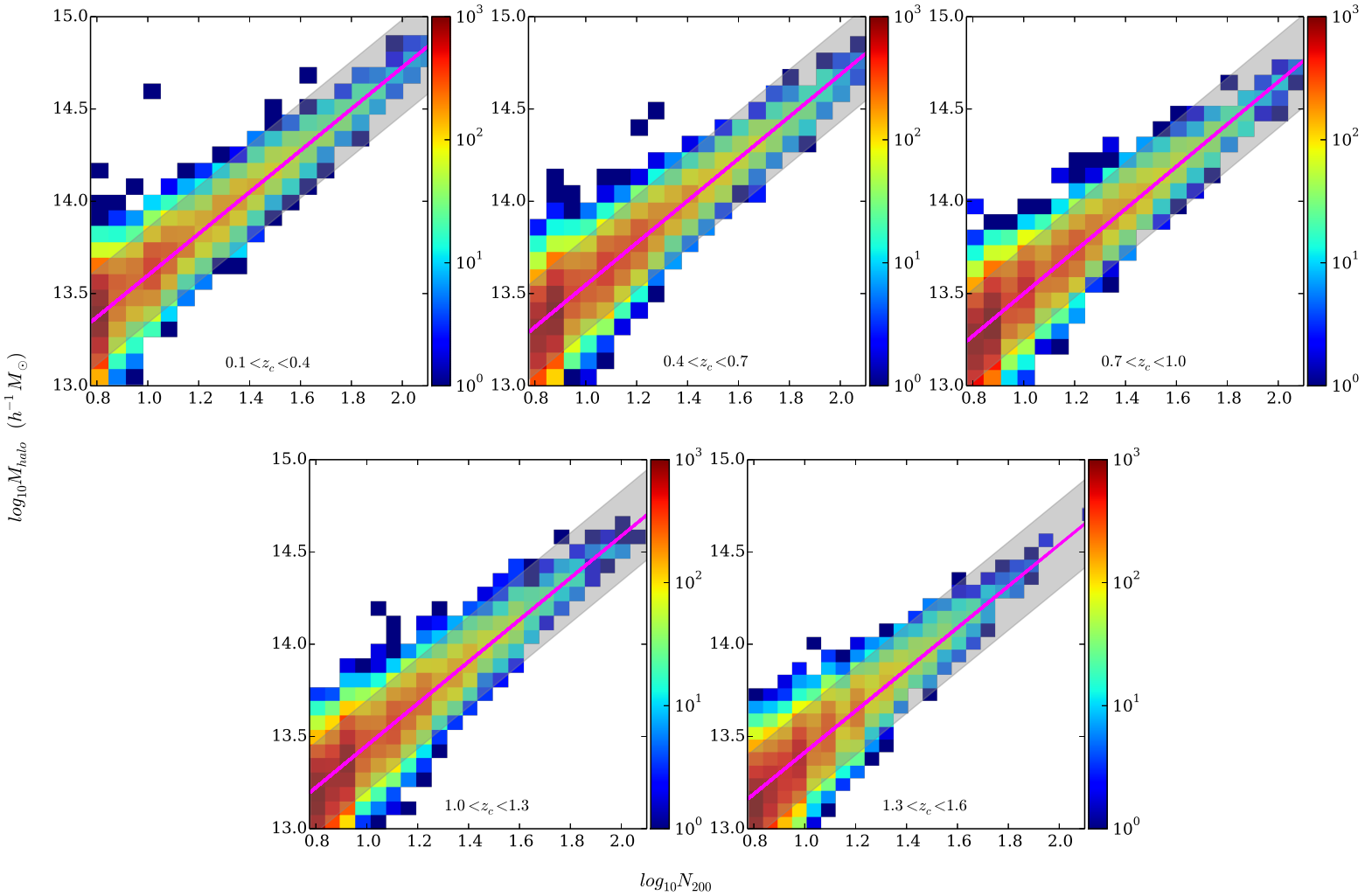

Figure 6.16: A 2D histogram plot of richness (N_{200}) vs mass (M_{halo}) along with the fit (*magenta lines*) performed using the generic equation as mentioned in Table 6.9 for the 5 redshift ranges. Red spots denote more dense regions and blue spots denote the less dense regions. The grey shaded region denotes the 2σ confidence limits.

$\log_{10}(M_{halo}) = a + b \times \log_{10}(N_{200})$		
Redshift range	a	b
0.1< z <0.4	12.46 ± 0.005	1.12 ± 0.004
0.4< z <0.7	12.40 ± 0.003	1.14 ± 0.003
0.7< z <1.0	12.35 ± 0.003	1.15 ± 0.002
1.0< z <1.3	12.31 ± 0.003	1.14 ± 0.002
1.3< z <1.6	12.28 ± 0.003	1.13 ± 0.003

Table 6.9: The parameters obtained by fitting the scaling relation between mass and richness for the 5 different redshift slices chosen. The generic form is $\log_{10}(M_{halo}) = a + b \times \log_{10}(N_{200})$

6.3.2 Scatter in the mass-richness relation

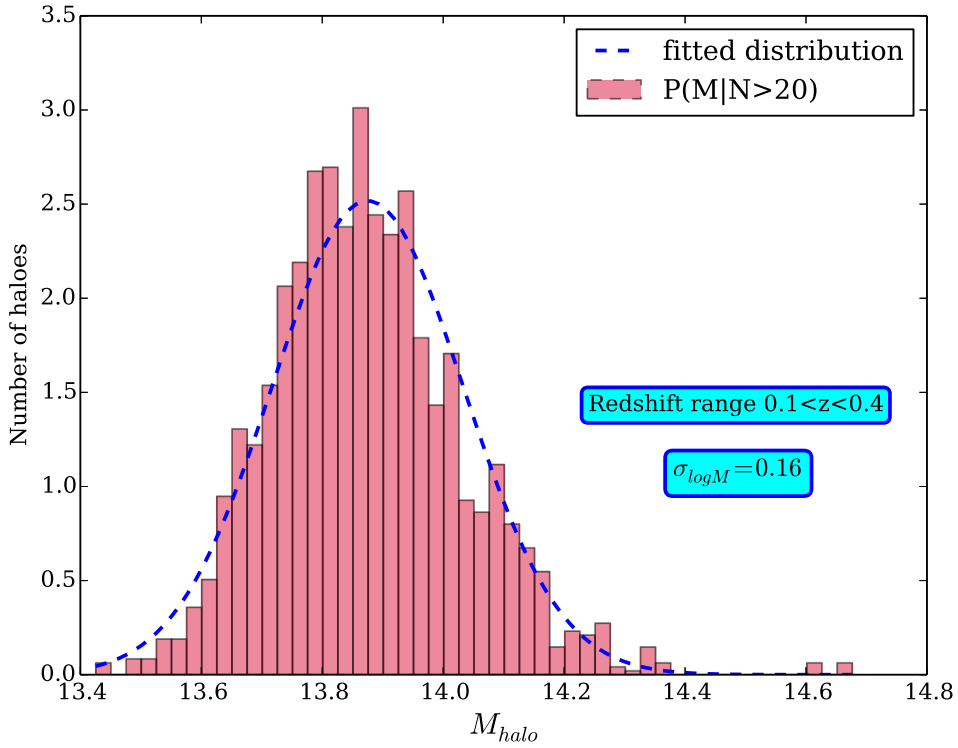

Figure 6.17: The distribution of those clusters within an arbitrary redshift range of $0.1 < z < 0.4$ and above a richness cut of $N_{200} > 20$. The best-fit line to the distribution is given by the dashed line and is made using Equation 6.13.

We will be analysing the scatter that exists between the mass-richness relation, the evolution of the two-point correlation function with both richness and redshift, along with the

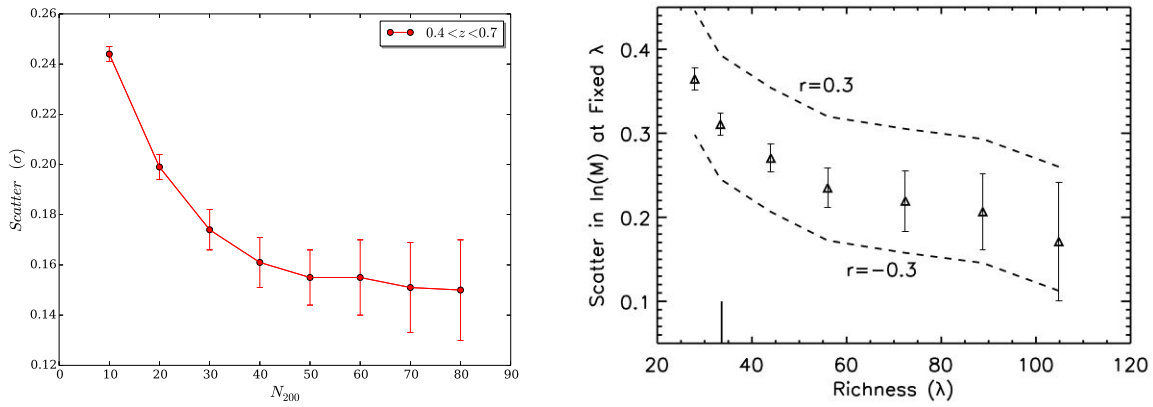

(a) (b)

Figure 6.18: *Left panel:* The scatter in mass at a fixed richness cut. The scatter is estimated using all clusters above a given richness and not by using narrowly binned samples. *Right panel:* The scatter in mass at fixed richness estimated using all clusters above a given richness as calculated by Rykoff et al. (2012) for the maxBCG cluster sample. The dashed lines illustrate how the scatter changes as the correlation coefficient is varied between L_X and richness λ at fixed mass.

redshift evolution of bias obtained for our richness cut samples. To do so, the sample is split into 5 redshift slices, each of width 0.3 starting from $0.1 < z < 0.4$ up to $1.3 < z < 1.6$. The mass-richness plot is shown in Figure 6.16 for the first three redshift samples. It can be seen that mass and richness have a positive correlation, but we need to take into account the scatter that exists. This scatter as it can be seen from Figure 6.16 is larger at low mass/richness range and decreases at high mass/richness range.

To find the scaling relation of richness with mass, we fit the relation using a simple power-law (using the generic equation as mentioned in Table 6.9) for all the five redshift samples. The values obtained are given in Table 6.9.

To calculate the scatter at a given richness, we assume a lognormal distribution of M_{halo} as a function of N_{200}, which is given by the equation

$$p(M_{halo}|N_{200}) = \frac{1}{\sqrt{2\pi\sigma^2_{\log(M_{halo})}}} \exp\left[\frac{(\log(M_{halo}) - \mu)^2}{2\sigma^2_{\log(M_{halo})}}\right] \tag{6.13}$$

where μ is the mean and σ is the scatter.

So once we have the fit made to the mass-richness relation, the scatter at any arbitrary richness/mass can be found. We show the fit to the Gaussian distribution for an arbitrary richness cut sample ($N_{200} > 20$) within the redshift range $0.1 < z < 0.4$ in Figure 6.17. It can be seen that Equation 6.13 is a good approximation for the distribution seen in Figure 6.17 and that the scatter at this richness cut is $\sigma_{logM} = 0.16$.

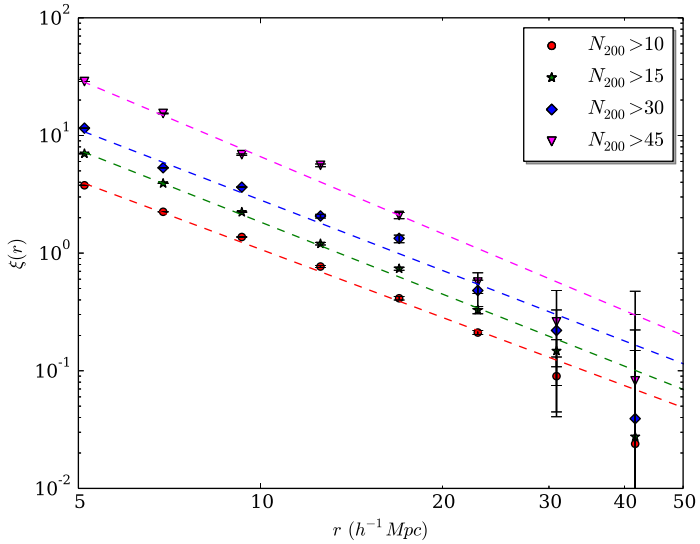

Figure 6.19: The two-point correlation function calculated for the redshift slice $0.4 < z_c < 0.7$ with increasing richness cuts. The points are colour coded as mentioned in the figure.

Another interesting feature of the scatter is to find out how the scatter in mass at a fixed richness cut evolves with richness. To do so we use an arbitrary subsample in the redshift range $0.4 < z < 0.7$ and calculate the scatter at a given richness cut using Equation 6.13. It can be found out that the scatter in mass at a fixed redshift slice appears to decrease with increasing richness cuts. The scatter (σ) appears to decrease at a much faster rate from a richness cut of $N_{200} > 10$ up to $N_{200} > 50$, beyond which the rate of the decrease in the scatter drops as it can be seen from Figure 6.18a. A similar study of the variation of the scatter in mass at a fixed richness cut has been performed by Rykoff et al. (2012) on the maxBCG cluster samples. The result obtained by Rykoff et al. (2012) is given in Figure 6.18b. It can be seen that a similar decline of the scatter with increasing richness is seen for their samples and above a richness cut of $\lambda > 60$, the decline in the scatter becomes less prominent. This behaviour according to Rykoff et al. (2012) is possible because the miscentering properties of the maxBCG clusters is expected to become important at $\lambda \approx 60$.

6.3.3 Two-point correlation function of richness cut samples

We calculate the two-point correlation function for samples with increasing richness cuts to see how they evolve. Although it can be seen from Figure 6.16 that mass and richness are positively correlated, we compare the evolution of $\xi(r)$ of our mass and richness cut samples. We choose 4 arbitrary richness cuts to find the evolution of the two-point correlation function with richness in an arbitrary redshift range $0.4 < z_c < 0.7$. It can be seen from Figure 6.19 how $\xi(r)$ evolves with increasing richness cuts in a given redshift slice. The best-fit parameters obtained for the fit are mentioned in Table 6.10. The evolution of $\xi(r)$ for our richness cut

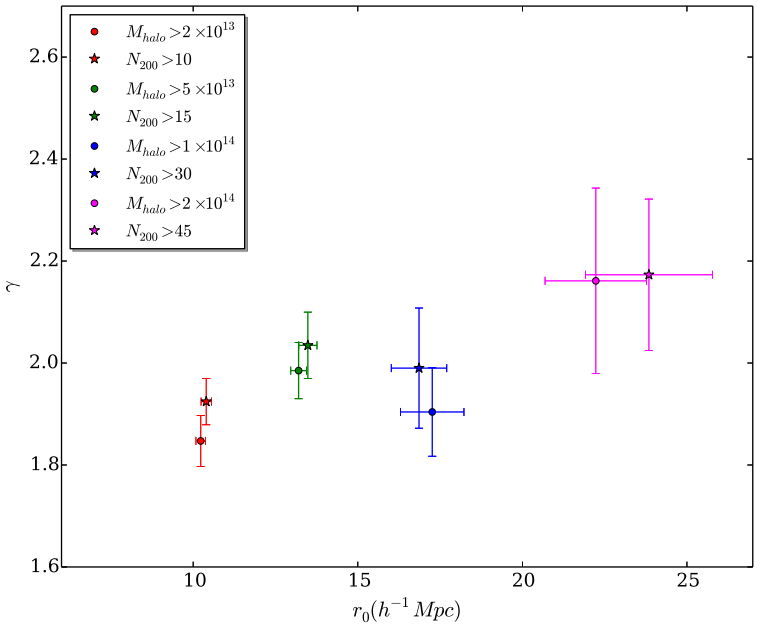

Figure 6.20: The best-fit parameters obtained for the richness cut samples and the mass cut samples within the redshift range $0.4 < z_c < 0.7$.

samples can be compared with the evolution of $\xi(r)$ obtained in Chapter 3 for our mass cut samples. It can be seen from Figure 6.20 that the evolution in richness is similar to what we obtained with increasing mass cut samples. But due to the scatter that exists between the mass-richness relation, a direct comparison between a richness cut sample and a mass cut sample cannot be made.

To find out how well richness in general can be used as a mass proxy, we calculate the bias for the four arbitrary richness cuts (N_{200} > 10,15,30 and 45) chosen at each of the 5 redshift bins (the same as in Section 5.4) and compare the same with the bias calculated for corresponding $\overline{M_{halo}}$ values obtained from the fit where $\overline{M_{halo}}$ is the mean mass obtained from the fit performed to the mass vs richness sample (the values for the fit are given in Table

N_{200}	r_0	γ
$N_{200} > 10$	10.39 ± 0.15	1.92 ± 0.13
$N_{200} > 15$	13.48 ± 0.33	2.03 ± 0.11
$N_{200} > 30$	16.86 ± 0.63	1.98 ± 0.15
$N_{200} > 45$	23.84 ± 1.38	2.17 ± 0.19

Table 6.10: The best-fit parameters obtained by fitting $\xi(r)$ for the four richness cut samples in the redshift range $0.4 < z_c < 0.7$.

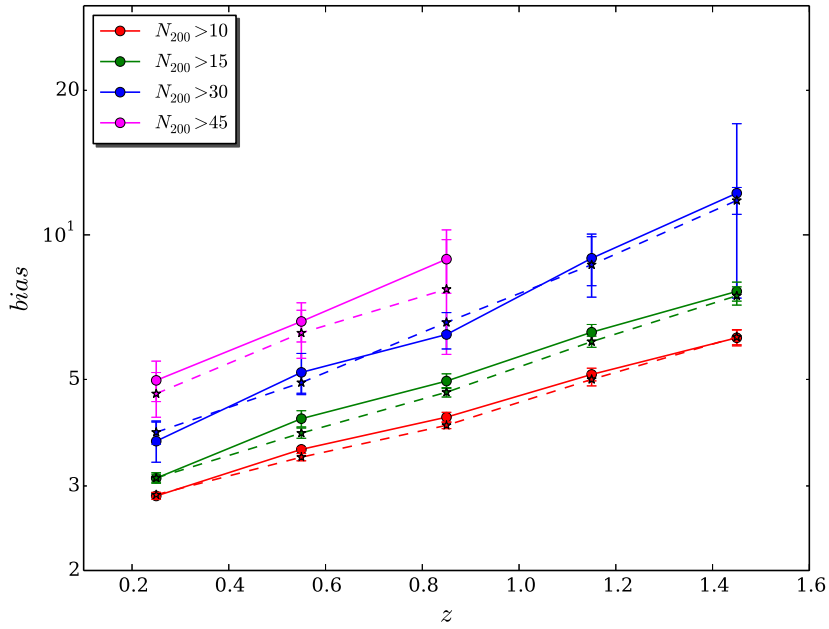

(a)

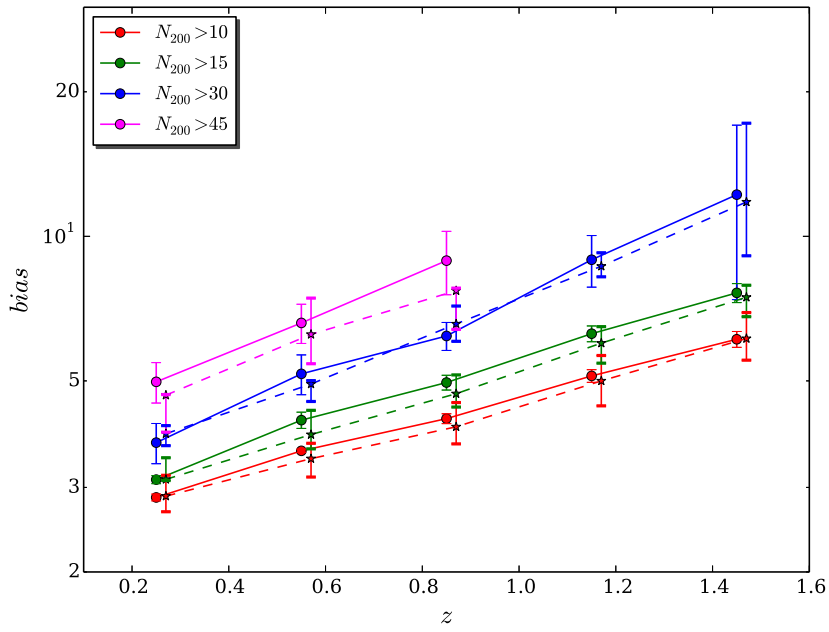

(b)

Figure 6.21: *On top:* The evolution of bias with redshift for clusters observed in the four richness cut samples. The dotted lines correspond to the bias of mean mass $\overline{M_{halo}}$ obtained from the fit of N_{200} vs M_{halo} relation. The error bars plotted for the bias of $\overline{M_{halo}}$ are the errors without considering the scatter in the richness vs mass relation. *Bottom:* The same as seen in the left plot, except that the error bars on the bias of $\overline{M_{halo}}$ are those when the 1σ scatter is considered. The median redshift of the mass samples have been shifted by 0.02 for visual clarity of the error bars.

z	N_{200}	bias (N_{200})	$\overline{M_{halo}}$ ($h^{-1}\,M_\odot$)	$\sigma_{log_{M_{halo}}}$	bias ($\overline{M_{halo}}$)	$N_{gal}(N_{200}\ cut)$	$N_{gal}(\overline{M_{halo}}\ cut)$
$0.1 < z_{cosmo} < 0.4$	$N_{200} > 10$	2.85±0.04	4.06×10^{13}	0.127	$2.87^{+0.30}_{-0.20}$	3668	4490
	$N_{200} > 15$	3.11±0.05	6.16×10^{13}	0.102	$3.21^{+0.24}_{-0.11}$	1994	2432
	$N_{200} > 30$	3.71±0.35	1.31×10^{14}	0.127	$3.88^{+0.15}_{-0.21}$	582	743
	$N_{200} > 45$	4.97±0.48	2.04×10^{14}	0.127	$4.46^{+0.21}_{-0.55}$	256	334
$0.4 < z_{cosmo} < 0.7$	$N_{200} > 10$	3.57±0.02	3.54×10^{13}	0.126	$3.44^{+0.26}_{-0.29}$	10075	12743
	$N_{200} > 15$	4.33±0.21	5.49×10^{13}	0.127	$3.86^{+0.47}_{-0.25}$	5066	6467
	$N_{200} > 30$	4.34±0.65	1.23×10^{14}	0.127	$4.92^{+0.39}_{-0.08}$	1321	1517
	$N_{200} > 45$	8.00±0.61	1.94×10^{14}	0.127	$7.38^{+2.26}_{-0.39}$	528	605
$0.7 < z_{cosmo} < 1.0$	$N_{200} > 10$	4.17±0.09	3.19×10^{13}	0.130	$4.01^{+0.49}_{-0.31}$	14053	17760
	$N_{200} > 15$	4.96±0.17	5.01×10^{13}	0.127	$4.70^{+0.44}_{-0.29}$	6568	8250
	$N_{200} > 30$	6.56±0.56	1.09×10^{14}	0.127	$6.57^{+0.58}_{-0.52}$	1401	1789
	$N_{200} > 45$	13.50±0.54	1.77×10^{14}	0.127	$11.74^{+3.45}_{-1.19}$	480	576
$1.0 < z_{cosmo} < 1.3$	$N_{200} > 10$	5.12±0.15	2.81×10^{13}	0.125	$4.99^{+0.64}_{-0.56}$	13714	18191
	$N_{200} > 15$	6.26±0.23	4.46×10^{13}	0.127	$5.99^{+0.49}_{-0.54}$	5838	7681
	$N_{200} > 30$	9.14±0.92	1.00×10^{14}	0.127	$8.66^{+0.57}_{-0.42}$	1029	1246
$1.3 < z_{cosmo} < 1.6$	$N_{200} > 10$	6.10±0.23	2.57×10^{13}	0.125	$6.12^{+0.81}_{-0.60}$	10621	14701
	$N_{200} > 15$	7.62±0.34	4.07×10^{13}	0.127	$7.46^{+0.44}_{-0.66}$	3850	5580
	$N_{200} > 30$	12.21±4.82	8.91×10^{13}	0.127	$11.79^{+5.40}_{-2.68}$	600	853

Table 6.11: The bias values obtained for the mass observable (richness cuts) and those obtained for the corresponding mass cuts taken from the mean mass ($\overline{M_{halo}}$) of the N_{200} vs M_{halo} plot considering the ± 1σ scatter. N_{gal} refers to the number of haloes above the corresponding richness/mass cuts considered.

6.9). The method we follow is:

1. Consider the N_{200} vs M_{halo} plot separately for all the 5 redshift slices (the same as chosen in Section 5.4) and perform the fit assuming a simple power-law form which gives us a mean fit line (as given by the *magenta line* in Figure 6.16).
2. Calculate the 1σ scatter at the four richness cuts used using Equation 6.13.
3. Add/subtract the above scatter from the mean fit line (passing through the N_{200} vs M_{halo} plot) to get the corresponding $\pm 1\sigma$ M_{halo} values.

Once we have done the above procedure, we calculate the bias (b) as defined by Equation 5.4 for all the $\overline{M_{halo}}$ samples along with their $\pm 1\sigma$ M_{halo} samples (the values of the same

are mentioned in Table 6.11). It can be seen from Figure 6.21a that the bias of all our $\overline{M_{halo}}$ cut samples follow exactly the same trend as their corresponding N_{200} cuts and are within $\pm 1\sigma$ uncertainty. But due to the large scatter that exists in the relation between mass and richness, the errors on the bias values obtained for the mass cut samples (as seen in Figure 6.21a) cannot be used if we want to compare it with the bias of the richness cut samples.

To compare the bias of the mean mass ($\overline{M_{halo}}$) corresponding to a specific richness, we use the $\pm 1\sigma$ $\overline{M_{halo}}$ bias values obtained from the scatter $\sigma_{\log_{M_{halo}}}$ as defined in Equation 6.13. As the scatter decreases with increasing mass/richness (see Table 6.11), we expect the errors on the bias of $\overline{M_{halo}}$ to follow a similar pattern. One can see from Figure 6.21b (also from Table 6.11) that it is not clearly evident for all the samples at all the redshift ranges. The reason for this behaviour is partly due to the statistical noise that affects the values of $\xi(r)$ for certain samples, i.e. there are lesser number of clusters at both $z < 0.4$ and $z > 1.3$ as it can be seen from Figure 5.5. The $\xi(r)$ values obtained for these samples are not clearly consistent and tend to fluctuate, i.e. deviate from a power-law, within the 5-50 Mpc range in which we calculate the bias. It is also due to the above factor, that the bias values calculated for the $N_{200} > 45$ sample have been done only in those ranges wherein $\xi(r)$ follows a power-law instead of the 5-50 Mpc as used for the other three richness cuts.

On the other hand, we can see that for the redshift range ($0.4 < z < 1.3$) the error on the bias obtained from the observable (i.e. the bias of, M_{halo} obtained from N_{200}) does decrease as expected with increase in mass. It can be visualised in Figure 6.21b and also from Table 6.11. Overall we see that the bias values calculated for a specific richness cut sample when compared with the corresponding $\overline{M_{halo}}$ sample taking into account the scatter that exists seem to fall within a 1σ precision for all the samples we have studied. The large error bars at lower ($z < 0.4$) and higher ($z > 1.3$) redshifts are due to the very few number of clusters available.

From the above studies, we can see that cluster mass and richness are tightly correlated. The best-fit parameters that we have obtained for our particular richness cut and mass cut samples are very similar. The bias of the richness cut samples also depict a similar evolution in richness (within 1σ) compared to the mass cut samples. But however, due to the scatter that exists in the mass-richness relation, we still cannot conclude whether a specific richness cut sample corresponds to a specific mass cut sample. There are also other complications such as projection effects, false positives etc., that arise in a real observational scenario that were not taken into account which needs to be addressed. Application of the above exercise on clusters detected from cluster finding algorithms needs to be addressed and will be pursued in a future work.

6.3.4 Combined effect of richness and photometric redshift errors on the two-point correlation function

So far we have only studied the evolution of the two-point correlation function with richness (N_{200}) cuts in cosmological redshift space and have recovered the correlation function from

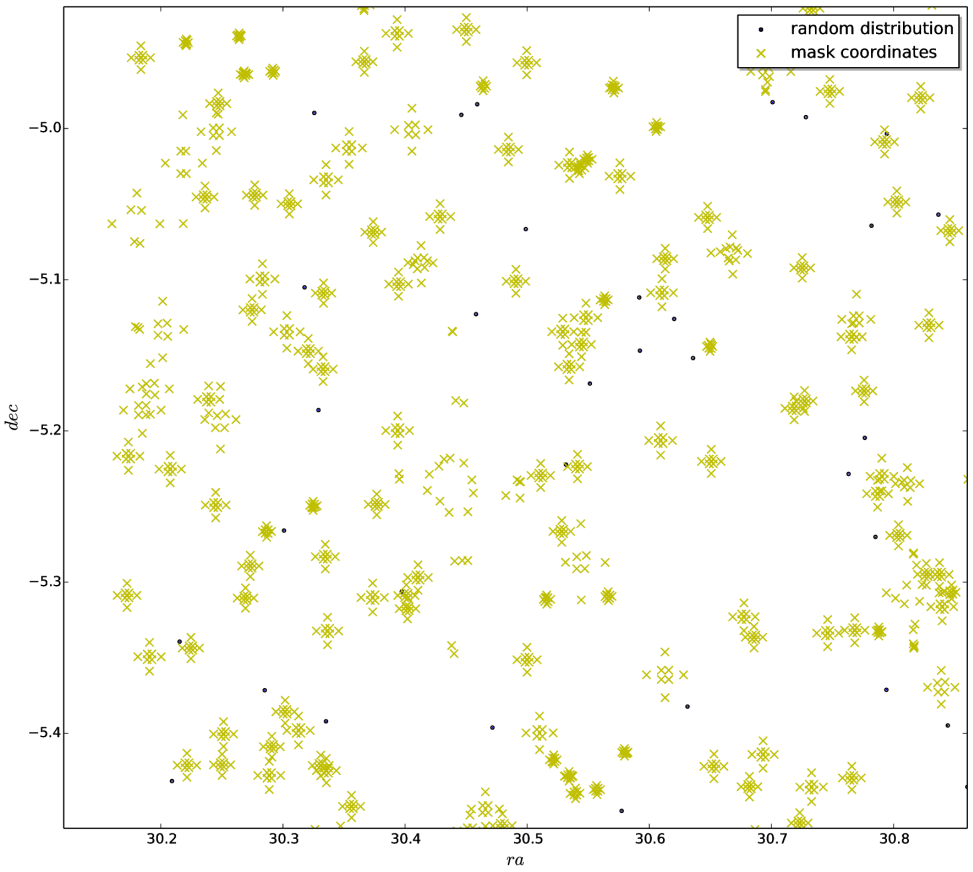

Figure 6.22: A subset of the RA and DEC of a random catalogue. The masked coordinates are plotted by the green crosses and the random coordinates are plotted by the blue dots.

photometric redshift catalogues that have been generated using the Gaussian approximation technique. In this section, we study the combined effect of the photometric redshift errors and richness cut on the two-point correlation function. It has been shown in Section 6.2.5 that by using the deprojection method, the two-point correlation function of mass cut cluster samples can be recovered within a given percentage depending on the photometric redshift uncertainty.

As a preliminary test, to evaluate the combined effect of photometric redshift errors and richness on the two-point correlation function, we select two richness cut samples ($N_{200} > 10$ and $N_{200} > 15$) with a photometric redshift uncertainty of $0.010 \times (1 + z_c)$, the same redshift uncertainty as used to test the effect of purity and completeness on the correlation function. We apply the deprojection method as explained in Section 6.2.2 to the richness cut samples and find out to which accuracy do we recover the real-space correlation function. The results

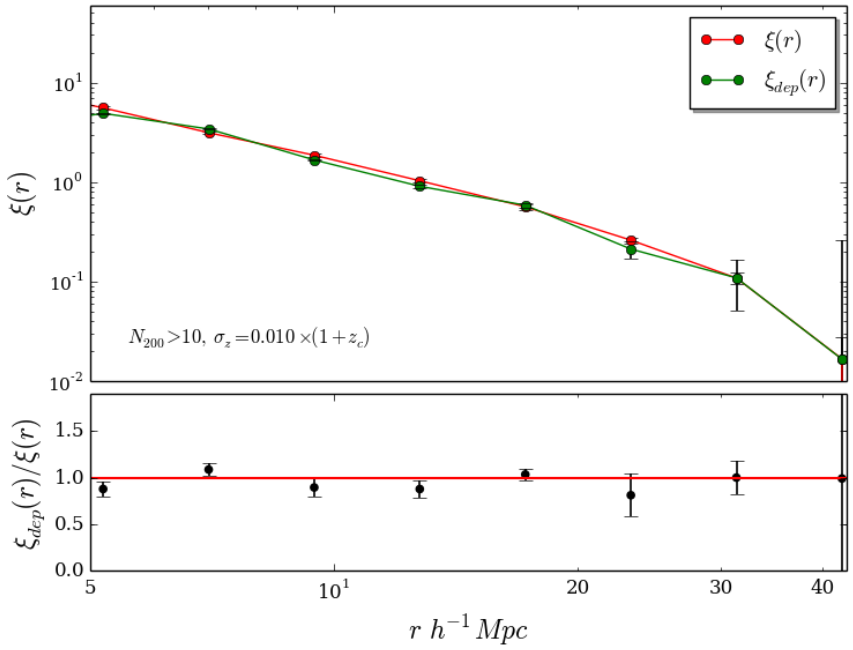

(a)

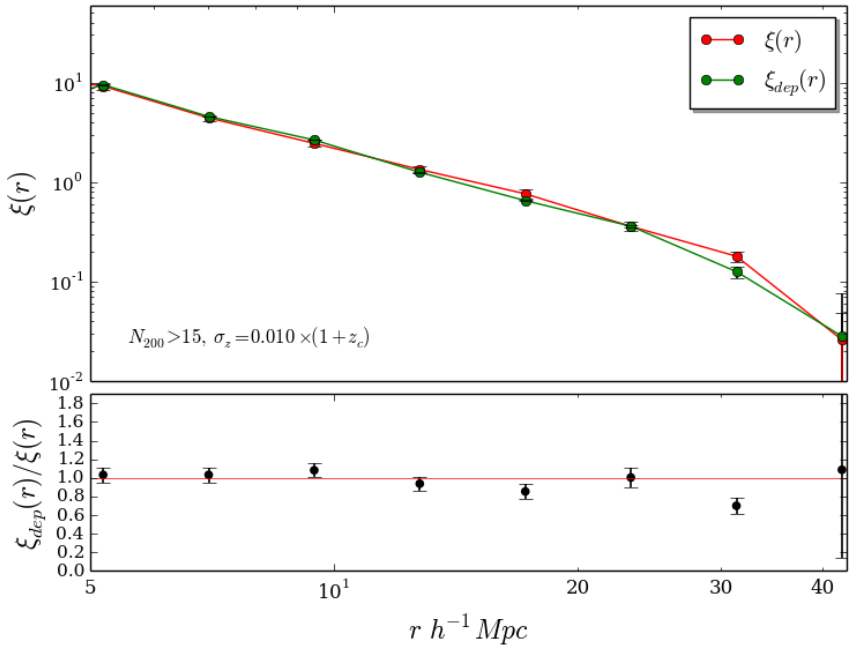

(b)

Figure 6.23: *On top:* The two-point correlation in real-space for the $N_{200} > 10$ richness cut sample within the redshift range $0.4 < z_c < 0.7$ as given by the *red line* along with the recovered real-space correlation function using the deprojection method for the same richness cut sample as given by the *green line*. *Bottom:* The two-point correlation in real-space for the $N_{200} > 15$ richness cut sample within the redshift range $0.4 < z_c < 0.7$ as given by the *red line* along with the recovered real-space correlation function using the deprojection method for the same richness cut sample as given by the *green line*. The lower panels in both the figures indicate the ratio $\xi_{dep}(r)/\xi(r)$. Error bars have been calculated using the jackknife-resampling method.

Table 6.12: The quality of recovery obtained for the two richness cut samples. The columns indicate: (1) Richness cut, (2) the values of $\Delta\xi$ and (3) $\widehat{\Delta\xi}$ for the sample with a photometric uncertainty of $0.010 \times (1 + z_c)$. The range of scales r used for the fit is fixed at 5-50 Mpc.

Richness	$\Delta\xi$	$\widehat{\Delta\xi}$
$N_{200} > 10$	0.069	0.065
$N_{200} > 15$	0.071	0.071

of the same can be seen in Figures 6.23a and 6.23b and the quality of the recovery as given by the averaged normalised residual $\Delta\xi$ and $\widehat{\Delta\xi}$ is given in Table 6.12.

It can be seen from the lower panels of Figures 6.23a and 6.23b that the ratio $\xi_{dep}(r)/\xi(r)$ fluctuates around 1 and is within 1σ at all scales for both the richness cut samples indicating that $\xi_{dep}(r)$ is not biased. One can also see from Table 6.12 that the real-space correlation function is recovered within 7% for the $N_{200} > 10$ sample and within 8% for the $N_{200} > 15$ sample.

For this preliminary test, we have restricted ourselves to a photometric redshift uncertainty of $0.010 \times (1 + z_c)$ and two richness cut samples $N_{200} > 10$ and $N_{200} > 15$. With regard to the redshift evolution of $\xi(r)$ for the richness cut samples with varying photometric redshift errors, we expect the recovery of the correlation function to follow a similar trend as obtained for the mass cut samples as seen in Section 6.2.5 and Figure 6.11.

6.4 Application on observational catalogues: CFHTLS survey

All the tests performed so far on the recovery of the correlation function have been done on simulated cluster catalogues. In Section 6.2.2 we have tested the effects of redshift errors on the correlation function and have shown that they can be recovered using the deprojection method up to photometric uncertainties of $\sigma_z = 0.05 \times (1 + z)$. We have also calculated the redshift evolution of the two-point correlation function for richness cut samples from the simulated catalogue along with the redshift evolution of the bias. In Section 6.2.6 and 6.3.4 we have shown the effects of purity and completeness separately on the recovery of the correlation function and also the combined effects of richness and photometric redshift errors on the recovery. These are effects that have to be taken into account when one applies the method on real cluster catalogues. We make use of the data from Canada-France-Hawaii-Telescope Legacy Survey (CFHTLS) and apply the deprojection method on the observational cluster catalogue for which clusters have been detecting using a cluster finding algorithm.

The CFHTLS is composed of four separate Wide fields, divided into 171 individual pointings, covering a total area of 155 deg^2. We use the T0007 (7^{th} and final release) produced by Terapix, based on the data collected from MegaCam (Cuillandre et al., 2012). With a

Number of clusters	8,806
Redshift range	$0.02 < z_{phot} < 1.26$
Area [deg^2]	~ 65
$\bar{z}$	0.536

Table 6.13: Properties of the CFHTLS galaxy cluster sample used in this work.

total sky coverage of 8.5×7.5 deg^2 extending up to a redshift of $z \sim 1.3$ (Cuillandre et al., 2012), the W1 field (largest of the 4 fields covered by the CFHTLS survey) is used for the cluster selection. The deprojection method is then applied to estimate the correlation function on CFHTLS detected galaxy cluster samples using WAZP (Benoist et al. in prep). The main properties of the clusters used in this work is mentioned in Table 6.13. The data release T0007 catalogue of clusters makes use of u*, g$'$, r$'$, i$'$, z$'$ photometry and z_{phot} computed with LePhare (Ilbert et al., 2009).

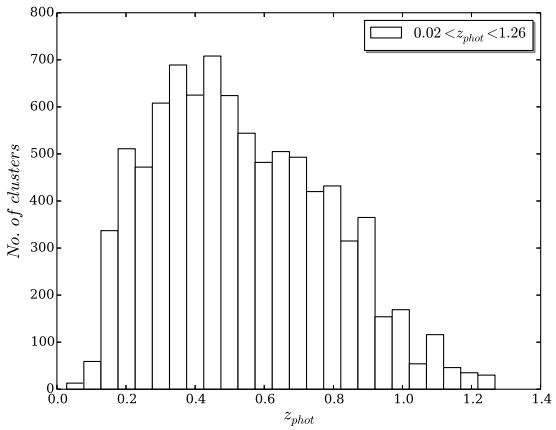

Figure 6.24: Redshift distribution of the entire CFHTLS W1 field clusters within $0.02 < z_{phot} < 1.26$.

6.4.1 Creating the random catalogue

Some regions of the sky are assumed to be "bad" because they are at close proximity with stars or border areas of the survey. These regions are usually "masked" to remove the noise from these sources, but on the other hand we loose data detected at these regions. It is usually better to remove them completely than including them for our final analyses. These masks are in the regions needed to be masked are usually not in a particular position of the survey coverage, and so do not bias the projected cluster distribution. The CFHTLS T0007 release makes use of Terapix masks generated on all the four wide fields and the details of the same

can be found in Cuillandre et al. (2012). We however add a few more masks to certain regions according to our scientific goals.

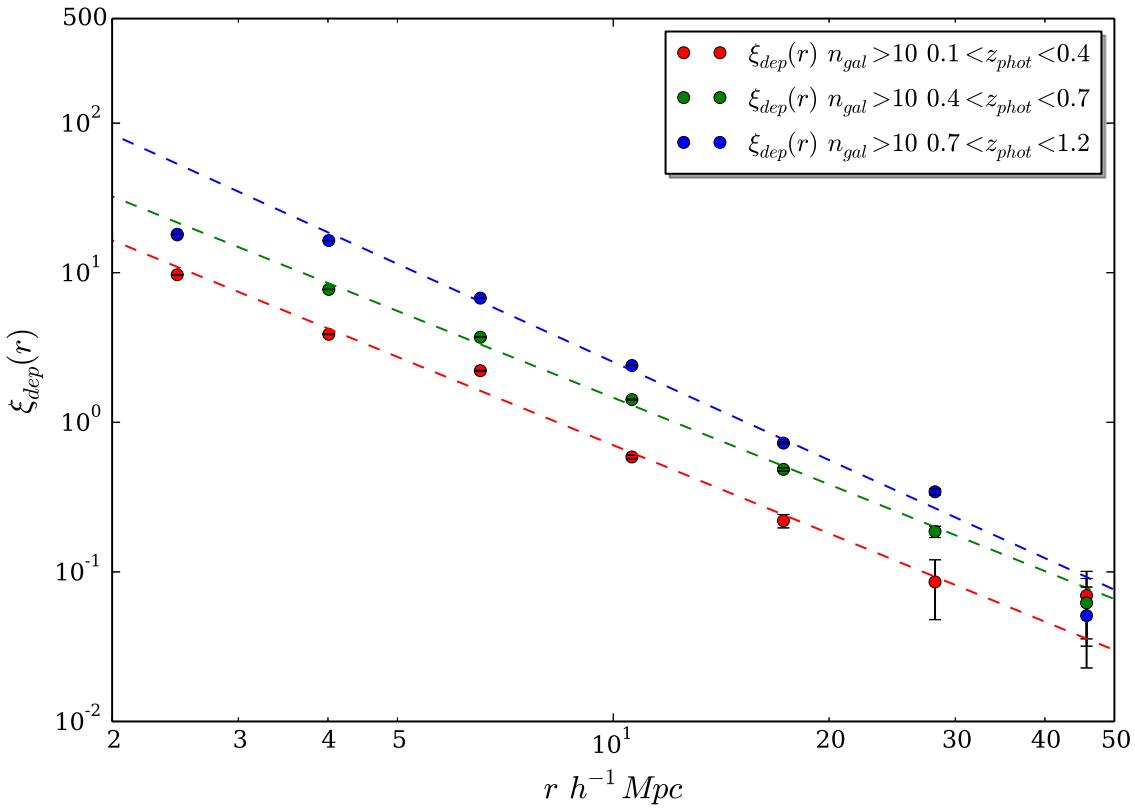

Figure 6.25: The correlation function for the CFHTLS clusters with a given richness cut $N_{gal} > 10$ in 3 different redshift ranges. The dashed lines show the corresponding power-law best fits. The parameter values for the fits can be found in Table 6.14.

For the random catalogue the RA and DEC are first assigned randomly within the survey limits. We then remove those points that fall inside the masks (in our case the masks are in the form of polygons). For the final random catalogue used to calculate the two-point correlation function, we only include those points that fall outside the masked regions. In Figure 6.22 we plot a subset of RA and DEC for one of our random catalogues. Here the masked regions (which are polygons) are given by the green crosses and the blue points represent our random coordinates.

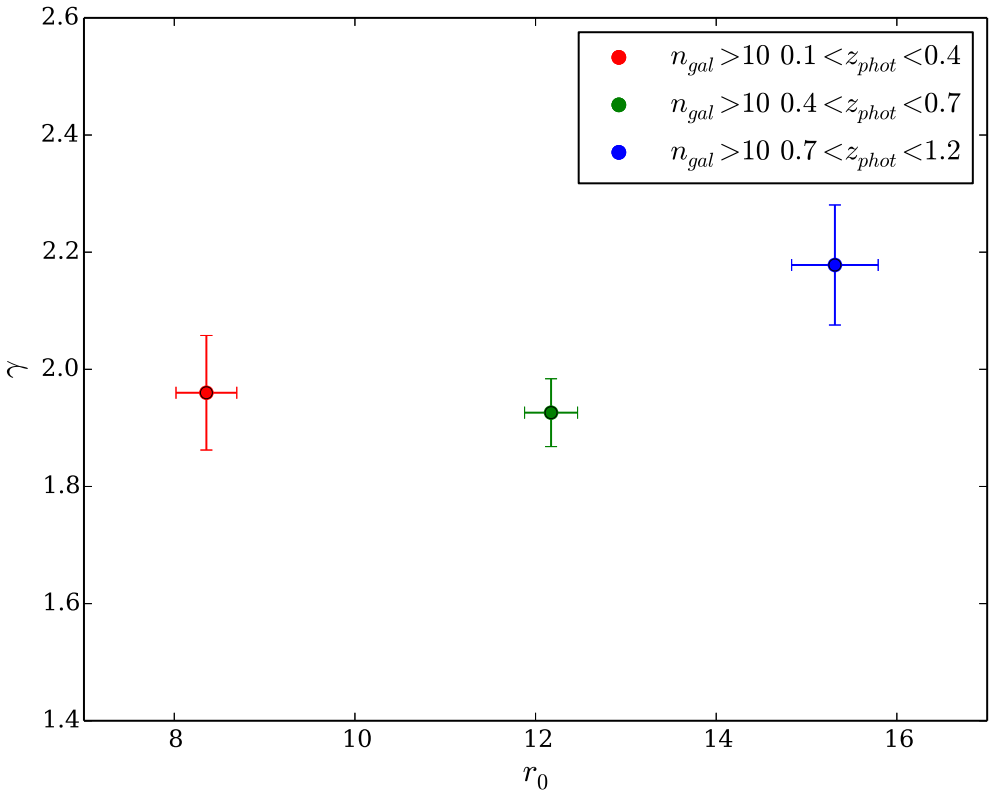

Figure 6.26: The r_0 vs γ as obtained from the fit to the $\xi(r)$ for the clusters with a richness cut $N_{gal} > 10$. The parameter values for the fits can be found in Table 6.14.

Mass	z	r_0	γ	Number of objects
$N_{gal} > 10$	$0.1 < z < 0.4$	8.35±0.33	1.95±0.09	1119
	$0.4 < z < 0.7$	12.17±0.29	1.92±0.05	1501
	$0.7 < z < 1.2$	15.31±0.47	2.09±0.10	761

Table 6.14: The parameters obtained from the fit for the correlation function $\xi(r)$ for the CFHTLS cluster sample with $N_{gal} > 10$.

6.4.2 Two-point correlation function: Richness cut photometric redshift samples

We have clusters within a richness range $5 < N_{gal} < 95$, but the richness peaks close to $N_{gal} \sim 10$. For the redshift evolution of the cluster correlation function, we use a richness cut of $N_{gal} > 10$ so that we are sure that we will have enough clusters to account for statistics and that the contamination by false detections is limited. We separate the clusters into three redshift bins ($0.1 < z < 0.4$, $0.4 < z < 0.7$ and $0.7 < z < 1.2$). The width of the redshift bins are chosen similar to that of the simulations as done in Chapter 3. For the final bin, we choose a much larger bin width ($0.7 < z_{phot} < 1.2$) as one can see from Figure 6.24 that we fall short of clusters above a redshift $z_{phot} \sim 0.8$. Once we have separated our samples into redshift slices, we calculate the deprojected correlation function (see Section 6.2.2) for these samples and estimate the best fit parameters r_0 and γ.

The photometric redshift uncertainty for galaxies observed from the CFHTLS T0007 release is close to $\sigma_z = 0.03 \times (1 + z)$. We have seen in Section 6.2.5 that $\xi(r)$ can be recovered within 10% errors for a photometric uncertainty of $\sigma_z = 0.030 \times (1 + z)$ (also seen in Figure 6.9).

It can be seen from Figure 6.25 and Figure 6.26 that the evolution of the clustering strength with redshift for a fixed richness threshold cut ($N_{gal} > 10$) is significantly detected. The slope obtained from the best-fit for all the three redshift ranges is close to $\gamma = 1.8$, which is the universal value expected for galaxy clusters (Bahcall and West, 1992; Governato et al., 1999; Basilakos and Plionis, 2004; Estrada et al., 2009; Hong et al., 2012, and references therein). We would like to understand the richness evolution of the correlation function in terms of mass. Scaling of richness with other mass proxies such as weak-lensing masses from CFHT-Lens or X-ray proxies from XXL can be analysed to understand it.

6.5 Conclusions from this chapter

1. Photometric redshift errors affect only the line of sight distance and not the transverse plane, so correlation is lost only in one direction which destroys isotropy. These er-

rors increase with redshift according to $\sigma_z = \sigma_{(z=0)} \times (1 + z_c)$. We create photometric redshifts based on Gaussian distribution with known dispersion and mean and try to recover the real-space correlation function.
Weighting all the clusters according to the method mentioned in Section 6.2.4 to overcome the effect of the top-hat distribution of cluster selection in a photometric redshift window does not seem to work very well, i.e. $\xi(r)$ is overestimated. The results of the same are mentioned in Section 6.2.4.2. So we make use the deprojection method as mentioned in Section 6.2.2 with the same cut in the photometric redshift window as compared to the cosmological redshift window.
The recovery of the real-space correlation function using the deprojection method for galaxy clusters seems to work even for high redshift uncertainties. We recover $\xi(r)$ well within 7% on the average for scales $5 < r < 50\ h^{-1}$Mpc even for a cluster catalogue with a redshift uncertainty of $\sigma_{(z=0)} = 0.010$ and well within 9% on the average for samples with $\sigma_{(z=0)} = 0.030$. We also fitted both the real-space correlation function and the projected correlation function using their corresponding fitting equations. The parameters obtained from the fit for the mock photometric samples were then compared with the same obtained for the z_c parent sample with $M_{halo} > 5 \times 10^{13}\ h^{-1}\ M_\odot$. We find that for almost all of our mock photometric samples, the correlation length is close to $r_0 = 13.16 \pm 0.17$ (fixed slope $\gamma = 2.0$) and $r_0 = 13.20 \pm 0.23$ (free slope), the values obtained for the z_c sample.

2. By applying the deprojection method to calculate $\xi_{dep}(r)$ for the catalogues with a redshift uncertainty of $\sigma_{(z=0)} = 0.005, 0.010, 0.030$ and 0.050, the redshift evolution of the correlation function was studied and compared with the z_c sample. We find that the best-fit parameters obtained for all the photo-z samples are within the 1σ uncertainty of the best-fit parameters obtained for the z_c sample in all the redshift ranges studied up to $z \approx 2.1$.

3. The redshift and mass evolution of the bias obtained for all the photometric redshift samples is compared with the redshift and mass evolution obtained for the cosmological redshift samples with the same redshift and mass cut. Up to a mass cut of $M_{halo} > 5 \times 10^{13}\ h^{-1}\ M_\odot$ the bias is recovered within 1σ even for samples with a photometric redshift uncertainty of $\sigma_z = 0.050 \times (1+z_c)$ and up to a median redshift of $\bar{z} \sim 1.8$. For the sample with a mass cut of $M_{halo} > 1 \times 10^{14}\ h^{-1}\ M_\odot$ the same trend is seen up to a median redshift of $\bar{z} \sim 1.5$. For the maximum mass cut $M_{halo} > 2 \times 10^{14}\ h^{-1}\ M_\odot$, the bias is recovered within 1σ, but the amplitude of the bias for the photometric samples above $0.005 \times (1 + z_c)$ increase when compared to the bias for the z_c sample. This we believe is due to the number of clusters that exists at this mass cut, which causes the two-point correlation function to deviate from a power-law at a very short distance scale. We also believe it can be due to the percentage of contaminants that are present in this mass cut sample for the three different photometric uncertainties.

4. We have compared the two richness definitions $N_{200}(total)$ and N_{200} with mass M_{halo} in different redshift slices. We find that the overall scatter between $N_{200}(total)$ and M_{halo} is larger compared to the overall scatter between N_{200} and M_{halo}. This is because of the evolution of the characteristic magnitude with redshift for N_{200} and for $N_{200}(total)$ we include all the galaxies within a virial radii regardless of the redshift. We also notice that this scatter becomes similar at high redshifts as both the richness definitions at high redshifts include almost the same galaxies.

5. There exists scatter in the mass-richness relation and this scatter increases with decreasing richness/mass cut. To calculate the scatter at a given richness, we assume a lognormal distribution of M_{halo} as a function of N_{200}. We find that the above approximation seems to be a good fit for the mass distribution above a given richness cut. We also find that the scatter in mass at a given richness cut decreases at a much faster rate from a richness cut of $N_{200} > 10$ up to $N_{200} > 50$, beyond which the rate of the decrease of the scatter drops. A similar result is obtained by Rykoff et al. (2012) for the richness cut samples from the maxBCG catalogue.

6. We calculate the two-point correlation function for samples with increasing richness cuts to see how they evolve. We find out that the evolution in richness is similar to that obtained for our mass cut samples and we also get similar best-fit parameters from the fit to $\xi(r)$ assuming the power-law approximation as mentioned in Equation 3.13.

7. Due to the scatter that exists between the mass-richness relation, one cannot directly compare a given mass cut sample and richness cut sample. To do so, we calculate the bias for four arbitrary richness cut samples chosen at each of the 5 redshift bins and compare the same with the bias calculated for the corresponding $\overline{M_{halo}}$ samples, with $\overline{M_{halo}}$ being the mean mass obtained from the fit performed to the mass-richness sample using the generic equation as mentioned in Table 6.9.
   We find out that the bias values calculated for a specific richness cut sample when compared with the corresponding $\overline{M_{halo}}$ sample taking into account the scatter that exists seem to fall within a 1σ precision for all the samples we study.

8. We calculate $\xi(r)$ for optically selected clusters detected from the CFHTLS survey. The clusters are detected using wavelet adaptive method (Benoist et al. in prep) and we choose different richness cut samples from the catalogue. We find that by applying the deprojection method to these photometric cluster catalogues, we are able to recover the real-space correlation function and get best-fit parameters that are comparable to that expected for a cluster catalogue.

Chapter 7

General conclusions and future prospects

Contents

7.1 Summary of this thesis

In this thesis we have focused on galaxy clusters and their usage towards constraining cosmological parameters.

In Chapter 1, we discussed the the history of the current cosmological framework, reviewed some of the theoretical foundations of cosmology and also the theoretical framework of large-scale structure formation.

In Chapter 2, we discussed some of the key issues related to galaxy clusters, i.e. how they are detected and how their masses are measured.

In Chapter 3, we introduced the two-point correlation function, and revisited some of the historical studies of the galaxy and cluster two-point correlation function.

In Chapter 4, a brief introduction towards utilising galaxy clusters as cosmological probes was discussed.

These four chapters have laid the foundation towards understanding some of the core concepts of large-scale structure formation, cosmology using galaxy clusters and also some of the concepts used in this thesis. The results obtained in this thesis have been divided into two chapters.

In Chapter 5, the two-point correlation function and its evolution with both mass and redshift were studied. To do so we made use of a simulated cluster catalogue provided by Merson et al. (2013). We have verified that the amplitude of $\xi(r)$ increases with both mass

and redshift. The cluster bias was calculated for our samples and we found out that it closely followed the theoretical bias function of Tinker et al. (2010). We also fitted the $r_0 - d$ relation for our redshift samples using a simple power-law model and found out that it matches with the relation obtained by Younger et al. (2005) for another set of simulated clusters (following a similar cosmology).

In Chapter 6, the evolution of $\xi(r)$ with both mass and redshift was studied, but for ideal samples derived from photometric redshifts (created using a Gaussian approximation). We have shown that we could recover the real-space correlation function based on a deprojection method with different uncertainties and found out that the real-space two-point correlation function could be recovered within 10% for a photometric redshift sample with an uncertainty of $\sigma_z = 0.030 \times (1 + z_c)$. The redshift and mass evolution of $\xi_{dep}(r)$ (recovered real-space correlation funciton) was compared with $\xi(r)$ (correlation function of the cosmological redshift sample) and we found out that the best-fit parameter obtained were within 1σ uncertainty even up to a redshift of $z \approx 2.0$ for all the photometric redshift samples with different uncertainties considered.

The evolution of the cluster bias (with both mass and redshift) obtained from our photometric cluster catalogues were compared with the bias obtained from our cosmological cluster catalogue. We found out that up to a mass cut of $M_{halo} > 5 \times 10^{13}\ h^{-1}\ M_{\odot}$ the bias was recovered within 1σ even for the sample affected by the largest photometric redshift errors ($\sigma_z = 0.050 \times (1 + z_c)$) up to a median redshift of $\widetilde{z} \sim 1.8$. For the sample with $M_{halo} > 1 \times 10^{14}\ h^{-1}\ M_{\odot}$ the same trend was found up to a median redshift of $\widetilde{z} \sim 1.4$ and for the sample with $M_{halo} > 2 \times 10^{14}\ h^{-1}\ M_{\odot}$, the bias was recovered within 1σ but the amplitude of the bias for the photometric samples above $0.005 \times (1 + z_c)$ increase when compared to the bias obtained for the z_c sample due to less statistics.

We calculated $\xi(r)$ in bins of richness N_{200} to calculate the evolution of the two-point correlation function and tried to recover $\xi(> mass)$ by exploiting the mass-richness relation. The mean scatter in the mass-richness relation was calculated assuming a lognormal distribution of M_{halo} as a function of N_{200}. The $\xi(r)$ for four arbitrary richness cut samples was calculated and compared with the same obtained for the mass cut samples for which the mass was obtained from the fit of the $M_{halo} - N_{200}$ relation. By comparing the best-fit parameters obtained we found out that the evolution in richness is similar to that obtained for our mass cut samples.

To compare our richness and mass cut samples, we calculated the bias for our richness cut samples and compared the same with the bias calculated for the corresponding $\overline{M_{200}}$ samples. The bias for a specific richness cut was found to fall within 1σ precision for all the samples we studied.

As a preliminary attempt towards working with real observational data, we applied the deprojection method and calculated the $\xi(r)$ for a sample of optically selected clusters from the CFHTLS survey. We found out that the best-fit parameters obtained follows the general trend expected from galaxy cluster catalogues (Bahcall and Soneira, 1983; Basilakos and

Plionis, 2004; Estrada et al., 2009, and references therein).

Below, we present extensions of this work, which, as an ultimate goal, is to constrain cosmological parameters using galaxy cluster information.

7.2 Future perspectives

The aim of this thesis was to specifically find out how redshift errors affect the two-point correlation function and to what extent can they be recovered and how. The results obtained are just one piece of the "puzzle". Our study should be extended towards a broader perspective so that constraints on cosmological parameters can be obtained.

Galaxy cluster counts obtained from cluster catalogues have been used to constrain cosmological parameters (Fang and Haiman, 2007; Mana et al., 2013; Planck Collaboration et al., 2015, and references therein). But it has been shown that by combining the cluster two-point correlation information with cluster counts, constraints obtained on the cosmological parameters are improved (Majumdar and Mohr, 2004; Sartoris et al., 2016; Lacasa and Rosenfeld, 2016, and references therein). In addition to the above, it has been shown that cluster mass observables can be connected with the bias of the two-point correlation function to do a self calibrated cosmological analysis. (Majumdar and Mohr, 2003; Lima and Hu, 2004). More recently, Baxter et al. (2016) have measured the clustering biases of clusters selected from the redMaPPer catalogue (Rykoff et al., 2014) and by using the measured correlation functions along with the predicted bias $b(M)$, calibrated the mass richness relation. Baxter et al. (2016) mention that although their constraints (on the amplitude of the mass-richness relation) are affected by systematic uncertainties, the constraints on some of their parameters such as the slope of the mass richness relation are strongly affected by statistical rather than systematic uncertainties. Ongoing and future large-scale surveys such as DES (The Dark Energy Survey Collaboration, 2005), KIDS (de Jong et al., 2013), VIKING (Edge et al., 2013), LSST (LSST Dark Energy Science Collaboration, 2012) and Euclid (Laureijs et al., 2011, 2014) probe large volumes (reducing the cosmic variance) and observe high redshift galaxies. The larger the volume probed by a survey, the larger is the statistical information, and thus lower are the errors. Thus, studies similar to those done by Baxter et al. (2016) can be performed on these large surveys, by expecting the errors on the parameters obtained to be comparatively lesser.

But for most of these large-scale surveys, the majority of the redshifts measured will be via photometry. Our exercise has shown that the two-point correlation function can be recovered within 10% for photometric cluster catalogues with an uncertainty of $\sigma_z = 0.03 \times (1+z)$ even up to a redshift of $z \sim 2.0$. The cluster counts along with the two-point correlation function measured from these surveys should thus indicate the level of precision with which we can recover the cosmological parameters.

However, for observational catalogues, there exist several intricacies that need to be taken

into account. We describe below some of the major points that should be addressed if one wants to make use of $\xi_{CL}(r)$ to constrain cosmology.

Application on the output of cluster finders: Cluster finding algorithms (within the Euclid consortium) based on different approaches have been performed on simulated catalogues. These algorithms (having different definitions of the richness) provide as output a realistic richness estimate, and cluster catalogues with varying purity and completeness, which should be incorporated along with the photometric redshift uncertainties to measure $\xi(r)$. We can try to find out if the $\xi(> N_{gal}, z_{phot}, \mathrm{SF})$ (where SF is the selection function) measured from the output of the cluster finders can be used to derive $\xi(M, z_c)$ (z_c is the cosmological redshift) and thus constrain the mass.

Application on larger simulations: As cosmological probes require simulations with large volumes, experiments can be repeated on other cosmological simulations with a better mass resolution, more volume, a different way of identifying dark matter particles (other than the Friends-Of-Friends algorithm used in our simulation) and different ways in which galaxies are included. This test can be utilised to find if the results obtained follow the same general trend irrespective of the differences in the simulations and also to find whether an increase in the mass resolution and volume of the simulation decreases the errors associated with the results. Simulations such as MICE (Crocce et al., 2010), Euclid flagship "full sky" simulations etc. exist, that can be utilised for these tests.

Baryon acoustic oscillations: As tracers of the biggest collapsed structures, galaxy clusters are more strongly clustered than galaxies. The spatial clustering signal of galaxy clusters is strongly amplified with respect to the underlying matter distribution, with the bias parameter b reaching values of ~ 3 and above as we have seen in Section 5.6. Measurements of $\xi(r)$ of galaxy clusters have recently provided detections of the BAO peak (Estrada et al., 2009; Hütsi, 2010; Hong et al., 2012). In order to observe these relatively small fluctuations, surveys with large volumes (to reduce cosmic variance) are required, and these large volumes will be fulfilled by ongoing and future surveys in the upcoming years. But for most of these surveys, the majority of redshifts measured will be via photometry, which will have a larger error associated with them compared to their spectroscopic counterparts.

It has been shown by Veropalumbo et al. (2014) that photometric redshift errors can have a significant impact at the BAO scales, i.e. they broaden the BAO feature, causing a loss of information at scales where the BAO peak is measured. We would like to try to use the deprojection method to recover the real-space correlation function from photometric redshift surveys, and make an attempt to detect the BAO feature from the measurements of $\xi(r)$ from these cluster surveys. However, all the issues that real observational catalogues face must be taken into account.

Appendix A

NFW profiles of the haloes in the simulation

A.1 Selecting individual clusters from the data

The data used here is a 100 deg^2 catalogue extracted from the 500 deg^2 simulated cluster catalogue (Merson et al., 2013) as described in Section 5.2. The data contains details (RA, DEC, redshift, etc.) of all the galaxies present. The details of all the properties of the galaxies are mentioned in Table A.1. Each galaxy has it's own specific `idrep` (the simulation "box" in which the galaxy is present) and `DHaloID` (the ID of the dark matter halo in which the galaxy is present). To extract individual cluster members, we need to match all those galaxies with the same `idrep` and `DHaloID`. By doing so we make sure that we do not repeat (add) the same galaxies in different clusters.

Property	Description
DHaloID	ID of the dark matter halo in the simulation
GalaxyID	ID of the galaxy in the simulation
idrep	ID of the simulation "box"
is_central	0 or 1 according to whether the galaxy is central or not
r	line of sight comoving distance to the galaxy
zcosmo	cosmological redshift of galaxy
RA	right ascension of galaxy
DEC	declination of galaxy
mhhalo	mass of the host halo

Table A.1: The properties of the galaxies in the catalogue

A.2 Calculating the distance to the central galaxy

After extracting the halos and their corresponding galaxy members, we find out the central galaxy of each halo using the property `is_central`. If a galaxy has `is_central` == 1, then

it is the central galaxy in the dark matter halo and all the other galaxies in the halo have `is_central` == 0 and are the satellite galaxies.

In order to calculate the density profiles, we find the distance of all the satellite galaxies to the central galaxy in the halo. The distance to the center is given by the equation

$$r = \frac{\theta \times D_L}{1+z} \tag{A.1}$$

where $D_L \rightarrow$ line of sight comoving distance, $z \rightarrow$ redshift, $\theta \rightarrow$ angular separation in radians. Angular separation is given by:

$$\theta = cos^{-1}\left[(cos(\alpha_1 - \alpha_2) \times cos(\delta_1 - \delta_2)) + (sin(\delta_1) \times sin(\delta_2))\left[1 - cos(\alpha_1 - \alpha_2)\right]\right] \tag{A.2}$$

where $\alpha_1, \delta 1$ are the RA, DEC of the central galaxy of the halo respectively. α_2, δ_2 are the RA and DEC of the satellite galaxies respectively.

A.3 The mass bins and density profiles

A.3.1 The mass bin selection

The mass of the host halo ($M_\odot h^{-1}$) is provided in the column `mhhalo`. For this analysis we make use of M_{200}, which is the mass of the halo contained within R_{200}. R_{200} is the distance from the center of the halo at which the density of the halo is equal to 200 times the critical density ρ_c. The critical density evolves with redshift and is given by:

$$\rho_c(z) = \frac{3H_0^2}{8\pi G} \times \left(\Omega_\lambda + \Omega_0(1+z)^3\right) \tag{A.3}$$

where G is the gravitational constant = 4.29×10^{-9}(km/s)^{2}MpcM$_\odot^{-1}$ The value of M_{200} can be inferred from the radius through:

$$M_{200} = \frac{4}{3}\pi R_{200}^3\, \rho_{200} \tag{A.4}$$

where $\rho_{200} = 200\rho_c(z)$ (i.e, 200 times the critical density). We have selected 4 mass bin samples in varying mass ranges and the details of the same are given in Table A.2. By selecting varying mass ranges we can spot the differences in the density profiles more easily.

A.3.2 The projected NFW profiles

Now we have calculated the R_{200}, the distance to central galaxy in the halo r and M_{200}. To calculate the projected number density (Σ) profiles of the haloes, the number of galaxies is counted and binned by their projected radial distance from the central galaxy. We make several bins in evenly spaced annuli (the region bounded by two concentric circles) and count the number of galaxies in each bin (N). The number density is given by,

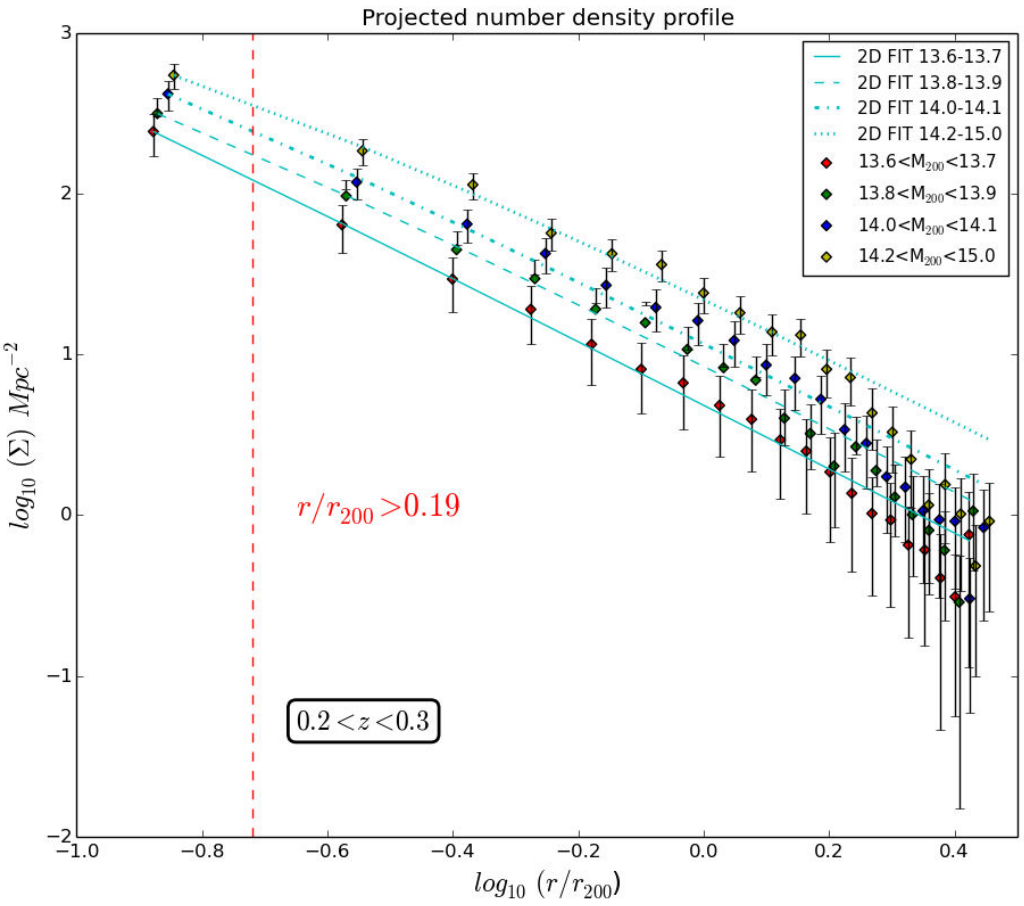

Figure A.1: The projected NFW density profiles for the four mass bins and their corresponding fits in a log-log plot. The redshift range considered is $0.2 < z < 0.3$. The fits here are made by equation A.7. The best fitting NFW profiles are shown by the cyan coloured lines and the dotted red line indicates the region from which the fit has been performed. The final mass range (in $\log_{10}$) has been widened to $14.2 < \log_{10}(M_{200}) < 15.0$ so as to include more haloes. The best fitting concentrations (c) are listed in Table A.2. Poisson error bars have been used.

$$\Sigma = \frac{N}{A} \quad (N/Mpc^2) \tag{A.5}$$

where $A \rightarrow$ area of the annuli, $N \rightarrow$ number of galaxies within the area. The NFW density profile (Navarro et al., 1996) is given by,

$$\rho(r) = \frac{\delta_c \rho_c}{(r/r_s)(1 + r/r_s)^2} \tag{A.6}$$

where $\rho_c \rightarrow$ critical density, $\delta_c \rightarrow$ characteristic over-density of the halo and $r_s \rightarrow$ characteristic scale length. r_s is the distance from the center of the halo where the density of the halo (ρ) changes from $\rho \propto r^{-1}$ to $\rho \propto r^{-3}$. The scale length r_s is also specified by the concentration parameter, and defined as $c = \dfrac{r_{200}}{r_s}$. To find out the projected density, we integrate along the line of sight and the integral can be analytically solved (Bartelmann, 1996) and expressed as:

$$\Sigma(x) = \begin{cases} \frac{2\delta_c\rho_c r_s}{x^2-1}\left[1 - \frac{2}{\sqrt{1-x^2}}\tan\, h^{-1}\sqrt{\frac{1-x}{1+x}}\right] & x < 1, \\ \frac{2\delta_c\rho_c r_s}{3} & x = 1, \\ \frac{2\delta_c\rho_c r_s}{x^2-1}\left[1 - \frac{2}{\sqrt{x^2-1}}\tan^{-1}\sqrt{\frac{x-1}{x+1}}\right] & x > 1, \end{cases} \tag{A.7}$$

where $x = \dfrac{r}{r_s}$. By using the above equation, we can find the best fitting amplitudes and concentrations for the projected NFW profiles.

To perform our fit, we consider three samples in different redshift ranges and varying mass ranges as previously mentioned. From Figure A.1 we can see that the NFW profile does seem to fit quite well the density profiles of the haloes irrespective of the mass. At smaller scales $0.1 < r/r_{200} < 1.6$ Mpc, the fit seems to be good and at larger scales $r/r_{200} > 1.6$ Mpc the fit seems to overestimate the density. This is partly because of the very few number of haloes that exist at these distance scales (see Table A.2). This also has an effect on the error bars that exist at larger scales. It is also wise to note that the final mass range has been widened to $14.2 < \log_{10}(M_{200}) < 15.0$ as we don't find many haloes in the range $14.2 < \log_{10}(M_{200}) < 14.3$, and by doing so we make sure our sample is statistically significant. The fit performed has not been done from the centre of the halo but from a distance $r/r_{200} > 0.19$. This is because the fit tends to over-predict the concentrations by a huge margin if performed from the centre.

The fit has also been performed for two more redshift ranges ($0.3 < z < 0.5$ and $0.5 < z < 0.7$) and we note that the NFW profile does seem to fit well. The fit can be seen in Figure A.2.

The error bars used here are Poisson error bars, which are given by:

$$\sigma = \frac{\sqrt{N}}{A} \tag{A.8}$$

For the first sample in the range $0.2 < z < 0.3$ (red line in Figure A.3) we find that there seems to be a decrease in the concentration with increasing mass, (i.e $c \propto m^{-1}$). This tells us that the most massive haloes ($\log_{10}(M_{200}) > 14.0$) seem to be less centrally populated compared to the less massive ones ($\log_{10}(M_{200}) < 14.0$). Whereas for the other two samples in range $0.3 < z < 0.5$ (green line in Figure A.3) and $0.5 < z < 0.7$ (blue line in Figure A.3) we find a slight increase of concentration with increasing mass, but is not a continuous trend.

Mass Bin ($\log_{10}(M_{200})$)	Redshift range	Number of haloes	concentration (c)
13.6< $\log_{10}(M_{200})$ <13.7	0.2 < z < 0.3	84	13.61±3.68
13.8< $\log_{10}(M_{200})$ <13.9	0.2 < z < 0.3	36	9.99±3.16
14.0< $\log_{10}(M_{200})$ <14.1	0.2 < z < 0.3	23	5.10±2.25
14.2< $\log_{10}(M_{200})$ <15.0	0.2 < z < 0.3	8	5.44±2.33
13.6< $\log_{10}(M_{200})$ <13.7	0.3 < z < 0.5	312	5.70±2.38
13.8< $\log_{10}(M_{200})$ <13.9	0.3 < z < 0.5	142	8.17±2.85
14.0< $\log_{10}(M_{200})$ <14.1	0.3 < z < 0.5	77	6.76±2.60
14.2< $\log_{10}(M_{200})$ <15.0	0.3 < z < 0.5	105	7.90±2.81
13.6< $\log_{10}(M_{200})$ <13.7	0.5 < z < 0.7	456	5.02±2.24
13.8< $\log_{10}(M_{200})$ <13.9	0.5 < z < 0.7	257	4.20±2.04
14.0< $\log_{10}(M_{200})$ <14.1	0.5 < z < 0.7	125	5.71±2.38
14.2< $\log_{10}(M_{200})$ <15.0	0.5 < z < 0.7	127	8.27±2.87

Table A.2: The properties of the haloes and their corresponding concentrations obtained from the fit.

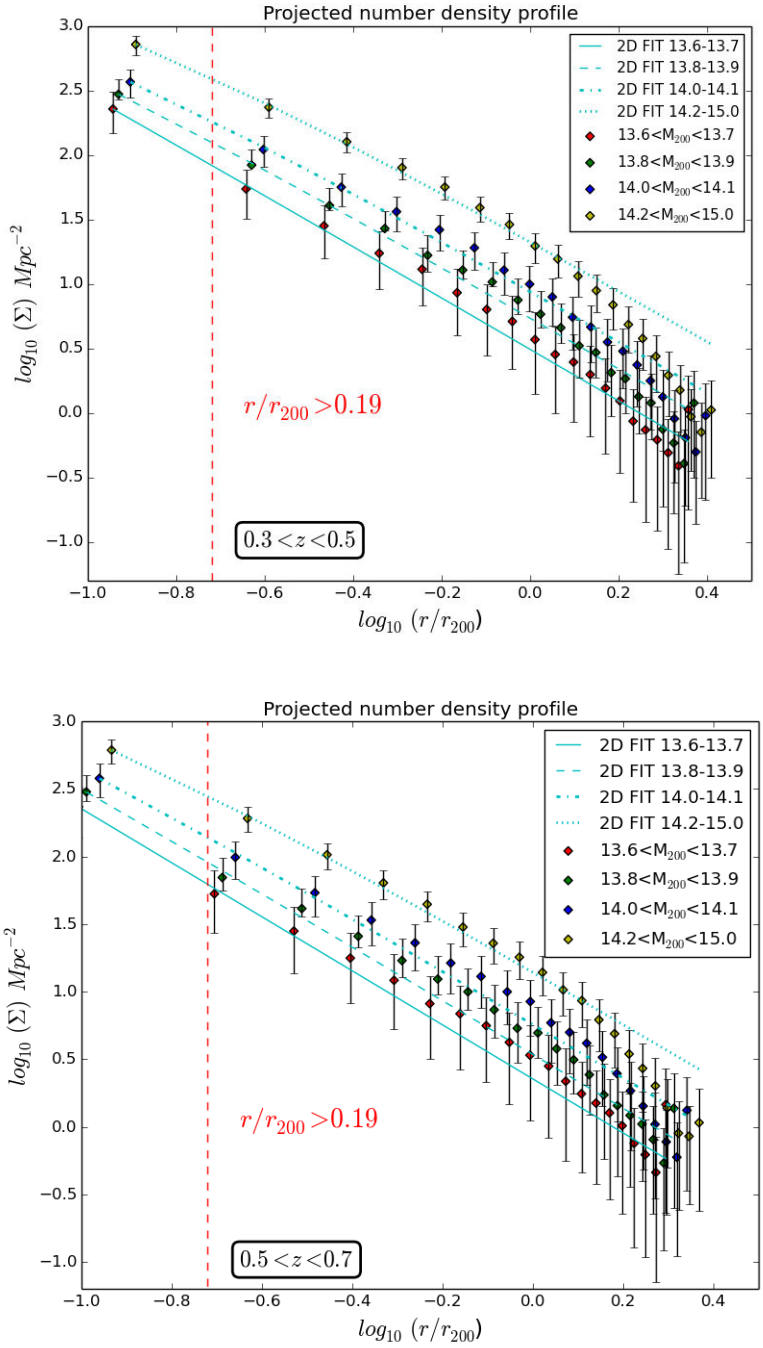

Figure A.2: *On top:* The projected NFW density profiles for the redshift range $0.3 < z < 0.5$, *Bottom:* the projected NFW density profiles for the redshift range $0.5 < z < 0.7$. The best fitting NFW profiles are shown by the cyan coloured lines and the dotted red line indicates the region from which the fit has been performed. The best fitting concentrations (c) are listed in Table A.2. Poisson error bars have been used.

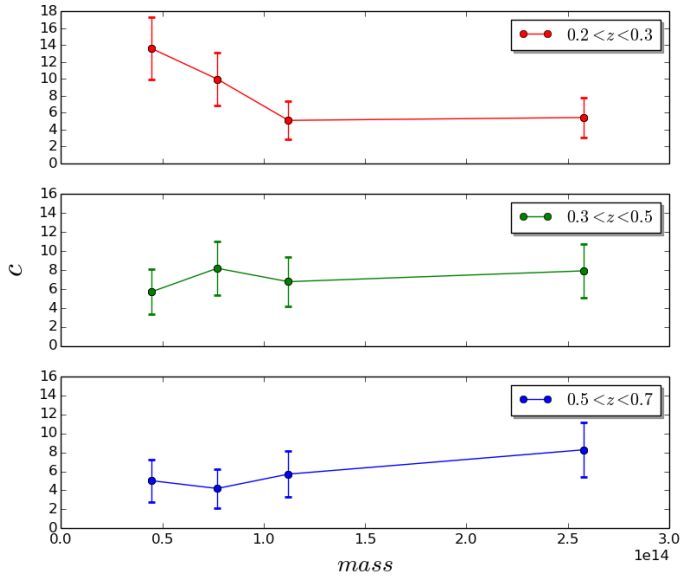

Figure A.3: The variation of the concentration with mass for the three redshift ranges considered. It is wise to note that the x-axis is mass and all the numbers shown are to be multiplied by 10^{14}.

Appendix B

Luminosity function & selection effects: Malmquist bias, K-correction

Large scale structure surveys are designed to observe structures at a very high redshift. At these large distances the number of structures that are observed decreases drastically because of the way in which most of the surveys are built, i.e. they are flux limited so that only bright objects are observed at larger distances. This introduces a selection bias called the Malmquist bias as objects below a certain brightness are not observed. To account for this incompleteness, one needs to know the selection function $\varphi(r)$ which provides the probability that an object at a given distance r is included in the sample. This is called as the radial selection function that is estimated from the luminosity function $\phi(L)$.

B.1 Luminosity function

Luminosity functions, $\phi(L)$, measure the comoving number density of galaxies per luminosity bin:

$$dN = \phi(L) dL dV \tag{B.1}$$

where dN denotes the number of observed galaxies in a volume dV within the luminosity range $[L, L + dL]$. There are several ways in which $\phi(L)$ can be estimated, but the most common way of estimating it is through the Schechter function (Schechter, 1976):

$$\phi(L) dL = \phi^* \left(\frac{L}{L^*}\right)^{\alpha} \exp\left(\frac{-L}{L^*}\right) \frac{dL}{L^*} \tag{B.2}$$

where ϕ^* (with units of $h^3 \mathrm{Mpc}^{-3}$) is a normalisation factor that defines the overall density of galaxies and L^* is the characteristic luminosity that separates the faint galaxy range where the power-law with exponent α dominates. α defines the faint-end slope that is seen in the luminosity function when plotted and is usually negative, which implies that there are more galaxies with faint luminosities in the sample. The luminosity function varies with morphological type, environmental properties and redshift because of the galactic evolution. In Figure B.1 we show the best-fit analytic expression to observed composite cluster luminosity distribution as obtained by Schechter (1976) for 13 rich clusters as studied by Oemler (1974).

The open circles show the composite constructed excluding four possible cD galaxies [1] and the filled black circles show the effect if they were included in the plot.

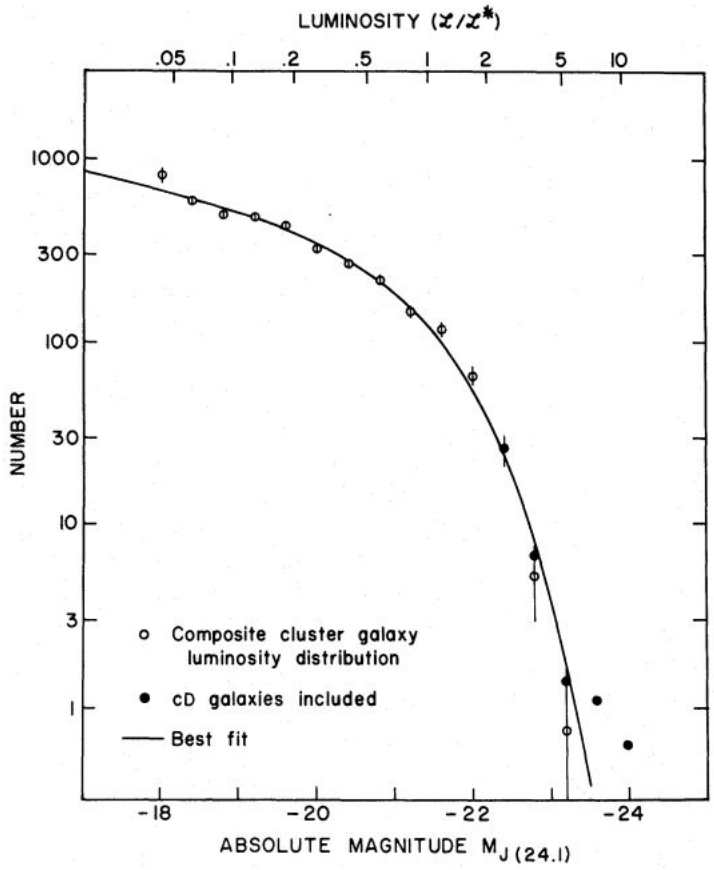

Figure B.1: Best-fit analytic expression to the observed composite cluster galaxy distribution. The filled black circles show the effect of including the cD type galaxies in the composite. Credits: Schechter (1976)

B.2 Eliminating the Malmquist bias

There are a few ways in which one can avoid the Malmquist bias. The first method is to limit the sample, often called as volume limited sample, where only those objects that are within the limiting magnitude at a given distance are included, the remaining objects are removed. This sub-sample selected should be free of the Malmquist bias. The major disadvantage of

[1] It is a subtype of the type-D giant elliptical galaxy and has a large halo of stars. They are usually found near the centres of rich galaxy clusters and are known popularly as supergiant ellipticals or central dominant galaxies.

this method is that many objects are lost and this results in the sample being less statistically significant. Another method is to make use of a weighted mean to account for the relative contribution at each magnitude. Each object's contribution to the average absolute magnitude can be weighted by $1/V_{max}$ where V_{max} is the maximum volume over which the objects could have been seen. Bright objects which have a lower absolute magnitude will be given a lesser weight compared to the less bright objects with a higher absolute magnitude so that the overall effect can be nullified.

There are other selection effects that affect cluster samples, such as construction of masks in a given field, fibre collisions in spectrograph's etc. The sky is not equally transparent in all directions, as we know that the Milky way contains dust that obscures our view in several directions. Also since the shape of the Milky way is flat, objects that lie in a low galactic latitude plane are more obscured compared to other objects. This effect needs to be considered when we are computing the real brightness of a cluster, which depends on the direction of the line of sight.

B.3 K-correction

For very deep samples when magnitude needs to be calculated, K-correction is often made.

$$M = m - 5(\log_{10} D_L - 1) K_{corr} \tag{B.3}$$

where M is the absolute magnitude, m is the apparent magnitude, D_L is the luminosity distance as in Equation 1.27 and 1.28 and K_{corr} is the K-correction. This allows the measurement of the magnitude from the object at a redshift z to be converted to an equivalent measurement in the rest frame [2] of the object as the observed wavelength of the object measured is always greater than the emitted wavelength. If objects are measured at all wavelengths, there would be no need for K-correction, but objects are measured through a single filter which sees only one part of the entire spectrum redshifted into the frame of the observer. K-correction needs to be made for comparing objects at different redshifts through the same filter.

[2] It is the frame in which the particle is at rest. Whenever an object in the Universe is measured, due to the expansion of space, the object is constantly moving.

Appendix C

Paper published

Astronomy & Astrophysics manuscript no. recovery_paper
December 8, 2016

Evolution of the real-space correlation function from next generation cluster surveys

Recovering the real-space correlation function from photometric redshifts

Srivatsan Sridhar[1]⋆, Sophie Maurogordato[1], Christophe Benoist[1], Alberto Cappi[1,2], and Federico Marulli[2,3,4]

[1] Université Côte d'Azur, OCA, CNRS, Lagrange, UMR 7293, CS 34229, 06304, Nice Cedex 4, France. e-mail: ssridhar@oca.eu
[2] INAF - Osservatorio Astronomico di Bologna, via Ranzani 1, I-40127, Bologna, Italy.
[3] Dipartimento di Fisica e Astronomia - Università di Bologna, viale Berti Pichat 6/2, I-40127 Bologna, Italy
[4] INFN - Sezione di Bologna, viale Berti Pichat 6/2, I-40127 Bologna,Italy

Received XXX; Accepted 01/12/2016

ABSTRACT

Context. The next generation of galaxy surveys will provide cluster catalogues probing an unprecedented range of scales, redshifts, and masses with large statistics. Their analysis should therefore enable us to probe the spatial distribution of clusters with high accuracy and derive tighter constraints on the cosmological parameters and the Dark Energy equation of state. However, for the majority of these surveys, redshifts of individual galaxies will be mostly estimated by multiband photometry which implies non-negligible errors on redshift resulting in potential difficulties in recovering the real-space clustering.
Aims. In this paper, we investigate to which accuracy it is possible to recover the real-space two-point correlation function of galaxy clusters from cluster catalogues based on photometric redshifts, and test our ability to detect and measure the redshift and mass evolution of the correlation length r_0 and of the bias parameter b(M,z) as a function of the uncertainty on the cluster redshift estimate.
Methods. We calculate the correlation function for cluster sub-samples covering various mass and redshift bins selected from a 500 deg^2 light-cone limited to H<24 (Merson et al. 2013). In order to simulate the distribution of clusters in photometric redshift space, we assign to each cluster a redshift randomly extracted from a Gaussian distribution having a mean equal to the cluster cosmological redshift and a dispersion equal to σ_z. The dispersion is varied in the range $\sigma_{(z=0)}=\frac{\sigma_z}{1+z_c} = 0.005, 0.010, 0.030$ and 0.050, in order to cover the typical values expected in forthcoming surveys. The correlation function in real-space is then computed through estimation and deprojection of $w_p(r_p)$, following the method proposed for galaxies by Arnalte-Mur et al. (2009). Four mass ranges (from $M_{halo} > 2 \times 10^{13}\ h^{-1}M_\odot$ to $M_{halo} > 2 \times 10^{14}\ h^{-1}M_\odot$) and six redshift slices covering the redshift range [0,2] are investigated, first using cosmological redshifts and then for the four photometric redshift configurations.
Results. From the analysis of the light-cone in cosmological redshifts we find a clear increase of the correlation amplitude as a function of redshift and mass. The evolution of the derived bias parameter b(M,z) is in fair agreement with the theoretical expectation by Tinker et al. (2010). We also confirm the existence of the $r_0 - d$ relation shown by Younger et al. (2005) up to our highest mass, highest redshift sample tested ($z = 2, M_{halo} > 2 \times 10^{14}\ h^{-1}M_\odot$). From our pilot sample limited to $M_{halo} > 5 \times 10^{13}\ h^{-1}M_\odot (0.4 < z < 0.7)$, we find that the real-space correlation function can be recovered by deprojection of $w_p(r_p)$ within an accuracy of 5% for $\sigma_z = 0.001 \times (1 + z_c)$ and within 10% for $\sigma_z = 0.03 \times (1 + z_c)$. For higher dispersions (besides $\sigma_z > 0.05 \times (1 + z_c)$), the recovery becomes noisy and difficult. The evolution of the correlation in redshift and mass is clearly detected for all σ_z tested, but requires a large binning in redshift to be detected significantly between individual redshift slices when increasing σ_z. The best-fit parameters (r_0 and γ) as well as the bias obtained from the deprojection method for all σ_z are within the 1σ uncertainty of the z_c sample.

Key words. galaxies: clusters: general – (cosmology:) large-scale structure of Universe – techniques: photometric – methods: statistical

1. Introduction

One of the major challenges in modern cosmology is to explain the observed acceleration of the cosmic expansion, determining if it is due to a positive cosmological constant, a time–varying dark energy component or a modified theory of gravity. Major galaxy surveys are currently ongoing or in preparation in order to address this fundamental question through the analysis of various complementary cosmological probes with different systematics, as for instance weak lensing, galaxy clustering (baryon acoustic oscillations, redshift-space distortions) and galaxy clusters. In fact galaxy cluster counts as a function of redshift and mass are sensitive to dark energy through their dependence on the volume element and on the structure growth rate. One intrinsic difficulty in constraining the cosmological models with galaxy cluster counts comes from uncertainties in cluster mass estimates and on the difficulty to calibrate related mass proxies. One can overcome this difficulty adding the information related to the clustering properties of clusters, due to the fact that their power spectrum amplitude depends mainly on the halo mass. When combining the redshift-averaged cluster power spectrum and the evolution of the number counts in a given survey, the constraints on the dark energy equation of state are dramatically improved (Majumdar & Mohr 2004). Recent cosmological forecasting based on galaxy clusters confirms that the figure of merit significantly increases when adding cluster clustering information (Sartoris et al. 2016).

⋆ email:ssridhar@oca.eu

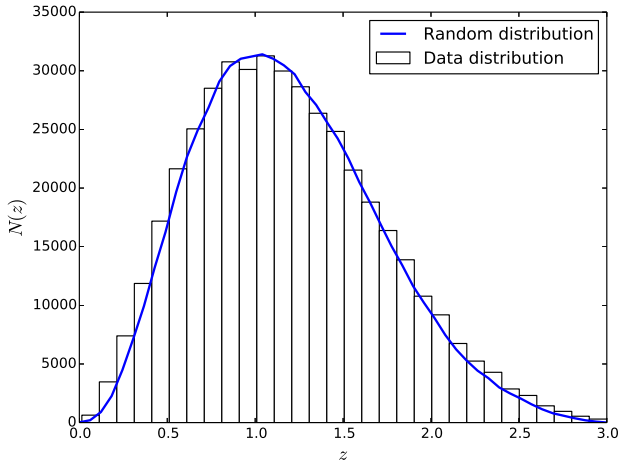

Fig. 1: Redshift distribution of the entire catalogue with $0.0 < z_c < 3.0$. The data distribution is shown as the histogram along with the *blue* line specifying the distribution of the random catalogue we use for calculating the two-point correlation function.

Cluster clustering can be measured through the two–point correlation function, the Fourier transform of the power spectrum, which is one of the most successful statistics for analysing clustering processes (Totsuji & Kihara 1969; Peebles 1980). In cosmology, it is a standard tool to test models of structure formation and evolution. The cluster correlation function is much higher than that of galaxies, as first shown by Bahcall & Soneira (1983) and Klypin & Kopylov (1983). This is a consequence of the fact that more massive haloes correspond to higher and rarer density fluctuations, which have a higher correlation amplitude (Kaiser 1984). Galaxy clusters are associated to the most massive virialised dark matter haloes, and as a consequence their correlation function is strongly amplified. The evolution of the cluster halo mass, bias and clustering has been addressed analytically (Mo & White 1996; Moscardini et al. 2000; Sheth et al. 2001), and also numerically (Governato et al. 1999; Angulo et al. 2005; Estrada et al. 2009). The increase of the correlation length with cluster mass and redshift has been used to constrain the cosmological model and the bias (Colberg et al. 2000; Bahcall et al. 2004; Younger et al. 2005)

The first large local surveys such as the SDSS (Eisenstein et al. 2011) have led to a significant progress in this field. Clustering properties of cluster catalogues derived from SDSS were done by Estrada et al. (2009), Hütsi (2010) and Hong et al. (2012). More recently, Veropalumbo et al. (2014) have shown the first unambiguous detection of the BAO peak in a spectroscopic sample of 25000 clusters selected from the SDSS, and measured the peak location at $104 \pm 7\ h^{-1}$Mpc . Large surveys at higher redshifts which are ongoing (DES, BOSS, KIDS, Pan-STARRS) or in preparation (eROSITA, LSST, Euclid) open a new window for the analysis of cluster clustering. The wide areas covered will give access to unprecedented statistics (∼100,000 clusters expected with Dark Energy Survey, eROSITA and Euclid survey) that will allow us to cover the high mass, high redshift tail of the mass distribution, to control cosmic variance, and to map the large scales at which the BAO signature is expected (∼ 100Mpc).

However, to use clusters as cosmological probes, among the several difficulties to be overcome is the impact of photometric redshift errors. While some of these surveys have (in general partially) a spectroscopic follow up, many forthcoming large galaxy surveys will have only the photometric information in multiple bands, so that their cluster catalogues will be built on the basis of state-of-the-art photometric redshifts. Using those instead of real redshifts will cause a positional uncertainty along the line of sight inducing a damping of clustering at small scales and a smearing of the acoustic peak (Estrada et al. 2009). It is therefore of major interest to check the impact of this effect on the recovery of the real-space correlation function. Our objective is to optimize the analysis of cluster clustering from forthcoming cluster catalogues that will be issued from the ongoing/future large multiband photometric surveys. Here we focus on the determination of the two-point correlation function, and the aim of our paper is i) to determine the clustering properties of galaxy clusters from state-of-the-art simulations where galaxy properties are derived from semi-analytical modelling (Merson et al. 2013), and ii) to test how much the clustering properties evidenced on ideal mock catalogues can be recovered when degrading the redshift information to reproduce the photometric uncertainty on redshift expected in future cluster experiments.

The paper is organised as follows. In Section 2 we describe the simulation we work with. In Section 3 we investigate the two-point correlation function evolution with redshift and mass without any error on the redshift to check consistency with theory. The bias is calculated for different mass cut samples along with the evaluation of clustering strength with mass at different redshift and compared with the theoretical expectation of Tinker et al. (2010). We also calculate the mean intercluster comoving separation (d) and compare it with r_0 and perform an analytic fit to this r_0 vs d relation. Section 4 presents the deprojection method we use to recover the real-space correlation function from mock photometric catalogues generated using a Gaussian approximation technique. The results obtained from the deprojection method along with the redshift evolution of the samples with redshift uncertainty are presented. In Section 5, the overall results obtained from our study are summarized and discussed.

2. Simulations

We use a public light-cone catalogue constructed using a semi-analytic model of galaxy formation (Merson et al. 2013) onto the N-body dark matter halo merger trees of the Millennium Simulation, based on a ΛCDM cosmological model with the following parameters: $\Omega_M, \Omega_\Lambda, \Omega_b, h = 0.25, 0.75, 0.045, 0.73$ (Springel et al. 2005), corresponding to the first year results from the Wilkinson Microwave Anisotropy Probe (Spergel et al. 2007). The Millennium simulation was carried out using a modified version of the GADGET2 code (Springel 2005). Haloes in the simulation were resolved with a minimum of 20 particles, with a resolution of $M_{halo} = 1.72{\times}10^{10} h^{-1} M_\odot$ ($M_\odot$ represent the mass of the Sun). The groups of dark matter particles in each snapshot were identified through a Friends-Of-Friends algorithm (FOF) following the method introduced by Davis et al. (1985).

However, the algorithm was improved with respect to the original FOF, to avoid those cases where the FOF algorithm merge groups connected for example by a bridge, while they should be considered instead as separated haloes (Merson et al. 2013).

The linking length parameter for the initial FOF haloes is $b = 0.2$. Notice however that haloes were identified with a method different from the standard FOF. The FOF algorithm was initially applied to find the haloes, but then their substructures were identified using the so-called SUBFIND algorithm: depending on the evolution of the substructures and their merging, a new final halo

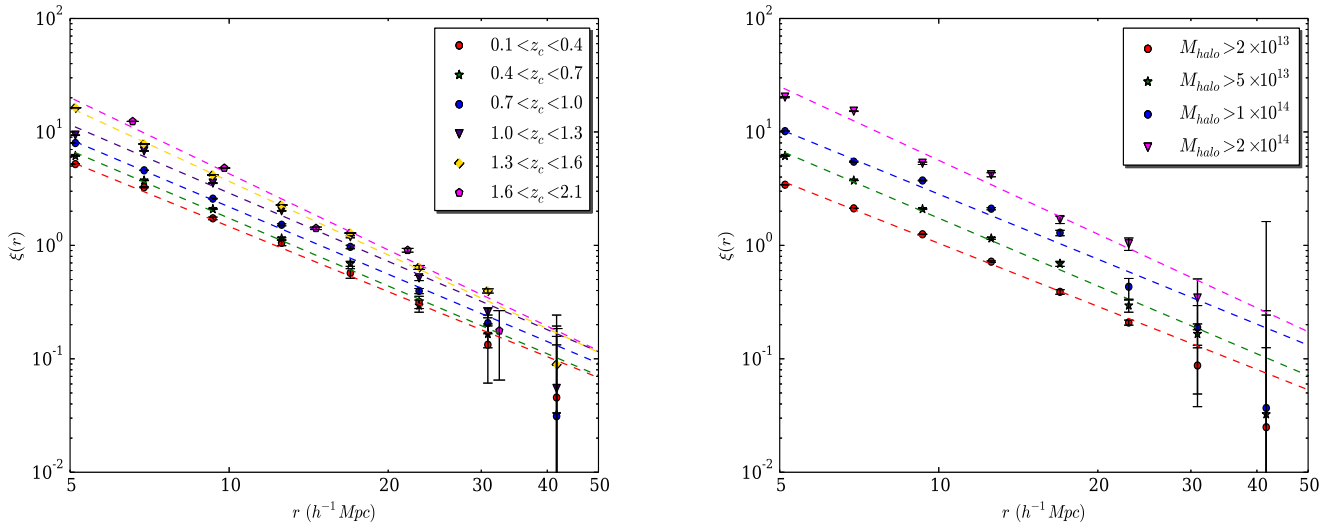

(a) (b)

Fig. 2: *Left panel*: The correlation functions for clusters with $M_{halo} > 5 \times 10^{13}\ h^{-1}\ M_{\odot}$ in 6 different redshift slices. The dashed lines show the corresponding power-law best-fits. The parameter values for the fits can be found in Table 1. *Right panel*: The correlation functions in the redshift slice $0.4 < z_c < 0.7$ for 4 different mass cuts (with units $h^{-1}\ M_{\odot}$). The dashed lines show the corresponding power-law best-fits. The parameter values for the fits can be found in Table 1. Error bars are the square root of the diagonal values of the covariance matrix calculated from the jackknife resampling method.

catalogue was built. The details of this method are described by Jiang et al. (2014).

A comparison between the masses obtained with this improved D-TREES algorithm, M_{halo}, and the classical M_{FOF}, and their relation with M_{200}, was done by Jiang et al. (2014), where it is shown that at redshift $z = 0$ on average, M_{halo} overestimates M_{200}, but by a lower factor with respect to M_{FOF}: they found that only 5% of haloes have $M_{halo}/M_{200} > 1.5$. However, when comparing the halo mass function of the simulation with that expected from the Tinker et al. (2010) approximation, it appears that there is a dependence on redshift, and beyond $z \approx 0.3$ the M_{halo}/M_{200} ratio becomes less than 1 (Mauro Roncarelli, private communication). This has to be taken into account in further analysis using the masses.

Galaxies were introduced in the light-cone using the Lagos 12 GALFORM model (Lagos et al. 2012). The GALFORM model populates dark matter haloes with galaxies using a set of differential equations to determine how the baryonic components are regulated by "subgrid" physics. These physical processes are explained in detail in a series of papers (Bower et al. 2006; Font et al. 2008; Lagos et al. 2012; Merson et al. 2013; Guo et al. 2013; Gonzalez-Perez et al. 2014). The area covered by the light-cone is 500 deg^2; the final mock catalogue is magnitude–limited to $H = 24$ (to mimic the Euclid completeness) with a maximum redshift at $z = 3$.

For each galaxy the mock catalogue provides different quantities, such as the identifier of the halo in which it resides, the magnitude in various passbands, right ascension and declination, and the redshift, both cosmological and including peculiar velocities. For each halo in the cluster mass range (see below), the redshift was estimated as the mean of the redshifts of its galaxies, while the central right ascension and declination were estimated as those of the brightest cluster galaxy (BCG), and by construction, the BCG is the centre of mass of the halo.

3. Evolution of the real-space two-point correlation function in the simulations

3.1. Estimation of the two-point correlation function

In order to measure the clustering properties of a distribution of objects, one of the most commonly used quantitative measure is the two-point correlation function (Totsuji & Kihara 1969; Davis & Peebles 1983). We can express the probability $dP_{12}(r)$ of finding two objects at the infinitesimal volumes dV_1 and dV_2 separated by a vector distance $\mathbf{r}$ (assuming homogeneity and isotropy on large scales, $r = |\mathbf{r}|$):

$$dP_{12} = n^2[1 + \xi(r)]dV_1dV_2 \tag{1}$$

where n is the mean number density and the two–point correlation function $\xi(r)$ measures the excess probability of finding the pair relative to a Poisson distribution.

Among the various estimators of the correlation function discussed in the literature we use the Landy & Szalay (1993) estimator, which has the best performance (comparable to the Hamilton (1993) estimator) and is the most popular, being less sensitive to the size of the random catalogue and better in handling edge corrections (Kerscher et al. 2000):

$$\xi(r) = \frac{DD(r) - 2DR(r) + RR(r)}{RR(r)} \tag{2}$$

where DD is the number of data-data pairs counted within a spherical shell of radius r and $r + dr$, DR refers to the number of data-random pairs and RR refers to the random-random pairs.

The peculiar motions of galaxies produce redshift-space distortions that have to be taken into account in order to recover the real-space clustering (Kaiser 1987); this means that Equation 2 cannot be used directly to estimate the 3D real-space correlation

function when distances are derived from redshifts. We will use it only for the analysis of simulations, where the cosmological redshift is available.

The real-space correlation function is expected to follow a power-law as a function of the separation r (Peebles 1980):

$$\xi(r) = \left(\frac{r}{r_0}\right)^{-\gamma} \quad (3)$$

where r_0 is the correlation length and γ is the slope.

The random catalogues we use reproduce the cluster redshift selection function, estimated by smoothing the cluster redshift distribution through a kernel density estimation method. The bandwidth of the kernel is carefully adjusted in order to follow the global shape but not the clustering fluctuations in the redshift distribution. To ensure that we use a Gaussian kernel two times larger than the bin size, and sample the data in 30 redshift bins. Figure 1 shows the redshift distributions of the simulation and of the random catalogue for the whole sample. The random catalogue is 10 times denser than the simulated sample in order to minimize the effect of shot noise.

In the following, we estimate the correlation functions for different sub-samples of the original catalogue with different cuts in redshift and limiting mass.

Errors are calculated from the covariance matrices using the jackknife resampling method (Zehavi et al. 2005; Norberg et al. 2011). To perform a jackknife estimate we divide the data into N equal sub-samples and we calculate the two-point correlation function omitting one sub-sample at a time. For k jackknife samples and i bins, the covariance matrix is then given by:

$$C_{ij} = \frac{N-1}{N}\sum_{k=1}^{N}(\xi_i^k - \bar{\xi}_i)(\xi_j^k - \bar{\xi}_j) \quad (4)$$

where $\bar{\xi}_i$ is the average of the values obtained for bin i. We make use of $N = 9$ sub-samples in our calculation.

To measure the two-point correlation function for all our samples, we use `CosmoBolognaLib` (Marulli et al. 2016), a large set of Open Source C++ libraries for cosmological calculations. [1]

3.2. Redshift evolution of the cluster correlation function

The redshift evolution of the cluster correlation function has been studied both observationally (Bahcall & Soneira 1983; Huchra et al. 1990; Peacock & West 1992; Croft et al. 1997; Borgani et al. 1999; Veropalumbo et al. 2016), numerically (Bahcall et al. 2004; Younger et al. 2005; Marulli et al. 2015) and theoretically (Mo & White 1996; Governato et al. 1999; Moscardini et al. 2000; Sheth et al. 2001). Two main results are prominent from these works:

- The cluster correlation amplitude increases with redshift for both low- and high-mass clusters.
- The increase of the correlation amplitude with redshift is stronger for more massive clusters compared to low mass ones.

Future large surveys are expected to probe the high redshift domain with good statistics. This will enable us to study the redshift evolution of clustering on a large range of redshifts and provide independent cosmological tests (Younger et al. 2005). In this section, we investigate the expected redshift evolution of the cluster correlation function in the redshift range [0,2], assuming a concordant ΛCDM model and using the light cone catalogue detailed in Section 2.

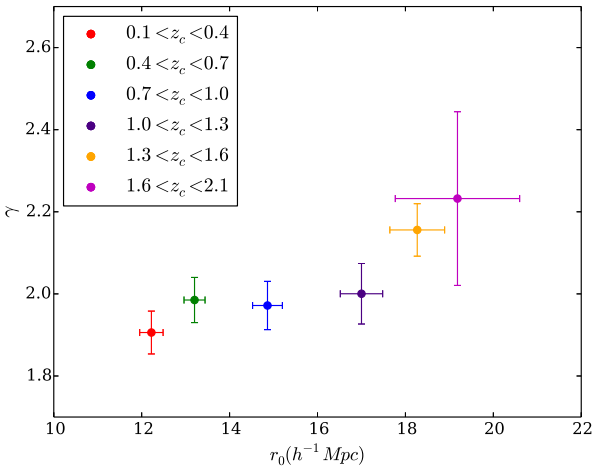

Fig. 3: The evolution of r_0 and γ for clusters observed in different redshift slices and with mass $M_{halo} > 5 \times 10^{13}\ h^{-1}\ M_\odot$. The values of r_0 and γ can be found in the second panel of Table 1.

The correlation functions for clusters with a mass cut of $M_{halo} > 5 \times 10^{13}\ h^{-1}\ M_\odot$ are estimated in six redshift slices, from $0.1 < z_c < 0.4$ to $1.6 < z_c < 2.1$ (where z_c refers to the cosmological redshift), and are shown in Figure 2a. The figure shows that, as expected, the amplitude of the cluster correlation function increases with redshift.

For each sub-sample, the correlation function is fitted by a power-law (Equation 3) leaving both r_0 and γ as free parameters. The results of the fits can be visualised in Figure 3. The redshift range, the values of the best-fit parameters, the number of clusters, and the bias (discussed in Section 3.4) for each sub-sample are given in the second panel of Table 1. The fit is performed in the range $5 - 50h^{-1}$ Mpc and the error bars are obtained using the jackknife estimate method (see Section 3.1).

The power-law has a relatively stable slope varying between 1.9 and 2.1. In the two highest redshift slices, however, the slope appears to be slightly higher, but the variation is at the $\sim 2\sigma$ level for the $1.3 < z_c < 1.6$ sub-sample and at the $\sim 1\sigma$ level for the $1.6 < z_c < 2.1$ sub-sample. On the average, $\gamma \approx 2.0$, is close to the measured value for galaxy clusters as done by Totsuji & Kihara (1969) and Bahcall & West (1992) on observed galaxy clusters.

On the contrary, the increase in the correlation length is systematic and statistically significant. When we fix the slope at $\gamma = 2.0$, r_0 is shown to increase from $11.97 \pm 0.25\ h^{-1}$ Mpc for the lowest redshift slice ($0.1 < z_c < 0.4$), to $20.05 \pm 1.13\ h^{-1}$ Mpc for the highest redshift slice ($1.6 < z_c < 2.1$). Our results can be compared to Younger et al. (2005)(see their Figure 5) and are in good agreement with their analysis of the high-resolution simulations of Hopkins et al. (2005).

[1] More information about `CosmoBolognaLib` can be found at `http://apps.difa.unibo.it/files/people/federico.marulli3/CosmoBolognaLib/Doc/html/index.html`

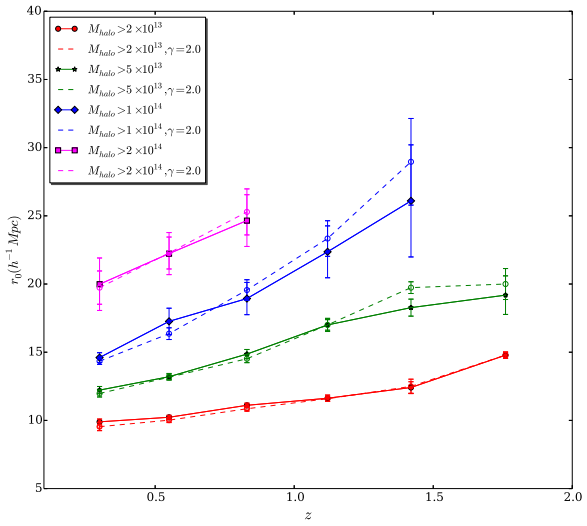

Fig. 4: The evolution of r_0 with redshift for different limiting masses (with units h^{-1} $M_\odot$). The filled symbols connected by solid lines correspond to the free slope fits, while the the open symbols connected by dashed lines correspond to a fixed slope $\gamma = 2.0$. The different limiting masses are colour coded as shown in the figure. The values of r_0 and γ for all the samples can be found in Table 1.

3.3. The redshift evolution of clustering as a function of mass

In this section we investigate the redshift evolution of clustering as a function of mass. For this purpose, 4 different mass thresholds are considered: $M_{halo} > 2 \times 10^{13}$ h^{-1} $M_\odot$, $M_{halo} > 5 \times 10^{13}$ h^{-1} $M_\odot$, $M_{halo} > 1 \times 10^{14}$ h^{-1} $M_\odot$ and $M_{halo} > 2 \times 10^{14}$ h^{-1} $M_\odot$. The analysis is performed in the same redshift slices previously defined. The correlation function is fitted with a power-law as it can be seen from Figure 2b, both with a free slope and with a fixed slope $\gamma = 2.0$. The mass range, the values of the best-fit parameters, the number of clusters, and the bias for each sub-sample are given in the four panels of Table 1. Each panel corresponds to a different selection in mass. In both cases, the correlation length r_0 increases with the limiting mass at any redshift and increases with redshift at any limiting mass, as shown in Figure 4. The higher the mass threshold, the larger is the increase of r_0 with redshift. For example, the ratio of the correlation lengths for the [1.3-1.6] and the [0.1-0.4] redshift slices is 1.25 with $M_{halo} > 2 \times 10^{13}$ h^{-1} $M_\odot$, while it reaches 1.8 with $M_{halo} > 1 \times 10^{14}$ h^{-1} $M_\odot$. For the largest limiting mass ($M_{halo} > 2 \times 10^{14}$ h^{-1} $M_\odot$), the number of clusters becomes small at high z and the analysis must be limited to $z = 1$.

We can again compare our results with the analysis of Younger et al. (2005). who used a Tree Particle Mesh (TPM) code (Bode & Ostriker 2003) to evolve $N = 1260^3$ particles in a box of 1500 h^{-1}Mpc, reaching a redshift $z \approx 3.0$. We find a good agreement (see their Figure 5) for the common masses and redshift ranges tested; our analysis probes the correlation function of $M_{halo} > 1 \times 10^{14}$ h^{-1} $M_\odot$ clusters up to $z \approx 1.6$, and of $M_{halo} > 2 \times 10^{14}$ h^{-1} $M_\odot$ clusters up to $z \approx 0.8$, thus extending the $r_0(z)$ evolution shown by Younger et al. (2005) to higher redshifts for these high mass clusters.

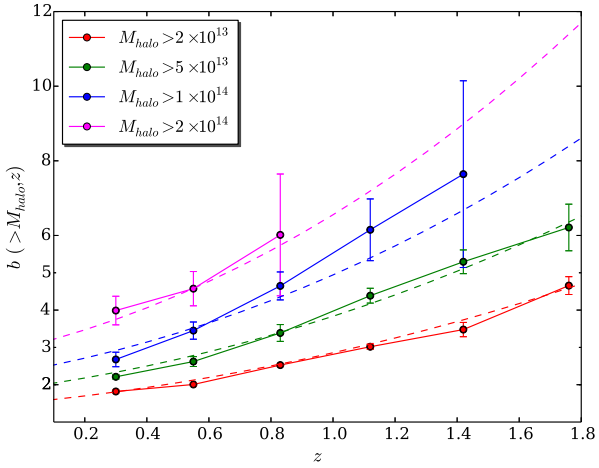

Fig. 5: The bias as a function of redshift for different limiting masses (with units h^{-1} $M_\odot$) where the solid lines just connect the points. The dashed line is the theoretical expectation of the bias as given by Tinker et al. (2010) for the same limiting masses and evolving redshift. The different limiting masses are colour coded as shown in the figure. The bias values for all the samples can be found in Table 1.

3.4. Bias evolution

Starting from the initial matter density fluctuations, structures grow with time under the effect of gravity. The distribution of haloes, hence of galaxies and clusters, is biased with respect to the underlying matter distribution, and on large scales it is expected that the bias is linear:

$$\left(\frac{\Delta\rho}{\rho}\right)_{light} = b \times \left(\frac{\Delta\rho}{\rho}\right)_{mass} \tag{5a}$$

where b is the bias factor and ρ is the density. The higher the halo mass, the higher the bias.

The amplitude of the halo correlation function is amplified by a b^2 factor with respect to the matter correlation function:

$$\xi(r)_{light} = b^2 \times \xi(r)_{mass} \tag{5b}$$

The amplitude of the matter correlation function increases with time and decreases with redshift, but the halo bias decreases with time and increases with redshift. As a result, the cluster correlation amplitude increases with redshift, as it is clear in Figure 3.

We estimate the cluster bias through Equation 5b. The power spectrum of the dark matter distribution is calculated with the cosmological parameters of the light-cone we use and we obtain its Fourier transform $\xi(r)$. We use the function `xi_DM` from the class `Cosmology` from `CosmoBolognaLib`. The comparison is not straightforward because, as we have previously noticed, in the simulation halo masses are not M_{200}, but the so–called Dhalos masses M_{halo}.

The evolution of bias with redshift for the 4 sub-samples with different limiting masses is shown in Figure 5 along with the theoretical predictions of Tinker et al. (2010) for the same limiting masses used. The values of the bias for the different sub-samples are provided in Table 1. It can be seen that at fixed

Table 1: The best-fit values of the parameters of the real-space correlation function $\xi(r)$ for the light-cone at different (1) mass thresholds and (2) redshift ranges. For each sample we quote (3) the correlation length r_0, (4) slope γ, (5) correlation length r_0 at fixed slope $\gamma = 2.0$, (6) number of clusters $N_{clusters}$ and (7) the bias b obtained.

Mass (h^{-1} $M_\odot$)	z	r_0 (h^{-1}Mpc)	γ	r_0 ($\gamma = 2.0$) (h^{-1}Mpc)	$N_{clusters}$	bias
$M_{halo} > 2 \times 10^{13}$	$0.1 < z_c < 0.4$	9.89±0.20	1.76±0.05	9.53±0.29	10492	1.81±0.03
	$0.4 < z_c < 0.7$	10.22±0.14	1.84±0.04	10.01±0.17	27224	2.00±0.03
	$0.7 < z_c < 1.0$	11.10±0.15	1.87±0.04	10.85±0.17	35133	2.52±0.02
	$1.0 < z_c < 1.3$	11.62±0.23	1.98±0.05	11.58±0.19	31815	3.01±0.06
	$1.3 < z_c < 1.6$	12.41±0.42	2.13±0.09	12.49±0.52	22978	3.37±0.19
	$1.6 < z_c < 2.1$	14.78±0.21	2.06±0.05	14.78±0.22	18931	4.65±0.23
$M_{halo} > 5 \times 10^{13}$	$0.1 < z_c < 0.4$	12.22±0.26	1.90±0.05	11.97±0.25	3210	2.21±0.05
	$0.4 < z_c < 0.7$	13.20±0.23	1.98±0.05	13.16±0.17	7301	2.62±0.13
	$0.7 < z_c < 1.0$	14.86±0.33	1.97±0.05	14.52±0.28	8128	3.38±0.22
	$1.0 < z_c < 1.3$	17.00±0.48	2.00±0.07	17.00±0.38	5963	4.38±0.19
	$1.3 < z_c < 1.6$	18.26±0.62	2.15±0.06	19.73±0.43	3365	5.29±0.31
	$1.6 < z_c < 2.1$	19.18±1.41	2.23±0.21	20.05±1.13	2258	6.21±0.62
$M_{halo} > 1 \times 10^{14}$	$0.1 < z_c < 0.4$	14.60±0.35	1.93±0.06	14.33±0.24	1119	2.67±0.19
	$0.4 < z_c < 0.7$	17.26±0.96	1.90±0.08	16.35±0.42	2228	3.45±0.23
	$0.7 < z_c < 1.0$	18.93±1.18	2.08±0.12	19.55±0.75	2072	4.64±0.37
	$1.0 < z_c < 1.3$	22.36±1.90	2.11±0.17	23.33±1.30	1221	6.15±0.82
	$1.3 < z_c < 1.6$	26.09±4.10	2.28±0.30	28.96±3.17	590	7.64±2.50
$M_{halo} > 2 \times 10^{14}$	$0.1 < z_c < 0.4$	19.98±1.92	1.95±0.22	19.73±1.22	322	3.98±0.38
	$0.4 < z_c < 0.7$	22.23±1.54	2.16±0.18	22.27±1.17	538	4.57±0.45
	$0.7 < z_c < 1.0$	24.65±1.89	2.19±0.29	25.28±1.68	407	6.01±1.63

redshifts more massive clusters have a higher bias; at fixed mass threshold the bias increases with redshift, and evolves faster at higher redshifts. It can also be seen clearly that the bias obtained for the haloes from the simulations are in good agreement with the predictions by Tinker et al. (2010).

At high redshifts ($z > 0.8$) the bias recovered from the simulations seems to slightly diverge from the theoretical predictions, especially for the $M_{halo} > 1 \times 10^{14}\ h^{-1}\ M_\odot$ sample, but this can be explained by the dependence on redshift for the M_{halo}/M_{200} ratio which becomes smaller than 1 at these redshifts as previously mentioned. The discrepancy is not significant as our bias measurements are well within 1σ precision from the theoretical expectations.

3.5. The r_0 - d relation

The dependence of the bias on the cluster mass is based on theory. A complementary and empirical characterization of the cluster correlation function is the dependence of the correlation length r_0 as a function of the mean cluster comoving separation d (Bahcall & Soneira 1983; Croft et al. 1997; Governato et al. 1999; Bahcall et al. 2003), where:

$$d = \sqrt[3]{\frac{1}{\rho}} \quad (6)$$

and ρ is the mean number density of the cluster catalogue on a given mass threshold.

According to the theory, more massive clusters have a higher bias, therefore a higher r_0; as they are also more rare, they have also a larger mean separation: therefore it is expected that r_0 increases with d, i.e. $r_0 = \alpha\, d^\beta$.

This relation has been investigated both in observational data (Bahcall & West 1992; Estrada et al. 2009) and in numerical simulations (Bahcall et al. 2003; Younger et al. 2005). Younger et al. (2005) gave an analytic approximation in the ΛCDM case in the redshift range z = 0-0.3 for $20 \leq d \leq 60\ h^{-1}$Mpc, with $\alpha = 1.7$ and $\beta = 0.6$.

We determine the r_0 dependence with d for the various subsamples previously defined. The results obtained for a free γ along with the best fit obtained for both free and fixed $\gamma = 2$ are shown in Figure 6.

The best-fit parameters for the r_0 - d relation in the redshift range $0 \leq z \leq 2.1$ and for the cluster mean separation range $20 \leq d \leq 140 h^{-1}$Mpc are, $\alpha = 1.77 \pm 0.08$ and $\beta = 0.58 \pm 0.01$.

The r_0 - d relation which appears to be scale–invariant with redshift, is consistent with what was found by Younger et al. (2005) and is also consistent with the theoretical predictions of Estrada et al. (2009) (see their figure 7).

The scale invariance of the $r_0 - d$ relation up to a redshift $z \approx 2.0$ implies that the increase of the cluster correlation strength

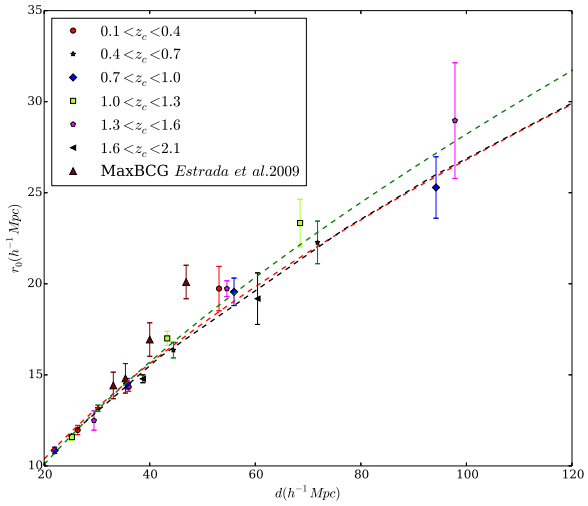

Fig. 6: The evolution of r_0 with d for clusters of different masses in different redshift slices. The points plotted are for the fixed slope $\gamma = 2.0$. The *green* dashed line shows the fit when $\gamma = 2.0$ and the *red* dashed line shows the overall fit obtained for the data points considering a free slope. The analytic approximation in the ΛCDM case obtained by Younger et al. (2005) is shown by the dashed *black* line. The different redshift slices are colour coded as mentioned in the figure.

with redshift is matched by the increase of the mean cluster separation d. It suggests that the cluster mass hierarchy does not evolve significantly in the tested redshift range: for example, the most massive clusters at an earlier epoch will still be among the most massive at the current epoch.

4. Estimating the correlation function with photometric redshifts

Large redshift surveys such as the Sloan Digital Sky Survey (Eisenstein et al. 2011), VVDS (Le Fèvre et al. 2005), VIPERS (Garilli et al. 2014; Guzzo et al. 2014) have revolutionized our tridimensional vision of the Universe. However, as spectroscopic follow up is a very time consuming task, priority has been given either to the sky coverage or to the depth of the survey. An alternative way of recovering the redshift information is to derive it from imaging in multiple bands when available, using the technique of photometry (Ilbert et al. 2006, 2009) While the accuracy of spectroscopic redshifts cannot be reached, this method can be successfully used for several purposes as for instance cluster detection. Several major surveys that will provide imaging in multiple bands and thereby photometric redshifts are in progress or in preparation. For instance, the ongoing Dark Energy Survey aims to cover about 5000 deg^2 on the sky with a photometric accuracy of $\sigma_z \approx 0.08$ out to $z \approx 1$ (Sánchez et al. 2014). Future surveys such as LSST (Ivezic et al. 2008; LSST Science Collaboration et al. 2009) and Euclid (Laureijs et al. 2011) are expected to make a significant leap forward. For instance, the Euclid Wide Survey, planned to cover 15000 deg^2, is expected to deliver photometric redshifts with uncertainties lower than $\sigma_z/(1+z) < 0.05$ (and possibly $\sigma_z/(1+z) < 0.03$) (Laureijs et al. 2011) over the redshift range [0,2]. The performances of photometric redshift measurements have significantly increased over the last decade, making it possible to perform different kinds of clustering analysis which were previously the exclusive domain of spectroscopic surveys. In this section we investigate how well we can recover the cluster correlation function for a sample of clusters with photometric redshifts and test the impact of the photometric redshift errors in redshift and mass bins.

4.1. Generation of the photometric redshift distribution of haloes

From the original light-cone we extract mock cluster samples with photometric redshifts; these are assigned to each cluster by random extraction from a Gaussian distribution with mean equal to the cluster cosmological redshift and standard deviation equal to the assumed photometric redshift error of the sample.

In this way we build five mock samples with errors $\sigma_{(z=0)} = \sigma_z/(1+z_c) = 0.001, 0.005, 0.010, 0.030, 0.050$. These values have been chosen to span the typical uncertainties expected in the context of upcoming large surveys.

The photometric redshift uncertainties in upcoming surveys are expected to be within $0.03 < \sigma_z/(1+z) < 0.05$ for galaxies and within $0.01 < \sigma_z/(1+z) < 0.03$ for clusters (Ascaso et al. 2015). Ideally, the error on the cluster redshift should scale proportionally to $N_{mem}{}^{-1/2}$ (where N_{mem} is the number of cluster members), therefore for clusters with 10 detected members the error would be reduced by a factor 3; but of course contamination from non-member galaxies will affect the redshift estimate.

4.2. Recovering the real-space correlation function: the method

In the following we will take into account separately the line of sight π and the transverse r_p components of the two–point correlation function. Photometric redshifts affect only the line of sight component, introducing an anisotropy in the π-r_p plane: the redshift–space correlation function will have a lower amplitude and steeper slope with respect to the real-space correlation function (Arnalte-Mur et al. 2009).

In order to recover the real-space correlation function of the photometric redshift mocks, we apply the deprojection method (Arnalte-Mur et al. 2009; Marulli et al. 2012). The method is based on Davis & Peebles (1983) and Saunders et al. (1992). Pairs are counted at different separations parallel (π) and perpendicular (r_p) to the line of sight.

The comoving redshift space separation of the pair is defined as $\mathbf{s} \equiv \mathbf{x_2} - \mathbf{x_1}$ and the line of sight vector is $\mathbf{l} = \frac{1}{2}(\mathbf{x_1} + \mathbf{x_2})$ (Fisher et al. 1994). The parallel and perpendicular distances to the pair are given by:

$$\pi = \frac{\mathbf{s}.\mathbf{l}}{|\mathbf{l}|} \tag{7a}$$

$$r_p = \sqrt{|\mathbf{s}|^2 - \pi^2} \tag{7b}$$

where $\bar{z} = \frac{1}{2}(z_1 + z_2)$. Counting pairs in both (r_p, π) dimensions will then provide the anisotropic correlation function $\xi(r_p, \pi)$. The projected correlation function can be derived from $\xi(r_p, \pi)$ by:

$$w_p(r_p) = \int_{-\infty}^{+\infty} \xi(r_p, \pi) d\pi \tag{8}$$

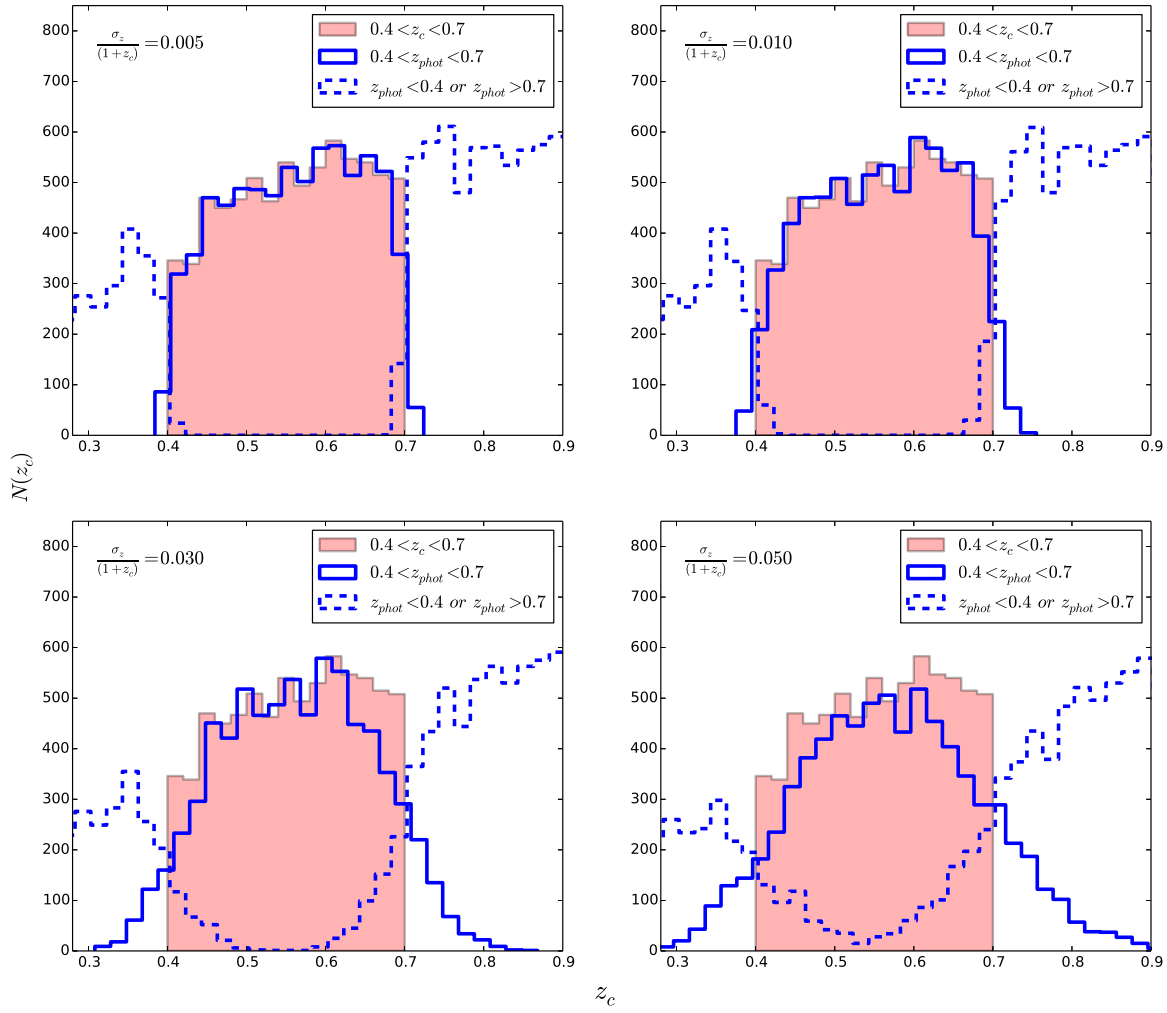

Fig. 7: Distribution of clusters selected in the top-hat cosmological redshift window compared with the clusters selected in the top-hat photometric redshift window. Filled histograms correspond to distribution of clusters as a function of cosmological redshift when the top-hat selection is done using the cosmological redshift within the range $0.4 < z < 0.7$. Solid blue lines correspond to distribution of clusters as a function of cosmological redshift when the top-hat selection is done using the different photometric uncertainties we have used ($\sigma_z/(1 + z_c)$ = 0.005,0.010,0.030 and 0.050) with the range $0.4 < z < 0.7$ and the dashed blue lines correspond to the distribution of clusters as a function of cosmological redshift when the top-hat selection is done using photometric redshifts outside the range $0.4 < z < 0.7$.

Table 2: Main parameters used for the analysis of the original catalogue and the 5 mock photometric redshift catalogues: (1) the redshift uncertainty, (2) the maximum values of π_{max} and (3) $r_{p(max)}$, (4) the values of $\Delta\xi$, (5) $\widehat{\Delta\xi}$. The range of scales r used for the fit is fixed at 5-50 Mpc.

Redshift uncertainty $\left(\frac{\sigma_z}{1+z_c}\right)$	π_{max} $(h^{-1}Mpc)$	$r_{p(max)}$ $(h^{-1}Mpc)$	$\Delta\xi$	$\widehat{\Delta\xi}$
0.000	50	400	0.028	0.031
0.001	60	400	0.042	0.052
0.005	130	400	0.055	0.055
0.010	300	400	0.065	0.063
0.030	400	400	0.091	0.080
0.050	550	400	0.148	0.109

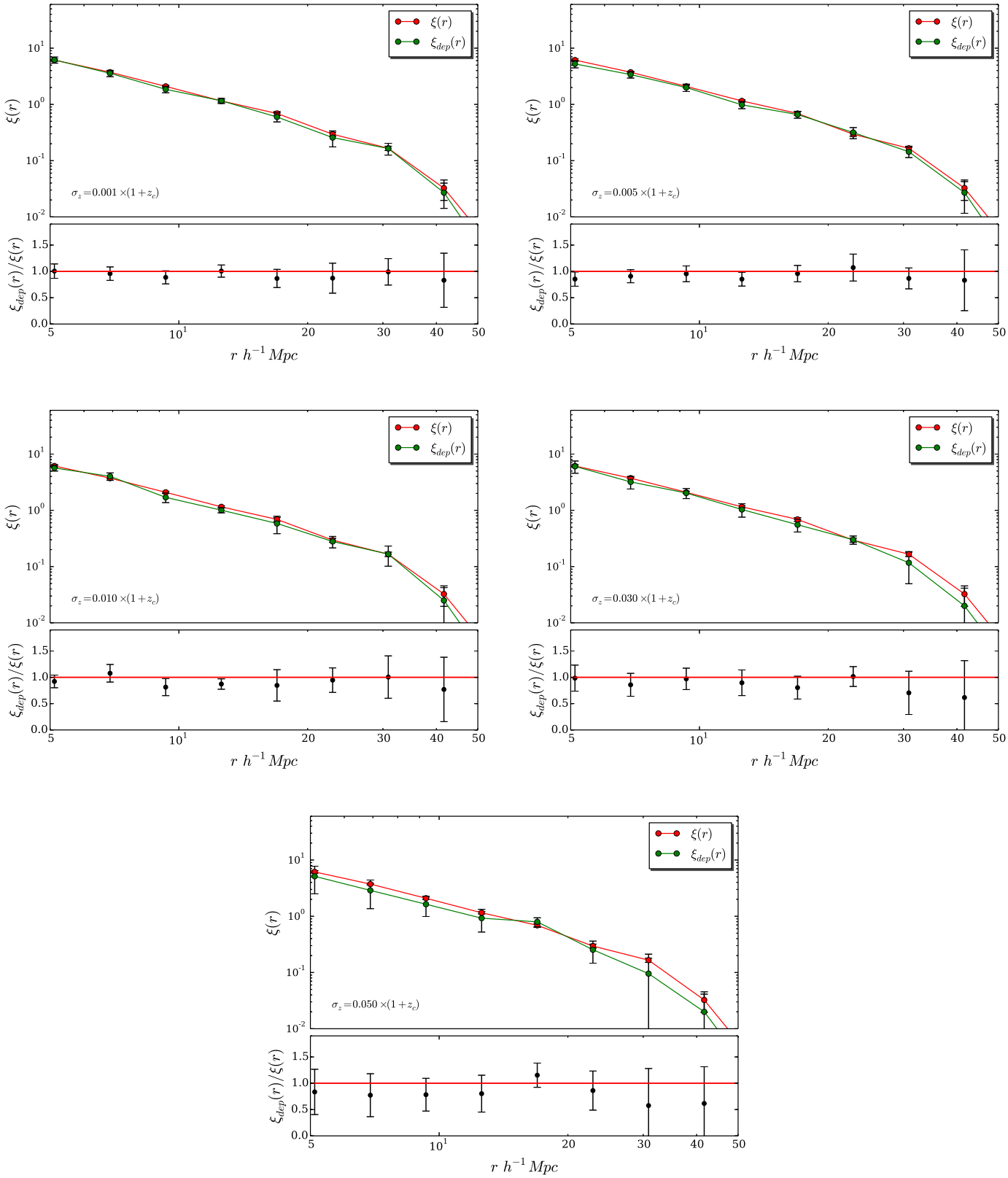

Fig. 8: The recovered correlation function (*green line*) compared with the real-space correlation function (*red line*) for 5 mock photometric samples in the redshift range $0.4 < z < 0.7$, with increasing redshift uncertainty. Values of the best-fit parameters obtained are given in Table 2 and the quality of the recovery for each sample is given in Table 3.

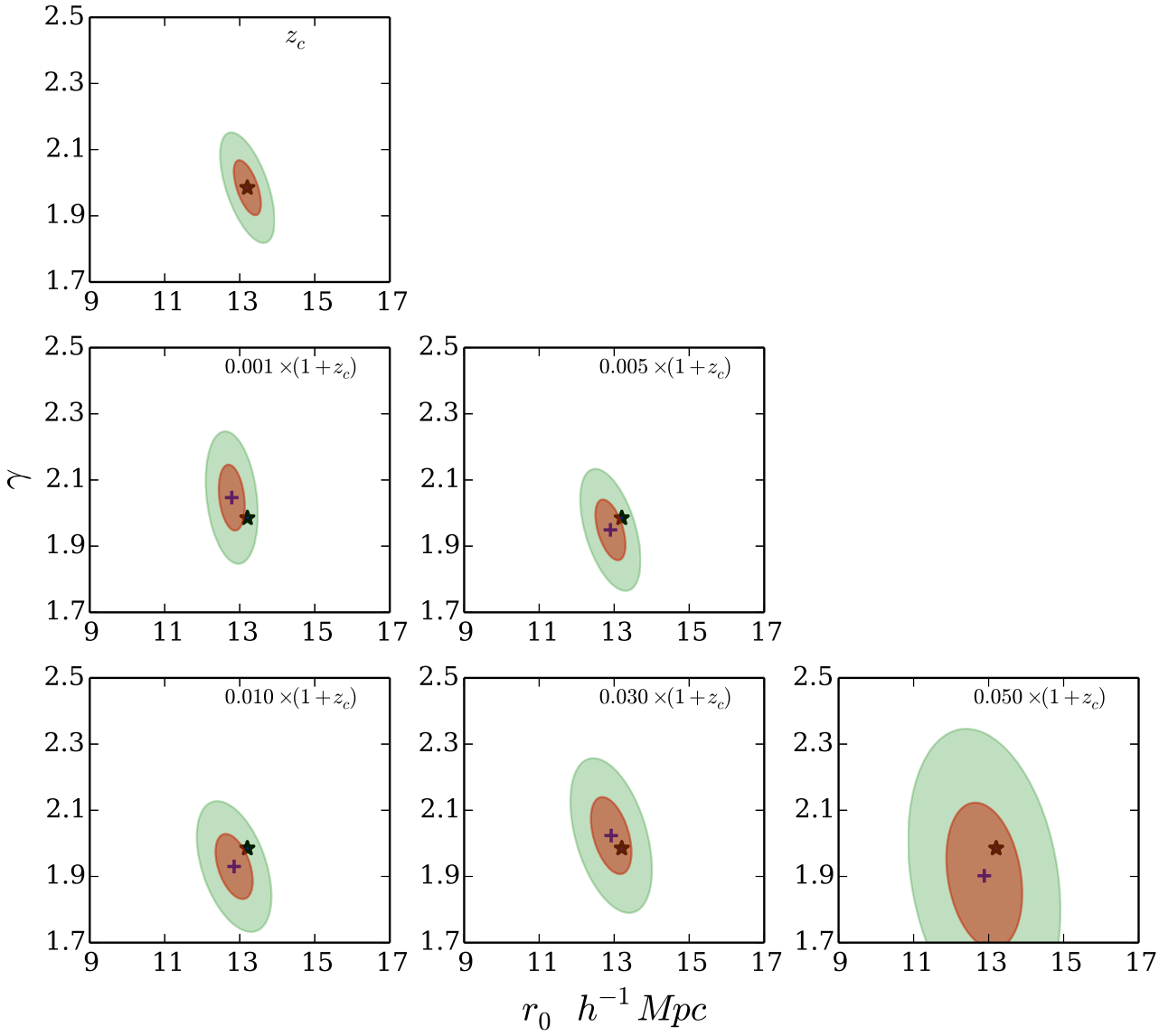

Fig. 9: The 1 σ (shaded *brown*) and 3 σ (shaded *green*) error ellipses for the parameters r_0 and γ. *Top panel:* The original catalogue with cosmological redshifts *Central and bottom panels:* Mock catalogues with increasing photometric redshift errors. The solid star represents the center of the ellipse for the original catalogue, while the cross denotes the centres of the other ellipses.

The projected correlation function $w_p(r_p)$ (Farrow et al. 2015) is related to the real-space correlation function $\xi(r)$ by Equation 9:

$$w_p(r_p) = 2 \int_{r_p}^{\infty} r dr \xi(r)(r^2 - r_p^2)^{-1/2} \tag{9}$$

which can be inverted to obtain the real-space correlation function:

$$\xi(r) = \frac{-1}{\pi} \int_{r}^{\infty} w'(r_p)(r_p^2 - r^2)^{-1/2} dr_p \tag{10}$$

Theoretically, the upper limits of integration are infinite, but in practice we need to choose finite values both in Equation 8 and Equation 10 which then become:

$$w_p(r_p, \pi_{max}) = \int_0^{\pi_{max}} \xi(r_p, \pi) d\pi \tag{11}$$

and

$$\xi(r) = \frac{-1}{\pi} \int_{r}^{r_{pmax}} w'(r_p)(r_p^2 - r^2)^{-1/2} dr_p \tag{12}$$

where π_{max} and $r_{p_{max}}$ refer respectively to the maximum line of sight separation and the maximum transverse separation.

Given that above a certain value of π, pairs are uncorrelated and $\xi(r_p, \pi)$ drops to zero, it is possible to find an optimal choice for π_{max}. This will be explained in detail in Section 4.3.2. We estimate the real-space correlation function following the method

Table 3: The best-fit parameters obtained for the real-space correlation function $\xi(r)$ of the original sample and the recovered deprojected correlation function $\xi_{dep}(r)$ for the mock photometric redshift samples. We quote the (1) redshift uncertainty, (2) the correlation length r_0, (3) slope γ. The mass cut used is $M_{halo} > 5 \times 10^{13}\ h^{-1}\ M_{\odot}$ and the fit range is fixed at 5-50 Mpc. The fits have been performed both with fixed ($\gamma = 2.0$) and free slope.

Redshift uncertainty $\left(\frac{\sigma_z}{1+z_c}\right)$	r_0 $(h^{-1}Mpc)$	γ
z_c	13.16±0.17	2.0 (*fixed*)
	13.20±0.23	1.97±0.05
0.001	12.82±0.17	2.0 (*fixed*)
	12.91±0.22	2.02±0.05
0.005	12.52±0.22	2.0 (*fixed*)
	12.89±0.26	1.94±0.06
0.010	12.33±0.28	2.0 (*fixed*)
	12.84±0.63	1.93±0.08
0.030	12.29±0.30	2.0 (*fixed*)
	12.91±0.72	2.02±0.12
0.050	11.73±0.65	2.0 (*fixed*)
	12.88±0.76	1.90±0.14

of Saunders et al. (1992). We use a step function to calculate $w_p(r_p)$, where $w_p(r_p) = w_{p(i)}$ in the logarithmic interval centred on $r_{p(i)}$, and we sum up in steps using the equation:

$$\xi(r_{p(i)}) = \frac{-1}{\pi} \sum_{j \geq i} \frac{w_{p(j+1)} - w_{p(j)}}{r_{p(j+1)} - r_{p(j)}} \; ln\left(\frac{r_{p(j+1)} + \sqrt{r^2_{p(j+1)} - r^2_{p(i)}}}{r_{p(j)} + \sqrt{r^2_{p(j)} - r^2_{p(i)}}} \right) \quad (13)$$

Assuming that the correlation function follows a perfect power–law, $w_p(r_p)$ is given by the formula:

$$w_p(r_p) = r_p \left(\frac{r_0}{r_p}\right)^{\gamma} \frac{\Gamma(\frac{1}{2})\Gamma(\frac{\gamma-1}{2})}{\Gamma(\frac{\gamma}{2})} \quad (14)$$

where Γ is the Euler's gamma function.

We compare the values of r_0 (with fixed slope) obtained from the fit of the recovered deprojected correlation function $\xi_{dep}(r)$ using Equation 3. We also compared the values from the fit of $w_p(r_p)$ with the same fixed slope using Equation 14 and found it to be similar to what we obtain for the recovered deprojected correlation function $\xi_{dep}(r)$.

4.3. Application to a cluster mock catalogue

4.3.1. Photo-z catalogue selection

As a first test, we apply the formalism described in the previous section to a mock cluster sample within the fixed redshift slice $0.4 < z < 0.7$.

For each cluster, we assign a photometric redshift z_{phot} following the probability $P(z_{phot}|z_c) = G(z_c, \sigma_z)$ where $\sigma_z = \sigma_{(z=0)} \times (1 + z_c)$. As mentioned in Crocce et al. (2011), doing the selection in a top-hat photometric redshift window and in a top-hat cosmological redshift window with the same boundaries is not equivalent. Figure 7 compares the distribution in cosmological redshift of the clusters selected in the top-hat cosmological redshift window $0.4 < z_c < 0.7$ (given by the filled histogram), the clusters selected by the top hat photometric redshift window $0.4 < z_{phot} < 0.7$ (given by the solid blue line) and the clusters for which the photometric redshifts are outside the slice limits [0.4,0.7] (given by the dashed blue line) for four of our photometric samples. The distribution in cosmological redshift $N(z_c)$ of the objects selected by the top-hat z_{phot} window is broader than that selected by the top-hat z_c window, and this effect increases with increasing σ_z. When performing the selection in z_{phot} window rather than in z_c window, a fraction of clusters with z_c outside these slice limits but with z_{phot} within the slice limits [0.4,0.7] are included, resulting then as contaminants. The distribution of clusters with z_{phot} outside the window [0.4,0.7] is also shown as a dashed blue line. It shows that a fraction of clusters with z_{phot} outside [0.4,0.7] have z_c within the slice limits [0.4,0.7]. These objets are then lost by the top-hat photometric redshift selection.

The fraction of contaminating and missing clusters depends on the photometric redshift uncertainty and also on the $N(z)$ distribution. We calculate the fraction of common objects between the top hat z_{phot} and z_c selections for the different σ_z and redshift windows considered. It varies from 99% to 70% for samples with $\sigma_z/(1+z_c) = 0.001$ (at $z \approx 0.1$) to $\sigma_z/(1+z_c) = 0.050$ (at $z \approx 1.3$) respectively. Only the samples with $\sigma_z/(1+z_c) = 0.050$ and above a redshift of $z > 0.7$ have less than 80% objects in common, as we know that the photo-z error scales as $\sigma_z = \sigma_{(z=0)} \times (1 + z_c)$. In our case there are four samples that fall in this category (fourth panel of Table A.1). For all the other samples we choose, the average fraction of common clusters is more than 80% and so by choosing a direct cut in photo-z space, we expect that the final clustering is not affected by a huge margin. To calculate the effect of $N(z)$ on contaminated and missing clusters, we calculate both the mean and median redshift for the photometric redshift samples we have. It can be seen from Table A.2 that both the mean and the median redshift do not vary much when compared to the same of the cosmological redshift sample. The percentage of contaminants for each redshift slice and given photometric uncertainty along with the $N_{clusters}$ in z_c and z_{phot} window and the number of common clusters is mentioned in Table A.1.

4.3.2. Selecting the integration limits

$\xi(r_p, \pi)$ is calculated on a grid with logarithmically spaced bins both in r_p and π. The maximum value of r_p depends on the survey dimension in the transverse plane. In the redshift range $0.4 < z < 0.7$, the maximum separation across the line of sight direction in our light-cone is $\approx 500\ h^{-1}$Mpc. For the upper limit of integration in Equation 12 we fixed a value $r_{p(max)} = 400\ h^{-1}$Mpc, corresponding to 80 percent of the maximum transversal separation. For higher redshift samples we are aware that the maximum separation across the line of sight increases, but we find that the

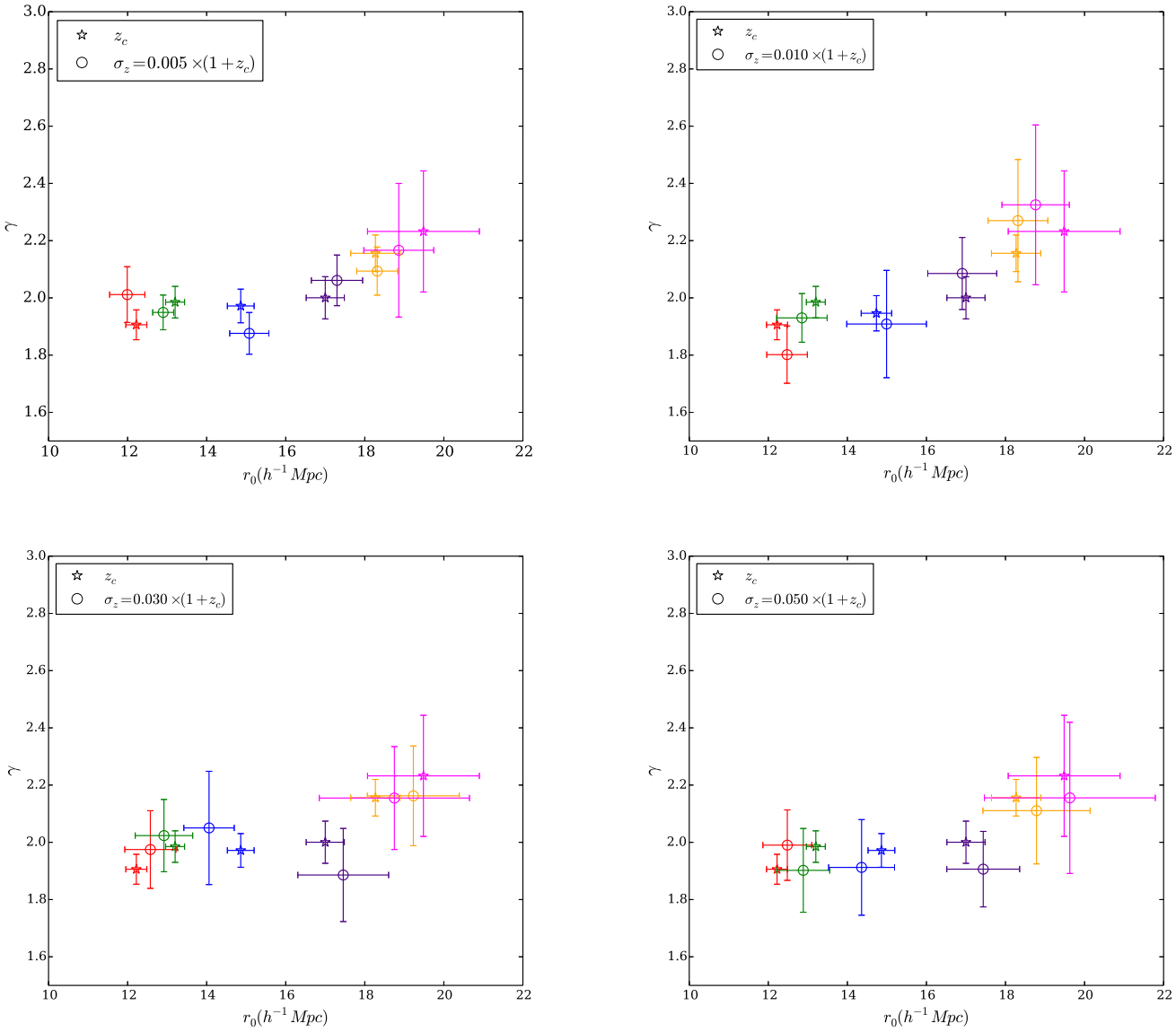

Fig. 10: The evolution of r_0 and γ with redshift for clusters with a mass cut $M_{halo} > 5 \times 10^{13}\ h^{-1}\ M_\odot$ for samples with increasing redshift uncertainty ($\sigma_z/(1+z_c) = 0.005$, 0.010, 0.030 and 0.050). *Red* ($0.1 < z < 0.4$), *Green* ($0.4 < z < 0.7$), *Blue* ($0.7 < z < 1.0$), *Indigo* ($1.0 < z < 1.3$), *Gold* ($1.3 < z < 1.6$), *Magenta* ($1.6 < z < 2.1$).

value of 400 h^{-1}Mpc includes almost all correlated pairs without adding any noise.

In the case of clusters where we have low statistics as compared to galaxy catalogues, the choice of the bin width must be taken into account, if not the Poisson noise will dominate. A convergence test is performed for choosing the number and the width of bins in r_p and π_{max}.

Since higher photometric errors produce larger redshift space distortions, a different value of π_{max} has to be fixed for each photometric redshift mock. We determine its value in the following way. We recover the real-space correlation function with the method described in Section 4.2, using increasing values of π_{max}. Initially the amplitude of $\xi_{dep}(r)$ is underestimated because many correlated pairs are not taken into account; it increases when increasing π_{max} up to a maximum value, beyond which it starts to fluctuate and noise starts to dominate. Applying this test to each mock, we select the π_{max} value corresponding to the maximum recovered amplitude.

We show an example of the π_{max} test for the photometric sample with $\sigma_z = 0.010 \times (1 + z_c)$. It can be seen from Figure 11 that the amplitude of the correlation function increases with increasing π_{max}, but only up to a certain value, which we call as the maximum recovered amplitude. It can be seen that integrating the function above this value of π_{max} only results in noise.

It is clear from our tests on simulations (see Figure 11) that there is an optimal π_{max} value; integrating beyond that limit increases the noise. In future work on observed cluster samples, using the data themselves, we can examine the value of the observed correlation amplitude as a function of π_{max}, choosing the π_{max} value providing the maximum correlation amplitude.

We have checked that by applying this method to the original light-cone with cosmological redshifts we correctly recover its

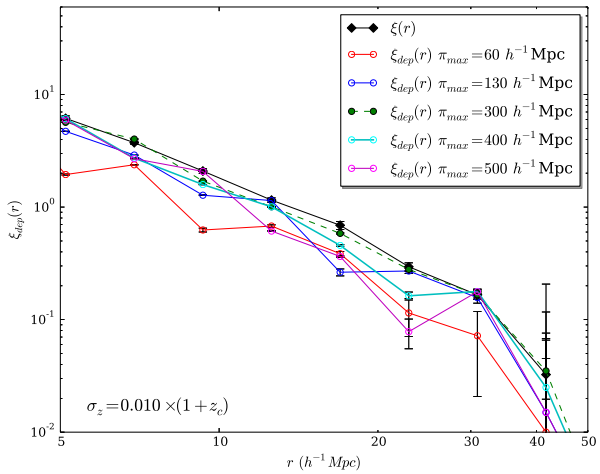

Fig. 11: The recovered correlation function with different values of π_{max} (as colour coded in the figure) for the sample with $\sigma_z = 0.010 \times (1 + z_c)$ in the redshift range $0.4 < z < 0.7$. The black line joining the diamonds in both the plots is the real-space correlation function calculated for the cosmological redshift sample (same as the red line in Figure 8). Poisson error bars are plotted just for convenience.

real-space correlation function. The values of π_{max} used for our reference sample ($0.4 < z < 0.7$) are given in Table 2.

4.3.3. The quality of the recovery

In Figure 8 we compare $\xi_{dep}(r)$ of our five mocks with the real-space correlation function $\xi(r)$. It is clear that $\xi_{dep}(r)$ reproduces quite well $\xi(r)$, but shows increasing fluctuations with increasing σ_z. The ratio $\xi_{dep}(r)/\xi(r)$ is slightly smaller than 1 but within 1σ at all scales for all the mocks up to $\sigma_z/(1 + z_c) = 0.05$.

The quality of the recovery is determined using $\Delta\xi$, an "average normalised residual" defined by Arnalte-Mur et al. (2009) as:

$$\Delta\xi = \frac{1}{N} \sum_i \left| \frac{\xi_{dep}(r_i) - \xi(r_i)}{\xi(r_i)} \right| \tag{15}$$

where r_i refers to the values in the i^{th} bin considered and $\xi(r_i)$ is the real-space correlation function.

In the case of real data, where z_c is not available, one can still calculate the quality of the recovery using the covariance matrix and is defined as:

$$\widehat{\Delta\xi} = \frac{1}{N} \sum_i \frac{\sqrt{C_{ii}}}{|\xi_{dep}(r_i)|} \tag{16}$$

wherein we use the covariance matrix that we have obtained using the jackknife resampling method mentioned in Equation 4. The values of $\Delta\xi$ and $\widehat{\Delta\xi}$ estimated in the range 5-50 h^{-1}Mpc, are listed in Table 2.

One can see from Table 2 that for the lowest photometric error considered, $\sigma_z/(1 + z_c) = 0.001$, the real-space correlation function is recovered within 5%. For $\sigma_z/(1 + z_c) = 0.005$ and $\sigma_z/(1 + z_c) = 0.010$ it is recovered within 7%, within 9% for $\sigma_z/(1+z_c) = 0.030$ and finally within 15% for $\sigma_z/(1+z_c) = 0.05$.

The best-fit parameters of the deprojected correlation functions are shown in Table 3. The fitting is performed with both a free and fixed slope $\gamma = 2.0$. The correlation length obtained for our 5 mock photometric samples is consistent within $\sim 1\sigma$ with the real-space correlation length $r_0 = 13.20 \pm 0.23$ h^{-1}Mpc and $r_0 = 13.16 \pm 0.17$ h^{-1}Mpc obtained for the z_c sample for $\xi(r)$ (free slope) and $\xi(r)$ (fixed slope) respectively. The best-fit r_0 obtained for this particular sample ($0.4 < z_c < 0.7$) seems to have a value that is always lower, regardless of the photometric uncertainty, when compared to the r_0 obtained for the true z_c sample. This is just a coincidence and is not always the case, as it can be seen for other samples with different redshift limits. When the slope is set free, direct comparison of r_0 between the samples cannot be made and so in Figure 9 we plot the 3 sigma error ellipses around the best-fit values of r_0 and γ for all the mocks. As expected, the errors on both r_0 and γ increase with the photometric error, but are always within $\sim 1\sigma$ with respect to the real space values.

We also applied the deprojection method for higher photometric redshift errors to test how far the method could be applied. It was found that from $\sigma_z/(1 + z_c) = 0.1$, the error on the recovery is very large and the recovered correlation function becomes biased.

4.3.4. Recovering the redshift evolution of the correlation function from sub-samples selected using photometric redshifts

We check how accurately we can follow the redshift evolution of the cluster real-space correlation function when using photometric redshifts and the deprojection method to retrieve the real-space correlation function. We have previously shown this for the light-cone with cosmological redshifts in Figure 3.

For this purpose, we analyse 4 mocks with redshift uncertainties of $\sigma_z/(1 + z_c) = 0.005, 0.010, 0.030$ and 0.050 respectively, in 5 redshift slices, from $0.1 < z < 0.4$ to $1.6 < z < 2.1$ with the same mass cut $M_{halo} > 5 \times 10^{13}$ h^{-1} $M_\odot$ as done in Section 3.2. The results are shown in Figure 10 and the values of the best-fit parameters for all the 4 photometric samples are given in Table A.2 in the Appendix section along with the number of clusters ($N_{clusters}$) and the mean and median redshift for each sample.

Figure 10 shows the evolution of the best-fit parameters r_0 and γ for the different redshift slices. The four panels correspond to the different photometric redshift errors tested. It can be compared to Figure 3 which shows the values of r_0 and γ estimated for the same redshift slices but using cosmological redshifts. The fits are performed in the range within which $\xi(r)$ can be described using a power-law. As in Figure 3, r_0 and γ are shown to increase with redshift but the errors on their estimates become larger as the photometric redshift error increases. As a result, the error bars on the r_0 estimates for consecutive redshift slices tested tend to superimpose when considering large values of σ_z. The increase of r_0 with redshift remains detectable, but a larger binning in redshift is requested to detect this effect significantly when working with large σ_z. One can note that the parameters estimated from the deprojected correlation function are within 1σ from the ones estimated directly in real-space, and that remains true even for high redshifts and for high values of the photometric errors. The large error bars for the last two redshift slices ($1.3 < z < 1.6$ and $1.6 < z < 2.1$) are both due to the small number of clusters at high redshift (see the histogram shown in Figure 1) and the scaling of the photometric error $\sigma_z = \sigma_{(z=0)} \times (1 + z_c)$. However, it can be seen that the low number of clusters makes the correlation function hard to measure even using cosmological redshifts. From our tests we can conclude that the correlation function can be recovered from photometric redshift surveys us-

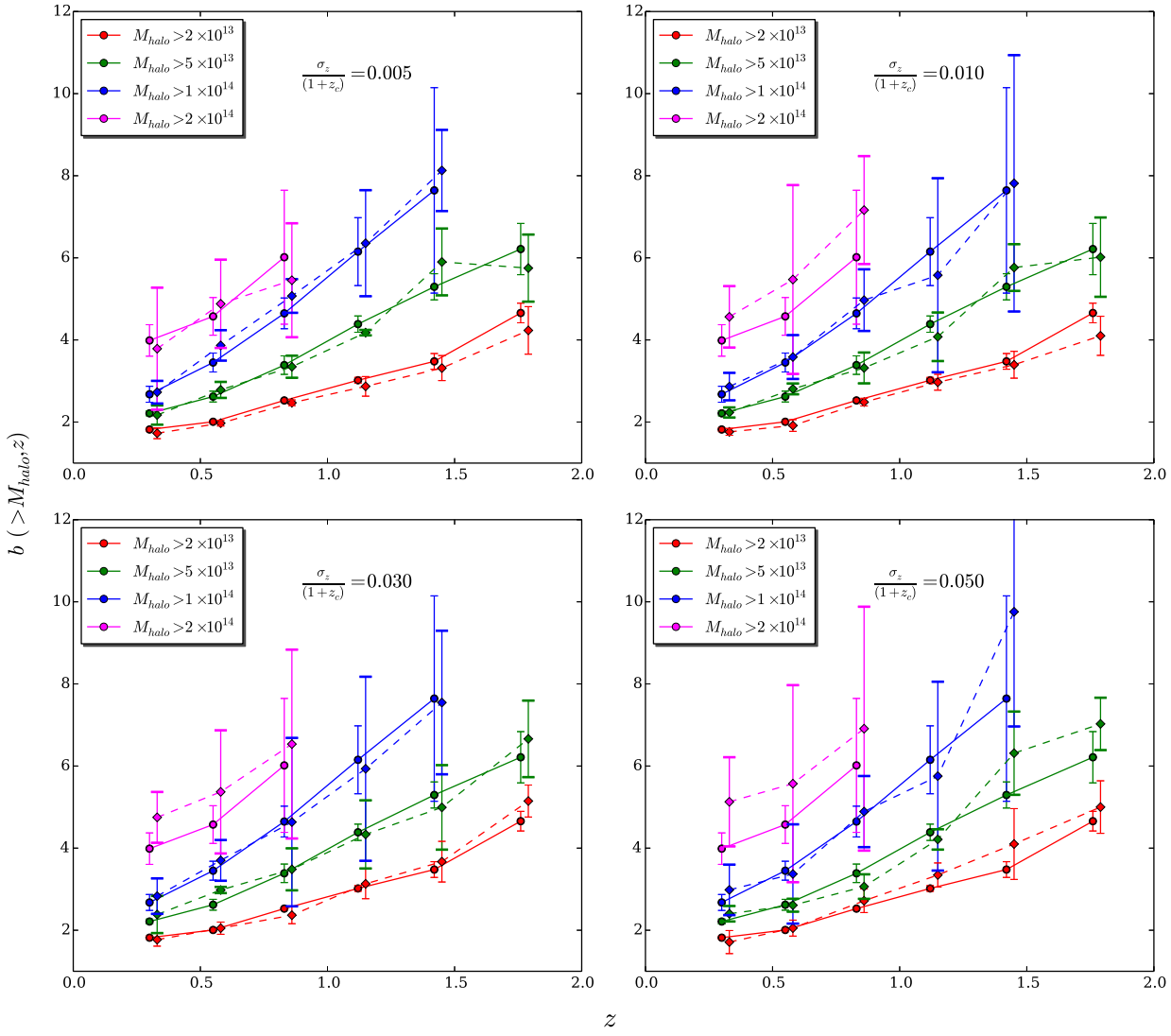

Fig. 12: The evolution of bias with redshift and mass (with units $h^{-1}\ M_\odot$) for the z_c sample (*solid lines*) compared with the photometric samples (*dashed lines*) with redshift uncertainties of $\sigma_z/(1+z_c) = 0.005, 0.010, 0.030$ and $\sigma_z/(1+z_c) = 0.050$.

ing the deprojection method up to a redshift of $z \approx 2.0$ within 10% percent with a photometric redshift error of $\sigma_z/(1+z_c) = 0.030$. In this sense, the recovery performed with this method can be considered as successful. Even in the last redshift slice chosen ($1.6 < z < 2.1$), the correlation function can be recovered within 1σ for all the four photometric redshift uncertainties tested. It can be numerically visualised in the last panel of Table A.2. This point is of particular importance as the $1.5 < z < 2.0$ redshift range has been shown to be very discriminant for constraining cosmological parameters with clusters (Sartoris et al. 2016).

We also estimate the bias as defined in Section 3.4 for $\sigma_z/(1+z_c) = 0.005, 0.010, 0.030$ and 0.050. Our values are given in Tables A.3 and A.4 in the Appendix section along with the number of clusters ($N_{clusters}$) in each sample. The results can be seen in Figure 12. The bias values obtained for the photo-z samples are consistent with the values obtained for the reference sample and are within 1σ error bars. For the first two mass cut samples ($M_{halo} > 2\times10^{13}\ h^{-1}\ M_\odot$ and $5\times10^{13}\ h^{-1}\ M_\odot$), the calculated bias from the photometric samples are within 1σ even up to a median redshift of $z \approx 1.8$. Up to a mass cut of $M_{halo} > 1\times10^{14}\ h^{-1}\ M_\odot$ one can see that the redshift evolution of the bias can be traced very well (even up to redshifts of $z \approx 1.5$).

However we notice that for the highest mass cut sample ($M_{halo} > 2\times10^{14}\ h^{-1}\ M_\odot$) chosen, only the bias values obtained for the photometric sample with $\sigma_z/(1+z_c) = 0.005$ seem to be similar to that obtained by the reference sample. The remaining three photometric samples depict a much higher bias (even though they fall within 1σ) when compared to the reference sample. One reason for this behaviour and also for the large error bars for this mass cut sample is due to the smaller abundance of clusters at this mass threshold cut as it can be seen from Table A.3 and A.4. We also believe that it can be due to the percentage of contaminants that are present in this mass cut sample for three different photometric uncertainties. We have calculated the contaminants for this mass cut sample and they seem to be higher at

certain redshifts when compared to the contaminants at the same redshifts found for the low mass cut samples.

However up to mass cut of $M_{halo} > 5 \times 10^{13}\ h^{-1}\ M_{\odot}$, the evolution in redshift and mass of the bias is clearly distinguished, that too up to the highest redshift tested ($z \approx 2.1$).

5. Discussion and conclusions

In future, most of the cluster detections in large galaxy surveys will be based on photometric catalogues Therefore the main aim of this work was to apply a method for recovering the spatial two–point correlation function $\xi(r)$ of clusters using only photometric redshifts and assess its performance.

In order to estimate the real-space correlation function $\xi(r)$, we applied a method originally developed to correct for peculiar velocity distortions, first estimating the projected correlation function $w_p(r_p)$, then applying Equation 12 to deproject it.

For our analysis we used the 500 deg^2 light-cone of Merson et al. (2013). Mock photometric redshifts were generated from the cosmological redshifts assuming a Gaussian error $\sigma_z = \sigma_{(z=0)} \times (1 + z_c)$ (as described in Section 4.1). This represents a first approximation, sufficient for the scope of the present work; a more realistic approach will have to include real photo-z distributions and catastrophic failures.

Here are our main results.

1. We directly estimate the cluster correlation function in real-space (i.e. using cosmological redshifts) for sub-samples of the light-cone in different redshift intervals and with different mass thresholds (see Section 3.2 and 3.3). As expected, we find an increasing clustering strength with both redshift and mass threshold. At a fixed mass threshold, the correlation amplitude increases with redshift, while at a fixed redshift the correlation amplitude increases with mass threshold. The increase of the correlation amplitude with redshift is larger for more massive haloes: for example, for $M_{halo} > 2 \times 10^{13}\ h^{-1}\ M_{\odot}$, $r_0 = 9.89 \pm 0.20$ at $z = 0.25$ and $r_0 = 12.41 \pm 0.42$ at $z = 1.45$; for $M_{halo} > 1 \times 10^{14}\ h^{-1}\ M_{\odot}$, $r_0 = 14.60 \pm 0.35$ at $z = 0.25$ and $r_0 = 26.09 \pm 4.10$ at $z = 1.45$.
2. We fit the relation between the clustering length r_0 and the mean intercluster distance d in the redshift interval $0.1 \leq z \leq 2.1$ up to $z \approx 2.0$, finding $r_0 = 1.77 \pm 0.08(d)^{0.58\pm0.01}\ h^{-1}$Mpc, which is consistent with the relation $r_0 = 1.70(d)^{0.60}\ h^{-1}$Mpc obtained by Younger et al. (2005) for the local redshift range $0 \leq z \leq 0.3$.
3. We estimate the bias parameter directly in real-space (using cosmological redshifts), with different mass thresholds. Analogously to the correlation amplitude, the bias increases with redshift, and the increase is larger for more massive clusters. Our results are consistent with Estrada et al. (2009) and with the theoretical prediction of Tinker et al. (2010).
4. We finally apply the deprojection method to recover the real-space correlation function $\xi(r)$ of different sub-samples using photometric redshifts. We recover $\xi(r)$ within $\sim 7\%$ on scales $5 < r < 50\ h^{-1}$Mpc with a photometric error of $\sigma_z/(1 + z_c) = 0.010$ and within $\sim 9\%$ for samples with $\sigma_z/(1 + z_c) = 0.030$; the best–fit parameters of the recovered real–space correlation function, as well as the bias, are within 1σ of the corresponding values for the direct estimate in real-space, up to $z \sim 2$.

Our results are promising in view of future surveys such as Euclid and LSST that will provide state-of-the-art photometric redshifts over an unprecedented range of redshift scales. This work represents the first step towards a more complete analysis taking into account the different observational problems to be faced when determining cluster clustering from real data. We are planning to extend this study to the use of more realistic photo-z errors. We are also planning to apply the deprojection method to cluster catalogues produced by cluster detection algorithms. This implies taking into account the selection function of the cluster catalogue, and investigate the impact of purity and completeness on clustering. Another important issue to be faced is that mass in general is not available for cluster catalogues derived from data so that a proxy of mass such as richness has to be used. The fact that the scatter of the relation between mass and richness introduces another uncertainty has to be taken into account when using clusters for constraining the cosmological parameters (see e.g. (Berlind et al. 2003; Kravtsov et al. 2004; Zheng et al. 2005; Rozo et al. 2009; Rykoff et al. 2012)). Another important constraint for cosmological parameters is given by the BAO feature in the two-point correlation function (Veropalumbo et al. 2014, 2016). As we have pointed out in Section 2, the size of the light-cone we used (500 deg^2) is not large enough to detect the BAO feature. It will be interesting to extend this analysis to forthcoming all-sky simulations to test if the BAO feature can be detected using photometric redshifts, and if so with which accuracy, in next generation surveys.

Acknowledgements. We thank Dr. Alex Merson (University College London) and Carlton Baugh (Durham University) for kindly providing their simulation on which this work is based on. We thank Dr. Pablo Arnalte-Mur (Universitat de València) for a detailed discussion on the deprojection method used and Gianluca Castignani for giving us insights into the subjects of error analysis and other statistical methods used in this research. We would also like to thank the anonymous referee for helpful comments. Srivatsan Sridhar is supported by the Erasmus Mundus Joint Doctorate Program by Grant Number 2013-1471 from the agency EACEA of the European Commission. This research made use of TOPCAT and STIL: Starlink Table/VOTable Processing Software developed by Taylor (2005) and also the Code for Anisotropies in the Microwave Background (CAMB) (Lewis et al. 2000; Howlett et al. 2012). The Millennium Simulation databases (Lemson & Virgo Consortium 2006) used in this paper and the web application providing online access to them were constructed as part of the activities of the German Astrophysical Virtual Observatory. Srivatsan Sridhar would also like to thank Sridhar Krishnan, Revathy Sridhar and Madhumitha Srivatsan for their support and encouragement during this work.

References

Angulo, R. E., Baugh, C. M., Frenk, C. S., et al. 2005, MNRAS, 362, L25
Arnalte-Mur, P., Fernández-Soto, A., Martínez, V. J., et al. 2009, MNRAS, 394, 1631
Ascaso, B., Mei, S., & Benítez, N. 2015, MNRAS, 453, 2515
Bahcall, N. A., Dong, F., Hao, L., et al. 2003, ApJ, 599, 814
Bahcall, N. A., Hao, L., Bode, P., & Dong, F. 2004, ApJ, 603, 1
Bahcall, N. A. & Soneira, R. M. 1983, ApJ, 270, 20
Bahcall, N. A. & West, M. J. 1992, ApJ, 392, 419
Berlind, A. A., Weinberg, D. H., Benson, A. J., et al. 2003, ApJ, 593, 1
Bode, P. & Ostriker, J. P. 2003, ApJS, 145, 1
Borgani, S., Plionis, M., & Kolokotronis, V. 1999, MNRAS, 305, 866
Bower, R. G., Benson, A. J., Malbon, R., et al. 2006, MNRAS, 370, 645
Colberg, J. M., White, S. D. M., Yoshida, N., et al. 2000, MNRAS, 319, 209
Crocce, M., Cabré, A., & Gaztañaga, E. 2011, MNRAS, 414, 329
Croft, R. A. C., Dalton, G. B., Efstathiou, G., Sutherland, W. J., & Maddox, S. J. 1997, MNRAS, 291, 305
Davis, M., Efstathiou, G., Frenk, C. S., & White, S. D. M. 1985, ApJ, 292, 371
Davis, M. & Peebles, P. J. E. 1983, ApJ, 267, 465
Eisenstein, D. J., Weinberg, D. H., Agol, E., et al. 2011, AJ, 142, 72
Estrada, J., Sefusatti, E., & Frieman, J. A. 2009, ApJ, 692, 265
Farrow, D. J., Cole, S., Norberg, P., et al. 2015, MNRAS, 454, 2120
Fisher, K. B., Davis, M., Strauss, M. A., Yahil, A., & Huchra, J. P. 1994, MNRAS, 267, 927
Font, A. S., Bower, R. G., McCarthy, I. G., et al. 2008, MNRAS, 389, 1619
Garilli, B., Guzzo, L., Scodeggio, M., et al. 2014, A&A, 562, A23
Gonzalez-Perez, V., Lacey, C. G., Baugh, C. M., et al. 2014, MNRAS, 439, 264

Governato, F., Babul, A., Quinn, T., et al. 1999, MNRAS, 307, 949
Guo, Q., White, S., Angulo, R. E., et al. 2013, MNRAS, 428, 1351
Guzzo, L., Scodeggio, M., Garilli, B., et al. 2014, A&A, 566, A108
Hamilton, A. J. S. 1993, ApJ, 417, 19
Hong, T., Han, J. L., Wen, Z. L., Sun, L., & Zhan, H. 2012, ApJ, 749, 81
Hopkins, P. F., Bahcall, N. A., & Bode, P. 2005, ApJ, 618, 1
Howlett, C., Lewis, A., Hall, A., & Challinor, A. 2012, JCAP, 1204, 027
Huchra, J. P., Henry, J. P., Postman, M., & Geller, J., M. 1990, ApJ, 365, 66
Hütsi, G. 2010, MNRAS, 401, 2477
Ilbert, O., Arnouts, S., McCracken, H. J., et al. 2006, A&A, 457, 841
Ilbert, O., Capak, P., Salvato, M., et al. 2009, ApJ, 690, 1236
Ivezic, Z., Tyson, J. A., Abel, B., et al. 2008, ArXiv e-prints [arXiv:0805.2366]
Jiang, L., Helly, J. C., Cole, S., & Frenk, C. S. 2014, MNRAS, 440, 2115
Kaiser, N. 1987, MNRAS, 227, 1
Kerscher, M., Szapudi, I., & Szalay, A. S. 2000, ApJ, 535, 13
Klypin, A. A. & Kopylov, A. I. 1983, Soviet Astronomy Letters, 9, 41
Kravtsov, A. V., Berlind, A. A., Wechsler, R. H., et al. 2004, ApJ, 609, 35
Lagos, C. d. P., Bayet, E., Baugh, C. M., et al. 2012, MNRAS, 426, 2142
Landy, S. D. & Szalay, A. S. 1993, ApJ, 412, 64
Laureijs, R., Amiaux, J., Arduini, S., et al. 2011, ArXiv e-prints [arXiv:1110.3193]
Le Fèvre, O., Vettolani, G., Garilli, B., et al. 2005, A&A, 439, 845
Lemson, G. & Virgo Consortium, t. 2006, ArXiv Astrophysics e-prints [astro-ph/0608019]
Lewis, A., Challinor, A., & Lasenby, A. 2000, Astrophys. J., 538, 473
LSST Science Collaboration, Abell, P. A., Allison, J., et al. 2009, ArXiv e-prints [arXiv:0912.0201]
Majumdar, S. & Mohr, J. J. 2004, ApJ, 613, 41
Marulli, F., Bianchi, D., Branchini, E., et al. 2012, MNRAS, 426, 2566
Marulli, F., Veropalumbo, A., & Moresco, M. 2016, Astronomy and Computing, 14, 35
Marulli, F., Veropalumbo, A., Moscardini, L., Cimatti, A., & Dolag, K. 2015, ArXiv e-prints [arXiv:1505.01170]
Merson, A. I., Baugh, C. M., Helly, J. C., et al. 2013, MNRAS, 429, 556
Mo, H. J. & White, S. D. M. 1996, MNRAS, 282, 347
Moscardini, L., Matarrese, S., Lucchin, F., & Rosati, P. 2000, MNRAS, 316, 283
Norberg, P., Gaztañaga, E., Baugh, C. M., & Croton, D. J. 2011, MNRAS, 418, 2435
Peacock, J. A. & West, M. J. 1992, MNRAS, 259, 494
Peebles, P. J. E. 1980, The large-scale structure of the universe
Rozo, E., Rykoff, E. S., Koester, B. P., et al. 2009, ApJ, 703, 601
Rykoff, E. S., Koester, B. P., Rozo, E., et al. 2012, ApJ, 746, 178
Sánchez, C., Carrasco Kind, M., Lin, H., et al. 2014, MNRAS, 445, 1482
Sartoris, B., Biviano, A., Fedeli, C., et al. 2016, MNRAS, 459, 1764
Saunders, W., Rowan-Robinson, M., & Lawrence, A. 1992, MNRAS, 258, 134
Sheth, R. K., Mo, H. J., & Tormen, G. 2001, MNRAS, 323, 1
Spergel, D. N., Bean, R., Doré, O., et al. 2007, ApJS, 170, 377
Springel, V. 2005, MNRAS, 364, 1105
Springel, V., White, S. D. M., Jenkins, A., et al. 2005, Nature, 435, 629
Taylor, M. B. 2005, in Astronomical Society of the Pacific Conference Series, Vol. 347, Astronomical Data Analysis Software and Systems XIV, ed. P. Shopbell, M. Britton, & R. Ebert, 29
Tinker, J. L., Robertson, B. E., Kravtsov, A. V., et al. 2010, ApJ, 724, 878
Totsuji, H. & Kihara, T. 1969, PASJ, 21, 221
Veropalumbo, A., Marulli, F., Moscardini, L., Moresco, M., & Cimatti, A. 2014, MNRAS, 442, 3275
Veropalumbo, A., Marulli, F., Moscardini, L., Moresco, M., & Cimatti, A. 2016, MNRAS, 458, 1909
Younger, J. D., Bahcall, N. A., & Bode, P. 2005, Astrophys. J., 622, 1
Zehavi, I., Zheng, Z., Weinberg, D. H., et al. 2005, ApJ, 630, 1
Zheng, Z., Berlind, A. A., Weinberg, D. H., et al. 2005, ApJ, 633, 791

Appendix A: Values of best-fit parameters from the two-point correlation fit and bias values for photometric redshift catalogues

Table A.2 shows the values of the best-fit parameters (as shown in Figure 10) for the two-point correlation function of the four sub-samples with redshift errors $\sigma_z/(1+z_c) = 0.005, 0.010, 0.030$ and 0.050, and the corresponding values obtained for the parent catalogue with cosmological redshift (z_c).

For the same four sub-samples and the parent sample with cosmological redshift (z_c), tables A.3 and A.4 show the bias values (see also Figure 12).

Table A.1: The number of clusters in a given redshift range for z_c and z_{phot} with mass cut $M_{halo} > 5 \times 10^{13}\ h^{-1}\ M_{\odot}$. The z_{phot} uncertainties are $\sigma_z/(1+z_c) = 0.005, 0.010, 0.030$ and 0.050. (1) Redshift range, (2) number of clusters in z_c window, (3) number of clusters in z_{phot} window, (4) common clusters, (5) uncommon clusters and (6) the percentage of contaminants are quoted.

Redshift range	Clusters in z_c window	Clusters in z_{phot} window	Common	Uncommon	% contaminants
		$\sigma_z = 0.005 \times (1+z_c)$			
$0.1< z <0.4$	3210	3214	3160	50	1.55
$0.4< z <0.7$	7301	7310	7162	139	1.90
$0.7< z <1.0$	8128	8088	7933	195	2.39
$1.0< z <1.3$	5963	6001	5842	121	2.02
$1.3< z <1.6$	3365	3356	3252	113	3.35
$1.6< z <2.1$	2258	2251	2197	61	2.70
		$\sigma_z = 0.010 \times (1+z_c)$			
$0.1< z <0.4$	3210	3216	3115	95	2.95
$0.4< z <0.7$	7301	7338	7042	259	3.54
$0.7< z <1.0$	8128	8095	7745	383	4.71
$1.0< z <1.3$	5963	5973	5676	287	4.81
$1.3< z <1.6$	3365	3350	3144	221	6.56
$1.6< z <2.1$	2258	2239	2133	125	5.53
		$\sigma_z = 0.030 \times (1+z_c)$			
$0.1< z <0.4$	3210	3196	2884	326	10.15
$0.4< z <0.7$	7301	7396	6492	809	11.08
$0.7< z <1.0$	8128	8053	6972	1156	14.22
$1.0< z <1.3$	5963	5880	4958	1005	16.85
$1.3< z <1.6$	3365	3388	2712	653	19.40
$1.6< z <2.1$	2258	2251	1922	336	14.88
		$\sigma_z = 0.050 \times (1+z_c)$			
$0.1< z <0.4$	3210	3205	2647	563	17.53
$0.4< z <0.7$	7301	7433	5906	1395	19.10
$0.7< z <1.0$	8128	7937	6153	1975	24.29
$1.0< z <1.3$	5963	5859	4294	1669	27.98
$1.3< z <1.6$	3365	3352	2248	1117	33.19
$1.6< z <2.1$	2258	2277	1717	541	23.95

Table A.2: The parameters obtained from the fit for the real-space correlation function $\xi(r)$ on the ideal zero-error simulation for the different redshift cut catalogues and the same obtained from the photometric redshift catalogues with $\sigma_z/(1+z_c) = 0.005, 0.010, 0.030$ and 0.050. (1) redshift cut used, (2) photometric uncertainty $\sigma_z/(1+z_c)$, (3) correlation length r_0, (4) slope γ and (5) the number of clusters $N_{clusters}$, (6) median redshift and (7) mean redshift.

Redshift range	$\sigma_z/(1+z_c)$	$r_0\ h^{-1}$Mpc	γ	$N_{clusters}$	Median z	Mean z
$0.1 < z < 0.4$	z_c	12.22±0.26	1.90±0.05	3210	0.30	0.29
	0.005	11.99±0.44	2.01±0.09	3214	0.30	0.29
	0.010	12.47±0.51	1.80±0.10	3216	0.30	0.29
	0.030	12.57±0.64	1.97±0.13	3196	0.30	0.28
	0.050	12.48±0.61	1.99±0.12	3205	0.29	0.28
$0.4 < z < 0.7$	z_c	13.20±0.23	1.98±0.05	7301	0.56	0.55
	0.005	12.89±0.26	1.94±0.06	7310	0.56	0.55
	0.010	12.84±0.63	1.93±0.08	7338	0.56	0.56
	0.030	12.91±0.72	2.02±0.12	7396	0.56	0.55
	0.050	12.88±0.76	1.90±0.14	7433	0.56	0.55
$0.7 < z < 1.0$	z_c	14.86±0.33	1.97±0.05	8128	0.84	0.84
	0.005	15.07±0.49	1.87±0.07	8088	0.84	0.84
	0.010	14.99±1.00	1.90±0.18	8095	0.84	0.84
	0.030	14.06±0.63	2.05±0.19	8053	0.84	0.84
	0.050	14.36±0.83	1.91±0.16	7937	0.84	0.84
$1.0 < z < 1.3$	z_c	17.00±0.48	2.00±0.07	5963	1.13	1.13
	0.005	17.29±0.64	2.06±0.08	6001	1.13	1.13
	0.010	16.90±0.87	2.08±0.12	5973	1.13	1.14
	0.030	17.45±1.14	1.88±0.16	5880	1.13	1.14
	0.050	17.43±0.92	1.90±0.13	5859	1.13	1.14
$1.3 < z < 1.6$	z_c	18.26±0.62	2.15±0.06	3365	1.43	1.43
	0.005	18.31±0.51	2.09±0.08	3356	1.43	1.43
	0.010	18.31±0.75	2.26±0.21	3350	1.43	1.43
	0.030	19.22±1.16	2.16±0.17	3388	1.42	1.43
	0.050	18.78±1.35	2.11±0.18	3352	1.43	1.43
$1.6 < z < 2.1$	z_c	19.48±1.41	2.23±0.21	2258	1.76	1.79
	0.005	18.86±0.88	2.16±0.23	2251	1.77	1.79
	0.010	18.76±0.85	2.32±0.27	2239	1.77	1.79
	0.030	18.74±1.89	2.15±0.17	2251	1.77	1.79
	0.050	19.62±2.16	2.15±0.26	2277	1.77	1.79

Table A.3: The bias values obtained for the first 2 photometric redshift catalogues ($\sigma_z/(1+z_c)$ = 0.005 and 0.010) with the 4 mass threshold cuts in the 5 redshift bins used. (1) Photometric uncertainty $\sigma_z/(1+z_c)$, (2) mass cut M_{halo} cut, (3) redshift range, (4) the bias and (5) the number of clusters $N_{clusters}$ are given.

$\sigma_z/(1+z_c)$	Mass ($h^{-1}\ M_\odot$)	Redshift range	Bias	$N_{clusters}$
0.005	2×10^{13}	$0.1<z<0.4$	1.71±0.13	10521
		$0.4<z<0.7$	1.97±0.06	27224
		$0.7<z<1.0$	2.46±0.06	35045
		$1.0<z<1.3$	2.86±0.23	31845
		$1.3<z<1.6$	3.31±0.30	23017
		$1.6<z<2.1$	4.23±0.57	18904
	5×10^{13}	$0.1<z<0.4$	2.17±0.23	3214
		$0.4<z<0.7$	2.78±0.19	7310
		$0.7<z<1.0$	3.34±0.26	8088
		$1.0<z<1.3$	4.17±0.06	6001
		$1.3<z<1.6$	6.10±0.81	3356
		$1.6<z<2.1$	5.75±0.81	2251
	1×10^{14}	$0.1<z<0.4$	2.72±0.27	1116
		$0.4<z<0.7$	3.86±0.37	2231
		$0.7<z<1.0$	5.07±0.41	2065
		$1.0<z<1.3$	6.35±1.29	1218
		$1.3<z<1.6$	8.12±0.98	594
	2×10^{14}	$0.1<z<0.4$	3.78±1.48	316
		$0.4<z<0.7$	4.88±1.07	544
		$0.7<z<1.0$	5.45±1.38	399
0.010	2×10^{13}	$0.1<z<0.4$	1.76±0.08	10536
		$0.4<z<0.7$	1.91±0.14	27283
		$0.7<z<1.0$	2.48±0.09	35022
		$1.0<z<1.3$	2.96±0.19	31763
		$1.3<z<1.6$	3.39±0.32	23021
		$1.6<z<2.1$	4.10±0.47	18898
	5×10^{13}	$0.1<z<0.4$	2.23±0.12	3216
		$0.4<z<0.7$	2.80±0.13	7338
		$0.7<z<1.0$	3.31±0.37	8095
		$1.0<z<1.3$	4.07±0.59	5973
		$1.3<z<1.6$	5.76±0.56	3350
		$1.6<z<2.1$	6.01±0.96	2239
	1×10^{14}	$0.1<z<0.4$	2.86±0.33	1124
		$0.4<z<0.7$	3.58±0.53	2235
		$0.7<z<1.0$	4.96±0.75	2069
		$1.0<z<1.3$	5.57±2.36	1210
		$1.3<z<1.6$	7.81±3.12	587
	2×10^{14}	$0.1<z<0.4$	4.56±0.74	318
		$0.4<z<0.7$	5.47±2.3	547
		$0.7<z<1.0$	7.16±1.31	394

Table A.4: The bias values obtained for the last 2 photometric redshift catalogues ($\sigma_z/(1+z_c)$ = 0.030 and 0.050) with the 4 mass threshold cuts in the 5 redshift bins used. (1) Photometric uncertainty $\sigma_z/(1+z_c)$, (2) mass cut M_{halo} cut, (3) redshift range, (4) the bias and (5) the number of clusters $N_{clusters}$ are given.

$\sigma_z/(1+z_c)$	Mass ($h^{-1}\ M_\odot$)	Redshift range	Bias	$N_{clusters}$
0.030	2×10^{13}	$0.1<z<0.4$	1.77±0.15	10581
		$0.4<z<0.7$	2.05±0.14	27475
		$0.7<z<1.0$	2.36±0.20	34849
		$1.0<z<1.3$	3.13±0.36	31457
		$1.3<z<1.6$	3.67±0.49	23028
		$1.6<z<2.1$	5.14±0.38	18863
	5×10^{13}	$0.1<z<0.4$	2.38±0.45	3196
		$0.4<z<0.7$	2.97±0.07	7396
		$0.7<z<1.0$	3.48±0.51	8053
		$1.0<z<1.3$	4.33±0.83	5880
		$1.3<z<1.6$	4.99±1.02	3388
		$1.6<z<2.1$	6.66±0.93	2251
	1×10^{14}	$0.1<z<0.4$	2.83±0.43	1115
		$0.4<z<0.7$	3.70±0.49	2253
		$0.7<z<1.0$	4.63±2.05	2041
		$1.0<z<1.3$	5.93±2.24	1228
		$1.3<z<1.6$	7.54±1.74	580
	2×10^{14}	$0.1<z<0.4$	4.74±0.61	317
		$0.4<z<0.7$	5.37±1.50	554
		$0.7<z<1.0$	6.53±2.30	383
0.050	2×10^{13}	$0.1<z<0.4$	1.71±0.28	10835
		$0.4<z<0.7$	2.05±0.19	27570
		$0.7<z<1.0$	2.71±0.28	34575
		$1.0<z<1.3$	3.34±0.29	31168
		$1.3<z<1.6$	4.20±0.86	22733
		$1.6<z<2.1$	5.01±0.63	18889
	5×10^{13}	$0.1<z<0.4$	2.40±0.18	3205
		$0.4<z<0.7$	2.62±0.21	7443
		$0.7<z<1.0$	3.06±0.29	7937
		$1.0<z<1.3$	4.21±0.24	5859
		$1.3<z<1.6$	6.31±1.01	3352
		$1.6<z<2.1$	7.02±0.63	2277
	1×10^{14}	$0.1<z<0.4$	2.98±0.61	1109
		$0.4<z<0.7$	3.37±1.20	2258
		$0.7<z<1.0$	4.89±0.86	1992
		$1.0<z<1.3$	5.75±2.30	1257
		$1.3<z<1.6$	9.75±2.79	562
	2×10^{14}	$0.1<z<0.4$	5.12±1.08	311
		$0.4<z<0.7$	5.57±2.40	560
		$0.7<z<1.0$	6.91±2.97	370

List of Figures

List of Tables

Bibliography

Abell, G. O. (1958). The Distribution of Rich Clusters of Galaxies. ApJS, 3:211. (Cited in page 42.)

Abell, G. O., Corwin, Jr., H. G., and Olowin, R. P. (1989). A catalog of rich clusters of galaxies. ApJS, 70:1–138. (Cited in page 42.)

Allen, S. W., Evrard, A. E., and Mantz, A. B. (2011). Cosmological Parameters from Observations of Galaxy Clusters. ARA&A, 49:409–470. (Cited in pages 48, 51, 71, 75 and 210.)

Anderson, L., Aubourg, E., Bailey, S., Bizyaev, D., Blanton, M., Bolton, A. S., Brinkmann, J., Brownstein, J. R., Burden, A., Cuesta, A. J., da Costa, L. A. N., Dawson, K. S., de Putter, R., Eisenstein, D. J., Gunn, J. E., Guo, H., Hamilton, J.-C., Harding, P., Ho, S., Honscheid, K., Kazin, E., Kirkby, D., Kneib, J.-P., Labatie, A., Loomis, C., Lupton, R. H., Malanushenko, E., Malanushenko, V., Mandelbaum, R., Manera, M., Maraston, C., McBride, C. K., Mehta, K. T., Mena, O., Montesano, F., Muna, D., Nichol, R. C., Nuza, S. E., Olmstead, M. D., Oravetz, D., Padmanabhan, N., Palanque-Delabrouille, N., Pan, K., Parejko, J., Pâris, I., Percival, W. J., Petitjean, P., Prada, F., Reid, B., Roe, N. A., Ross, A. J., Ross, N. P., Samushia, L., Sánchez, A. G., Schlegel, D. J., Schneider, D. P., Scóccola, C. G., Seo, H.-J., Sheldon, E. S., Simmons, A., Skibba, R. A., Strauss, M. A., Swanson, M. E. C., Thomas, D., Tinker, J. L., Tojeiro, R., Magaña, M. V., Verde, L., Wagner, C., Wake, D. A., Weaver, B. A., Weinberg, D. H., White, M., Xu, X., Yèche, C., Zehavi, I., and Zhao, G.-B. (2012). The clustering of galaxies in the SDSS-III Baryon Oscillation Spectroscopic Survey: baryon acoustic oscillations in the Data Release 9 spectroscopic galaxy sample. MNRAS, 427:3435–3467. (Cited in pages 22 and 83.)

Andreon, S. and Hurn, M. A. (2010). The scaling relation between richness and mass of galaxy clusters: a Bayesian approach. MNRAS, 404:1922–1937. (Cited in pages 51 and 52.)

Arnalte-Mur, P., Fernández-Soto, A., Martínez, V. J., Saar, E., Heinämäki, P., and Suhhonenko, I. (2009). Recovering the real-space correlation function from photometric redshift surveys. MNRAS, 394:1631–1639. (Cited in pages 120, 122 and 135.)

Ascaso, B., Mei, S., and Benítez, N. (2015). Apples to apples A^2 - I. Realistic galaxy simulated catalogues and photometric redshift predictions for next-generation surveys. MNRAS, 453:2515–2532. (Cited in page 120.)

Babcock, H. W. (1939). The rotation of the Andromeda Nebula. *Lick Observatory Bulletin*, 19:41–51. (Cited in page 17.)

Bahcall, N. A. (1996). Clusters and superclusters of galaxies. *ArXiv Astrophysics e-prints*. (Cited in pages 40, 95 and 135.)

Bahcall, N. A. and Cen, R. (1992). Galaxy clusters and cold dark matter - A low-density unbiased universe? ApJ, 398:L81–L84. (Cited in pages 73 and 210.)

Bahcall, N. A., Dong, F., Hao, L., Bode, P., Annis, J., Gunn, J. E., and Schneider, D. P. (2003). The Richness-dependent Cluster Correlation Function: Early Sloan Digital Sky Survey Data. ApJ, 599:814–819. (Cited in pages 82, 110, 111 and 114.)

Bahcall, N. A., Hao, L., Bode, P., and Dong, F. (2004). Evolution of the Cluster Correlation Function. ApJ, 603:1–6. (Cited in pages 94 and 98.)

Bahcall, N. A. and Lubin, L. M. (1994). Resolving the beta-discrepancy for clusters of galaxies. ApJ, 426:513–515. (Cited in page 45.)

Bahcall, N. A. and Oh, S. P. (1996). The Peculiar Velocity Function of Galaxy Clusters. ApJ, 462:L49. (Cited in page 119.)

Bahcall, N. A. and Soneira, R. M. (1983). The spatial correlation function of rich clusters of galaxies. ApJ, 270:20–38. (Cited in pages 56, 63, 64, 94, 110, 172 and 209.)

Bahcall, N. A. and West, M. J. (1992). The cluster correlation function - Consistent results from an automated survey. ApJ, 392:419–423. (Cited in pages 56, 111 and 168.)

Bardeen, J. M., Bond, J. R., Kaiser, N., and Szalay, A. S. (1986). The statistics of peaks of Gaussian random fields. ApJ, 304:15–61. (Cited in page 28.)

Bartelmann, M. (1996). Arcs from a universal dark-matter halo profile. A&A, 313:697–702. (Cited in page 178.)

Basilakos, S. and Plionis, M. (2004). Modelling the two-point correlation function of galaxy clusters in the Sloan Digital Sky Survey. MNRAS, 349:882–888. (Cited in pages 66, 67, 85, 168, 172 and 210.)

Baugh, C. (2000). *Correlation Function and Power Spectra in Cosmology*. (Cited in page 56.)

Baugh, C. M., Gaztanaga, E., and Efstathiou, G. (1995). A comparison of the evolution of density fields in perturbation theory and numerical simulations - II. Counts-in-cells analysis. MNRAS, 274:1049–1070. (Cited in pages 60 and 61.)

Baxter, E. J., Rozo, E., Jain, B., Rykoff, E., and Wechsler, R. H. (2016). Constraining the mass-richness relationship of redMaPPer clusters with angular clustering. MNRAS, 463:205–221. (Cited in page 173.)

Belenkiy, A. (2012). Alexander Friedmann and the origins of modern cosmology. *Physics Today*, 65(10):38. (Cited in page 3.)

Benítez, N. (2000). Bayesian Photometric Redshift Estimation. ApJ, 536:571–583. (Cited in page 119.)

Bennett, C. L., Larson, D., Weiland, J. L., Jarosik, N., Hinshaw, G., Odegard, N., Smith, K. M., Hill, R. S., Gold, B., Halpern, M., Komatsu, E., Nolta, M. R., Page, L., Spergel, D. N., Wollack, E., Dunkley, J., Kogut, A., Limon, M., Meyer, S. S., Tucker, G. S., and Wright, E. L. (2013). Nine-year Wilkinson Microwave Anisotropy Probe (WMAP) Observations: Final Maps and Results. ApJS, 208:20. (Cited in page 5.)

Benoist, C., Maurogordato, S., da Costa, L. N., Cappi, A., and Schaeffer, R. (1996). Biasing in the Galaxy Distribution. ApJ, 472:452. (Cited in pages 60, 61, 62 and 209.)

Berlind, A. A., Weinberg, D. H., Benson, A. J., Baugh, C. M., Cole, S., Davé, R., Frenk, C. S., Jenkins, A., Katz, N., and Lacey, C. G. (2003). The Halo Occupation Distribution and the Physics of Galaxy Formation. ApJ, 593:1–25. (Cited in page 152.)

Beutler, F., Blake, C., Colless, M., Jones, D. H., Staveley-Smith, L., Campbell, L., Parker, Q., Saunders, W., and Watson, F. (2011). The 6dF Galaxy Survey: baryon acoustic oscillations and the local Hubble constant. MNRAS, 416:3017–3032. (Cited in page 22.)

Binney, J. and Tremaine, S. (2008). *Galactic Dynamics: Second Edition*. Princeton University Press. (Cited in page 48.)

Blake, C. and Bridle, S. (2005). Cosmology with photometric redshift surveys. MNRAS, 363:1329–1348. (Cited in page 120.)

Blake, C., Kazin, E. A., Beutler, F., Davis, T. M., Parkinson, D., Brough, S., Colless, M., Contreras, C., Couch, W., Croom, S., Croton, D., Drinkwater, M. J., Forster, K., Gilbank, D., Gladders, M., Glazebrook, K., Jelliffe, B., Jurek, R. J., Li, I.-H., Madore, B., Martin, D. C., Pimbblet, K., Poole, G. B., Pracy, M., Sharp, R., Wisnioski, E., Woods, D., Wyder, T. K., and Yee, H. K. C. (2011). The WiggleZ Dark Energy Survey: mapping the distance-redshift relation with baryon acoustic oscillations. MNRAS, 418:1707–1724. (Cited in page 22.)

Blanton, M. R., Brinkmann, J., Csabai, I., Doi, M., Eisenstein, D., Fukugita, M., Gunn, J. E., Hogg, D. W., and Schlegel, D. J. (2003). Estimating Fixed-Frame Galaxy Magnitudes in the Sloan Digital Sky Survey. AJ, 125:2348–2360. (Cited in page 119.)

Bode, P. and Ostriker, J. P. (2003). Tree Particle-Mesh: An Adaptive, Efficient, and Parallel Code for Collisionless Cosmological Simulation. ApJS, 145:1–13. (Cited in page 101.)

Böhringer, H. and Werner, N. (2010). X-ray spectroscopy of galaxy clusters: studying astrophysical processes in the largest celestial laboratories. A&A Rev., 18:127–196. (Cited in page 50.)

Bond, J. R., Efstathiou, G., and Silk, J. (1980). Massive neutrinos and the large-scale structure of the universe. *Physical Review Letters*, 45:1980–1984. (Cited in page 15.)

Borgani, S. and Guzzo, L. (2001). X-ray clusters of galaxies as tracers of structure in the Universe. Nature, 409:39–45. (Cited in pages 65, 98 and 209.)

Borgani, S. and Kravtsov, A. (2011). Cosmological Simulations of Galaxy Clusters. *Advanced Science Letters*, 4:204–227. (Cited in page 89.)

Borgani, S., Plionis, M., and Kolokotronis, V. (1999). Cosmological constraints from the clustering properties of the X-ray Brightest Abell-type Cluster sample. MNRAS, 305:866–874. (Cited in page 94.)

Bower, R. G., Benson, A. J., Malbon, R., Helly, J. C., Frenk, C. S., Baugh, C. M., Cole, S., and Lacey, C. G. (2006). Breaking the hierarchy of galaxy formation. MNRAS, 370:645–655. (Cited in page 91.)

Cen, R. (2012). The Nature of Damped Lyα Systems and Their Hosts in the Standard Cold Dark Matter Universe. ApJ, 748:121. (Cited in page 46.)

Chandra observatory and Digitised Sky Survey (2016). Intracluster medium of abell 2199. `https://en.wikipedia.org/wiki/Intracluster_medium`. [Online; accessed 11-July-2016]. (Cited in pages 44 and 209.)

Cohn, J. D., Evrard, A. E., White, M., Croton, D., and Ellingson, E. (2007). Red-sequence cluster finding in the Millennium Simulation. MNRAS, 382:1738–1750. (Cited in page 119.)

Coil, A. L. (2013). *The Large-Scale Structure of the Universe*, page 387. (Cited in page 58.)

Coles, P. and Plionis, M. (1991). Topology in two dimensions. I - The Lick Galaxy Catalogue. MNRAS, 250:75–88. (Cited in pages 59 and 209.)

Colless, M., Dalton, G., Maddox, S., Sutherland, W., Norberg, P., Cole, S., Bland-Hawthorn, J., Bridges, T., Cannon, R., Collins, C., Couch, W., Cross, N., Deeley, K., De Propris, R., Driver, S. P., Efstathiou, G., Ellis, R. S., Frenk, C. S., Glazebrook, K., Jackson, C., Lahav, O., Lewis, I., Lumsden, S., Madgwick, D., Peacock, J. A., Peterson, B. A., Price, I., Seaborne, M., and Taylor, K. (2001). The 2dF Galaxy Redshift Survey: spectra and redshifts. MNRAS, 328:1039–1063. (Cited in page 66.)

Collister, A. A. and Lahav, O. (2004). ANNz: Estimating Photometric Redshifts Using Artificial Neural Networks. PASP, 116:345–351. (Cited in page 120.)

Connolly, A. J., Csabai, I., Szalay, A. S., Koo, D. C., Kron, R. G., and Munn, J. A. (1995). Slicing Through Multicolor Space: Galaxy Redshifts from Broadband Photometry. AJ, 110:2655. (Cited in page 120.)

Copi, C. J., Schramm, D. N., and Turner, M. S. (1995). Big-Bang Nucleosynthesis and the Baryon Density of the Universe. *Science*, 267:192–199. (Cited in page 6.)

Crocce, M., Cabré, A., and Gaztañaga, E. (2011). Modelling the angular correlation function and its full covariance in photometric galaxy surveys. MNRAS, 414:329–349. (Cited in page 124.)

Crocce, M., Fosalba, P., Castander, F. J., and Gaztañaga, E. (2010). Simulating the Universe with MICE: the abundance of massive clusters. MNRAS, 403:1353–1367. (Cited in page 174.)

Croft, R. A. C., Dalton, G. B., Efstathiou, G., Sutherland, W. J., and Maddox, S. J. (1997). The richness dependence of galaxy cluster correlations: results from a redshift survey of rich APM clusters. MNRAS, 291:305–313. (Cited in pages 94 and 110.)

Csabai, I., Connolly, A. J., Szalay, A. S., and Budavári, T. (2000). Reconstructing Galaxy Spectral Energy Distributions from Broadband Photometry. AJ, 119:69–78. (Cited in page 119.)

Cuillandre, J.-C. J., Withington, K., Hudelot, P., Goranova, Y., McCracken, H., Magnard, F., Mellier, Y., Regnault, N., Bétoule, M., Aussel, H., Kavelaars, J. J., Fernique, P., Bonnarel, F., Ochsenbein, F., and Ilbert, O. (2012). Introduction to the CFHT Legacy Survey final release (CFHTLS T0007). In *Society of Photo-Optical Instrumentation Engineers (SPIE) Conference Series*, volume 8448 of *Society of Photo-Optical Instrumentation Engineers (SPIE) Conference Series*, page 0. (Cited in pages 164, 165 and 166.)

Curvature of the Universe (2016). Curvature of the universe, wikipedia. `https://en.wikipedia.org/wiki/Shape_of_the_universe`. [Online; accessed 29-July-2016]. (Cited in page 12.)

da Costa, L. N., Geller, M. J., Pellegrini, P. S., Latham, D. W., Fairall, A. P., Marzke, R. O., Willmer, C. N. A., Huchra, J. P., Calderon, J. H., Ramella, M., and Kurtz, M. J. (1994). A complete southern sky redshift survey. ApJ, 424:L1–L4. (Cited in page 61.)

Davis, M., Efstathiou, G., Frenk, C. S., and White, S. D. M. (1985a). The evolution of large-scale structure in a universe dominated by cold dark matter. ApJ, 292:371–394. (Cited in page 15.)

Davis, M., Efstathiou, G., Frenk, C. S., and White, S. D. M. (1985b). The evolution of large-scale structure in a universe dominated by cold dark matter. ApJ, 292:371–394. (Cited in page 90.)

Davis, M., Huchra, J., Latham, D. W., and Tonry, J. (1982). A survey of galaxy redshifts. II - The large scale space distribution. ApJ, 253:423–445. (Cited in page 60.)

Davis, M. and Peebles, P. J. E. (1983). A survey of galaxy redshifts. V - The two-point position and velocity correlations. ApJ, 267:465–482. (Cited in pages 54, 56 and 122.)

de Jong, J. T. A., Verdoes Kleijn, G. A., Kuijken, K. H., and Valentijn, E. A. (2013). The Kilo-Degree Survey. *Experimental Astronomy*, 35:25–44. (Cited in page 173.)

de Lapparent, V., Geller, M. J., and Huchra, J. P. (1988). The mean density and two-point correlation function for the CfA redshift survey slices. ApJ, 332:44–56. (Cited in page 60.)

de Propris, R., Eisenhardt, P. R., Stanford, S. A., and Dickinson, M. (1998). The Infrared Luminosity Function of Galaxies in the Coma Cluster. ApJ, 503:L45–L48. (Cited in page 152.)

Dietrich, J. P., Böhnert, A., Lombardi, M., Hilbert, S., and Hartlap, J. (2012). The origin of peak-offsets in weak-lensing maps. MNRAS, 419:3547–3552. (Cited in page 118.)

Dodelson, S., Gates, E. I., and Turner, M. S. (1996). Cold Dark Matter. *Science*, 274:69–75. (Cited in page 15.)

Edge, A., Sutherland, W., Kuijken, K., Driver, S., McMahon, R., Eales, S., and Emerson, J. P. (2013). The VISTA Kilo-degree Infrared Galaxy (VIKING) Survey: Bridging the Gap between Low and High Redshift. *The Messenger*, 154:32–34. (Cited in page 173.)

Efstathiou, G. (1996). Observations of Large-Scale Structure in the Universe. In Schaeffer, R., Silk, J., Spiro, M., and Zinn-Justin, J., editors, *Cosmology and Large Scale Structure*, page 133. (Cited in pages 54 and 56.)

Efstathiou, G., Davis, M., White, S. D. M., and Frenk, C. S. (1985). Numerical techniques for large cosmological N-body simulations. ApJS, 57:241–260. (Cited in page 15.)

Eisenstein, D. J. and Hu, W. (1998). Baryonic Features in the Matter Transfer Function. ApJ, 496:605–614. (Cited in page 102.)

Eisenstein, D. J., Weinberg, D. H., Agol, E., Aihara, H., Allende Prieto, C., Anderson, S. F., Arns, J. A., Aubourg, É., Bailey, S., Balbinot, E., and et al. (2011). SDSS-III: Massive Spectroscopic Surveys of the Distant Universe, the Milky Way, and Extra-Solar Planetary Systems. AJ, 142:72. (Cited in page 43.)

Eisenstein, D. J., Zehavi, I., Hogg, D. W., Scoccimarro, R., Blanton, M. R., Nichol, R. C., Scranton, R., Seo, H.-J., Tegmark, M., Zheng, Z., Anderson, S. F., Annis, J., Bahcall, N., Brinkmann, J., Burles, S., Castander, F. J., Connolly, A., Csabai, I., Doi, M., Fukugita, M., Frieman, J. A., Glazebrook, K., Gunn, J. E., Hendry, J. S., Hennessy, G., Ivezić, Z., Kent, S., Knapp, G. R., Lin, H., Loh, Y.-S., Lupton, R. H., Margon, B., McKay, T. A., Meiksin, A., Munn, J. A., Pope, A., Richmond, M. W., Schlegel, D., Schneider, D. P., Shimasaku, K., Stoughton, C., Strauss, M. A., SubbaRao, M., Szalay, A. S., Szapudi, I., Tucker, D. L.,

Yanny, B., and York, D. G. (2005). Detection of the Baryon Acoustic Peak in the Large-Scale Correlation Function of SDSS Luminous Red Galaxies. ApJ, 633:560–574. (Cited in pages 21, 22, 83 and 209.)

Ellis, J., Hagelin, J. S., Nanopoulos, D. V., Olive, K., and Srednicki, M. (1984). Supersymmetric relics from the big bang. *Nuclear Physics B*, 238:453–476. (Cited in page 15.)

ESA/Hubble Press Release (2013). New hubble image of galaxy cluster abell 1689. http://www.spacetelescope.org/news/heic1317/. [Online; accessed 06-June-2016]. (Cited in page 41.)

Estrada, J., Sefusatti, E., and Frieman, J. A. (2009). The Correlation Function of Optically Selected Galaxy Clusters in the Sloan Digital Sky Survey. ApJ, 692:265–282. (Cited in pages 67, 68, 82, 84, 85, 111, 113, 115, 168, 173, 174, 210 and 213.)

Evrard, A. E. (1988). Beyond N-body - 3D cosmological gas dynamics. MNRAS, 235:911–934. (Cited in page 87.)

Evrard, A. E. (1990). Formation and evolution of X-ray clusters - A hydrodynamic simulation of the intracluster medium. ApJ, 363:349–366. (Cited in page 45.)

Fang, W. and Haiman, Z. (2007). Constraining dark energy by combining cluster counts and shear-shear correlations in a weak lensing survey. Phys. Rev. D, 75(4):043010. (Cited in pages 81 and 173.)

Farrow, D. J., Cole, S., Norberg, P., Metcalfe, N., Baldry, I., Bland-Hawthorn, J., Brown, M. J. I., Hopkins, A. M., Lacey, C. G., Liske, J., Loveday, J., Palamara, D. P., Robotham, A. S. G., and Sridhar, S. (2015). Galaxy and mass assembly (GAMA): projected galaxy clustering. MNRAS, 454:2120–2145. (Cited in page 122.)

Feldmann, R., Carollo, C. M., Porciani, C., Lilly, S. J., Capak, P., Taniguchi, Y., Le Fèvre, O., Renzini, A., Scoville, N., Ajiki, M., Aussel, H., Contini, T., McCracken, H., Mobasher, B., Murayama, T., Sanders, D., Sasaki, S., Scarlata, C., Scodeggio, M., Shioya, Y., Silverman, J., Takahashi, M., Thompson, D., and Zamorani, G. (2006). The Zurich Extragalactic Bayesian Redshift Analyzer and its first application: COSMOS. MNRAS, 372:565–577. (Cited in page 119.)

Fernández-Soto, A., Lanzetta, K. M., Chen, H.-W., Pascarelle, S. M., and Yahata, N. (2001). On the Compared Accuracy and Reliability of Spectroscopic and Photometric Redshift Measurements. ApJS, 135:41–61. (Cited in pages 119 and 120.)

Fioc, M. and Rocca-Volmerange, B. (1997). PEGASE: a UV to NIR spectral evolution model of galaxies. Application to the calibration of bright galaxy counts. A&A, 326:950–962. (Cited in page 152.)

Firth, A. E., Lahav, O., and Somerville, R. S. (2003). Estimating photometric redshifts with artificial neural networks. MNRAS, 339:1195–1202. (Cited in page 120.)

Fixsen, D. J. (2009). The Temperature of the Cosmic Microwave Background. ApJ, 707:916–920. (Cited in page 7.)

Font, A. S., Bower, R. G., McCarthy, I. G., Benson, A. J., Frenk, C. S., Helly, J. C., Lacey, C. G., Baugh, C. M., and Cole, S. (2008). The colours of satellite galaxies in groups and clusters. MNRAS, 389:1619–1629. (Cited in page 91.)

Frenk, C. S., White, S. D. M., Efstathiou, G., and Davis, M. (1985). Cold dark matter, the structure of galactic haloes and the origin of the Hubble sequence. Nature, 317:595–597. (Cited in page 15.)

Fry, J. N. (1996). The Evolution of Bias. ApJ, 461:L65. (Cited in page 102.)

Fujita, Y. (1998). Quantitative Estimates of Environmental Effects on the Star Formation Rate of Disk Galaxies in Clusters of Galaxies. ApJ, 509:587–594. (Cited in page 41.)

Gao, L., Springel, V., and White, S. D. M. (2005). The age dependence of halo clustering. MNRAS, 363:L66–L70. (Cited in page 36.)

Geller, M. J. and Huchra, J. P. (1983). Groups of galaxies. III - The CfA survey. ApJS, 52:61–87. (Cited in page 60.)

Gillessen, S., Eisenhauer, F., Trippe, S., Alexander, T., Genzel, R., Martins, F., and Ott, T. (2009). Monitoring Stellar Orbits Around the Massive Black Hole in the Galactic Center. ApJ, 692:1075–1109. (Cited in page 39.)

Giovanelli, R., Haynes, M. P., Wegner, G., da Costa, L. N., Freudling, W., and Salzer, J. J. (1996). A Test of the Lauer-Postman Bulk Flow. ApJ, 464:L99. (Cited in page 72.)

Gonzalez-Perez, V., Lacey, C. G., Baugh, C. M., Lagos, C. D. P., Helly, J., Campbell, D. J. R., and Mitchell, P. D. (2014). How sensitive are predicted galaxy luminosities to the choice of stellar population synthesis model? MNRAS, 439:264–283. (Cited in page 91.)

Goto, T., Sekiguchi, M., Nichol, R. C., Bahcall, N. A., Kim, R. S. J., Annis, J., Ivezić, Ž., Brinkmann, J., Hennessy, G. S., Szokoly, G. P., and Tucker, D. L. (2002). The Cut-and-Enhance Method: Selecting Clusters of Galaxies from the Sloan Digital Sky Survey Commissioning Data. AJ, 123:1807–1825. (Cited in page 66.)

Gott, III, J. R., Jurić, M., Schlegel, D., Hoyle, F., Vogeley, M., Tegmark, M., Bahcall, N., and Brinkmann, J. (2005). A Map of the Universe. ApJ, 624:463–484. (Cited in pages 39 and 40.)

Governato, F., Babul, A., Quinn, T., Tozzi, P., Baugh, C. M., Katz, N., and Lake, G. (1999). Properties of galaxy clusters: mass and correlation functions. MNRAS, 307:949–966. (Cited in pages 82, 94, 98, 110 and 168.)

Gunn, J. E. and Gott, III, J. R. (1972). On the Infall of Matter Into Clusters of Galaxies and Some Effects on Their Evolution. ApJ, 176:1. (Cited in page 25.)

Guo, Q., White, S., Angulo, R. E., Henriques, B., Lemson, G., Boylan-Kolchin, M., Thomas, P., and Short, C. (2013). Galaxy formation in WMAP1 and WMAP7 cosmologies. MNRAS, 428:1351–1365. (Cited in page 91.)

Hamilton, A. J. S. (1993). Toward Better Ways to Measure the Galaxy Correlation Function. ApJ, 417:19. (Cited in pages 54 and 55.)

Hamuy, M., Maza, J., Phillips, M. M., Suntzeff, N. B., Wischnjewsky, M., Smith, R. C., Antezana, R., Wells, L. A., Gonzalez, L. E., Gigoux, P., Navarrete, M., Barrientos, F., Lamontagne, R., della Valle, M., Elias, J. E., Phillips, A. C., Odewahn, S. C., Baldwin, J. A., Walker, A. R., Williams, T., Sturch, C. R., Baganoff, F. K., Chaboyer, B. C., Schommer, R. A., Tirado, H., Hernandez, M., Ugarte, P., Guhathakurta, P., Howell, S. B., Szkody, P., Schmidtke, P. C., and Roth, J. (1993). The 1990 Calan/Tololo Supernova Search. AJ, 106:2392–2407. (Cited in page 19.)

Hoekstra, H. (2007). A comparison of weak-lensing masses and X-ray properties of galaxy clusters. MNRAS, 379:317–330. (Cited in pages 49, 51 and 52.)

Hoessel, J. G., Gunn, J. E., and Thuan, T. X. (1980). The photometric properties of brightest cluster galaxies. I - Absolute magnitudes in 116 nearby Abell clusters. ApJ, 241:486–492. (Cited in pages 72 and 210.)

Hogg, D. W. (1999). Distance measures in cosmology. *ArXiv Astrophysics e-prints*. (Cited in pages 14 and 15.)

Hong, T., Han, J. L., Wen, Z. L., Sun, L., and Zhan, H. (2012). The Correlation Function of Galaxy Clusters and Detection of Baryon Acoustic Oscillations. ApJ, 749:81. (Cited in pages 68, 71, 74, 82, 84, 85, 168, 174 and 210.)

Hopkins, P. F., Bahcall, N. A., and Bode, P. (2005). Cluster Alignments and Ellipticities in ΛCDM Cosmology. ApJ, 618:1–15. (Cited in page 98.)

Hoyle, F. (1948). A New Model for the Expanding Universe. MNRAS, 108:372. (Cited in page 4.)

Hoyle, F., Burbidge, G., and Narlikar, J. V. (1993). A quasi-steady state cosmological model with creation of matter. ApJ, 410:437–457. (Cited in page 4.)

Hubble, E. (1929). A Relation between Distance and Radial Velocity among Extra-Galactic Nebulae. *Proceedings of the National Academy of Science*, 15:168–173. (Cited in page 3.)

Hubble sequence (2016). Hubble sequence — Wikipedia, the free encyclopedia. https://en.wikipedia.org/wiki/Hubble_sequence. [Online; accessed 06-June-2016]. (Cited in page 40.)

Huchra, J. P. and Geller, M. J. (1982). Groups of galaxies. I - Nearby groups. ApJ, 257:423–437. (Cited in page 42.)

Huchra, J. P., Henry, J. P., Postman, M., and Geller, J., M. (1990). A deep Abell cluster redshift survey. ApJ, 365:66–85. (Cited in page 94.)

Hütsi, G. (2010). Power spectrum of the maxBCG sample: detection of acoustic oscillations using galaxy clusters. MNRAS, 401:2477–2489. (Cited in page 174.)

Ilbert, O., Capak, P., Salvato, M., Aussel, H., McCracken, H. J., Sanders, D. B., Scoville, N., Kartaltepe, J., Arnouts, S., Le Floc'h, E., Mobasher, B., Taniguchi, Y., Lamareille, F., Leauthaud, A., Sasaki, S., Thompson, D., Zamojski, M., Zamorani, G., Bardelli, S., Bolzonella, M., Bongiorno, A., Brusa, M., Caputi, K. I., Carollo, C. M., Contini, T., Cook, R., Coppa, G., Cucciati, O., de la Torre, S., de Ravel, L., Franzetti, P., Garilli, B., Hasinger, G., Iovino, A., Kampczyk, P., Kneib, J.-P., Knobel, C., Kovac, K., Le Borgne, J. F., Le Brun, V., Fèvre, O. L., Lilly, S., Looper, D., Maier, C., Mainieri, V., Mellier, Y., Mignoli, M., Murayama, T., Pellò, R., Peng, Y., Pérez-Montero, E., Renzini, A., Ricciardelli, E., Schiminovich, D., Scodeggio, M., Shioya, Y., Silverman, J., Surace, J., Tanaka, M., Tasca, L., Tresse, L., Vergani, D., and Zucca, E. (2009). Cosmos Photometric Redshifts with 30-Bands for 2-deg^2. ApJ, 690:1236–1249. (Cited in pages 119 and 165.)

Ivezic, Z., Tyson, J. A., Abel, B., Acosta, E., Allsman, R., AlSayyad, Y., Anderson, S. F., Andrew, J., Angel, R., Angeli, G., Ansari, R., Antilogus, P., Arndt, K. T., Astier, P., Aubourg, E., Axelrod, T., Bard, D. J., Barr, J. D., Barrau, A., Bartlett, J. G., Bauman, B. J., Beaumont, S., Becker, A. C., Becla, J., Beldica, C., Bellavia, S., Blanc, G., Blandford, R. D., Bloom, J. S., Bogart, J., Borne, K., Bosch, J. F., Boutigny, D., Brandt, W. N., Brown, M. E., Bullock, J. S., Burchat, P., Burke, D. L., Cagnoli, G., Calabrese, D., Chandrasekharan, S., Chesley, S., Cheu, E. C., Chiang, J., Claver, C. F., Connolly, A. J., Cook, K. H., Cooray, A., Covey, K. R., Cribbs, C., Cui, W., Cutri, R., Daubard, G., Daues, G., Delgado, F., Digel, S., Doherty, P., Dubois, R., Dubois-Felsmann, G. P., Durech, J., Eracleous, M., Ferguson, H., Frank, J., Freemon, M., Gangler, E., Gawiser, E., Geary, J. C., Gee, P., Geha, M., Gibson, R. R., Gilmore, D. K., Glanzman, T., Goodenow, I., Gressler, W. J., Gris, P., Guyonnet, A., Hascall, P. A., Haupt, J., Hernandez, F., Hogan, C., Huang, D., Huffer, M. E., Innes, W. R., Jacoby, S. H., Jain, B., Jee, J., Jernigan, J. G., Jevremovic, D., Johns, K., Jones, R. L., Juramy-Gilles, C., Juric, M., Kahn, S. M., Kalirai, J. S., Kallivayalil, N., Kalmbach, B., Kantor, J. P., Kasliwal, M. M., Kessler, R., Kirkby, D., Knox,

L., Kotov, I., Krabbendam, V. L., Krughoff, S., Kubanek, P., Kuczewski, J., Kulkarni, S., Lambert, R., Le Guillou, L., Levine, D., Liang, M., Lim, K., Lintott, C., Lupton, R. H., Mahabal, A., Marshall, P., Marshall, S., May, M., McKercher, R., Migliore, M., Miller, M., Mills, D. J., Monet, D. G., Moniez, M., Neill, D. R., Nief, J., Nomerotski, A., Nordby, M., O'Connor, P., Oliver, J., Olivier, S. S., Olsen, K., Ortiz, S., Owen, R. E., Pain, R., Peterson, J. R., Petry, C. E., Pierfederici, F., Pietrowicz, S., Pike, R., Pinto, P. A., Plante, R., Plate, S., Price, P. A., Prouza, M., Radeka, V., Rajagopal, J., Rasmussen, A., Regnault, N., Ridgway, S. T., Ritz, S., Rosing, W., Roucelle, C., Rumore, M. R., Russo, S., Saha, A., Sassolas, B., Schalk, T. L., Schindler, R. H., Schneider, D. P., Schumacher, G., Sebag, J., Sembroski, G. H., Seppala, L. G., Shipsey, I., Silvestri, N., Smith, J. A., Smith, R. C., Strauss, M. A., Stubbs, C. W., Sweeney, D., Szalay, A., Takacs, P., Thaler, J. J., Van Berg, R., Vanden Berk, D., Vetter, K., Virieux, F., Xin, B., Walkowicz, L., Walter, C. W., Wang, D. L., Warner, M., Willman, B., Wittman, D., Wolff, S. C., Wood-Vasey, W. M., Yoachim, P., Zhan, H., and for the LSST Collaboration (2008). LSST: from Science Drivers to Reference Design and Anticipated Data Products. *ArXiv e-prints*. (Cited in page 120.)

Jahoda, K. and DUET Collaboration (2003). DUET - The Dark Universe Exploration Telescope. *Astronomische Nachrichten*, 324:132–135. (Cited in page 79.)

Jenkins, A., Frenk, C. S., White, S. D. M., Colberg, J. M., Cole, S., Evrard, A. E., Couchman, H. M. P., and Yoshida, N. (2001). The mass function of dark matter haloes. MNRAS, 321:372–384. (Cited in pages 27, 28, 29 and 80.)

Jiang, L., Helly, J. C., Cole, S., and Frenk, C. S. (2014). N-body dark matter haloes with simple hierarchical histories. MNRAS, 440:2115–2135. (Cited in pages 90, 91 and 210.)

Jing, Y. P., Mo, H. J., and Börner, G. (1998). Spatial Correlation Function and Pairwise Velocity Dispersion of Galaxies: Cold Dark Matter Models versus the Las Campanas Survey. ApJ, 494:1–12. (Cited in pages 36 and 61.)

Kaiser, N. (1984). On the spatial correlations of Abell clusters. ApJ, 284:L9–L12. (Cited in pages 32 and 65.)

Kaiser, N. (1987). Clustering in real space and in redshift space. MNRAS, 227:1–21. (Cited in page 57.)

Kamionkowski, M. (1998). Possible Relics from New Physics in the Early Universe: Inflation, the Cosmic Microwave Background, and Particle Dark Matter. *ArXiv Astrophysics e-prints*. (Cited in pages 18 and 209.)

Kang, H., Cen, R., Ostriker, J. P., and Ryu, D. (1994). Hot gas in the cold dark matter scenario: X-ray clusters from a high-resolution numerical simulation. ApJ, 428:1–16. (Cited in page 87.)

Katz, N. and White, S. D. M. (1993). Hierarchical galaxy formation - Overmerging and the formation of an X-ray cluster. ApJ, 412:455–478. (Cited in page 87.)

Kauffmann, G., Colberg, J. M., Diaferio, A., and White, S. D. M. (1999). Clustering of galaxies in a hierarchical universe - I. Methods and results at z=0. MNRAS, 303:188–206. (Cited in pages 34 and 35.)

Kerscher, M., Szapudi, I., and Szalay, A. S. (2000). A Comparison of Estimators for the Two-Point Correlation Function. ApJ, 535:13–16. (Cited in page 55.)

Klypin, A. A. and Kopylov, A. I. (1983). The Spatial Covariance Function for Rich Clusters of Galaxies. *Soviet Astronomy Letters*, 9:41–44. (Cited in pages 63 and 64.)

Klypin, A. A., Trujillo-Gomez, S., and Primack, J. (2011). Dark Matter Halos in the Standard Cosmological Model: Results from the Bolshoi Simulation. ApJ, 740:102. (Cited in page 89.)

Koester, B. P., McKay, T. A., Annis, J., Wechsler, R. H., Evrard, A., Bleem, L., Becker, M., Johnston, D., Sheldon, E., Nichol, R., Miller, C., Scranton, R., Bahcall, N., Barentine, J., Brewington, H., Brinkmann, J., Harvanek, M., Kleinman, S., Krzesinski, J., Long, D., Nitta, A., Schneider, D. P., Sneddin, S., Voges, W., and York, D. (2007). A MaxBCG Catalog of 13,823 Galaxy Clusters from the Sloan Digital Sky Survey. ApJ, 660:239–255. (Cited in pages 43, 66 and 84.)

Komatsu, E., Dunkley, J., Nolta, M. R., Bennett, C. L., Gold, B., Hinshaw, G., Jarosik, N., Larson, D., Limon, M., Page, L., Spergel, D. N., Halpern, M., Hill, R. S., Kogut, A., Meyer, S. S., Tucker, G. S., Weiland, J. L., Wollack, E., and Wright, E. L. (2009). Five-Year Wilkinson Microwave Anisotropy Probe Observations: Cosmological Interpretation. ApJS, 180:330–376. (Cited in pages 15 and 89.)

Komatsu, E., Smith, K. M., Dunkley, J., Bennett, C. L., Gold, B., Hinshaw, G., Jarosik, N., Larson, D., Nolta, M. R., Page, L., Spergel, D. N., Halpern, M., Hill, R. S., Kogut, A., Limon, M., Meyer, S. S., Odegard, N., Tucker, G. S., Weiland, J. L., Wollack, E., and Wright, E. L. (2011). Seven-year Wilkinson Microwave Anisotropy Probe (WMAP) Observations: Cosmological Interpretation. ApJS, 192:18. (Cited in pages 11 and 22.)

Kravtsov, A. V., Berlind, A. A., Wechsler, R. H., Klypin, A. A., Gottlöber, S., Allgood, B., and Primack, J. R. (2004). The Dark Side of the Halo Occupation Distribution. ApJ, 609:35–49. (Cited in page 152.)

Kravtsov, A. V., Vikhlinin, A., and Nagai, D. (2006). A New Robust Low-Scatter X-Ray Mass Indicator for Clusters of Galaxies. ApJ, 650:128–136. (Cited in page 51.)

Lacasa, F. and Rosenfeld, R. (2016). Combining cluster number counts and galaxy clustering. J. Cosmology Astropart. Phys., 8:005. (Cited in pages 81 and 173.)

Lagos, C. d. P., Bayet, E., Baugh, C. M., Lacey, C. G., Bell, T. A., Fanidakis, N., and Geach, J. E. (2012). Predictions for the CO emission of galaxies from a coupled simulation of galaxy formation and photon-dominated regions. MNRAS, 426:2142–2165. (Cited in page 91.)

Landy, S. D. and Szalay, A. S. (1993). Bias and variance of angular correlation functions. ApJ, 412:64–71. (Cited in page 55.)

Lauer, T. R. and Postman, M. (1992). The Hubble flow from brightest cluster galaxies. ApJ, 400:L47–L50. (Cited in pages 72 and 73.)

Laureijs, R., Amiaux, J., Arduini, S., Augueres, J. ., Brinchmann, J., Cole, R., Cropper, M., Dabin, C., Duvet, L., Ealet, A., and et al. (2011). Euclid Definition Study Report. *ArXiv e-prints*. (Cited in pages 78, 86, 98, 99, 120, 121 and 173.)

Laureijs, R., Racca, G., Stagnaro, L., Salvignol, J.-C., Lorenzo Alvarez, J., Saavedra Criado, G., Gaspar Venancio, L., Short, A., Strada, P., Colombo, C., Buenadicha, G., Hoar, J., Kohley, R., Vavrek, R., Mellier, Y., Berthe, M., Amiaux, J., Cropper, M., Niemi, S., Pottinger, S., Ealet, A., Jahnke, K., Maciaszek, T., Pasian, F., Sauvage, M., Wachter, S., Israelsson, U., Holmes, W., Seiffert, M., Cazaubiel, V., Anselmi, A., and Musi, P. (2014). Euclid mission status. In *Space Telescopes and Instrumentation 2014: Optical, Infrared, and Millimeter Wave*, volume 9143 of Proc. SPIE, page 91430H. (Cited in pages 120 and 173.)

Lemaître, G. (1927). Un Univers homogène de masse constante et de rayon croissant rendant compte de la vitesse radiale des nébuleuses extra-galactiques. *Annales de la Société Scientifique de Bruxelles*, 47:49–59. (Cited in page 3.)

Lemaître, G. (1931). The Beginning of the World from the Point of View of Quantum Theory. Nature, 127:706. (Cited in page 4.)

Lemson, G. and Virgo Consortium, t. (2006). Halo and Galaxy Formation Histories from the Millennium Simulation: Public release of a VO-oriented and SQL-queryable database for studying the evolution of galaxies in the LambdaCDM cosmogony. *ArXiv Astrophysics e-prints*. (Cited in pages 28 and 87.)

Lewis, A. and Bridle, S. (2002). Cosmological parameters from CMB and other data: A Monte Carlo approach. Phys. Rev. D, 66(10):103511. (Cited in page 102.)

Li, L., Zhang, Y., Zhao, Y., and Yang, D. (2006). Multi-parameter estimating photometric redshifts with artificial neural networks. *ArXiv Astrophysics e-prints*. (Cited in page 120.)

Liddle, A. (2003). *An Introduction to Modern Cosmology, Second Edition*. (Cited in page 11.)

Lima, M. and Hu, W. (2004). Self-calibration of cluster dark energy studies: Counts in cells. Phys. Rev. D, 70(4):043504. (Cited in page 173.)

Limber, D. N. (1954). The Analysis of Counts of the Extragalactic Nebulae in Terms of a Fluctuating Density Field. II. ApJ, 119:655. (Cited in page 56.)

Limber, D. N. and Mathews, W. G. (1960). The Dynamical Stability of Stephan's Quintet. ApJ, 132:286. (Cited in page 48.)

Lloyd-Davies, E. J., Romer, A. K., Mehrtens, N., Hosmer, M., Davidson, M., Sabirli, K., Mann, R. G., Hilton, M., Liddle, A. R., Viana, P. T. P., Campbell, H. C., Collins, C. A., Dubois, E. N., Freeman, P., Harrison, C. D., Hoyle, B., Kay, S. T., Kuwertz, E., Miller, C. J., Nichol, R. C., Sahlén, M., Stanford, S. A., and Stott, J. P. (2011). The XMM Cluster Survey: X-ray analysis methodology. MNRAS, 418:14–53. (Cited in page 44.)

Longair, M. S. (2008). *Galaxy Formation*. (Cited in pages 6, 7 and 47.)

Loveday, J., Maddox, S. J., Efstathiou, G., and Peterson, B. A. (1995). The Stromlo-APM redshift survey. 2: Variation of galaxy clustering with morphology and luminosity. ApJ, 442:457–468. (Cited in page 62.)

Loveday, J., Peterson, B. A., Maddox, S. J., and Efstathiou, G. (1996). The Stromlo-APM Redshift Survey. IV. The Redshift Catalog. ApJS, 107:201. (Cited in page 61.)

LSST Dark Energy Science Collaboration (2012). Large Synoptic Survey Telescope: Dark Energy Science Collaboration. *ArXiv e-prints*. (Cited in pages 78, 86, 98, 99, 120 and 173.)

Maddox, S. J., Efstathiou, G., Sutherland, W. J., and Loveday, J. (1990). The APM galaxy survey. I - APM measurements and star-galaxy separation. MNRAS, 243:692–712. (Cited in pages 56 and 60.)

Majumdar, S. and Mohr, J. J. (2003). Importance of Cluster Structural Evolution in Using X-Ray and Sunyaev-Zeldovich Effect Galaxy Cluster Surveys to Study Dark Energy. ApJ, 585:603–610. (Cited in page 173.)

Majumdar, S. and Mohr, J. J. (2004). Self-Calibration in Cluster Studies of Dark Energy: Combining the Cluster Redshift Distribution, the Power Spectrum, and Mass Measurements. ApJ, 613:41–50. (Cited in pages , 79, 80, 81, 82, 173, 210 and 213.)

Mana, A., Giannantonio, T., Weller, J., Hoyle, B., Hütsi, G., and Sartoris, B. (2013). Combining clustering and abundances of galaxy clusters to test cosmology and primordial non-Gaussianity. MNRAS, 434:684–695. (Cited in pages 76, 77, 173 and 210.)

Manera, M., Sheth, R. K., and Scoccimarro, R. (2010). Large-scale bias and the inaccuracy of the peak-background split. MNRAS, 402:589–602. (Cited in page 105.)

Marulli, F., Bianchi, D., Branchini, E., Guzzo, L., Moscardini, L., and Angulo, R. E. (2012). Cosmology with clustering anisotropies: disentangling dynamic and geometric distortions in galaxy redshift surveys. MNRAS, 426:2566–2580. (Cited in page 122.)

Marulli, F., Veropalumbo, A., and Moresco, M. (2016). CosmoBolognaLib: C++ libraries for cosmological calculations. *Astronomy and Computing*, 14:35–42. (Cited in page 92.)

Matarrese, S., Coles, P., Lucchin, F., and Moscardini, L. (1997). Redshift evolution of clustering. MNRAS, 286:115–132. (Cited in page 35.)

Matter-energy content of the Universe, Planck (2015). Matter-energy content of the universe, planck. `http://planck.cf.ac.uk/results/cosmic-microwave-background`. [Online; accessed 22-July-2016]. (Cited in page 16.)

McGaugh, S., Lelli, F., and Schombert, J. (2016). The Radial Acceleration Relation in Rotationally Supported Galaxies. *ArXiv e-prints*. (Cited in page 18.)

McGaugh, S. S. (2015). A tale of two paradigms: the mutual incommensurability of ΛCDM and MOND. *Canadian Journal of Physics*, 93:250–259. (Cited in page 18.)

Menanteau, F., González, J., Juin, J.-B., Marriage, T. A., Reese, E. D., Acquaviva, V., Aguirre, P., Appel, J. W., Baker, A. J., Barrientos, L. F., Battistelli, E. S., Bond, J. R., Das, S., Deshpande, A. J., Devlin, M. J., Dicker, S., Dunkley, J., Dünner, R., Essinger-Hileman, T., Fowler, J. W., Hajian, A., Halpern, M., Hasselfield, M., Hernández-Monteagudo, C., Hilton, M., Hincks, A. D., Hlozek, R., Huffenberger, K. M., Hughes, J. P., Infante, L., Irwin, K. D., Klein, J., Kosowsky, A., Lin, Y.-T., Marsden, D., Moodley, K., Niemack, M. D., Nolta, M. R., Page, L. A., Parker, L., Partridge, B., Sehgal, N., Sievers, J., Spergel, D. N., Staggs, S. T., Swetz, D., Switzer, E., Thornton, R., Trac, H., Warne, R., and Wollack, E. (2010). The Atacama Cosmology Telescope: Physical Properties and Purity of a Galaxy Cluster Sample Selected via the Sunyaev-Zel'dovich Effect. ApJ, 723:1523–1541. (Cited in page 45.)

Meneghetti, M., Rasia, E., Merten, J., Bellagamba, F., Ettori, S., Mazzotta, P., Dolag, K., and Marri, S. (2010). Weighing simulated galaxy clusters using lensing and X-ray. A&A, 514:A93. (Cited in page 49.)

Merson, A. I., Baugh, C. M., Helly, J. C., Gonzalez-Perez, V., Cole, S., Bielby, R., Norberg, P., Frenk, C. S., Benson, A. J., Bower, R. G., Lacey, C. G., and Lagos, C. d. P. (2013). Lightcone mock catalogues from semi-analytic models of galaxy formation - I. Construction and application to the BzK colour selection. MNRAS, 429:556–578. (Cited in pages 89, 90, 91, 114, 171, 175 and 210.)

Milgrom, M. (1983). A modification of the Newtonian dynamics as a possible alternative to the hidden mass hypothesis. ApJ, 270:365–370. (Cited in page 17.)

Milgrom, M. (2016). MOND impact on and of the recently updated mass-discrepancy-acceleration relation. *ArXiv e-prints*. (Cited in page 18.)

Millennium II simulation (2016). Millennium ii simulation – redshift evolution of halo. http://wwwmpa.mpa-garching.mpg.de/galform/millennium-II/. [Online; accessed 1-July-2016]. (Cited in pages 88 and 210.)

Mo, H. J. and White, S. D. M. (1996). An analytic model for the spatial clustering of dark matter haloes. MNRAS, 282:347–361. (Cited in pages 29, 32, 34, 35, 94, 103 and 104.)

Mo, H. J. and White, S. D. M. (2002). The abundance and clustering of dark haloes in the standard ΛCDM cosmogony. MNRAS, 336:112–118. (Cited in pages 36 and 209.)

Moscardini, L., Matarrese, S., Lucchin, F., and Rosati, P. (2000a). Predicting the clustering of X-ray selected galaxy clusters in flux-limited surveys. MNRAS, 316:283–298. (Cited in page 35.)

Moscardini, L., Matarrese, S., Lucchin, F., and Rosati, P. (2000b). Predicting the clustering of X-ray selected galaxy clusters in flux-limited surveys. MNRAS, 316:283–298. (Cited in page 94.)

Mushotzky, R. F. (1984). X-ray emission from clusters of galaxies. *Physica Scripta Volume T*, 7:157–162. (Cited in page 50.)

Nagai, D., Vikhlinin, A., and Kravtsov, A. V. (2007). Testing X-Ray Measurements of Galaxy Clusters with Cosmological Simulations. ApJ, 655:98–108. (Cited in pages 48 and 51.)

Navarro, J. F., Frenk, C. S., and White, S. D. M. (1995). Simulations of X-ray clusters. MNRAS, 275:720–740. (Cited in page 87.)

Navarro, J. F., Frenk, C. S., and White, S. D. M. (1996). The Structure of Cold Dark Matter Halos. ApJ, 462:563. (Cited in pages 30, 31, 40, 177 and 209.)

NED Caltech (2016). Galaxy cluster bias. https://ned.ipac.caltech.edu/level5/Sept03/Peacock/Peacock6_2.html. [Online; accessed 13-June-2016]. (Cited in page 33.)

Norberg, P., Gaztañaga, E., Baugh, C. M., and Croton, D. J. (2011). Statistical analysis of galaxy surveys - IV. An objective way to quantify the impact of superstructures on galaxy clustering statistics. MNRAS, 418:2435–2450. (Cited in page 93.)

Oemler, Jr., A. (1974). The Systematic Properties of Clusters of Galaxies. Photometry of 15 Clusters. ApJ, 194:1–20. (Cited in page 183.)

Oguri, M. (2009). Self-Calibrated Cluster Counts as a Probe of Primordial Non-Gaussianity. *Physical Review Letters*, 102(21):211301. (Cited in page 81.)

Padmanabhan, N., Xu, X., Eisenstein, D. J., Scalzo, R., Cuesta, A. J., Mehta, K. T., and Kazin, E. (2012). A 2 per cent distance to z = 0.35 by reconstructing baryon acoustic oscillations - I. Methods and application to the Sloan Digital Sky Survey. MNRAS, 427:2132–2145. (Cited in page 22.)

Paraficz, D., Kneib, J.-P., Richard, J., Morandi, A., Limousin, M., Jullo, E., and Martinez, J. (2012). The Bullet cluster at its best: weighing stars, gas and dark matter. *ArXiv e-prints*. (Cited in pages 42, 43 and 209.)

Peacock, J. A. and West, M. J. (1992). The power spectrum of Abell cluster correlations. MNRAS, 259:494–504. (Cited in page 94.)

Peebles, P. J. E. (1970). Structure of the Coma Cluster of Galaxies. AJ, 75:13. (Cited in page 87.)

Peebles, P. J. E. (1975). Statistical analysis of catalogs of extragalactic objects. VI - The galaxy distribution in the Jagellonian field. ApJ, 196:647–651. (Cited in page 59.)

Peebles, P. J. E. (1980). *The large-scale structure of the universe*. (Cited in pages , 54, 56 and 57.)

Percival, W. J., Cole, S., Eisenstein, D. J., Nichol, R. C., Peacock, J. A., Pope, A. C., and Szalay, A. S. (2007). Measuring the Baryon Acoustic Oscillation scale using the Sloan Digital Sky Survey and 2dF Galaxy Redshift Survey. MNRAS, 381:1053–1066. (Cited in page 22.)

Percival, W. J., Reid, B. A., Eisenstein, D. J., Bahcall, N. A., Budavari, T., Frieman, J. A., Fukugita, M., Gunn, J. E., Ivezić, Ž., Knapp, G. R., Kron, R. G., Loveday, J., Lupton, R. H., McKay, T. A., Meiksin, A., Nichol, R. C., Pope, A. C., Schlegel, D. J., Schneider, D. P., Spergel, D. N., Stoughton, C., Strauss, M. A., Szalay, A. S., Tegmark, M., Vogeley, M. S., Weinberg, D. H., York, D. G., and Zehavi, I. (2010). Baryon acoustic oscillations in the Sloan Digital Sky Survey Data Release 7 galaxy sample. MNRAS, 401:2148–2168. (Cited in page 22.)

Perlmutter (2003). Supernova observations. `http://www-supernova.lbl.gov/PhysicsTodayArticle.pdf`. [Online; accessed 22-July-2016]. (Cited in pages 20 and 209.)

Perlmutter, S., Aldering, G., Goldhaber, G., Knop, R. A., Nugent, P., Castro, P. G., Deustua, S., Fabbro, S., Goobar, A., Groom, D. E., Hook, I. M., Kim, A. G., Kim, M. Y., Lee, J. C., Nunes, N. J., Pain, R., Pennypacker, C. R., Quimby, R., Lidman, C., Ellis, R. S., Irwin, M., McMahon, R. G., Ruiz-Lapuente, P., Walton, N., Schaefer, B., Boyle, B. J., Filippenko, A. V., Matheson, T., Fruchter, A. S., Panagia, N., Newberg, H. J. M., Couch, W. J., and Project, T. S. C. (1999). Measurements of Ω and Λ from 42 High-Redshift Supernovae. ApJ, 517:565–586. (Cited in pages , 15 and 19.)

Pierre, M., Pacaud, F., Adami, C., Alis, S., Altieri, B., Baran, N., Benoist, C., Birkinshaw, M., Bongiorno, A., Bremer, M. N., Brusa, M., Butler, A., Ciliegi, P., Chiappetti, L., Clerc, N., Corasaniti, P. S., Coupon, J., De Breuck, C., Democles, J., Desai, S., Delhaize, J., Devriendt, J., Dubois, Y., Eckert, D., Elyiv, A., Ettori, S., Evrard, A., Faccioli, L., Farahi, A., Ferrari, C., Finet, F., Fotopoulou, S., Fourmanoit, N., Gandhi, P., Gastaldello, F., Gastaud, R., Georgantopoulos, I., Giles, P., Guennou, L., Guglielmo, V., Horellou, C., Husband, K., Huynh, M., Iovino, A., Kilbinger, M., Koulouridis, E., Lavoie, S., Le Brun, A. M. C., Le Fevre, J. P., Lidman, C., Lieu, M., Lin, C. A., Mantz, A., Maughan, B. J., Maurogordato, S., McCarthy, I. G., McGee, S., Melin, J. B., Melnyk, O., Menanteau, F., Novak, M., Paltani, S., Plionis, M., Poggianti, B. M., Pomarede, D., Pompei, E., Ponman, T. J., Ramos-Ceja, M. E., Ranalli, P., Rapetti, D., Raychaudury, S., Reiprich, T. H., Rottgering, H., Rozo, E., Rykoff, E., Sadibekova, T., Santos, J., Sauvageot, J. L., Schimd, C., Sereno, M., Smith, G. P., Smolčić, V., Snowden, S., Spergel, D., Stanford, S., Surdej, J., Valageas, P., Valotti, A., Valtchanov, I., Vignali, C., Willis, J., and Ziparo, F. (2016). The XXL Survey. I. Scientific motivations - XMM-Newton observing plan - Follow-up observations and simulation programme. A&A, 592:A1. (Cited in page 44.)

Planck Collaboration, Ade, P. A. R., Aghanim, N., Alves, M. I. R., Armitage-Caplan, C., Arnaud, M., Ashdown, M., Atrio-Barandela, F., Aumont, J., Aussel, H., and et al. (2014). Planck 2013 results. I. Overview of products and scientific results. A&A, 571:A1. (Cited in page 5.)

Planck Collaboration, Ade, P. A. R., Aghanim, N., Arnaud, M., Ashdown, M., Aumont, J., Baccigalupi, C., Baker, M., Balbi, A., Banday, A. J., and et al. (2011). Planck early results. I. The Planck mission. A&A, 536:A1. (Cited in pages 45 and 79.)

Planck Collaboration, Ade, P. A. R., Aghanim, N., Arnaud, M., Ashdown, M., Aumont, J., Baccigalupi, C., Banday, A. J., Barreiro, R. B., Bartlett, J. G., and et al. (2015). Planck 2015 results. XXIV. Cosmology from Sunyaev-Zeldovich cluster counts. *ArXiv e-prints*. (Cited in pages 15, 56, 77, 78, 173 and 210.)

Planck Collaboration, Ade, P. A. R., Aghanim, N., Arnaud, M., Ashdown, M., Aumont, J., Baccigalupi, C., Banday, A. J., Barreiro, R. B., Bartlett, J. G., and et al. (2016). Planck 2015 results. XIII. Cosmological parameters. A&A, 594:A13. (Cited in page 11.)

Postman, M., Lubin, L. M., Gunn, J. E., Oke, J. B., Hoessel, J. G., Schneider, D. P., and Christensen, J. A. (1996). The Palomar Distant Clusters Survey. I. The Cluster Catalog. AJ, 111:615. (Cited in page 42.)

Pratt, G. W., Croston, J. H., Arnaud, M., and Böhringer, H. (2009). Galaxy cluster X-ray luminosity scaling relations from a representative local sample (REXCESS). A&A, 498:361–378. (Cited in page 50.)

Press, W. H. and Schechter, P. (1974). Formation of Galaxies and Clusters of Galaxies by Self-Similar Gravitational Condensation. ApJ, 187:425–438. (Cited in pages 23, 26, 27, 28, 29, 32 and 35.)

Riess, A. G., Macri, L., Casertano, S., Lampeitl, H., Ferguson, H. C., Filippenko, A. V., Jha, S. W., Li, W., and Chornock, R. (2011). A 3% Solution: Determination of the Hubble Constant with the Hubble Space Telescope and Wide Field Camera 3. ApJ, 730:119. (Cited in page 19.)

Riess, A. G., Press, W. H., and Kirshner, R. P. (1995). Determining the motion of the local group using type IA supernovae light curve shapes. ApJ, 445:L91–L94. (Cited in page 72.)

Rines, K. and Diaferio, A. (2006). CIRS: Cluster Infall Regions in the Sloan Digital Sky Survey. I. Infall Patterns and Mass Profiles. AJ, 132:1275–1297. (Cited in pages 51, 52 and 209.)

Rozo, E., Rykoff, E., Koester, B., Nord, B., Wu, H.-Y., Evrard, A., and Wechsler, R. (2011). Extrinsic Sources of Scatter in the Richness-mass Relation of Galaxy Clusters. ApJ, 740:53. (Cited in pages 50, 119 and 151.)

Rozo, E., Rykoff, E. S., Koester, B. P., McKay, T., Hao, J., Evrard, A., Wechsler, R. H., Hansen, S., Sheldon, E., Johnston, D., Becker, M., Annis, J., Bleem, L., and Scranton, R. (2009). Improvement of the Richness Estimates of maxBCG Clusters. ApJ, 703:601–613. (Cited in pages 50, 52 and 152.)

Rozo, E., Wechsler, R. H., Rykoff, E. S., Annis, J. T., Becker, M. R., Evrard, A. E., Frieman, J. A., Hansen, S. M., Hao, J., Johnston, D. E., Koester, B. P., McKay, T. A., Sheldon, E. S., and Weinberg, D. H. (2010). Cosmological Constraints from the Sloan Digital Sky Survey maxBCG Cluster Catalog. ApJ, 708:645–660. (Cited in page 79.)

Ruhl, J., Ade, P. A. R., Carlstrom, J. E., Cho, H.-M., Crawford, T., Dobbs, M., Greer, C. H., Halverson, N. w., Holzapfel, W. L., Lanting, T. M., Lee, A. T., Leitch, E. M., Leong, J., Lu, W., Lueker, M., Mehl, J., Meyer, S. S., Mohr, J. J., Padin, S., Plagge, T., Pryke, C., Runyan, M. C., Schwan, D., Sharp, M. K., Spieler, H., Staniszewski, Z., and Stark, A. A. (2004). The South Pole Telescope. In Bradford, C. M., Ade, P. A. R., Aguirre, J. E., Bock, J. J., Dragovan, M., Duband, L., Earle, L., Glenn, J., Matsuhara, H., Naylor, B. J., Nguyen, H. T., Yun, M., and Zmuidzinas, J., editors, *Z-Spec: a broadband millimeter-wave grating spectrometer: design, construction, and first cryogenic measurements*, volume 5498 of Proc. SPIE, pages 11–29. (Cited in pages 45 and 79.)

Rykoff, E. S., Koester, B. P., Rozo, E., Annis, J., Evrard, A. E., Hansen, S. M., Hao, J., Johnston, D. E., McKay, T. A., and Wechsler, R. H. (2012). Robust Optical Richness Estimation with Reduced Scatter. ApJ, 746:178. (Cited in pages 50, 151, 152, 156, 157 and 170.)

Rykoff, E. S., Rozo, E., Busha, M. T., Cunha, C. E., Finoguenov, A., Evrard, A., Hao, J., Koester, B. P., Leauthaud, A., Nord, B., Pierre, M., Reddick, R., Sadibekova, T., Sheldon, E. S., and Wechsler, R. H. (2014). redMaPPer. I. Algorithm and SDSS DR8 Catalog. ApJ, 785:104. (Cited in page 173.)

Ryle, M. and Clarke, R. W. (1961). An examination of the steady-state model in the light of some recent observations of radio sources. MNRAS, 122:349. (Cited in page 4.)

Sarazin, C. L. (1986). X-ray emission from clusters of galaxies. *Reviews of Modern Physics*, 58:1–115. (Cited in page 49.)

Sarazin, C. L. and Graney, C. M. (1991). Optical coronal emission lines from cooling flows in elliptical galaxies and galaxy clusters. ApJ, 375:532–543. (Cited in page 49.)

Sartoris, B., Biviano, A., Fedeli, C., Bartlett, J. G., Borgani, S., Costanzi, M., Giocoli, C., Moscardini, L., Weller, J., Ascaso, B., Bardelli, S., Maurogordato, S., and Viana, P. T. P. (2016). Next generation cosmology: constraints from the Euclid galaxy cluster survey. MNRAS, 459:1764–1780. (Cited in pages , 68, 71, 74, 78, 79, 141, 173 and 210.)

Saunders, W., Rowan-Robinson, M., and Lawrence, A. (1992). The spatial correlation function of IRAS galaxies on small and intermediate scales. MNRAS, 258:134–146. (Cited in pages 122 and 124.)

Schechter, P. (1976). An analytic expression for the luminosity function for galaxies. ApJ, 203:297–306. (Cited in pages 183, 184 and 212.)

Seldner, M., Siebers, B., Groth, E. J., and Peebles, P. J. E. (1977). New reduction of the Lick catalog of galaxies. AJ, 82:249–256. (Cited in page 53.)

Seljak, U., Makarov, A., McDonald, P., Anderson, S. F., Bahcall, N. A., Brinkmann, J., Burles, S., Cen, R., Doi, M., Gunn, J. E., Ivezić, Ž., Kent, S., Loveday, J., Lupton, R. H., Munn, J. A., Nichol, R. C., Ostriker, J. P., Schlegel, D. J., Schneider, D. P., Tegmark, M., Berk, D. E., Weinberg, D. H., and York, D. G. (2005). Cosmological parameter analysis including SDSS Lyα forest and galaxy bias: Constraints on the primordial spectrum of fluctuations, neutrino mass, and dark energy. Phys. Rev. D, 71(10):103515. (Cited in page 109.)

Sereno, M., Veropalumbo, A., Marulli, F., Covone, G., Moscardini, L., and Cimatti, A. (2015). New constraints on σ_8 from a joint analysis of stacked gravitational lensing and clustering of galaxy clusters. MNRAS, 449:4147–4161. (Cited in page 68.)

Shane, C. and Wirtanen, C. (1967). *Public Lick Observatory, Vol. XXII, Part I.* (Cited in page 59.)

Shane, C. D. (1964). Lick Observatory: The First 75 Years. PASP, 76:77. (Cited in pages 53 and 56.)

Shectman, S. A., Landy, S. D., Oemler, A., Tucker, D. L., Lin, H., Kirshner, R. P., and Schechter, P. L. (1996). The Las Campanas Redshift Survey. ApJ, 470:172. (Cited in page 61.)

Sheth, R. K., Mo, H. J., and Tormen, G. (2001). Ellipsoidal collapse and an improved model for the number and spatial distribution of dark matter haloes. MNRAS, 323:1–12. (Cited in pages 32, 34, 35, 36, 37, 94, 103 and 104.)

Sheth, R. K. and Tormen, G. (1999). Large-scale bias and the peak background split. MNRAS, 308:119–126. (Cited in pages 29, 32, 34, 35, 36, 80 and 209.)

Simon, P. (2007). How accurate is Limber's equation? A&A, 473:711–714. (Cited in page 59.)

Smoot, G. F., Bennett, C. L., Kogut, A., Wright, E. L., Aymon, J., Boggess, N. W., Cheng, E. S., de Amici, G., Gulkis, S., Hauser, M. G., Hinshaw, G., Jackson, P. D., Janssen, M., Kaita, E., Kelsall, T., Keegstra, P., Lineweaver, C., Loewenstein, K., Lubin, P., Mather, J., Meyer, S. S., Moseley, S. H., Murdock, T., Rokke, L., Silverberg, R. F., Tenorio, L., Weiss, R., and Wilkinson, D. T. (1992). Structure in the COBE differential microwave radiometer first-year maps. ApJ, 396:L1–L5. (Cited in page 7.)

Spergel, D. N., Bean, R., Doré, O., Nolta, M. R., Bennett, C. L., Dunkley, J., Hinshaw, G., Jarosik, N., Komatsu, E., Page, L., Peiris, H. V., Verde, L., Halpern, M., Hill, R. S., Kogut, A., Limon, M., Meyer, S. S., Odegard, N., Tucker, G. S., Weiland, J. L., Wollack, E., and Wright, E. L. (2007). Three-Year Wilkinson Microwave Anisotropy Probe (WMAP) Observations: Implications for Cosmology. ApJS, 170:377–408. (Cited in page 90.)

Spergel, D. N., Verde, L., Peiris, H. V., Komatsu, E., Nolta, M. R., Bennett, C. L., Halpern, M., Hinshaw, G., Jarosik, N., Kogut, A., Limon, M., Meyer, S. S., Page, L., Tucker, G. S., Weiland, J. L., Wollack, E., and Wright, E. L. (2003). First-Year Wilkinson Microwave Anisotropy Probe (WMAP) Observations: Determination of Cosmological Parameters. ApJS, 148:175–194. (Cited in page 80.)

Springel, V. (2005). The cosmological simulation code GADGET-2. MNRAS, 364:1105–1134. (Cited in pages 90 and 101.)

Springel, V., White, S. D. M., Jenkins, A., Frenk, C. S., Yoshida, N., Gao, L., Navarro, J., Thacker, R., Croton, D., Helly, J., Peacock, J. A., Cole, S., Thomas, P., Couchman, H., Evrard, A., Colberg, J., and Pearce, F. (2005). Simulations of the formation, evolution and clustering of galaxies and quasars. Nature, 435:629–636. (Cited in pages 27, 28, 90 and 209.)

Strauss, M. A., Cen, R., Ostriker, J. P., Lauer, T. R., and Postman, M. (1995). Can standard cosmological models explain the observed Abell cluster bulk flow? ApJ, 444:507–519. (Cited in page 72.)

Sun, L., Fan, Z.-H., Tao, C., Kneib, J.-P., Jouvel, S., and Tilquin, A. (2009). Catastrophic Photo-z Errors and the Dark Energy Parameter Estimates with Cosmic Shear. ApJ, 699:958–967. (Cited in pages 121 and 211.)

Sunyaev, R. A. and Zeldovich, Y. B. (1972). The Observations of Relic Radiation as a Test of the Nature of X-Ray Radiation from the Clusters of Galaxies. *Comments on Astrophysics and Space Physics*, 4:173. (Cited in page 45.)

Suto, D., Kawahara, H., Kitayama, T., Sasaki, S., Suto, Y., and Cen, R. (2013). Validity of Hydrostatic Equilibrium in Galaxy Clusters from Cosmological Hydrodynamical Simulations. ApJ, 767:79. (Cited in pages 46 and 48.)

Tegmark, M. (1997). Measuring Cosmological Parameters with Galaxy Surveys. *Physical Review Letters*, 79:3806–3809. (Cited in page 80.)

Tegmark, M., Blanton, M. R., Strauss, M. A., Hoyle, F., Schlegel, D., Scoccimarro, R., Vogeley, M. S., Weinberg, D. H., Zehavi, I., Berlind, A., Budavari, T., Connolly, A., Eisenstein, D. J., Finkbeiner, D., Frieman, J. A., Gunn, J. E., Hamilton, A. J. S., Hui, L., Jain, B., Johnston, D., Kent, S., Lin, H., Nakajima, R., Nichol, R. C., Ostriker, J. P., Pope, A., Scranton, R., Seljak, U., Sheth, R. K., Stebbins, A., Szalay, A. S., Szapudi, I., Verde, L., Xu, Y., Annis, J., Bahcall, N. A., Brinkmann, J., Burles, S., Castander, F. J., Csabai, I., Loveday, J., Doi, M., Fukugita, M., Gott, III, J. R., Hennessy, G., Hogg, D. W., Ivezić, Ž., Knapp, G. R., Lamb, D. Q., Lee, B. C., Lupton, R. H., McKay, T. A., Kunszt, P., Munn, J. A., O'Connell, L., Peoples, J., Pier, J. R., Richmond, M., Rockosi, C., Schneider, D. P., Stoughton, C., Tucker, D. L., Vanden Berk, D. E., Yanny, B., York, D. G., and SDSS Collaboration (2004). The Three-Dimensional Power Spectrum of Galaxies from the Sloan Digital Sky Survey. ApJ, 606:702–740. (Cited in pages 58 and 209.)

Tegmark, M., Hamilton, A. J. S., Strauss, M. A., Vogeley, M. S., and Szalay, A. S. (1998). Measuring the Galaxy Power Spectrum with Future Redshift Surveys. ApJ, 499:555–576. (Cited in page 103.)

The Dark Energy Survey Collaboration (2005). The Dark Energy Survey. *ArXiv Astrophysics e-prints*. (Cited in pages 120 and 173.)

Thuan, T. X. and Gunn, J. E. (1976). A new four-color intermediate-band photometric system. PASP, 88:543–547. (Cited in page 72.)

Tinker, J., Kravtsov, A. V., Klypin, A., Abazajian, K., Warren, M., Yepes, G., Gottlöber, S., and Holz, D. E. (2008). Toward a Halo Mass Function for Precision Cosmology: The Limits of Universality. ApJ, 688:709–728. (Cited in pages 29, 74, 77 and 90.)

Tinker, J. L., Robertson, B. E., Kravtsov, A. V., Klypin, A., Warren, M. S., Yepes, G., and Gottlöber, S. (2010). The Large-scale Bias of Dark Matter Halos: Numerical Calibration

and Model Tests. ApJ, 724:878–886. (Cited in pages 36, 37, 103, 104, 105, 106, 108, 109, 110, 115, 172, 209, 210 and 211.)

Tinker, J. L., Weinberg, D. H., Zheng, Z., and Zehavi, I. (2005). On the Mass-to-Light Ratio of Large-Scale Structure. ApJ, 631:41–58. (Cited in page 36.)

Totsuji, H. and Kihara, T. (1969). The Correlation Function for the Distribution of Galaxies. PASJ, 21:221. (Cited in pages , 53, 56 and 59.)

Tucker, D. L., Oemler, Jr., A., Kirshner, R. P., Lin, H., Shectman, S. A., Landy, S. D., Schechter, P. L., Muller, V., Gottlober, S., and Einasto, J. (1997). The Las Campanas Redshift Survey galaxy-galaxy autocorrelation function. MNRAS, 285:L5–L9. (Cited in pages 61 and 62.)

Veropalumbo, A., Marulli, F., Moscardini, L., Moresco, M., and Cimatti, A. (2014). An improved measurement of baryon acoustic oscillations from the correlation function of galaxy clusters at z 0.3. MNRAS, 442:3275–3283. (Cited in pages 22, 82 and 174.)

Veropalumbo, A., Marulli, F., Moscardini, L., Moresco, M., and Cimatti, A. (2016). Measuring the distance-redshift relation with the baryon acoustic oscillations of galaxy clusters. MNRAS, 458:1909–1920. (Cited in pages 22, 83, 85, 86, 210 and 213.)

Vikhlinin, A., Kravtsov, A. V., Burenin, R. A., Ebeling, H., Forman, W. R., Hornstrup, A., Jones, C., Murray, S. S., Nagai, D., Quintana, H., and Voevodkin, A. (2009). Chandra Cluster Cosmology Project III: Cosmological Parameter Constraints. ApJ, 692:1060–1074. (Cited in pages 73, 74 and 210.)

Vogelsberger, M., Genel, S., Springel, V., Torrey, P., Sijacki, D., Xu, D., Snyder, G., Nelson, D., and Hernquist, L. (2014). Introducing the Illustris Project: simulating the coevolution of dark and visible matter in the Universe. MNRAS, 444:1518–1547. (Cited in page 89.)

Voges, W., Aschenbach, B., Boller, T., Bräuninger, H., Briel, U., Burkert, W., Dennerl, K., Englhauser, J., Gruber, R., Haberl, F., Hartner, G., Hasinger, G., Kürster, M., Pfeffermann, E., Pietsch, W., Predehl, P., Rosso, C., Schmitt, J. H. M. M., Trümper, J., and Zimmermann, H. U. (1999). The ROSAT all-sky survey bright source catalogue. A&A, 349:389–405. (Cited in page 44.)

Wang, S., Khoury, J., Haiman, Z., and May, M. (2004). Constraining the evolution of dark energy with a combination of galaxy cluster observables. Phys. Rev. D, 70(12):123008. (Cited in page 80.)

Weinberg, D. H., Bullock, J. S., Governato, F., Kuzio de Naray, R., and Peter, A. H. G. (2015). Cold dark matter: Controversies on small scales. *Proceedings of the National Academy of Science*, 112:12249–12255. (Cited in page 32.)

Weinberg, D. H., Mortonson, M. J., Eisenstein, D. J., Hirata, C., Riess, A. G., and Rozo, E. (2013). Observational probes of cosmic acceleration. Phys. Rep., 530:87–255. (Cited in pages 22, 83 and 209.)

Wen, Z. L., Han, J. L., and Liu, F. S. (2009). Galaxy Clusters Identified from the SDSS DR6 and Their Properties. ApJS, 183:197–213. (Cited in pages 68, 84 and 85.)

Wen, Z. L., Han, J. L., and Liu, F. S. (2012). A Catalog of 132,684 Clusters of Galaxies Identified from Sloan Digital Sky Survey III. ApJS, 199:34. (Cited in pages 68, 85 and 94.)

White, S. D. M. (1976). The dynamics of rich clusters of galaxies. MNRAS, 177:717–733. (Cited in page 87.)

White, S. D. M., Davis, M., Efstathiou, G., and Frenk, C. S. (1987). Galaxy distribution in a cold dark matter universe. Nature, 330:451–453. (Cited in page 15.)

WMAP CMB radiation (2007). Cmb radiation, wmap. `http://map.gsfc.nasa.gov/media/121238/index.html`. [Online; accessed 22-July-2016]. (Cited in page 7.)

Wolf, M. (1924). Einige stärker bewegte Sterne in Coma und Virgo. *Astronomische Nachrichten*, 222:15. (Cited in page 3.)

Wright, E. L. (1995). Comments on the quasi-steady-state cosmology. MNRAS, 276:1421–1424. (Cited in page 4.)

Wu, H.-Y., Rozo, E., and Wechsler, R. H. (2008). The Effects of Halo Assembly Bias on Self-Calibration in Galaxy Cluster Surveys. ApJ, 688:729–741. (Cited in page 81.)

Younger, J. D., Bahcall, N. A., and Bode, P. (2005). Evolution of the cluster mass and correlation functions in lambda-CDM cosmology. *Astrophys. J.*, 622:1–6. (Cited in pages 68, 94, 95, 98, 101, 102, 111, 112, 113, 114, 115, 172 and 210.)

Zehavi, I., Blanton, M. R., Frieman, J. A., Weinberg, D. H., Mo, H. J., Strauss, M. A., Anderson, S. F., Annis, J., Bahcall, N. A., Bernardi, M., Briggs, J. W., Brinkmann, J., Burles, S., Carey, L., Castander, F. J., Connolly, A. J., Csabai, I., Dalcanton, J. J., Dodelson, S., Doi, M., Eisenstein, D., Evans, M. L., Finkbeiner, D. P., Friedman, S., Fukugita, M., Gunn, J. E., Hennessy, G. S., Hindsley, R. B., Ivezić, Ž., Kent, S., Knapp, G. R., Kron, R., Kunszt, P., Lamb, D. Q., Leger, R. F., Long, D. C., Loveday, J., Lupton, R. H., McKay, T., Meiksin, A., Merrelli, A., Munn, J. A., Narayanan, V., Newcomb, M., Nichol, R. C., Owen, R., Peoples, J., Pope, A., Rockosi, C. M., Schlegel, D., Schneider, D. P., Scoccimarro, R., Sheth, R. K., Siegmund, W., Smee, S., Snir, Y., Stebbins, A., Stoughton, C., SubbaRao, M., Szalay, A. S., Szapudi, I., Tegmark, M., Tucker, D. L., Uomoto, A., Vanden Berk, D., Vogeley, M. S., Waddell, P., Yanny, B., and York, D. G. (2002). Galaxy Clustering in Early Sloan Digital Sky Survey Redshift Data. ApJ, 571:172–190. (Cited in page 62.)

Zehavi, I., Zheng, Z., Weinberg, D. H., Frieman, J. A., Berlind, A. A., Blanton, M. R., Scoccimarro, R., Sheth, R. K., Strauss, M. A., Kayo, I., Suto, Y., Fukugita, M., Nakamura, O., Bahcall, N. A., Brinkmann, J., Gunn, J. E., Hennessy, G. S., Ivezić, Ž., Knapp, G. R., Loveday, J., Meiksin, A., Schlegel, D. J., Schneider, D. P., Szapudi, I., Tegmark, M., Vogeley, M. S., York, D. G., and SDSS Collaboration (2005). The Luminosity and Color Dependence of the Galaxy Correlation Function. ApJ, 630:1–27. (Cited in pages 61, 62, 93 and 209.)

Zheng, Z., Berlind, A. A., Weinberg, D. H., Benson, A. J., Baugh, C. M., Cole, S., Davé, R., Frenk, C. S., Katz, N., and Lacey, C. G. (2005). Theoretical Models of the Halo Occupation Distribution: Separating Central and Satellite Galaxies. ApJ, 633:791–809. (Cited in page 152.)

Zwicky, F., Herzog, E., Wild, P., Karpowicz, M., and Kowal, C. T. (1961). *Catalogue of galaxies and of clusters of galaxies, Vol. I.* (Cited in pages 53 and 56.)